SISSA
Scuola Internazionale Superiore di Studi Avanzati

Physics Area - PhD course in
Astrophysics and Cosmology



Binary neutron stars and binary black holes: from the Milky Way to the high-redshift Universe

Thesis submitted for the degree of
Doctor Philosophiae

Candidate:
Cecilia Sgalletta

Advisor:
Prof. Mario Spera
Co-advisors:
Prof. Andrea Lapi
Prof. Michela Mapelli

Academic Year 2024–2025

Abstract

The majority ($\gtrsim 70$ %) of massive stars lie in a binary. The role played by binary interactions is thus critical towards the understanding of current observations. In this thesis, I use the SEVN population synthesis code to explore several major challenges in the physics of binary evolution.

In my first work I incorporate pulsars' spins and magnetic fields evolution in SEVN. I evolve binary neutron star systems in a Milky-Way model to reproduce the merger rates, orbital properties and pulsars' properties of the Galactic binary neutron star population. The analysis reveals a strong dependence of the final observed population on the birth distributions of spin period and magnetic fields.

In my second work, I address the impact of the metal-dependent star formation rate (SFR) on the binary black hole (BBH) merger rate density. To this end, I adopt the most up-to-date observational scaling relations and I study how the BBH merger rate density varies over a wide grid of galaxy and binary evolution parameters. I show that assuming a realistic metal-dependent SFR evolution yields a BBH merger rate density higher than that inferred from gravitational wave data, even when accounting for uncertainties from low-mass galaxies. The analysis suggests that stellar evolution uncertainties are the main responsible for the discrepancy between the BBH merger rate density inferred from data and theoretical models.

Lastly, I evaluate envelope binding energies directly from the PARSEC stellar tracks for a vast range of stellar masses and metallicities, investigating the impact of different core-envelope boundary criteria and energy sources. I then implement the new binding energies in SEVN. The results show that the merger rate densities of binary compact objects, when using these new consistent binding energies, can differ by more than an order of magnitude compared to models employing precomputed fits.

Not all stories unfold the way we would like to. This is the end of a story that did not go as she had planned it to.
Yet learning to live by the unexpected is part of the game.

At last she smiled, as she looked back at the friends she made along the way.

Table of contents

List of figures 11

List of tables 13

Nomenclature 15

List of publications 17

1 Introduction 1
- 1.1 Observations . . . 2
  - 1.1.1 Pulsars . . . 3
  - 1.1.2 Gravitational waves . . . 5
- 1.2 Stellar evolution of massive stars . . . 8
  - 1.2.1 Stellar winds . . . 9
  - 1.2.2 Supernova explosions and natal kicks . . . 9
- 1.3 Binary stellar evolution . . . 12
  - 1.3.1 Roche potential . . . 12
  - 1.3.2 Orbital variations . . . 14
  - 1.3.3 Stability of mass transfer . . . 15
  - 1.3.4 Stable Roche-lobe overflow . . . 16
  - 1.3.5 Common envelope . . . 17
  - 1.3.6 Mass loss from a supernova explosion and natal kicks . . . 18
  - 1.3.7 Binary compact objects from the isolated formation channel . . . 19
- 1.4 Pulsars . . . 21
- 1.5 Binary compact objects across cosmic time . . . 24

2 SEVN 27
- 2.1 Single stellar evolution . . . 28
  - 2.1.1 Stellar evolution tables . . . 28
  - 2.1.2 PARSEC stellar tracks . . . 29
  - 2.1.3 Compact remnant formation . . . 30
- 2.2 Binary evolution . . . 33
  - 2.2.1 Roche-lobe overflow . . . 33
  - 2.2.2 Common envelope . . . 36

2.2.3 Stellar mergers . . . 37
2.2.4 Gravitational waves . . . 37

3 Binary neutron star populations in the Milky Way 39
3.1 Introduction . . . 39
3.2 Methods . . . 40
3.2.1 NS properties . . . 40
3.2.2 Initial conditions for the SEVN binary catalogues . . . 43
3.2.3 Milky Way models . . . 44
3.2.4 Populating the MW with BNSs . . . 46
3.2.5 Simulation set up . . . 48
3.2.6 Selection effects . . . 49
3.2.7 Statistical analysis . . . 53
3.3 Results . . . 55
3.3.1 Merger rates . . . 55
3.3.2 Orbital period – eccentricity . . . 57
3.3.3 $P - \dot{P}$ plane . . . 60
3.3.4 Selection effects . . . 60
3.3.5 Bayes factors . . . 63
3.3.6 Predictions for the SKA . . . 64
3.4 Discussion . . . 64
3.5 Summary and conclusions . . . 67

4 Merger rate density of binary black holes 71
4.1 Introduction . . . 71
4.2 Method . . . 73
4.2.1 Population-synthesis code SEVN . . . 73
4.2.2 Initial conditions . . . 74
4.2.3 Formation channels . . . 74
4.2.4 Observational scaling relations . . . 75
4.2.5 Merger rate density . . . 78
4.2.6 Summary of model parameters . . . 78
4.3 A comparative analysis of Universe models . . . 78
4.4 Results . . . 80
4.4.1 Merger efficiency and metallicity . . . 80
4.4.2 The impact of low-mass galaxies . . . 81
4.4.3 Cosmic merger rate density . . . 83
4.4.4 Formation channels . . . 84
4.5 Discussion . . . 85
4.6 Summary . . . 89

5 A revisited common envelope formalism in SEVN **91**
5.1 Introduction . . . 91
5.2 Method . . . 92
5.2.1 PARSEC . . . 92
5.2.2 Envelope binding energy . . . 93
5.2.3 SEVN . . . 94
5.2.4 Initial conditions for SEVN . . . 95
5.2.5 Merger rate density . . . 95
5.3 Results . . . 96
5.3.1 Binding energies . . . 96
5.3.2 Comparison with the literature . . . 99
5.3.3 Pure-He stars . . . 99
5.3.4 Merger rate density . . . 102
5.4 Discussion . . . 106
5.5 Summary . . . 107

6 Conclusions and future directions **109**
6.1 Galactic binary neutron star populations . . . 109
6.2 Binary black hole merger rate . . . 110
6.3 Envelope binding energies revisited . . . 110
6.4 Future prospects . . . 111
6.4.1 Pulsars' formation in dense environments . . . 111
6.4.2 Neutron star masses . . . 112
6.4.3 Why is the BBH merger rate density so high? . . . 112

Appendix A **115**
A.1 Kick prescriptions . . . 115
A.2 Masses . . . 115
A.3 SKA survey parameters . . . 115

Appendix B **119**
B.1 Observational scaling relations . . . 119
B.1.1 Galaxy stellar mass function . . . 119
B.1.2 Star formation rate . . . 119
B.1.3 Fundamental metallicity relations . . . 120
B.2 Merger rate densities . . . 121

References **123**

List of figures

1.1 Pulsar population from the ATNF pulsar catalogue . . . 4
1.2 Masses in the stellar graveyard . . . 6
1.3 BBH merger rate . . . 7
1.4 Dependence of stellar winds on metallicity . . . 8
1.5 Compact remnant masses spectrum for different metallicities . . . 11
1.6 Equipotential surfaces of the Roche potential . . . 13
1.7 BCOs formation channels . . . 20
1.8 Pulsars lighthouse model . . . 22
1.9 Cartoon of GWs across cosmic time . . . 25

2.1 PARSEC stellar tracks in the Hertzsprung-Russell diagram . . . 31
2.2 PARSEC pure-He stellar tracks in the Hertzsprung-Russell diagram . . . 31
2.3 Possible outcomes of compact remnant formation in SEVN . . . 32

3.1 Binary neutron star merger rates in the Milky-Way . . . 56
3.2 Orbital properties of the simulated binary neutron stars at present time . . . 58
3.3 Pulsar properties of present day binary neutron stars. . . . 59
3.4 Pulsar properties' distributions of present day binary neutron stars after the application of radio selection effects. . . . 61
3.5 Mean number of radio selected pulsars by model . . . 62
3.6 Cumulative distribution of the pulsar parameters $P_{\rm orb}$, e, P and $\dot{P}$. . . . 63
3.7 Two-dimensional likelihood distributions. . . . 64

4.1 SFR density across redshifts for different models considered. . . . 75
4.2 Schematic overview of the metal-dependent SFR models adopted. . . . 80
4.3 BBHs merger efficiency as a function o metallicity . . . 81
4.4 Galaxies contribution to the SFR density, for different metallicity thresholds 82
4.5 BBH merger rate density as a function of redshift for different models . . . 83
4.6 BBH merger rate density as a function of redshift for different BBH formation channels . . . 85
4.7 Effect of natal-kicks on the BBH merger rate density . . . 86

5.1 Envelope binding energies for H-rich stars evaluated from the PARSEC stellar tracks . . . 97

5.2 Envelope binding energies evolution colored by the outer convective envelope fraction . . . 98
5.3 Comparison of different envelope binding energy prescriptions for $Z = 10^{-11}$ 100
5.4 Comparison of different envelope binding energy prescriptions for $Z = 0.0001$ 101
5.5 Comparison of different envelope binding energy prescriptions for $Z = 0.01$ 102
5.6 Envelope binding energies for pure-He stars evaluated from the PARSEC stellar tracks . . . 103
5.7 BCO merger efficiency for different envelope binding energy prescriptions . 104
5.8 BCO merger rate densities for different envelope binding energy prescriptions 105
5.9 Envelope binding energies evolution colored by the total convective envelope fraction . . . 106

6.1 Compact remnant masses following the model by Woosley, Sukhbold, et al. (2020). . . . 113

A.1 BNS merger rate for different natal kick models . . . 116
A.2 NS masses distributions for different SN prescriptions . . . 116

B.1 SFR density as a function of galaxy mass and metallicity . . . 120
B.2 BBH cosmic merger rate densities for different fundamental metallicity relations . . . 121

List of tables

2.1 Fiducial model for the stability of mass transfer 34

3.1 Properties of the Milky-Way models 46
3.2 Spin periods and magnetic fields initial distributions. 48
3.3 Summary of the simulated models 50
3.4 Sample of radio pulsars 55
3.5 Present day binary neutron star merger rates in the Milky-Way 57
3.6 Bayes factors of the simulated models 65
3.7 Predicted number of pulsars in BNSs detectable by the SKA 65

4.1 Summary of the grid of parameters varied. 79

A.1 Adopted parameters for the LOW and MID SKA surveys 117

Nomenclature

BBH	binary black hole
BCO	binary compact object
BH	black hole
BHNS	black hole - neutron star
BNS	binary neutron star
CE	common envelope
CO	carbon-oxygen
GW	gravitational wave
H	hydrogen
He	helium
LVK	LIGO-Virgo-KAGRA
MS	main sequence
MW	Milky-Way
NS	neutron star
RLO	Roche-lobe overflow
SFR	star formation rate
SKA	Square Kilometer Array
SN	supernova
WD	white dwarf
ZAMS	zero-age main sequence

List of publications

1. **Cecilia Sgalletta**, Michela Mapelli, Lumen Boco, Filippo Santoliquido, M. Celeste Artale, Giuliano Iorio, Andrea Lapi and Mario Spera, *The more accurately the metal-dependent star formation rate is modeled, the larger the predicted excess of binary black hole mergers*, A&A **698**, A144 (2025). DOI:10.1051/0004-6361/202452757

2. Kendall G. Shepherd, Guglielmo Costa, Cristiano Ugolini, Guglielmo Volpato, Diego Bossini, **Cecilia Sgalletta**, Francesco Addari, Alessandro Bressan, Leo Girardi and Mario Spera, *Enhanced Mass Loss of Very Massive Stars: Impact on the Evolution, Binary Processes, and Remnant Mass Spectrum*, arXiv e-prints arXiv:2505.10206 (2025). DOI:10.48550/arXiv.2505.10206

3. Filippo Simonato, Stefano Torniamenti, Michela Mapelli, Giuliano Iorio, Lumen Boco, Franca De Domenico-Langer and **Cecilia Sgalletta**, *Impact of stellar winds on the pair-instability supernova rate*, arXiv e-prints arXiv:2505.07959 (2025). DOI:10.48550/arXiv.2505.07959

4. Marco Dall'Amico, Michela Mapelli, Giuliano Iorio, Guglielmo Costa, Stéphane Charlot, Erika Korb, **Cecilia Sgalletta** and Marie Lecroq, *Impact of accretion-induced chemically homogeneous evolution on stellar and compact binary populations*, A&A **695**, A221 (2025). DOI:10.1051/0004-6361/202453543

5. Francesco Gabrielli, Andrea Lapi, Lumen Boco, Cristiano Ugolini, Guglielmo Costa, **Cecilia Sgalletta**, Kendall Shepherd, Ugo N. Di Carlo, Alessandro Bressan, Marco Limongi and Mario Spera, *The cosmic rate of pair-instability supernovae*, Mon. Not. R. Astron. Soc. **534**, 151 (2024). DOI:10.1093/mnras/stae2048

6. Giuliano Iorio, Stefano Torniamenti, Michela Mapelli, Marco Dall'Amico, Alessandro A. Trani, Sara Rastello, **Cecilia Sgalletta**, Stefano Rinaldi, Guglielmo Costa, Bera A. Dahl-Lahtinen, Gastón J. Escobar, Erika Korb, M. Paola Vaccaro, Elena Lacchin, Benedetta Mestichelli, Ugo N. Di Carlo, Mario Spera and Manuel Arca Sedda, *The boring history of Gaia BH3 from isolated binary evolution*, A&A **690**, A144 (2024). DOI:10.1051/0004-6361/202450531

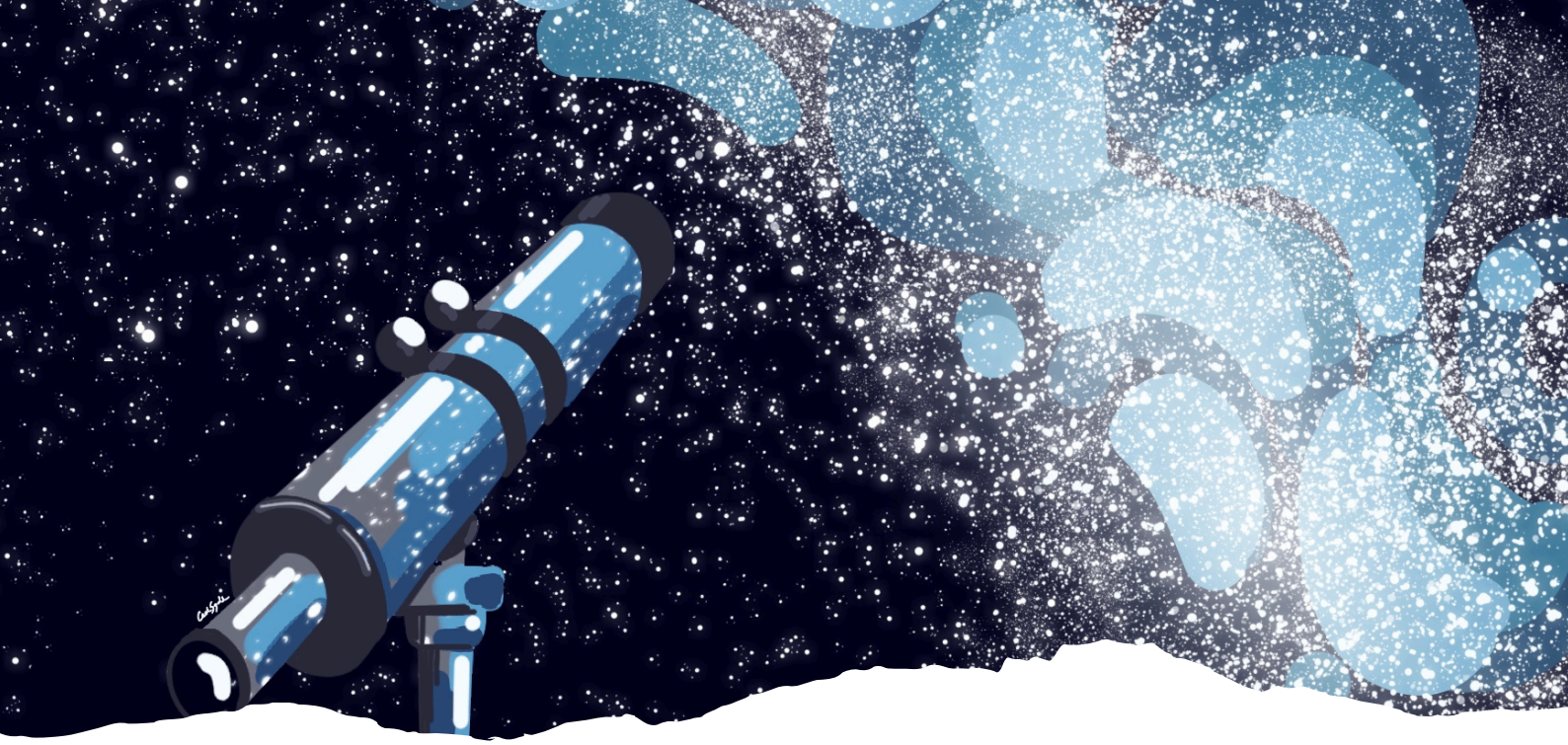
7. **Cecilia Sgalletta**, Giuliano Iorio, Michela Mapelli, M. Celeste Artale, Lumen Boco, Debatri Chattopadhyay, Andrea Lapi, Andrea Possenti, Stefano Rinaldi and Mario Spera, *Binary neutron star populations in the Milky Way*, Mon. Not. R. Astron. Soc. **526**, 2210 (2023). DOI:10.1093/mnras/stad2768

8. Giuliano Iorio, Michela Mapelli, Guglielmo Costa, Mario Spera, Gastón J. Escobar, **Cecilia Sgalletta**, Alessandro A. Trani, Erika Korb, Filippo Santoliquido, Marco Dall'Amico, Nicola Gaspari and Alessandro Bressan, *Compact object mergers: exploring uncertainties from*

stellar and binary evolution with SEVN, Mon. Not. R. Astron. Soc. **524**, 426 (2023). DOI:10.1093/mnras/stad1630

9. Ruggero Valli, Luca Graziani and the **LISA Synthetic UCB Catalogue Group**, *BinCodex: a common output format for binary population synthesis*, arXiv e-prints, art. arXiv:2311.03431 (2023). doi:10.48550/arXiv.2311.03431

10. Rosalba Perna, M. Celeste Artale, Yi-Han Wang, Michela Mapelli, Davide Lazzati, **Cecilia Sgalletta** and Filippo Santoliquido, *Host galaxies and electromagnetic counterparts to binary neutron star mergers across the cosmic time: detectability of GW170817-like events*, Mon. Not. R. Astron. Soc. **512**, 2654 (2022). DOI:10.1093/mnras/stac685



Chapter 1

Introduction

Over the past decades, the demography of compact objects has grown significantly. The vast pulsars' population, black holes (BHs) and neutron stars (NSs) X-ray binaries, the detections of gravitational waves (GWs) from binary compact object (BCO) mergers, and, more recently, the identification of quiescent BHs in binaries through astrometric data from Gaia, have all contributed to an increasingly rich and diverse population of compact objects.

Pulsars hold a prominent role within the astrophysical scenario. They serve as unique laboratories for tests of general relativity (e.g., Damour and Taylor, 1992; Kramer et al., 2006; Wex, 2014; Kramer et al., 2021) and for the study of the equation of state of super-dense matter (e.g., Özel, Psaltis, Güver, et al., 2016). The extreme precision of their pulses' arrivals can be compared to that of atomic clocks. It enables the study of nano-Hz GWs via pulsar timing arrays, which have recently reported a strong evidence for a GW background (Agazie et al., 2023; EPTA Collaboration et al., 2023; Reardon et al., 2023; Xu, Chen, et al., 2023; Miles et al., 2025). Furthermore, as the end-products of massive stellar evolution, pulsars are the imprints of their progenitors' evolutionary histories.

While pulsars are exceptional electromagnetic tools to investigate the properties of NSs and their companions, a new observational window opened with the detection of GWs in 2015. The first event, GW150914 (Abbott et al., 2016), proved evidence for the existence of binary black holes (BBHs). Following the initial detection, the binary neutron star (BNS) merger

event, GW170817 (Abbott et al., 2017c), immediately stood out. This event, accompanied by a short gamma-ray burst and a kilonova (Abbott et al., 2017a; Abbott et al., 2017d), marked the beginning of a new multi-messenger era. The following observational runs have further increased the GW catalog including, among others, the detection of black hole - neutron star (BHNS) mergers (Abbott et al., 2021b).

It is therefore important to acquire a thorough understanding of the evolutionary histories of massive binary stars, their interplay with the environment, and the formation of compact remnants, in order to accurately interpret both current and future astrophysical observations. Nevertheless, many aspects of massive star evolution and binary physics remain uncertain. Among the most problematic phases of evolution are the supernova (SN) explosion mechanism and the natal kicks imparted to newly formed compact objects. At least as uncertain are binary mass transfer processes and common envelope (CE) evolution. These processes have profound implications on the demography of BCOs, influencing their properties and formation channels. Finally, several questions regarding pulsars, particularly their birth properties and magnetic field evolution, are still unanswered.

This thesis focuses on the isolated formation channel of BCOs and aims to investigate some of these open questions. Specifically, I will adopt a comprehensive approach to explore the main binary evolution uncertainties from diverse perspectives: first, by examining the Galactic pulsar population, and then by analyzing the population of BBHs across cosmic time. In doing so, this thesis provides an exhaustive overview of some of the primary research questions in two key areas of astrophysics, namely, the study of pulsars and GWs. Finally, I will revisit the CE treatment in the population synthesis code SEVN (Spera and Mapelli, 2017; Spera, Mapelli, et al., 2019; Iorio et al., 2023) to improve our theoretical predictions.

The thesis is organized as follows. In this chapter, I present the state-of-the-art observational and theoretical framework relevant to compact objects. I describe the main processes shaping their final fates in both single and binary stellar evolution, and briefly outline how these evolutionary pathways are coupled with their environments. This chapter follows in part the book Tauris and van den Heuvel (2023) and integrates various reviews, primarily Mapelli (2021), Spera, Trani, et al. (2022), and Marchant and Bodensteiner (2024). Chapter 2 introduces the population synthesis code SEVN adopted in this work, detailing its main features. The following chapters present the main results of my research. Chapter 3 presents a detailed study of the Galactic pulsar population. Chapter 4 focuses on the cosmic merger rate density of BBHs and the uncertainties stemming from the cosmic star formation rate (SFR) . Chapter 5 describes the newly implemented CE formalism in SEVN, exploring its main implications for the properties of BCOs. Finally, I summarize the main results and discuss potential future directions in Chapter 6.

1.1 Observations

Massive stars are the progenitors of NSs and BHs. While they constitute $\lesssim 1\%$ of the total stellar population (Kroupa, 2001), they deeply influence their environments and drive some of the Universe's most intriguing astrophysical phenomena. Crucially, the majority of massive stars are not isolated but are part of binary or higher-order multiple systems (Levato et al.,

1987; Abt et al., 1990; Kobulnicky et al., 2007). Surveys targeting OB-stars, which are often considered as initial conditions for massive star evolution, find that $\gtrsim 70\%$ of these objects are in close binaries (e.g., Sana et al., 2012). A recent study by Moe et al. (2017) suggest that the binary fraction in close binaries is mass-dependent, approaching 100% for stars with masses $> 16\,M_\odot$. Therefore, it is clear that the evolution within binaries must be taken into account. Early evidence of the importance of binary interactions emerged in the 1950s, prompted by the Algol-type systems *paradox*. The main feature of Algol-type systems is that the more evolved star is also the one with the smaller mass (similarly to the Algol system, Goodricke, 1783). This seemingly contradicts with the fact that more massive stars evolve faster and thus have shorter lifetimes. The paradox was resolved by Crawford (1955). He proposed that an inversion of the system's initial mass ratio occurred after a mass transfer episode.

The role of binary interactions appeared increasingly compelling with later discoveries. Among the most interesting systems, stand out Centaurus X-3 (Schreier et al., 1972), the first discovered NS X-ray binary and Cygnus X-1 (Bolton, 1972; Webster et al., 1972), the first detection of a BH X-ray binary. Cygnus X-1 is especially interesting and continues to baffle astrophysicists. It consists of a BH with mass $\sim 20\,M_\odot$ orbiting a massive blue supergiant companion, HDE 226868. The BH spin is notably high, rotating at close to its maximum possible rate (Jiang, 2024). For this reason its formation is still not fully clear, although several possible scenarios have been proposed (e.g., Batta et al., 2017; Qin et al., 2019; Gallegos-Garcia, Fishbach, et al., 2022).

Most recently, the detection of GWs (Abbott et al., 2016; Abbott et al., 2017b; Abbott et al., 2021a; Abbott et al., 2021c; Abbott et al., 2023b; Abbott et al., 2023a) from merging compact binaries, including BBHs, BNSs, and BHNS systems, represented a turning point in astrophysics, confirming the final fate of close BCOs (see also Section 1.1.2).

Finally, a third class of observable BHs, emerged only in the past few years: quiescent BHs. These BHs are part of binary systems but do not emit in X-ray or in radio. The main techniques to uncover this class of BHs are astrometry or radial velocity measurements. In particular, the *Gaia* mission is expected to detect a few tens of such quiescent BHs (Breivik, Chatterjee, et al., 2017; Mashian et al., 2017; Yamaguchi et al., 2018; Janssens et al., 2022). The three BHs announced so far (El-Badry, Rix, Cendes, et al., 2023; El-Badry, Rix, Quataert, et al., 2023; Gaia Collaboration et al., 2024) have already enlightened the discussion in the astrophysical community. Among them, Gaia BH3 (Gaia Collaboration et al., 2024) is the first discovered quiescent BH with a mass $\gtrsim 30\,M_\odot$ and the first such high-mass stellar BH observed apart from GW binaries.

1.1.1 Pulsars

Pulsars were discovered in 1967 by Jocelyn Bell and Antony Hewish (Hewish et al., 1968). The first detection was soon followed by the identification of the Crab pulsar (Staelin et al., 1968). These observations marked a decisive moment, establishing pulsars as the first observed class of NSs. Early investigations quickly revealed their extreme properties, including magnetic field strengths reaching $10^{14} - 10^{16}$G. The discovery of the first pulsar in

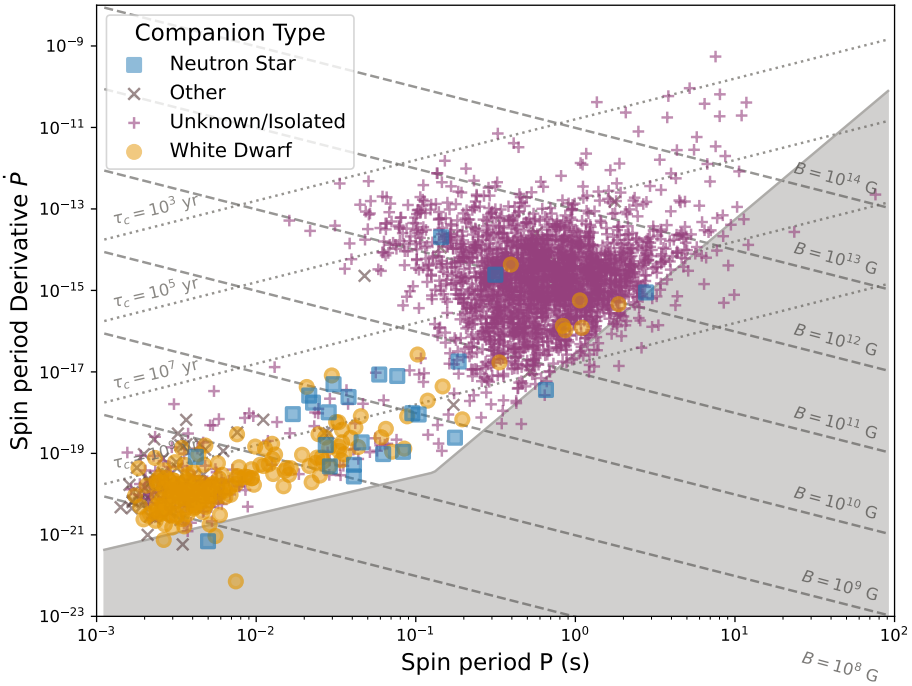


Fig. 1.1 Observed pulsars in the spin period P – spin period derivative $\dot{P}$ diagram. The pulsars data is taken from the ATNF pulsar catalogue (Manchester, Hobbs, et al., 2005). Isolated pulsars or those with unknown companion types are represented by purple crosses. Other colors and markers indicate different pulsars companion types: white dwarfs (WDs, ∘, orange) , NSs (□, blue), other types (×, gray). The gray shaded region marks the pulsar "death valley", adopting the model by Rudak et al. (1994). Dashed lines indicate points of constant surface magnetic field (B), decreasing from $B = 10^{14}$G at the top to $B = 10^{8}$G, at the bottom. Dotted lines denote constant characteristic age (τ_c), increasing from top ($\tau_c = 10^3$ yr) to bottom ($\tau_c = 10^9$ yr).

a binary system (Hulse et al., 1975) marked another breakthrough in the field. Indeed, the precise arrival times of the pulsar beam allowed for accurate measurements of the orbital dynamics and revealed the first BNS system. Finally, PSR J0737–3039 (Burgay et al., 2003; Lyne, Burgay, et al., 2004) is the first and only observed double pulsar system. Measurements of its orbit allowed unprecedented tests of gravity and equation of state (Morrison et al., 2004; Podsiadlowski et al., 2005; Bejger et al., 2005; Kramer et al., 2006; Kramer and Wex, 2009). Today, the known pulsar population has grown significantly, counting around 2400 observed pulsars. The next-generation radio detector, Square Kilometer Array (SKA) , is expected to boost this number even further (Keane, Bhattacharyya, et al., 2015).

Figure 1.1 shows these pulsars in the spin period (P) – spin period derivative ($\dot{P}$) plane. A glance at this figure reveals that pulsars can be broadly categorized into two main groups. A first bulk characterized by spin periods $P \sim 0.2 - 2$s and $\dot{P} \sim 10^{-16} - 10^{-12}$. These pulsars typically possess strong magnetic fields, on the order of $B \sim 10^{10} - 10^{13}$G. Moreover, the majority of them are isolated pulsars (purple crosses). A second cluster of objects can be distinguished in the lower left corner of the plot. These pulsars are characterized by much

shorter spin periods, $P \lesssim 30$ ms, hence their name of millisecond pulsars. They also exhibit lower magnetic fields ($B \lesssim 10^9$ G). As evident from the figure, most millisecond pulsars are part of a binary system. The high percentage of binaries suggests that their peculiar properties are directly linked to the evolution within the binary system itself. As I will describe in detail in Section 1.4 (see also Chapter 3), this process is known as *recycling*. During this time, mass and angular momentum are transferred from the companion star to the pulsar, leading to the pulsar's spin up (van den Heuvel, 1984; Bhattacharya et al., 1991; Lorimer, 2008). The gray-shaded region in the diagram illustrates the *death valley*, an area where no radio pulsars have been observed (Chen and Ruderman, 1993).

Further categories can be defined based on their observed properties. Among these stand out the *magnetars* (e.g., Duncan et al., 1992; Kaspi and Beloborodov, 2017), characterized by extreme magnetic fields ($B \sim 10^{14}$ G), *rotating radio transients* (e.g., Keane, Kramer, et al., 2011), *isolated X-ray dim NSs* (e.g., Popov et al., 2006; Kondratiev et al., 2009), *central compact objects* of SN remnants (e.g., Pavlov et al., 2004), *intermittent pulsars* such as *black widows* and *redbacks* (e.g., Roberts, 2013; Chen, Chen, et al., 2013). This variety underlines the complex nature of these objects. One of the challenges today is to formulate a coherent framework able to explain this wide array of observations (Kaspi, 2010).

Furthermore, several fundamental questions persist: How does a pulsar's magnetic field evolve? What are the birth properties of pulsars? How do NSs interact with their companions in binary systems? Addressing these questions is crucial for advancing our understanding of the physics and end-of-life stages of massive binary stars, as well as the SN process itself.

1.1.2 Gravitational waves

The advent of GWs, with the detection of GW150914, the first BBH merger opened a new window on the observable Universe. Since then, many more events have been recorded and the whole catalogue to date counts ~ 200 events (Abbott et al., 2021a; Abbott et al., 2023b). While the existence of BNSs was already known thanks to pulsar observations (e.g., Hulse et al., 1975), GWs offered the first confirmation of BBH and BHNS systems (Abbott et al., 2016; Abbott et al., 2021b). GW observations have also deeply impacted our understanding of stellar evolution. Prior to GW150914, most stellar models did not predict BH masses above $\sim 30\,M_\odot$. In fact, the BHs observed in X-ray binaries up to that moment had masses only up to $20\,M_\odot$ (Orosz, 2003; Özel, Psaltis, Narayan, and McClintock, 2010; Miller-Jones et al., 2021). GWs completely revolutionized the field. GW150914 itself involved BHs with masses of $35.6\,M_\odot$ and $30.6\,M_\odot$. GW170817 was the first BNS merger detected (Abbott et al., 2017c). Notably, it was also unquestionably associated with an electromagnetic counterpart. This detection confirmed the connection between BNS mergers, short gamma ray bursts and kilonovae (Abbott et al., 2017d).

GWs are further challenging existing stellar evolutionary models by providing observations of BHs within the theorized lower and upper mass gaps (e.g., Abbott et al., 2020a; Abbott et al., 2020b; Abbott et al., 2020c; Abac et al., 2024). For instance, GW190814 consists of a merger between a $23\,M_\odot$ BH and a lighter compact object of mass $2.59\,M_\odot$ (Abbott et al., 2020c). The latter is either one of the lightest BHs ever discovered or the

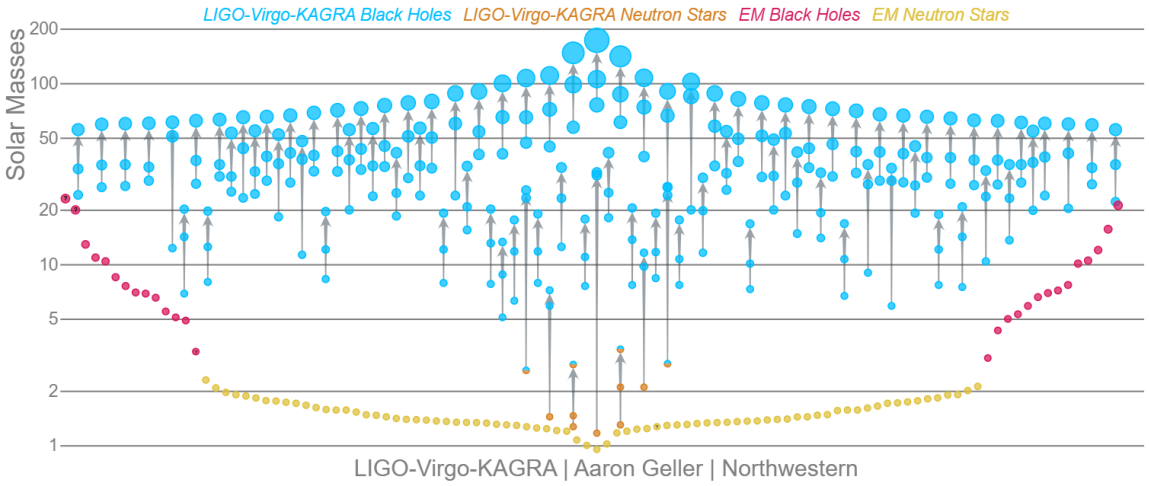


Fig. 1.2 Representation of the derived masses of compact objects from different observations. Blue: BH masses derived from the detected LIGO-Virgo-KAGRA (LVK) merger events in the O1–O3a runs. Orange: NS masses derived from the detected LVK merger events in the O1–O3a runs. Red: BH masses derived from X-ray binaries. Yellow: NS masses derived from electromagnetic observations. The objects are ordered arbitrarily along the x-axis. Image credit: Aaron Geller, Northwester University. The plot can be generated at this link.

heaviest NS observed so far. The BH mass distribution derived from X-ray observations indicates a dearth of objects with masses between $2\,M_\odot$ and $5\,M_\odot$, known as the lower mass gap (Özel, Psaltis, Narayan, and McClintock, 2010; Farr et al., 2011). The mass of the secondary object in GW190814 questions the existence of such gap.

Furthermore, stellar evolution theory predicts a gap in the mass spectrum of BHs between $\sim 60\,M_\odot$ and $100\,M_\odot$. This is because very massive stars (with initial masses $\gtrsim 120\,M_\odot$) end their lives with a powerful explosion that leaves no remnant, known as pair-instability SN. GW events are starting to populate this gap, e.g., GW190519, GW231123 (see Ruiz-Rocha et al., 2025, for a list of candidate intermediate mass BH events). For instance, GW190521 has component masses $85\,M_\odot$ and $66\,M_\odot$, and a merger product of $142\,M_\odot$ (Abbott et al., 2020b; Abbott et al., 2020d). Both progenitor BHs fall within the upper mass gap. Additionally, the merger product is the first observation of an intermediate mass BH (objects in the mass range $\sim 100-1000\,M_\odot$).

GW observations are still affected by large uncertainties in the estimate of the spins of the single compact objects. However, they provide reasonable constraints on a combination of the two compact object spins, known as effective spin ($\chi_{\rm eff}$) and defined (Damour, 2001):

$$\chi_{\rm eff} = \frac{(M_1\chi_1 + M_2\chi_2)}{M_1+M_2}\cdot\frac{\vec{L}}{L}. \tag{1.1}$$

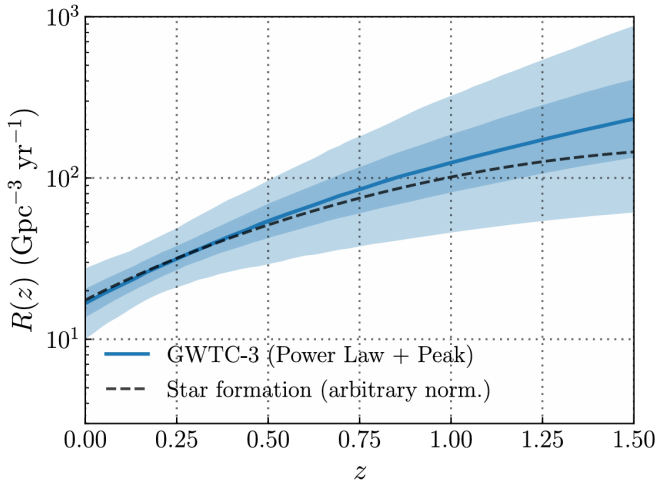


Fig. 1.3 BBH merger rate as a function of redshift, derived from GWTC-3 (Abbott et al., 2023b). The shaded regions represent the 50% (dark blue) and the 90% (light blue) credible bounds on the merger rate. The black dashed line shows the cosmic SFR with arbitrary scaling, for comparison (Madau and Dickinson, 2014). Image credit: Abbott et al. (2023a).

$\vec{L}$ is the orbital angular momentum of the binary, M_1 (M_2) and χ_1 (χ_2) are the mass and dimensionless spin parameters of the primary (secondary) compact object, respectively. The dimensionless spin parameters are defined $\chi_\mathrm{i} = S_\mathrm{i} c/(GM_\mathrm{i}^2)$ and S_i is the spin vector, c is the speed of light and G is the gravitational constant. The effective spin is bounded within the interval $\in [-1,1]$. $\chi_\mathrm{eff} = \pm 1$ indicates two maximally spinning BHs with their spins aligned $(+1)$ or anti-aligned (-1) with the orbital angular momentum. Conversely, $\chi_\mathrm{eff} = 0$ means the two BHs are either non-rotating or their spins lie on the orbital plane. Current GW observations found small values of χ_eff for most events (Abbott et al., 2019b; Abbott et al., 2019a; Abbott et al., 2021c; Abbott et al., 2023a). This contrasts with our knowledge of BH spins from X-ray observations (see e.g., Cygnus X-1, mentioned in section 1.1) that support a wider range of spin magnitudes, including high spins (Miller et al., 2015; Miller-Jones et al., 2021).

Finally, GW observations allowed us to estimate the merger rates of binary compact systems. The latest data release constrains the merger rate at redshift $z = 0$ for BNSs to be between 10 and 1700 Gyr^{-3}yr^{-1} and for BHNS to be between 7.8 and 140 Gyr^{-3}yr^{-1} (Abbott et al., 2023a). As shown in Figure 1.3, we can already see a dependence of the BBH merger rate density with redshift, even though our current sample is limited to $z \lesssim 1.5$. At a fiducial redshift $z = 0.2$, the BBH merger rate is constrained to be between 17.9 and 44 Gyr^{-3}yr^{-1}. With future next-generation GW detectors, we expect to go much beyond this limit and probe BBH mergers up to redshifts ~ 100 (Hall et al., 2019; Kalogera, Sathyaprakash, et al., 2021; Branchesi et al., 2023).

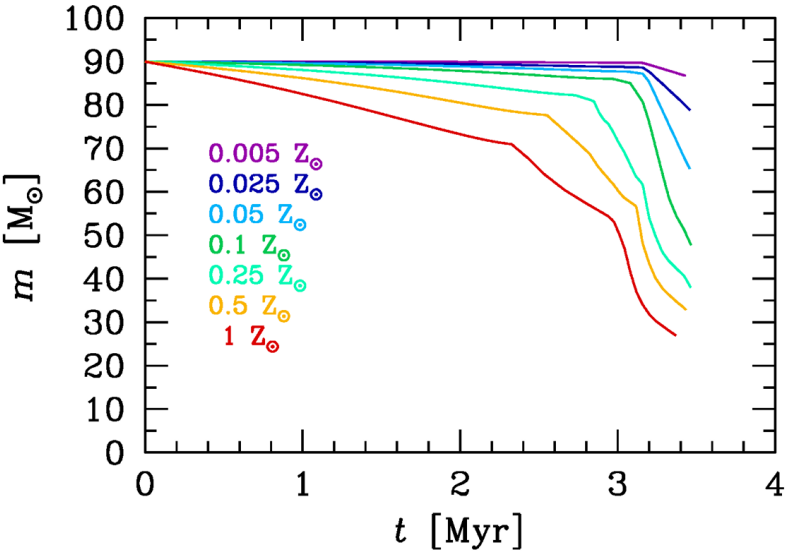


Fig. 1.4 Mass evolution as a function of time for a star with initial mass $M_{\rm ZAMS} = 90\,{\rm M}_\odot$. Different colors show the evolution of the same star for different metallicities, from $Z = 0.005\,{\rm Z}_\odot$ to $Z = {\rm Z}_\odot$. Plot obtained with the population synthesis code SEVN and the PARSEC stellar tracks. Image credit: Mapelli (2020).

1.2 Stellar evolution of massive stars

I now review the theory behind the formation of compact objects and its uncertainties, starting from stellar evolution. Stellar evolution begins on the zero-age main sequence (ZAMS) , when a star ignites hydrogen (H) in its core. Massive stars, with ZAMS masses $M_{\rm ZAMS} \gtrsim 8\,{\rm M}_\odot$ proceed the evolution with a chain of thermonuclear reactions until the formation of the iron-group elements in the core. The final compact remnant will be a NS ($8 \lesssim M_{\rm ZAMS}/M_\odot \lesssim 25$) or a BH ($M_{\rm ZAMS} \gtrsim 25 M_\odot$). The Chandrasekhar mass, $M_{\rm c} \simeq 1.44\,{\rm M}_\odot$, defines the maximum mass of a WD (Chandrasekhar, 1935). It is defined as the maximum mass that electron degeneracy pressure can sustain against gravitational collapse. Objects exceeding this limit will undergo further collapse, leading to the formation of a NS. In a similar way, it is possible to define the maximum mass that a degenerate pressure of a neutrons can sustain, known as the Tolman-Oppenheimer-Volkoff (TOV) limit (Oppenheimer et al., 1939; Tolman, 1939). This value is highly dependent on the assumed equation of state, introducing large uncertainties. Current estimates for the TOV limit range $M_{\rm TOV} \sim 1.5 - 3\,{\rm M}_\odot$ (Rhoades et al., 1974; Kalogera and Baym, 1996; Margalit et al., 2017). Moreover, several uncertainties in stellar evolution models can significantly impact the predicted final remnants. Key examples include the treatment of convection, dredge-up events, stellar wind mass loss, and nuclear reaction rates (see e.g., Woosley, Heger, et al., 2002).

1.2.1 Stellar winds

Radiation-driven winds play a key role in determining the evolution and final properties of massive stars. These winds arise from the interaction of radiation with matter in the stellar atmosphere. The underlying mechanism involves the exchange of energy and momentum between photons and atmospheric constituents like free electrons, ions, atoms, and dust grains. In hot massive stars, winds are primarily driven by the efficient coupling of photon momentum with the spectral lines of metal ions (Kudritzki et al., 2000; Vink, 2022). While H and helium (He) possess relatively few spectral lines in the UV (the peak emission band for massive stars), metals exhibit a rich and crowded spectrum in this region (Spera, Trani, et al., 2022). This mechanism highlights the strong dependence of wind efficiency on metallicity, with higher metallicities leading to more effective mass loss.

Vink et al. (2001) finds a dependence $\dot{M} \propto Z^{0.69}$ ($\dot{M} \propto Z^{0.64}$) for O (B) stars. Figure 1.4 shows the evolution of mass of a star with $M_{\rm ZAMS} = 90\,{\rm M}_\odot$ for different metallicities (different colors). The stars are evolved with the SEVN population synthesis code and the PARSEC stellar tracks (Costa, Shepherd, et al., 2025). For $Z = 0.005\,{\rm Z}_\odot$ the star retains most of its initial mass. Conversely, at high metallicities $Z = {\rm Z}_\odot$, it loses more than 2/3 of its initial mass (Mapelli, 2021).

Finally, stars near the Eddington limit experience enhanced mass loss, as shown in the model by Sabhahit et al. (2022). One of the effects of these enhanced winds is preventing the massive stars from significant expansion. This has a drastic impact on single and binary evolution (Kruckow, Andrews, et al., 2024; Shepherd et al., 2025; Simonato et al., 2025).

1.2.2 Supernova explosions and natal kicks

Core-collapse supernovae

As the core enriches in the iron-group elements, nuclear reactions can no longer support the stellar structure, that starts its collapse. With the rising temperature in the core a series of disintegration processes take place, ultimately leading to a significant enrichment of neutrons (see e.g., Woosley, Heger, et al., 2002, for a review). The collapse has a sudden halt when the inner part of the core reaches nuclear density and the repulsion due to the strong nuclear force prevents further collapse. The sudden halt, causes the bounce back and a shock wave into the still infalling matter of the outer core (bounce-shock mechanism, Colgate et al., 1966). The shock wave is still not enough to power the explosion and produce a successfull SN. A large role is played by neutrinos, that are produced in big quantities during the collapse. Due to the high densities of the core, not all neutrinos escape, they also interact with the matter behind the former shock wave and deposit their energy there. The energy deposited by the neutrinos is thought to be enough to revive the shock (delayed neutrino-driven mechanism, Bethe et al., 1985). Additional mechanisms have also been proposed, for example the SN can be driven by a fast-spinning magnetized NS (magnetorotational-driven explosion, Ostriker et al., 1971). The nature and mass of a compact remnant are linked to the progenitor star's SN explosion. If the explosion is successful, the compact remnant might be a NS or a BH, depending on the

amount of fallback material. Conversely, failed explosions lead to the direct collapse of the entire star, producing a BH.

From a computational point of view, modeling of the SN explosion is very challenging. Self-consistent 2D and 3D simulations (Müller, Janka, and Marek, 2012; Müller, Janka, and Heger, 2012) are computationally intensive and thus make it difficult to generate large-grids of models that can be used to infer the mass spectrum of compact remnants. On the other hand, while 1D simulations need to inject energy artificially in order for the explosion to take place, they offer a computationally more efficient alternative. O'Connor et al. (2011) and Ugliano et al. (2012) showed that the compactness parameter ξ_m is a good proxy for predicting which cores lead to a successful explosion:

$$\xi_{\mathrm{m}} = \frac{m/\mathrm{M}_\odot}{R(m)/1000\,\mathrm{km}}, \tag{1.2}$$

where $R(m)$ is the radius which encloses a given mass m.

Another simple approach is proposed by Fryer et al. (2012). They suggest that the mass of the compact remnant depend only on the carbon-oxygen (CO) core mass and the total final mass of the star. Fryer et al. (2012) further distinguished between two scenarios based on shock revival time: the delayed SN model, where shock is revived after $\gg 250$ ms and the available energy is significantly reduced, and the rapid SN model, characterized by shock revival within ~ 250 ms.

Pair-instability supernovae

Massive stars that develop cores above $\sim 30\,\mathrm{M}_\odot$ reach temperatures high enough at the end of carbon burning ($T \gtrsim 7 \times 10^8$K) to trigger pair-production reactions (Fowler et al., 1964; Barkat et al., 1967; Rakavy et al., 1967). The reactions remove free photons thereby decreasing the pressure and causing a sudden contraction of the CO core. For stars with He core masses between $\sim 32\,\mathrm{M}_\odot$ and $64\,\mathrm{M}_\odot$, the loss of support pressure causes a series of pulsations that enhance mass loss (pulsational pair-instability SN, Woosley, 2017). If the He core mass is larger ($\gtrsim 64\,\mathrm{M}_\odot$) the collapse triggers one single power pulse able to disrupt the entire star (pair-instability SN, Heger et al., 2002). Finally, if the He core is much more massive, $\gtrsim 135\,\mathrm{M}_\odot$ the star collapses directly into a BH (Woosley, 2017). Pair-instability SNe cause a gap in the mass spectrum of BHs (see Figure 1.5), with a lack of BHs between $\sim 50\,\mathrm{M}_\odot$ and $\sim 120\,\mathrm{M}_\odot$ (Belczynski, Holz, et al., 2016; Spera and Mapelli, 2017; Marchant, Renzo, et al., 2019; Marchant and Moriya, 2020). Notice however, that the lower and upper edges of the mass gap are subject to large uncertainties. For instance, considering different reaction rates for the $^{12}C(\alpha,\gamma)^{16}O$ causes a shift in the gap of more than $\sim 15\,\mathrm{M}_\odot$ (Farmer et al., 2019).

Natal kicks

Asymmetries in the matter and neutrino ejecta from SN explosions can impart a kick to the resulting compact object (Janka, 2012). Constraints on these natal kicks mainly come

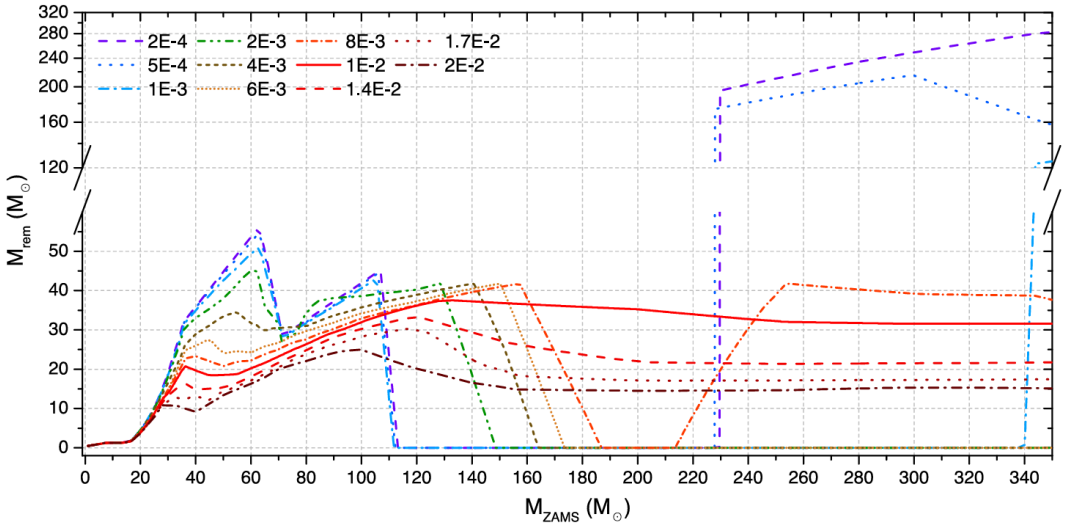


Fig. 1.5 Compact remnant masses ($M_{\rm rem}$) as a function of the ZAMS mass ($M_{\rm ZAMS}$). The stars are evolved with SEVN. Different linestyles and colors show the results for different metallicities, ranging from $Z = 10^{-4}$ to $Z = 10^{-2}$. Pair-instability SN open a gap in $M_{\rm rem}$, from $\sim 50\,{\rm M}_\odot$ to $\sim 120\,{\rm M}_\odot$. Notice that for high metallicities $Z \gtrsim 10^{-2}$, the stars never enter the pair-instability regime, due to the strong stellar winds. Image credit:Spera and Mapelli (2017).

from the velocity observations of isolated pulsars. Using these measurements, Hobbs et al. (2005) find that the best fit distribution is a maxwellian with root mean square $\sigma = 265\,{\rm km\,s^{-1}}$. Arzoumanian et al. (2002) and Verbunt et al. (2017) indicate that a bimodal velocity distribution is a better fit instead. Nevertheless, the main concern with this sample, is its potential bias towards high kicks (O'Doherty et al., 2023).

On the other hand, estimates of BH kicks are even more difficult to obtain. Most models rely on BHs in X-ray binary measurements (e.g., Repetto et al., 2012; Atri et al., 2019). In this way, Atri et al. (2019) find that a unimodal gaussian distribution with mean $107\,{\rm km\,s^{-1}}$ can explain the BH samples. However, the velocities of such objects are entangled with the velocity of the binary itself (Blaauw kick). Therefore, the kick estimates might be biased. More recently, Nagarajan et al. (2025) use the Gaia data to infer the BH kicks distribution. Their results point to a bimodal distribution, for a scenario consistent with the idea of some BHs receiving almost no kicks, after a failed SN, some other receiving strong kicks, as a result of a successful SN. Finally, Giacobbo and Mapelli (2018), Bray et al. (2016), and Bray et al. (2018) propose a model with the purpose of reproducing both the BH and NS kicks, while naturally accounting for the reduced kicks of electron-capture and ultra-stripped SNe. The model predicts a kick following:

$$v_{\rm kick} = f_{\rm H05} \frac{\langle m_{\rm NS} \rangle}{m_{\rm rem}} \frac{m_{\rm ej}}{\langle m_{\rm ej} \rangle}, \tag{1.3}$$

where $m_{\rm rem}$ is the mass of the compact remnant, $m_{\rm ej}$ is the mass of the ejecta, $\langle m_{\rm NS} \rangle$ and $\langle m_{\rm ej} \rangle$ are the average NS mass and the typical NS ejecta. $f_{\rm H05}$ is a number generated from

a Maxwellian probability density with one-dimensional root mean square $\sigma = 265\,\mathrm{km\,s^{-1}}$ (Hobbs et al., 2005).

1.3 Binary stellar evolution

As highlighted in the previous sections, most stars, especially the most massive ones, are found in binaries (Moe et al., 2017). Binary interactions have thus likely played a critical role in the systems that we observe today. These interactions are particularly relevant because of the impact they produce on the orbital properties of the system. To study their effects, let us consider a generic binary system, with stars of masses M_1 and M_2, orbital separation a and eccentricity e. The total angular momentum of this system is:

$$J = \sqrt{\frac{GM_1^2M_2^2a(1-e^2)}{M_1+M_2}} \tag{1.4}$$

where G is the gravitational constant. The rate of change in orbital separation can be derived by differentiating the previous equation:

$$\frac{\dot{a}}{a} = 2\frac{\dot{J}_{\rm orb}}{J_{\rm orb}} - 2\frac{\dot{M}_1}{M_1} - 2\frac{\dot{M}_2}{M_2} + \frac{\dot{M}_1+\dot{M}_2}{M_1+M_2} + 2\frac{e\dot{e}}{(1-e^2)}. \tag{1.5}$$

Since many processes involved do not conserve the mass or energy of the system, the orbital angular momentum is generally not conserved. The variation in orbital angular momentum can be expressed as the sum of the contributions from the single processes:

$$\frac{\dot{J}_{\rm orb}}{J_{\rm orb}} = \frac{\dot{J}_{\rm gw}}{J_{\rm orb}} + \frac{\dot{J}_{\rm mb}}{J_{\rm orb}} + \frac{\dot{J}_{\rm ls}}{J_{\rm orb}} + \frac{\dot{J}_{\rm ml}}{J_{\rm orb}}. \tag{1.6}$$

In the previous equation, $\dot{J}_{\rm gw}$ is the change in angular momentum due to GW radiation, $\dot{J}_{\rm mb}$ represents the contribution from magnetic braking, i.e., stellar wind coupled with the magnetic field of the star, relevant mainly for convective stars. $\dot{J}_{\rm ls}$ includes tidal spin-orbit exchanges of angular momentum. $\dot{J}_{\rm ml}$ is the orbital angular momentum variation due to mass lost from the system.

The equations 1.5 and 1.6 together constitute the angular momentum balance equation. They can be used to infer the behavior of a binary system in different situations. I will outline in the following sections some of the main processes that affect the evolution of a binary system, with a focus on the physics of mass transfer and the effects of mass loss. For a more detailed and complete review of the processes at play I refer to Spera, Trani, et al. (2022) and Tauris and van den Heuvel (2023).

1.3.1 Roche potential

Let us consider the binary system previously introduced. Under the assumptions that the two stars are spherical and co-rotating with the orbit, the gravitational potential of the system is

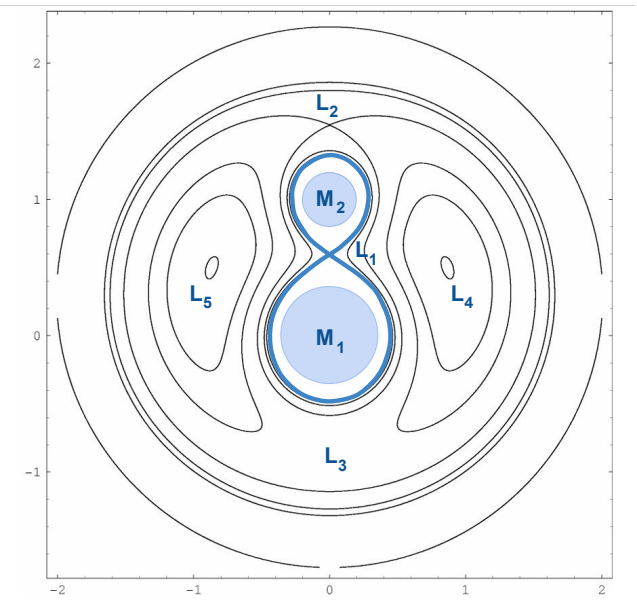


Fig. 1.6 Representation of the equipotential surfaces of the Roche potential, for a binary with two stars of masses M_1 and M_2. The eight-shaped blue line highlights the Roche lobes of the binary, which meet at the first Lagrangian point L_1.Other Lagrangian points are also indicated in the figure. Both the x and y axes are presented in units of the orbital separation. Figure adapted from: Benacquista et al. (2013).

described by the Roche potential. In a reference frame centered on the center of mass of the system, the potential can be written:

$$\Phi_R = -\frac{GM_1}{|\vec{r}-\vec{r}_1|} - \frac{GM_2}{|\vec{r}-\vec{r}_2|} - \frac{1}{2}(\vec{\Omega}\times\vec{r})^2, \tag{1.7}$$

where $\vec{r}$ is the position vector from the center of mass, $\vec{r}_1$ and $\vec{r}_2$ are the distances of M_1 and M_2 from the center of mass. In this approximation, it can be shown that the equipotential surfaces coincide with surfaces of constant pressure and constant density (Tauris and van den Heuvel, 2023). Therefore, this is the only ingredient needed to fully describe the binary system. Figure 1.6 illustrates the Roche potential in the orbital plane and shows some relevant equipotential surfaces. In particular, the figure highlights the positions of the five Lagrangian points (L_1, L_2, L_3, L_4 and L_5). These points satisfy the condition $\nabla\Phi = 0$, and represent thus points of equilibrium under the gravitational action of the two bodies. The point L_1 and the equipotential surface through it (highlighted blue line in the figure) hold particular interest in binary systems. The two pear-shaped volumes defined by this surface are called Roche lobes. Matter within each Roche lobe is under the gravitational pull of the closest star. Therefore, when a star fills its Roche lobe, matter can freely flow to the companion through the inner lagrangian point (L_1). This process is called Roche lobe overflow (RLO, Paczyński, 1971).

A binary system can be found in three different configurations, based on its geometrical properties:

- *detached*: if neither star fills its Roche lobe,

- *semi-detached*: if only one of the stars fills its Roche lobe,
- *contact system*: if both stars fill their Roche lobes.

A star is considered to be filling its Roche lobe if its radius exceeds the Roche lobe radius. The latter is defined as the radius of a sphere with the same volume as that contained by the Roche surface. Eggleton (1983) provide a useful approximate analytic expression for the Roche lobe radius:

$$\frac{R_{L,1}}{a} = \frac{0.49q_1^{2/3}}{0.6q_1^{2/3} + \ln(1+q_1^{1/3})}, \tag{1.8}$$

where a is the semi major axis of the orbit, q_1 is defined as the ratio between the two masses: $q_1 = M_1/M_2$.

1.3.2 Orbital variations

Before delving into the intricate casistic of binary mass transfer, let us have a general look at what happens to the binary whenever there is a mass exchange or mass loss. For the sake of simplicity let us assume a circular orbit ($e = 0$). This is not a strong approximation as tidal forces in close binaries are able to efficiently circularize the system in a short amount of time (Hut, 1981).

Let us first consider the case of conservative Roche lobe overflow, in which all the mass lost from the donor (of mass M_d) is accreted by the companion (of mass M_a), such that $\dot{M}_\mathrm{a} = -\dot{M}_\mathrm{d}$. In this simple case, the total mass of the system is constant, $\dot{M}_\mathrm{d} + \dot{M}_\mathrm{a} = 0$, and the total orbital angular momentum is conserved, $\dot{J}_\mathrm{orb} = 0$. Equation 1.5 thus simplifies to:

$$\frac{\dot{a}}{a} = -2\frac{\dot{M}_\mathrm{d}}{M_\mathrm{d}} + 2\frac{\dot{M}_\mathrm{d}}{M_\mathrm{a}}. \tag{1.9}$$

We can rewrite the previous equation as:

$$\frac{\dot{a}}{a} = -2\dot{M}_\mathrm{d}M_\mathrm{d}(1-q), \tag{1.10}$$

where I have introduced the mass ratio $q = M_\mathrm{d}/M_\mathrm{a}$. Therefore, if $q > 1$ (i.e., the donor mass is bigger than the accretor) the orbit shrinks, otherwise, it expands.

If the mass transfer is non-conservative, or more generally if mass is lost from the system, the orbital evolution is affected. The nature and magnitude of this effect depend on the specific modes of mass loss (Huang, 1963; Kruszewski, 1964; van den Heuvel, 1994a; Soberman et al., 1997). The main mass loss cases are summarized below:

1. *Jeans mode*. The donor star loses mass in the form of a fast wind, in this case the mass lost carries away the specific angular momentum of the donor star (Huang, 1963).
2. *Isotropic re-emission*. All the mass lost from the donor is transferred to the accretor, a fraction of this matter is then ejected from the vicinity of the accretor, carrying its

specific angular momentum (van den Heuvel and De Loore, 1973). For example, this is what happens when matter is transferred to a compact object. The accretion rate in this case is limited by the Eddington luminosity, causing the excess material to be expelled from the system (Bhattacharya et al., 1991).

3. *Circumbinary disk*. The particles escape through L_2 and L_3 and form a co-planar disk surrounding the binary (Huang, 1963; van den Heuvel and De Loore, 1973). This configuration causes tidal interactions between the disk and the binary, extracting angular momentum from the orbit (Artymowicz et al., 1994; Spruit et al., 2001).

1.3.3 Stability of mass transfer

The stability of mass transfer from a Roche lobe-filling star is determined by the rate of change in orbital separation with respect to the donor star's radius (e.g., Soberman et al., 1997). The formalism generally used to describe the stability of RLO is the one introduced in Webbink (1985). The approach he presents is based on the simplifying assumption $R \propto m^{\zeta}$. In this way, the stability criteria translate to a comparison among the exponents describing the donor star evolution and the Roche lobe evolution. let us define the two relevant mass-radius exponents:

- $\zeta_* = \partial \ln R_\mathrm{d} / \partial \ln M_\mathrm{d}$: this exponent describes the response of the donor star, with mass M_d and radius R_d, to mass loss
- $\zeta_{\mathrm{L,d}} = \partial \ln R_{\mathrm{L,d}} / \partial \ln M_\mathrm{d}$: this exponent describes the response of the Roche lobe radius ($R_{\mathrm{L,d}}$) to mass loss.

The variations in the donor star radius and relative Roche lobe are:

$$\frac{dR_\mathrm{d}}{dt} = \frac{\partial R_\mathrm{d}}{\partial t} + \zeta_* \frac{R_\mathrm{d}}{M_\mathrm{d}} \frac{dM_\mathrm{d}}{dt} \tag{1.11}$$

$$\frac{dR_\mathrm{L}}{dt} = \frac{\partial R_\mathrm{L}}{\partial t} + \zeta_\mathrm{L} \frac{R_\mathrm{L}}{M_\mathrm{d}} \frac{dM_\mathrm{d}}{dt}. \tag{1.12}$$

If $\zeta_\mathrm{L} > \zeta_*$ the Roche lobe is shrinking faster (or expanding slower) than the radius of the donor star, and the mass transfer is unstable. The latter can be unstable on a thermal timescale, if ζ_* describes the thermal response of the star ($\zeta_* = \zeta_\mathrm{th}$) or on a dynamical timescale, if ζ_* describes the adiabatic response of the star ($\zeta_* = \zeta_\mathrm{ad}$). Generally, donor stars with radiative envelopes tend to shrink in response to mass loss. Conversely, donor stars with deep convective envelopes typically expand in response to mass loss, often leading to dynamically unstable configurations (Hjellming et al., 1987). Dynamically unstable mass transfer is a runaway process. As more and more mass is transferred, the accreting star eventually finds itself completely engulfed. The ultimate fate of such a system then depends on the donor's evolutionary stage: if its core is not fully developed, a merger occurs, otherwise the system initiates a CE.

Under specific assumptions, it is possible to express the stability criteria as a function of a critical mass ratio q_crit, so that the mass transfer process becomes unstable for $q > q_\mathrm{crit}$

(Portegies Zwart and Verbunt, 1996; Tout et al., 1997; Hurley, Tout, et al., 2002; Eggleton, 2006).

1.3.4 Stable Roche-lobe overflow

During a stable mass transfer event, material flows from the donor to the accretor through the inner Lagrangian point L_1. We can give a rough estimate of the mass transfer rate using Bernoulli's equation. Let us consider an adiabatic, isentropic and irrotational fluid, with a flow parallel to the axis connecting the centers of the two stars, the estimated mass transfer rate is given by (Paczyński and Sienkiewicz, 1972; Ge, Hjellming, et al., 2010; Spera, Trani, et al., 2022):

$$\dot{M}_{\rm d} \simeq -\frac{M_{\rm d}}{P_{\rm orb}} \left(\frac{\Delta R}{R_{\rm L,d}} \right)^{n+\frac{3}{2}}, \tag{1.13}$$

where $P_{\rm orb}$ is the orbital period of the binary, $\Delta R = R_{\rm d} - R_{\rm L,d}$ is the Roche lobe filling factor and n is the polytropic index of the donor star's envelope.

Following the definition in Kippenhahn et al. (1967) it is possible to distinguish three different cases of mass transfer:

- Case A: The star fills its Roche lobe during the main sequence (MS).
- Case B: The star fills its Roche lobe after leaving the MS but before He ignition.
- Case C: The star fills its Roche lobe after core-He depletion.

Let us consider an example of evolution of a binary system. As the two stars evolve in a close binary system, they will expand on a nuclear timescale. At some point the most massive of the two will fill its Roche lobe and initiate a phase of mass transfer. Since in this case $q < 1$, the orbit shrinks potentially leading to an unstable situation. In fact, in this time, while the Roche lobe shrinks the donor star tends to expand to restore its equilibrium. This process happens on a thermal or a dynamical timescale, mainly depending on the evolutionary stage of the donor star. After the mass ratio is inverted, the mass transfer process slows down: the Roche lobe expands as a reaction to the mass transfer. The mass transfer can proceed following the nuclear timescale of the donor (typically what happens in a case A mass transfer) or stop completely (e.g., case B mass transfer, Marchant and Bodensteiner, 2024).

Case A and case B mass transfer, involve stars with radiative envelopes or mildly convective envelopes. Therefore, the mass transfer is thought to happen on a thermal timescale. Instead, in the case C the situation is very different. Stars at such evolved stages usually have a deep convective envelope. As discussed in the previous section, stars typically expand on a dynamical timescale to restore their equilibrium, bringing the mass transfer to a very short timescale. The accretor, might not be able to keep up with such large rates of transferred mass. For this reason, in most cases this configuration leads to the formation of a CE.

1.3.5 Common envelope

The CE phase is arguably one of the most important, yet poorly understood, phase in the evolution of close binary systems. During this stage, the cores of the two stars orbit within a shared envelope. The drag forces they experience lead to the dissipation of angular momentum, causing the system to shrink efficiently. The CE was first theorized by Paczynski (1976) to explain the star V 471 Tau, a compact binary composed of a white dwarf and a K dwarf. The orbital parameters observed for this system can only be explained assuming a phase of efficient spiral-in. It is now clear that the CE phase is involved in the evolution of many more systems. A notable example are the progenitors of GW sources (e.g., Belczynski, Kalogera, and Bulik, 2002; Dominik et al., 2012; Rodriguez, Chatterjee, et al., 2016; Giacobbo and Mapelli, 2018; Mapelli and Giacobbo, 2018; Belczynski, Klencki, et al., 2020; Zevin, Bavera, et al., 2021; Broekgaarden and Berger, 2021; Iorio et al., 2023; Sgalletta, Iorio, et al., 2023; Boesky et al., 2024a; Sgalletta, Mapelli, et al., 2025). Such systems, when on the MS, must have had orbital separations too wide for efficient GW emission, in order to accommodate the larger stellar radii. The CE is often invoked to bring the stellar cores close enough to merge via GW emission. This is particularly evident in the formation of merging BNS systems (see e.g., Iorio et al., 2023; Broekgaarden, Berger, et al., 2022). For similar reasons, the CE mechanism has been invoked to explain various other type of binaries, including cataclysmic variables, Type Ia SN progenitors, short gamma ray burst. Additionally, observed planetary nebulae containing close white dwarf binaries, might also be the results of a CE (see e.g., Ivanova, Justham, Chen, et al., 2013; Röpke et al., 2023).

A system can trigger a CE phase, as a consequence of a dynamically unstable mass transfer (see also Section 1.3.4),or after the occurrence of a Darwin instability (Darwin, 1879). The CE evolution itself comprises a phase of fast spiral-in, occurring on a dynamical timescale. During this period orbital energy is deposited into the envelope. This is followed by a self-regulating inspiral phase, which operates on a thermal timescale (Ivanova, Justham, Chen, et al., 2013). A CE is considered successful if the latter stage results in the ejection of the envelope. Otherwise, the inspiral continues until the two cores are tidally disrupted (Spera, Trani, et al., 2022).

A complete understanding of the CE process remains elusive due to its complexity. Hydrodynamic simulations face tough computational challenges in modeling this process. This is primarily due to the vast range of both spatial and temporal scales involved. Considering for example a NS within the envelope of a giant star, the simulation would need to have a spatial coverage from $\sim$ 10km (typical radius of a NS), to $\sim 1000\,\mathrm{R}_{\odot}$. Similarly, the timescales involved range from the dynamical timescale of the NS ($\sim$ 1s) to the thermal timescale of the envelope ($\sim$ 1000yr, Ivanova, Justham, Chen, et al., 2013). For this reason, hydrodynamic simulations typically cover only the initial plunge-in, proceeding on a dynamical timescale (e.g., Law-Smith et al., 2020).

Furthermore, the computational cost of hydrodynamic simulations makes them impractical for extensive population studies. For this reason, many simplified parametric models have been developed (Paczynski, 1976; van den Heuvel, 1976; Webbink, 1984; Livio et al., 1988; de Kool, 1990; Nelemans, Verbunt, et al., 2000; Nelemans and Tout, 2005). While these models lack predictive power, they are the most common tools for population synthesis

studies that aim to evolve large numbers of binaries. These parametric approaches typically rely on global conservation principles, neglecting the dynamic nature of the problem. The $\alpha\lambda-$formalism (van den Heuvel, 1976; Webbink, 1984; Livio et al., 1988) is one of the most common models. This formalism is based on an energy conservation principle: the orbital energy serves as the energy source for the ejection of the CE. Therefore, by comparing the envelope binding energy with the available orbital energy budget, it is possible to assess whether or not the CE is successful (i.e., if the envelope is ejected). This model relies on two parameters α and λ. α represents the efficiency of energy transfer from the orbit to the envelope. λ is a structural parameter which models the envelope binding energy. The envelope binding energy is typically parametrized as:

$$E_{\rm bind} = -\frac{G}{\lambda}\frac{M_{\rm d}M_{\rm env,d}}{R_{\rm d}}, \tag{1.14}$$

where $R_{\rm d}$ is the Roche lobe of the donor star at the onset of CE, $M_{\rm env,d}$ is the envelope mass of the donor star. In general, the value of λ varies several orders of magnitude and depends on the stellar mass and evolutionary phase of the donor star. This parameter can be derived from 1D stellar structure models (e.g., Dewi et al., 2000; Claeys et al., 2014; Kruckow, Tauris, Langer, Szécsi, et al., 2016; Klencki, Nelemans, Istrate, and Chruslinska, 2021). Nevertheless, the precise location of the core-envelope boundary is still uncertain. Different conditions can introduce variations in the model outcomes (see also Chapter 5, Dewi et al., 2000; De Marco et al., 2011; Kruckow, Tauris, Langer, Szécsi, et al., 2016). Finally, α measures how much orbital energy is used to unbind the envelope, therefore, by definition $\alpha \in [0,1]$. However, there may be additional energy sources contributing to unbind the envelope. These include recombination energy, tidal heating from stellar spin down/up (Kruckow, Tauris, Langer, Kramer, et al., 2018), nuclear fusion energy (Ivanova, Podsiadlowski, et al., 2002), enthalpy of the envelope (Ivanova and Chaichenets, 2011) and accretion energy that might drive outflows and jets (Soker, 2004; MacLeod and Ramirez-Ruiz, 2015; Soker, 2016; MacLeod, Antoni, et al., 2017). Accounting for these supplementary energy sources may lead to an effective $\alpha \gtrsim 1$. Notably, some recently proposed CE models appear to yield effective α values as large as 100 (Hirai et al., 2022). The $\alpha\lambda-$formalism presents several limitations. It does not allow for partial envelope ejection (Spera, Trani, et al., 2022). Additionally, this model does not reproduce the eccentricities of post-CE binaries, which have been observed to deviate from perfectly circular orbits (Lynch et al., 2012; Kawka et al., 2015; Kruckow, Neunteufel, et al., 2021). Finally, orbital changes in the $\alpha\lambda-$formalism are applied instantaneously. To address these aforementioned issues, new models have been proposed (e.g., Trani et al., 2022).

1.3.6 Mass loss from a supernova explosion and natal kicks

When a star explodes as a SN in a binary, it will affect the entire system, possibly disrupting the binary itself. As outlined in Section 1.2.2, asymmetric ejection of mass or neutrino losses during a SN can impart a significant velocity to the remnant, known as natal kick.

In a binary system, even spherically symmetric mass ejection can impart a recoil velocity to the system due to the sudden mass loss (Blaauw kick, Blaauw, 1961). This event can be considered as a variant of the *Jeans mode* described in Section 1.3.2. The same formalism can be applied to quantify changes in the orbital parameters. Following Tauris and van den Heuvel (2023), for a system with initially zero eccentricity and radius a_0, the post-explosion semimajor axis (a_1) is:

$$\frac{a_1}{a_0} = \frac{M}{M - \Delta M}, \tag{1.15}$$

where ΔM is the mass loss during the SN explosion, M is the total mass of the system. Therefore, if $\Delta M > M$ the system becomes unbound. In general, the eccentricity of the orbit is non zero after the explosion:

$$e = 1 - \frac{a_0}{a_1} = \frac{\Delta M}{M}. \tag{1.16}$$

Additional natal kicks, arising from asymmetric mass ejection or neutrino emission, can either tighten or unbind the system depending on their magnitude and direction (Janka, 2012).

1.3.7 Binary compact objects from the isolated formation channel

Binary neutron stars

The standard formation scenario for BNS systems is depicted in the top panel of Figure 1.7 (Flannery et al., 1975; De Loore et al., 1975; van den Heuvel, 1976; Srinivasan and van den Heuvel, 1982). The system starts with two OB-stars of masses $\sim 8-25\,\mathrm{M}_\odot$, massive enough to end their lives as NSs. The formation of a close BNS system requires an initially compact binary configuration, allowing for a first phase of mass transfer before the first SN explosion. If the system remains gravitationally bound, it may become observable as a pulsar+OB star and eventually as a high-mass X-ray binary. As the secondary star expands due to stellar evolution, it can initiate a second phase of mass transfer. Due to the advanced evolutionary stage of the donor, this mass transfer can quickly become dynamically unstable, possibly leading to the formation of a CE (Paczynski, 1976). The CE phase represents a pivotal step in the formation of a merging BNS system, allowing for an efficient shrinkage of the system (e.g., Broekgaarden, Berger, et al., 2022; Iorio et al., 2023). Successful ejection of the CE results in a system composed of a NS orbiting a He star. Another phase of mass transfer may occur, further stripping the companion and leading to an ultra-stripped SN (Suwa et al., 2015; De et al., 2018; Müller, Gay, et al., 2018). This stage can also contribute to spinning up the NS (see Section 1.4). Finally, also the secondary star explodes as a SN and, depending on the final orbital separation, the magnitude and direction of the natal kick, the system may remain bound. If the two NSs are sufficiently close, they will merge within a Hubble time through GW emission. I refer to Tauris, Kramer, et al. (2017) for a thorough review.

Binary black holes

Merging BBHs can form through several formation scenarios that can be broadly categorized into *isolated* and *dynamical*. The dynamical channel involves the formation of close BBHs

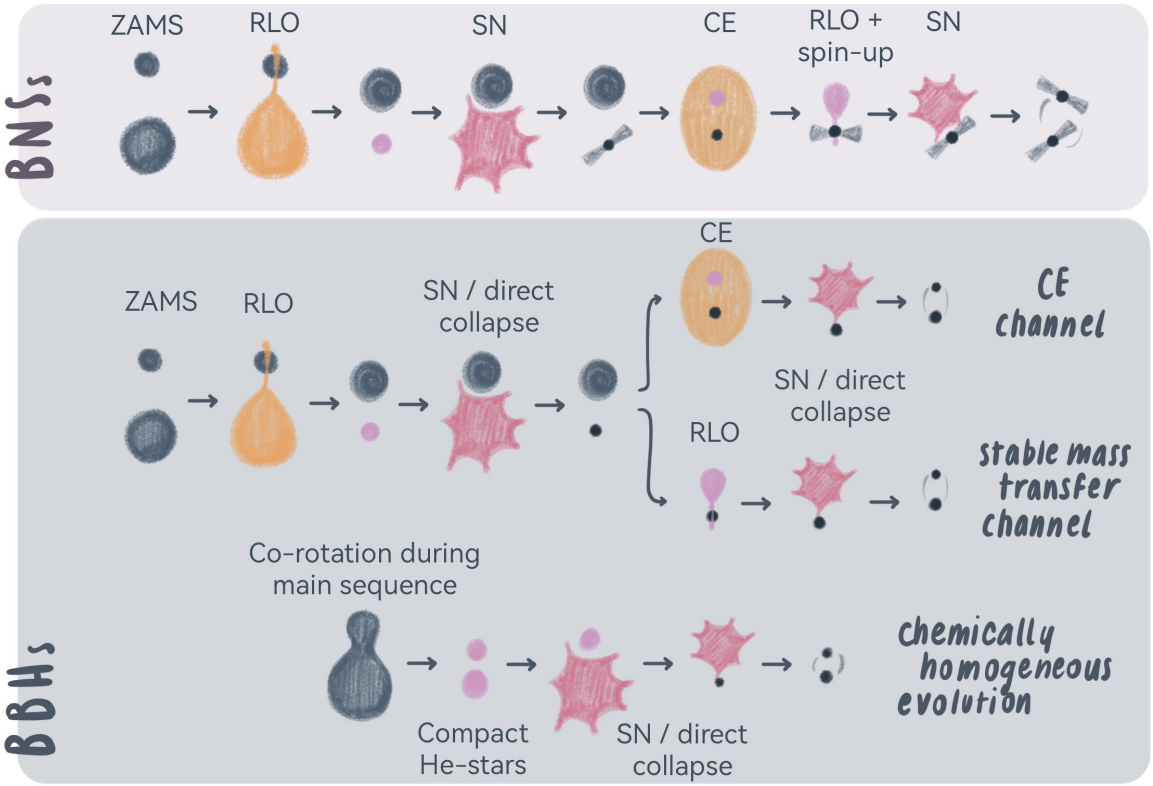


Fig. 1.7 Simplified illustrations of the main formation scenarios of close binary compact object systems. The top panel shows the standard BNSs formation channel, in which the system experiences a CE phase after the first compact remnant formation. The bottom panel shows the three main isolated formation channels of close BBHs. The CE channel, similar to the BNSs one; the stable mass transfer channel, during which the system experiences only stable mass transfer; chemically homogeneous evolution, in which the two stars are tidally locked during MS and remain compact throughout their whole life. Figure inspired by Tauris, Kramer, et al. (2017).

through gravitational encounters and exchange interactions in dense stellar environments (e.g., Sigurdsson et al., 1993; Portegies Zwart and McMillan, 2000; Banerjee et al., 2010; Samsing et al., 2014; Mapelli, 2016; Rodriguez, Chatterjee, et al., 2016; Di Carlo et al., 2020), or via hierarchical triple systems (e.g., Wen, 2003; Dall'Amico, Mapelli, Torniamenti, et al., 2024). This discussion will exclusively focus on the isolated formation channels, omitting stellar dynamics. The bottom panel of Figure 1.7 provides a simplified representation of the possible channels. One way to form close BBHs is via the CE channel. This scenario is very similar to the one outlined for BNSs. The main feature is that the system always enters a CE after the formation of the first BH. However, further sub-classifications can be made based on the evolution before the first compact remnant formation (e.g., Neijssel et al., 2019; Broekgaarden, Berger, et al., 2022; Iorio et al., 2023).

Merging BBHs can also form via a stable mass transfer channel (referred to as Channel II in Broekgaarden, Berger, et al., 2022; Iorio et al., 2023). In this case, if the system is tight enough, it may evolve through a dynamically stable RLO after the first BH formation. For stars with radiative or only slightly convective envelopes, this condition might hold up to mass ratios $q \sim 4$ (Tauris, van den Heuvel, and Savonije, 2000). Recent works suggest that this channel might contribute more than the CE one to the merging BBH population (see e.g., Marchant, Pappas, et al., 2021; Gallegos-Garcia, Berry, et al., 2021).

Finally, the last channel I will mention is the chemically homogeneous evolution (e.g., de Mink, Cantiello, et al., 2009; de Mink and Mandel, 2016; Marchant, Langer, et al., 2016; Dall'Amico, Mapelli, Iorio, et al., 2025). In this scenario, tidal interactions among the MS stars induce rapid rotation. The fast rotation allows for effective internal mixing. Therefore the star evolves with a chemically homogeneous interior. Such stars, consume all their H fuel and evolve into Wolf-Rayet stars. This kind of evolution prevents the stars from significantly expanding and for this reason the system might form a merging BBH without the need of any mass transfer.

1.4 Pulsars

In Section 1.1.1, I outlined the demographics of the observed pulsar population. Here, I will dive deeper into the pulsar model and explore the primary evolutionary scenarios of pulsars in binary systems, with a particular focus on those with NS companions.

Figure 1.8 illustrates a rotating NS, also known as the *lighthouse model* (Manchester and Taylor, 1977). As the NS rotates, its magnetic field guides and accelerates charged particles, forming a beam. Observers from Earth detect a pulse each time this beam crosses their line of sight. Pulsars steadily lose rotational energy at a rate $\dot{E}_{\rm rot}$. This is because of two main processes: magnetic dipole radiation, resulting from the rotation of their magnetic field ($\dot{E}_{\rm dip}$), and a wind of relativistic particles. While GW radiation also contributes to this energy loss, it is generally a second order effect compared to dipole radiation (Abadie et al., 2010). I will assume $\dot{E}_{\rm rot} = \dot{E}_{\rm dip}$ throughout the following discussion. Note that the equations in this Section assume the CGS system of units.

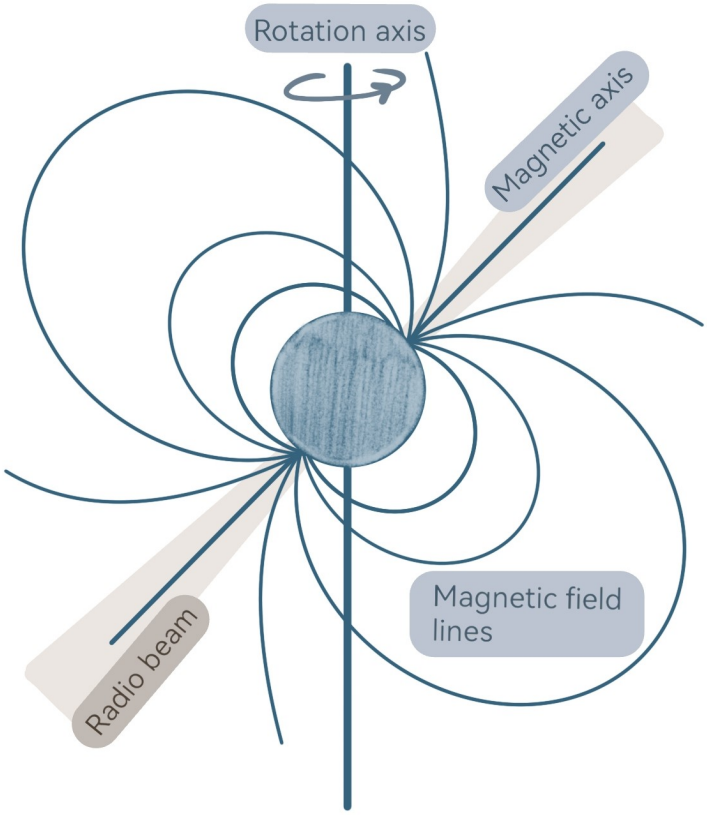


Fig. 1.8 Simplified illustration of a pulsar model. The radio beam of a pulsar is emitted in the same direction of its magnetic axis, which is misaligned with its rotation axis. As the pulsar spins, when this radio beam crosses an observer's line of sight from Earth, a pulse is recorded.

The energy loss rate due to magnetic dipole radiation is given by (Tauris and van den Heuvel, 2023):

$$\dot{E}_{\rm dip} = -\frac{2}{3c^3}|\ddot{\vec{m}}|^2 \qquad |\ddot{\vec{m}}| = BR^3\Omega^2 \sin\alpha_{\rm B}, \tag{1.17}$$

where c is the speed of light, $\vec{m}$ is the magnetic moment of the NS, R is its radius, B is its surface magnetic field, Ω is its angular velocity. $\alpha_{\rm B}$ is the angle between the NS's rotation axis and its magnetic axis. Therefore:

$$\dot{\Omega} = -\frac{2B^2R^6\Omega^3 \sin^2\alpha_{\rm B}}{3c^3 I} \tag{1.18}$$

where I used $\dot{E}_{\rm rot} = I\Omega\dot{\Omega}$, with I the moment of inertia of the pulsar. Under this assumption, for a given measured spin period ($P = 2\pi/\Omega$) and spin down rate ($\dot{P}$), the magnetic field B strength can be estimated:

$$B = \sqrt{\frac{3c^3 I}{8\pi R^6 \sin^2\alpha} P\dot{P}}. \tag{1.19}$$

The constant B lines in Figure 1.1 are computed in this way. From eq. 1.18 we see that $\dot{\Omega} \propto \Omega^3$. Integrating this relation and assuming the pulsars' initial spin period was much shorter than the current one, we can define the characteristic age of a pulsar (Manchester and Taylor, 1977):

$$\tau_c = \frac{P}{2\dot{P}}. \tag{1.20}$$

Notice however, that the characteristic age is not always a reliable estimator of a pulsar's real age. For example, this is the case for magnetars and recycled pulsars. In fact, their spin down mechanisms can significantly deviate from pure dipole radiation. The characteristic age might introduce large biases in their actual age. It is therefore useful to generalize Eq. 1.20:

$$\dot{\Omega} \propto \Omega^n \tag{1.21}$$

n is called braking index. In the case of dipole radiation $n = 3$.

A critical question in the evolution of isolated pulsars is whether their magnetic fields decay, and if so, over what timescale. Researchers have explored various magnetic field decay timescales(Gonthier et al., 2004; Faucher-Giguère et al., 2006; Kiel et al., 2008; Osłowski et al., 2011; Chattopadhyay et al., 2020; Chattopadhyay et al., 2021), ranging from a few Myr (Gunn et al., 1970) to much longer timescales, of the order ∼Gyr (Kulkarni, 1986).

As anticipated in Section 1.1.1, pulsars in binary systems can spin up by accreting matter from the companion, a process known as recycling (Bhattacharya et al., 1991). When matter flows toward the NS, it typically forms an accretion disk. However, close to the NS surface, its magnetic field disrupts the disk. At this point, called the Alfven radius, the material is channelled along the magnetic field lines. The NS can then accrete this material on the polar caps. This transition point is crucial as it determines the angular momentum exchanged between the disk and the NS. The radius where the magnetic pressure overcomes the ram pressure (Alfven radius) satisfies:

$$\frac{B(R_A)^2}{8\pi} \simeq \frac{1}{2}\rho v_{ff}^2, \tag{1.22}$$

where $B(R_A) = B\,(R/R_A)^3$, v_{ff} is the free-fall velocity and ρ is the mass density of the matter inflow. I refer to Tauris and van den Heuvel (2023) for a full derivation. Note that uncertainties in the accretion geometry can introduce a factor of 2 uncertainty in this value (Tauris and van den Heuvel, 2023). Once matter enters the NS magnetosphere, whether it successfully accretes depends on the co-rotation radius (the radius at which matter rotates synchronously with the NS) relative to the Alfven radius (Possenti et al., 1998). Specifically, if the Keplerian angular velocity of the infalling matter is lower than the NS angular velocity, the system enters a propeller regime. In this situation, matter cannot couple effectively with the magnetosphere. Therefore it escapes from the NS, carrying away angular momentum. The outward acceleration causes the NS to spin down. Eventually, the pulsar decelerates sufficiently to allow for accretion, leading to its subsequent spin up (for further details on the spin-up model, please refer to Chapter 3).

Finally, as a NS accretes matter, its magnetic field decays. This phenomenonis supported by observations (e.g., Taam et al., 1986; Shibazaki et al., 1989; van den Heuvel, 1994b). A widely used model for this decay assumes an exponential relationship:

$$B \propto \exp\left(-\frac{\Delta M}{\Delta M_{\rm d}}\right), \tag{1.23}$$

where, ΔM is the amount of mass accreted by the NS and $\Delta M_{\rm d}$ is the magnetic field decay timescale. Nevertheless, the exact mechanism governing magnetic field decay is still under debate. Furthermore, deriving an accurate decay rate from observational data to precisely constrain theoretical models proves to be a significant challenge.

We now have all the necessary information to interpret Figure 1.1 and understand the evolutionary scenarios that lead to its configurations. The pulsars observed with WD companions are predominantly millisecond pulsars. Most of them, are fully recycled pulsars. They are believed to be the outcome of prolonged mass transfer phases. Since the donor star is a low-mass star, the mass transfer phase can persist for extended periods of time. Conversely, pulsars with a NS companion occupy a region in the diagram between millisecond pulsars and isolated pulsars. This shows evidence for a mild recycling process. In the standard formation scenario of BNS systems, as detailed in Section 1.3.7, the first-born pulsar can indeed be recycled by its pure-He star companion. However, due to the much shorter evolutionary timescales of their massive star progenitors, these systems cannot achieve the extremely low spin periods characteristic of pulsars paired with WD companions.

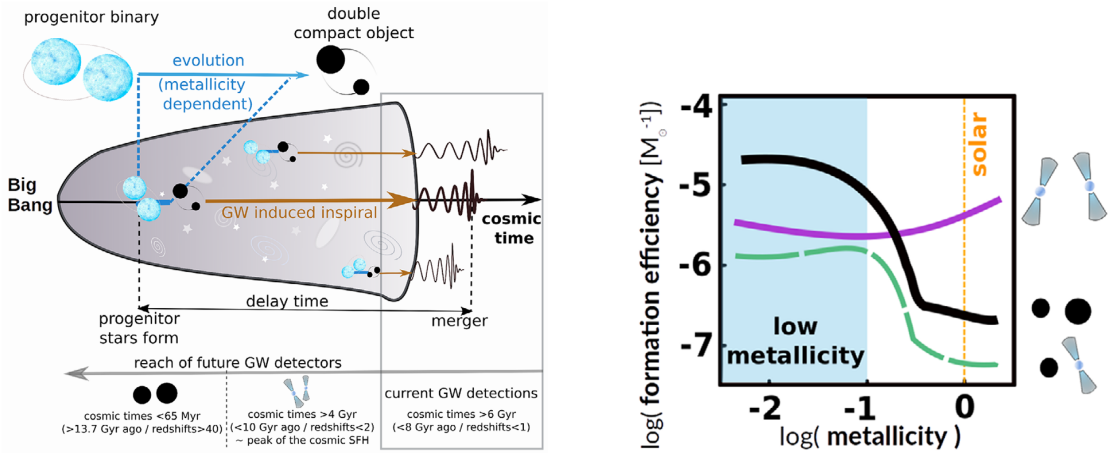
1.5 Binary compact objects across cosmic time

The observed population properties of merging binary compact objects provide a unique probe into the co-evolution of binary stellar systems and their host environments. GW events detected today are direct consequences of this complex interplay, offering insights into cosmic and galaxy evolution (Chruślińska, 2024). Moreover, next generation GW detectors, will allow us to observe events up to redshifts $z \gtrsim 10$ (Punturo et al., 2010), thus directly providing a look at the cosmic evolution.

Therefore, it is clear the importance of integrating the outcomes from binary evolution and the population of merging compact objects in the cosmological context. One way to achieve this, is by modeling the cosmic SFR density and the metallicity evolution with redshift (Madau and Dickinson, 2014; Madau and Fragos, 2017; Chruslinska, Nelemans, and Belczynski, 2019; Chruslinska and Nelemans, 2019; Boco, Lapi, Chruslinska, et al., 2021). In this way, the merger rate density for a class of binary compact objects is:

$$\mathscr{R}_{\rm BCO}(z) = \int_{z_{\rm max}}^{z} \frac{{\rm d}t(z')}{{\rm d}z'} \int_{Z_{\rm min}}^{Z_{\rm max}} \psi(z', Z)\, \eta_{\rm BCO}(Z)\, \mathscr{F}_{\rm BCO}(z', z, Z)\, {\rm d}Z\, {\rm d}z', \tag{1.24}$$

where t is the lookback time, $z_{\rm max}$ is the maximum considered redshift, $Z_{\rm min}$ and $Z_{\rm max}$ are the minimum and maximum considered metallicities, respectively. $\eta_{\rm BCO}(Z)$ is the merger efficiency for the considered class of BCOs, defined as the ratio between the number of



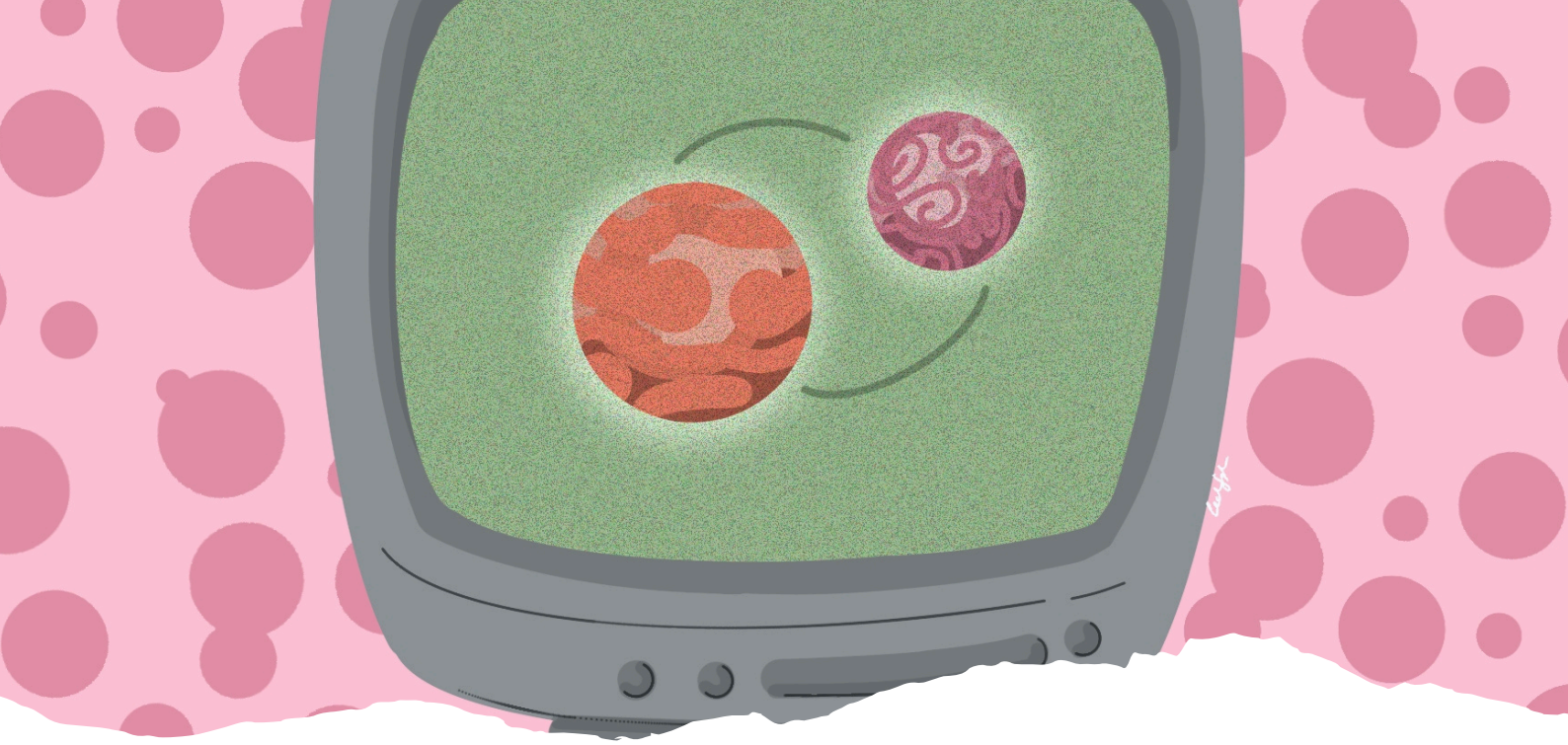
(a) **(b)**

Fig. 1.9 Simplified representation of BCO mergers across cosmic time (a). The systems we detect today, might have formed many Gyr ago, in different metallicities and environments. On the left (b), sketch of a typical dependence of the formation efficiency on redshift, considering different classes of binary compact objects. Image credits: Chruślińska (2024).

merging systems and the total simulated mass. The function $\mathscr{F}_{\rm BCO}(z',z,Z)$ is the rate of compact binaries that form at redshift z' with metallicity Z and merge at redshift z. The metal-dependent SFR $\psi(z',Z)$ provides the information on the SFR density at redshift z' and metallicity Z. This function can be evaluated using several approaches and approximations. The simplest way to model this relation is by assuming an average evolution of the cosmic SFR and metallicity (e.g., Santoliquido, Mapelli, Giacobbo, et al., 2021), for example using the models by Madau and Fragos (2017). A second, more detailed approach, consists in using data-driven observational scaling relations of galaxies (see e.g., Lapi et al., 2025, for a review) to model the metal-dependent SFR across cosmic time (e.g., Santoliquido, Mapelli, Giacobbo, et al., 2021; Sgalletta, Mapelli, et al., 2025).

The form of $\psi(z',Z)$ and its metallicity dependence is particularly important because of the heavy dependence of BCO mergers on metallicity (Neijssel et al., 2019; Chruslinska and Nelemans, 2019; Tang et al., 2020; Santoliquido, Mapelli, Giacobbo, et al., 2021; Briel et al., 2022; Broekgaarden, Berger, et al., 2022). As illustrated in Figure 1.9b , a striking feature is the sharp decline in the merging efficiency of BBHs at high metallicities. This results from the interplay of several factors (Belczynski, Dominik, et al., 2010; Mapelli, Ripamonti, et al., 2010). One primary factor is stellar winds, which are considerably stronger at high metallicities. Intense stellar winds prevent the formation of heavy BHs and at the same time favor loss of angular momentum, leading to wider binaries. Additionally, more massive BHs typically receive weaker natal kicks, thus increasing the odds for the system to remain bound after the compact object formation (Chruślińska, 2024). While the decline in merging efficiency at high metallicity is a consistent feature in the literature, the specific metallicity at which this occurs varies depending on the binary evolution model employed (see Chapter 5).

As a consequence, accurate modeling of the metallicity distribution, particularly its lower end, is essential for reliable predictions of binary compact object mergers. However, precise observational estimates of $\psi(z,Z)$ are challenging for several factors. First, observational uncertainties increase with higher redshifts and lower galaxy luminosities. This has a large impact especially on the low-metallicity tail of the SFR history. This is because galaxies at high redshifts and those with low masses (which are inherently fainter) are characterized by lower metallicities. Further biases are likely introduced due to the observational method itself (Maiolino et al., 2019; Cresci et al., 2019). In fact, observational surveys primarily trace the abundance of oxygen, whereas stellar simulations are sensitive to the iron abundance. Therefore, using the metallicity estimations directly from the observations might introduce biases, since these elements are synthesized by stars on different timescales.



Chapter 2

Binary population synthesis code: SEVN

Modeling the structure and evolution of stars is a highly complex task. Detailed stellar evolution codes must solve a set of fundamental equations, including the mass continuity equation, hydrostatic equilibrium condition, energy conservation, and changes in chemical composition. Codes of this type include MESA (Paxton, Bildsten, et al., 2011; Paxton, Marchant, et al., 2015), PARSEC (Bressan, Marigo, et al., 2012; Costa, Girardi, et al., 2019; Nguyen et al., 2022; Costa, Shepherd, et al., 2025; Shepherd et al., 2025), FRANEC (Degl'Innocenti et al., 2008), STARS (Eggleton, 1971; Eggleton, 1972), GENEC (Ekström et al., 2012; Georgy et al., 2012), BEC (Yoon, Langer, et al., 2006; Yoon, Woosley, et al., 2010). These one-dimensional hydrostatic codes are among the most advanced tools available for this purpose, being able to reproduce stellar evolution with remarkable fidelity. However, this level of detail comes at a substantial computational cost. Running these codes for large numbers of stars is extremely time-consuming and resource-intensive, often making the modeling of entire stellar populations impractical. The challenge becomes even greater when accounting for binary interactions, as many of the processes involved violate the hydrodynamical stability assumption.

Rapid population synthesis codes have been developed to overcome these limitations. These tools are designed to be computationally efficient and scalable, enabling the evolution of millions of both single and binary stellar systems within a short timescale. Population

synthesis codes typically rely on simplified evolutionary prescriptions. These types of codes include BSE (Hurley, Pols, et al., 2000; Hurley, Tout, et al., 2002), STARTRACK (Belczynski, Kalogera, and Bulik, 2002; Belczynski, Kalogera, Rasio, et al., 2008), BINARY_C (Izzard, Tout, et al., 2004; Izzard, Dray, et al., 2006; Izzard, Glebbeek, et al., 2009), MOBSE (Giacobbo, Mapelli, and Spera, 2018; Giacobbo and Mapelli, 2018), COMPAS (Riley, Agrawal, et al., 2022), COSMIC (Breivik, Coughlin, et al., 2020). Alternatively, they implement on-the-fly interpolation from precomputed stellar evolution grids, examples of these codes include SEVN (Spera and Mapelli, 2017; Spera, Mapelli, et al., 2019; Iorio et al., 2023), COMBINE (Kruckow, Tauris, Langer, Kramer, et al., 2018), BRUSSELS (De Donder et al., 1998; De Donder et al., 2004), METISSE (Agrawal et al., 2020), POSYDON (Fragos et al., 2023).

Thanks to their speed and versatility, rapid codes have been widely used for studying the formation of compact objects, predicting GW event rates, and characterizing populations of exotic systems such as X-ray binaries. In general, they constitute powerful tools to explore the statistical properties of stellar populations, bridging theoretical models with observational data.

Throughout my PhD I used and developed the Stellar EVolution for N-body systems (SEVN, Spera and Mapelli, 2017; Spera, Mapelli, et al., 2019; Mapelli, 2020; Iorio et al., 2023) code. SEVN is a rapid population synthesis code designed to model the evolution of both single and binary stars. SEVN employs on-the-fly interpolation of precomputed stellar evolution grids. This approach makes SEVN general and versatile: the stellar evolution models can be easily changed simply by replacing the look-up tables. Additionally, SEVN implements binary evolution through analytical and semi-analytical prescriptions. In the following sections I review the main features of the SEVN code, focusing in particular on the most relevant processes relative to my research. For a thorough description of the code I refer to Iorio et al. (2023).

2.1 Single stellar evolution

In this section you can find a brief outline of the general algorithm and a description of the stellar tracks employed in my works.

2.1.1 Stellar evolution tables

The properties of each star, uniquely identified by its initial stellar mass $M_{\rm ZAMS}$ and metallicity Z, are saved in look-up tables. Each table stores one specific stellar property. In order for SEVN to run, it requires at least seven tables. These include the main stellar properties: time, total stellar mass, He-core mass, CO-core mass, stellar radius, bolometric luminosity and stellar phase. Additional tables, such as the He-core and CO-core radii, convective envelope properties are optional. Moreover, SEVN needs an additional set of tables that trace the evolution of stars who have completely lost their H envelope (pure-He stars).

The tables can be generated from full stellar tracks using the code TRACKCRUNCHER. TRACKCRUNCHER minimizes the amount of saved time-steps, in order to optimize storage and runtime memory, while ensuring an error smaller than 2% during the interpolation.

When simulating the evolution of a star with initial mass $M_\star$ and metallicity $Z_\star$, SEVN interpolates between the four stellar tracks with $M_{\rm ZAMS}$ and Z closer to $(M_\star, Z_\star)$. To ensure consistency in the interpolation, SEVN relies on the stars' percentage of life rather than on the cosmic time (Spera, Mapelli, et al., 2019). This means that stellar properties are derived by interpolating the tracks at the same relative point within a given stellar evolutionary phase. This relative lifetime, denoted as $p_{\rm life}$ is obtained as:

$$p_{\rm life} = \frac{t - t_{0,\rm phase}}{\Delta t_{\rm phase}}, \tag{2.1}$$

where t is the time, $t_{0,\rm phase}$ is the starting time of the phase, and $\Delta t_{\rm phase}$ is the difference between the phase's ending and starting times. This approach guarantees that all the interpolating tracks have the same stellar phase as the simulated star. This is especially important for binary systems. Since many binary processes alter the properties of individual stars, SEVN can dynamically switch stellar tracks. This ensures that the new track, at the given $p_{\rm life}$ remains consistent with the star's updated properties.

2.1.2 PARSEC stellar tracks

In my works I made use of the tracks computed with the stellar evolutionary code PARSEC (PAdova and Trieste Stellar code Bressan, Marigo, et al., 2012; Costa, Girardi, et al., 2019; Costa, Bressan, et al., 2021; Nguyen et al., 2022; Costa, Shepherd, et al., 2025) v2.0 [1]. Here, I summarize only the main features of such tracks, for a complete description of them I refer to Costa, Shepherd, et al. (2025).

The grid of tracks include a comprehensive range of masses and metallicities. Specifically, tracks are available for 13 metallicities ranging from $Z = 10^{-11}$ to $Z = 0.03$. Initial stellar masses range from 2 to 600 $\rm M_\odot$ for $Z > 10^{-4}$ and extend up to 2000 $\rm M_\odot$ for $Z \leq 10^{-4}$. All tracks were computed assuming no rotation (see Nguyen et al., 2022, for rotating PARSEC stellar tracks).

PARSEC models stellar convection using the Schwarzschild criterion (Schwarzschild, 1958) to identify convective regions and the mixing-length theory (Böhm-Vitense, 1958) for convective energy transport. Additionally, the models incorporate core overshooting, allowing for the penetration of convective elements into radiatively stable regions. This process is modeled via the "ballistic" scheme (Bressan, Chiosi, et al., 1981), where the overshooting length, representing the maximum distance traversed by convective bubbles beyond the unstable boundary, is approximately 0.25 pressure scale heights.

Stellar evolution is stopped whenever the star approaches the onset of hydrodynamical instabilities. Therefore, stars with $2 \leq M_{\rm ZAMS}/\rm M_\odot \leq 9$ are evolved only until the early asymptotic giant branch phase. Whereas the tracks of more massive stars ($M_{\rm ZAMS} > 9\rm M_\odot$) continue until either the start of CO burning or the pair-instability SN regime. I show the PARSEC stellar tracks for three selected metallicities in Fig. 2.1.

I adopt also the pure-He stellar tracks provided by PARSEC. The pure-He tracks are computed for metallicities: $Z = 10^{-6}$, 0.0001, 0.0002, 0.0005, 0.001, 0.002, 0.004, 0.006,

[1] https://stev.oapd.inaf.it/PARSEC/index.html

0.008, 0.01, 0.02, 0.03 and 0.05. The zero-age He main sequence mass ($M_{\rm He}$) ranges from $0.36 M_\odot$ to $350 M_\odot$. I show the pure-He PARSEC stellar tracks for three selected metallicities in Fig. 2.2.

2.1.3 Compact remnant formation

A star evolves into a compact remnant when the evolution time exceeds the stellar lifetime. At this point, the star is classified as either a WD, a NS or a BH based on the final masses of its CO and He cores ($M_{\rm CO,f}$ and $M_{\rm He,f}$, respectively), as well as the SN prescriptions adopted. Figure 2.3 diagrammatically illustrates the possible outcomes.

In particular, a WD forms when the $M_{\rm CO,f} < 1.38\,M_\odot$. Moreover, WDs are further classified as follows:

- $M_{\rm ZAMS} < 2$: helium WD (HeWD) with a mass equal to $M_{\rm He,f}$.
- $M_{\rm He,f} < 1.6\,M_\odot$: carbon-oxygen WD (COWD) with a mass equal to $M_{\rm CO,f}$
- $M_{\rm He,f} \geq 1.6\,M_\odot$: oxygen-neon WD (ONeWD) with a mass equal to $M_{\rm CO,f}$

When $1.38\,M_\odot \leq M_{\rm CO,f} < 1.44\,M_\odot$ an electron-capture supernova (ECSN in the Figure) will produce a NS. The other cases ($M_{\rm CO,f} \geq 1.44\,M_\odot$) will leave behind either a NS or a BH, with a final mass dependent on the specific SN prescription adopted.

SEVN includes several prescriptions to model the core-collapse SNe, below I outline only the ones relevant to my work. The *delayed* and *rapid* prescriptions are based on the models by Fryer et al. (2012). Both models rely on a convection-enhanced, neutrino-driven mechanism for SN explosions. They differ in the amount of time that passes before the shock's revival: in the rapid model this occurs within the initial 250 ms post-collapse, whereas in the delayed model this is longer than 500ms. The mass of the resulting compact remnant $M_{\rm rem}$ is given by the sum of the proto-compact object's mass and any subsequent fallback material. By default, if $M_{\rm rem} < 3\,M_\odot$ the remnant is a NS, otherwise it is a BH. Two additional prescriptions, *delayed_Gauss* and *rapid_Gauss* are analogous to the *delayed* and *rapid* prescriptions, respectively, but introduce a different approach for determining NS masses. The latter are sampled from a Gaussian distribution with mean $1.33\,M_\odot$ and standard deviation $0.09\,M_\odot$. This distribution is derived from a fit to the masses of Galactic BNSs (Özel, Psaltis, Narayan, and Santos Villarreal, 2012; Kiziltan et al., 2013; Özel and Freire, 2016). The "gaussian" variants offer the advantage of successfully reproducing the observed masses of NSs (see also Appendix A.2).

Stars that end their life with $M_{\rm He,f} \gtrsim 32\,M_\odot$ enter the so-called pair-instability regime. Stars in this regime will experience a series of pulses that enhance mass loss (pulsational pair-instability supernovae, PPISN in the Figure), or completely destroy the star (pair-instability supernovae, PISN in the Figure). The specific mass boundaries and conditions for which this happens depend on the chosen model. The default model in SEVN is based on Mapelli, Spera, et al. (2020). A pulsational pair-instability SN is triggered if $M_{\rm He,f}$ is within 32 and $64\,M_\odot$, while a pair-instability SN is triggered for $64\,M_\odot \leq M_{\rm He,f} \leq 135\,M_\odot$. Stars with a He core

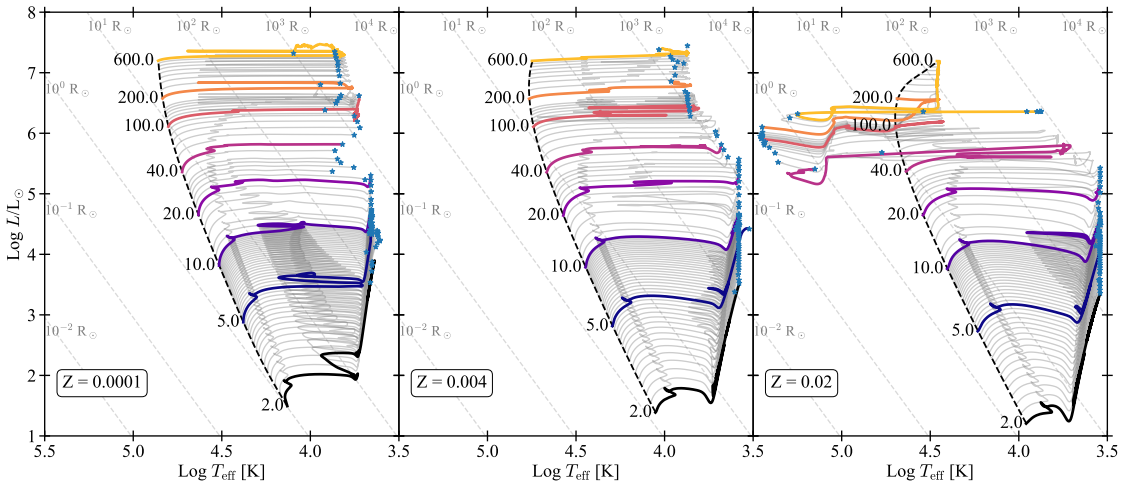


Fig. 2.1 Hertzsprung-Russell diagram of the PARSEC stellar tracks adopted in my works. The plots show different metallicities, from left to right: $Z = 0.0001$, 0.004, and 0.02. Each grey line shows the evolution of a track with a different initial mass $M_{\rm ZAMS}$. The colored lines highlight few of these stellar masses, from bottom to top: $M_{\rm ZAMS} = 2.0$, 5.0, 10.0, 20.0, 40.0, 100.0, 200.0, and 600.0 $M_\odot$. The end of the tracks is marked by a blue star. The dashed black line shows the ZAMS. The light grey dashed lines in the background show points of constant radius. Image credits: Iorio et al. (2023).

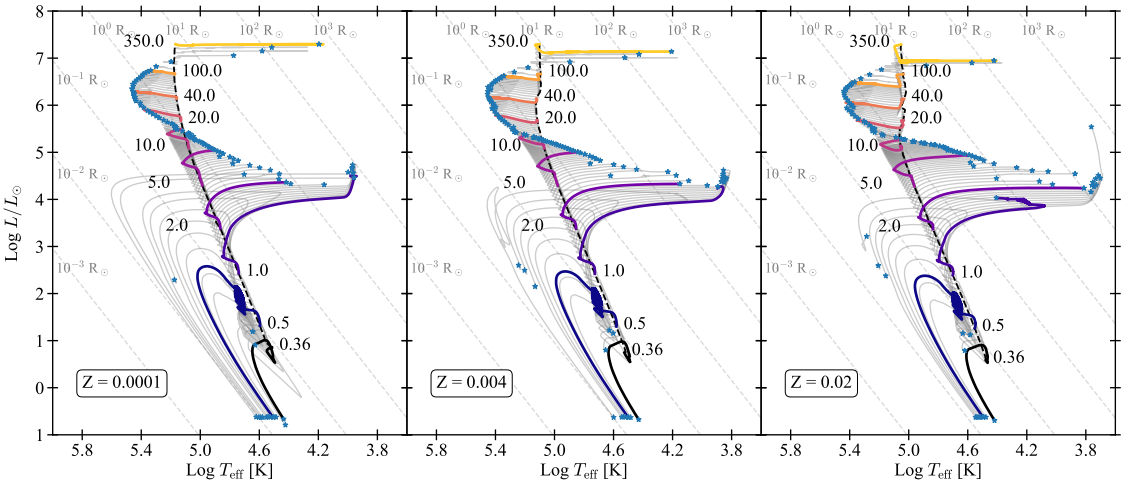


Fig. 2.2 Same as Fig. 2.1 but for pure-He PARSEC tracks. The colored lines highlight stellar masses: $M_{\rm He} = 0.36$, 0.5, 1.0, 2.0, 5.0, 10.0, 20.0, 40.0, 100.0, and 350.0 $M_\odot$. Image credits: Iorio et al. (2023).

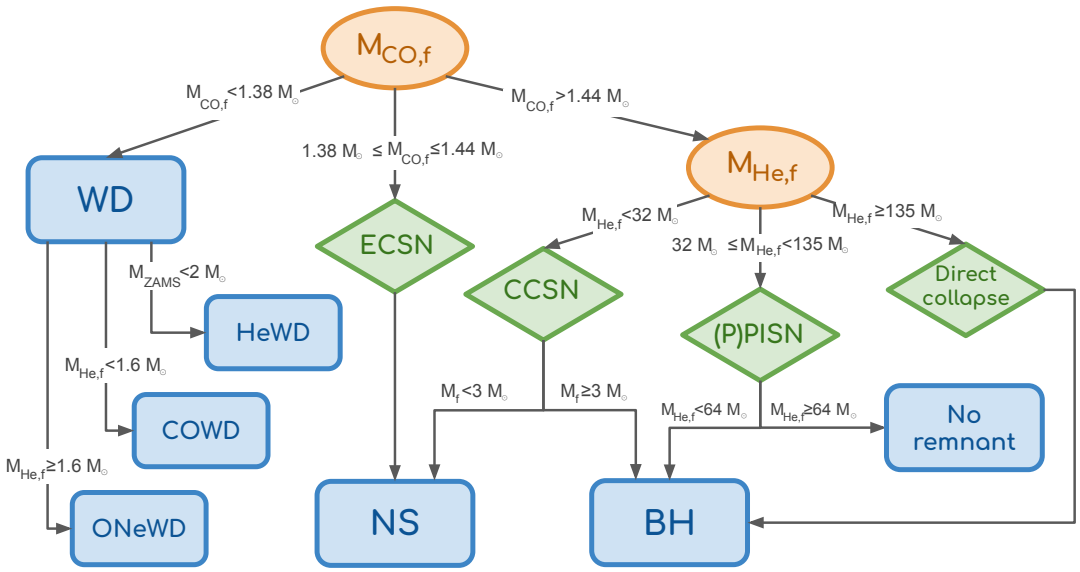


Fig. 2.3 Schematic representation of possible compact remnant formation outcomes within SEVN. In the figure, the $M_{\rm He,f}$ and $M_{\rm CO,f}$ stand for the final He and CO core masses, respectively. $M_{\rm f}$ is the total stellar mass at the end of its life. The mass boundaries separating core-collapse supernovae (CCSN), (pulsational) pair-instability supernovae ((P)PISN), and direct collapse are indicative only and refer to the fiducial model by Mapelli, Spera, et al. (2020).

mass bigger than $135\,{\rm M}_\odot$ directly collapse to a BH and the mass of the remnant is equal to the pre-SN mass of the progenitor, apart from the mass lost in neutrinos (Iorio et al., 2023).

Finally, after a SN the compact remnant receives a natal kick. SEVN includes several possibilities to model this phenomenon. By default, the kick magnitude is drawn from a Maxwellian distribution with 1D root-mean-square $\sigma_{\rm kick} = 265\,{\rm km\,s^{-1}}$ (Hobbs et al., 2005) and then re-scaled by the amount of mass ejected during the SN ($M_{\rm ej}$) and the mass of the remnant ($M_{\rm rem}$) according to:

$$v_{\rm kick} = f_{H05}\,\frac{\langle M_{\rm NS}\rangle}{M_{\rm rem}}\,\frac{M_{\rm ej}}{\langle M_{\rm ej}\rangle}, \tag{2.2}$$

where f_{H05} is a random number sampled from the aforementioned maxwellian distribution, $\langle M_{\rm NS}\rangle$ is the average NS mass and $\langle M_{\rm ej}\rangle$ is the average ejecta mass. Additional models included in SEVN draw the SN kicks directly from a maxwellian with $\sigma_{\rm kick} = 265\,{\rm km\,s^{-1}}$ (Hobbs et al., 2005), assuming no rescaling. The SN kicks are crucial in binary evolution, as they affect the orbital properties and can ultimately lead to the system disruption. SEVN updates the new orbital properties of the system after the kick, taking into account both the new relative orbital velocity and the lost mass (Blauuw kick, Blaauw, 1961).

2.2 Binary evolution

Currently, SEVN can only interpolate among single stellar evolution tracks. Therefore, all binary processes are included through analytical and semi-analytical prescriptions. SEVN models several binary processes, including stellar tides, wind mass transfer, collisions at periastron, RLO, CE evolution, stellar mergers, and orbital changes due to GW emission. The following sections describe the main processes and formalisms relevant to my works.

2.2.1 Roche-lobe overflow

In binary systems, RLO is a key process where one star expands to fill its gravitational equipotential surface and begins to transfer mass to its companion (see also section 1.3). This phenomenon significantly impacts the evolution of both stars and the binary system as a whole. SEVN triggers a RLO event if one of the stars' radii becomes larger than its Roche lobe radius. The latter is estimated as in Eggleton (1983):

$$\frac{R_L}{a} = \frac{0.49q^{2/3}}{0.6q^{2/3} + \ln(1+q^{1/3})}, \tag{2.3}$$

here, a is the semimajor axis and q is the mass ratio, $q = M_{\rm d}/M_{\rm a}$, where $M_{\rm d}$ is the mass of the donor star (the one overfilling its Roche-lobe) and $M_{\rm a}$ is the mass of the accretor star.

Stability of mass transfer

Once a mass transfer episode is initiated, there are different possible outcomes depending on how the stars respond to mass loss and mass accretion. In Section 1.3 I discussed the stability of mass transfer (Webbink, 1985) and how different mass transfer regimes can be distinguished by comparing the mass-radius exponents $\zeta_{\rm eq}$ and $\zeta_{\rm ad}$ with $\zeta_{\rm L}$. Under the assumption of conservative mass transfer, where both energy and angular momentum are conserved, these conditions on mass-radius exponents can be expressed as conditions on the mass ratios. It is common among binary population synthesis codes, including SEVN, to adopt the latter, more simple approach. Here, the mass ratio q is compared to some critical value $q_{\rm crit}$. If $q < q_{\rm crit}$ the mass transfer is considered stable; otherwise it is considered unstable on the dynamical timescale.

Generally, $q_{\rm crit}$ depends on the stellar evolutionary phase of the donor star and varies with the prescription adopted. In my works, I used the fiducial SEVN prescription, specifically the *QCRS* model in Iorio et al. (2023). Table 2.1 summarizes the $q_{\rm crit}$ values for this model. This prescription adopts the $q_{\rm crit}$ values by Hurley, Tout, et al. (2002), but assumes that mass transfer initiated by main-sequence stars and stars in the Hertzsprung gap is always stable. This assumption is based on the fact that stars in these evolutionary phases possess a radiative envelope, which causes them to shrink when they begin to lose mass. Following Hurley,

Donor stellar type	QCRS
Low mass main sequence	0.695
Main sequence	stable
Hertzsprung-gap	stable
Giant branch	Eq.2.4
core-He burning	3.0
He main sequence	3.0
He Hertzsprung-gap	0.784
WD	0.628

Table 2.1 Critical mass ratios $q_{\rm crit}$ as a function of donor stellar type for the fiducial QCRS model in SEVN. The "low mass main sequence" phase designates stars whose convective envelope constitutes at least 80% of their total mass during the main sequence. The term "stable" indicates that the mass transfer process is always stable. This table has been adapted from Iorio et al. (2023).

Tout, et al. (2002), stars with deep convective envelopes have their $q_{\rm crit}$ modeled as:

$$q_{\rm crit} = 0.362 + \frac{1}{3\left(1 - M_{\rm He,d}/M_{\rm d}\right)}, \tag{2.4}$$

where $M_{\rm He,d}$ represents the He-core mass of the donor star, and $M_{\rm d}$ its total mass.

Mass transfer rates

In the case of stable mass transfer, according to the $q_{\rm crit}$ conditions, SEVN evaluates the mass-loss rate according to:

$$\dot{M}_{\rm d} = -F(M_{\rm d}) \left(\ln \frac{R_{\rm d}}{R_{\rm L}}\right)^3 {\rm M}_\odot\,{\rm yr}^{-1}, \tag{2.5}$$

where $F(M_{\rm d})$ is a normalization factor (see eq. 24 in Iorio et al., 2023).

SEVN allows for non conservative mass transfer, therefore the amount of mass lost by the donor, $\dot{M}_{\rm d}$, can be larger than the one accreted, $\dot{M}_{\rm a}$. The accretion rate on the companion is parameterized as follows:

$$\dot{M}_{\rm a} = \begin{cases} \min\left(\dot{M}_{\rm Edd}, -f_{\rm MT}\dot{M}_{\rm d}\right) & \text{if the accretor is a compact object} \\ -f_{\rm MT}\dot{M}_{\rm d} & \text{otherwise.} \end{cases} \tag{2.6}$$

The previous equation implies that accretion on compact objects is limited by the Eddington rate, $\dot{M}_{\rm Edd}$, which is defined as:

$$\dot{M}_{\rm Edd} = 2.08 \times 10^{-3}\,{\rm M}_\odot\,{\rm yr}^{-1}\,\eta_{\rm Edd}(1+X)^{-1}\,\frac{R_{\rm a}}{{\rm R}_\odot}, \tag{2.7}$$

where R_a is the accretor's radius, and $X = 0.760 - 3.0Z$ is the hydrogen mass fraction of the accreted material. The constant $f_{MT} \in [0,1]$ represents the mass accretion efficiency. In my works I assume $f_{MT} = 0.5$.

Orbital variations

Mass transfer in a binary system deeply impacts not only the masses of its objects but also the system's orbital properties. Specifically, SEVN quantifies the angular momentum lost from the system $\Delta J_{orb,lost}$:

$$\Delta J_{orb,lost} = -|\Delta M_{loss}|\gamma_{RLO} a^2 \sqrt{1-e^2}\frac{2\pi}{P}, \tag{2.8}$$

where ΔM_{loss} is the mass lost from the system (non-zero if mass transfer is non conservative) and P is the orbital period. γ_{RLO} depends on the assumptions made about the lost mass. I adopt a model where the lost mass is emitted isotropically from the accretor, in which case:

$$\gamma_{RLO} = M_d^2/(M_a + M_d)^2. \tag{2.9}$$

Similarly, the loss and accretion of mass affect the spin angular momentum of both stars. The donor's spin angular momentum will decrease by:

$$\Delta J_{spin,d} = \Delta M_d R_L^2 \Omega_{spin,d} \tag{2.10}$$

while the accretor's spin will increase by:

$$\Delta J_{spin,a} = \Delta M_a \sqrt{G M_a R_{acc}}. \tag{2.11}$$

$\Omega_{spin,d}$ is the angular velocity of the donor star, and R_{acc} represents the accretion radius, effective radial point where the material from the donor interacts with the accreting object. Since the total angular momentum of the binary is conserved, changes in the spin angular momenta of the two stars directly translate into variations of the orbital angular momentum:

$$\Delta J_{orb,d} = -\Delta J_{spin,d} \quad \Delta J_{orb,a} = -\Delta J_{spin,a}. \tag{2.12}$$

Finally, the change in the semimajor axis Δa at the end of each timestep during RLO is given by:

$$\Delta a = \frac{\left(J_{orb} + \Delta J_{orb,lost} + \Delta J_{orb,d} + \Delta J_{orb,a}\right)^2 (M_d + M_a)}{G(1-e^2)M_d^2 M_a^2} - a, \tag{2.13}$$

where the masses (M_d and M_a) are considered after the mass exchanges within the current timestep.

2.2.2 Common envelope

The case of an unstable mass transfer leads either to a CE or a stellar merger. Stars without a distinct core-envelope separation (main sequence and He main sequence stars) generally merge directly during such an event. In contrast, other types of stars (giant like-stars) undergo a CE phase. The Hertzsprung-gap phase is particularly interesting in this context because these stars haven't developed a fully formed core yet. There's currently no consensus on whether Hertzsprung-gap stars can survive a CE event. In my work, I assume a pessimistic scenario where Hertzsprung-gap stars lead to a merger during an unstable mass transfer event.

The CE phase is a key evolutionary phase towards the formation of close BCO systems, as it rapidly and efficiently shrinks binary orbits (see also Section 1.3). In SEVN, the CE is modeled as an instantaneous process (it takes place in a single time-step), and it is implemented following the $\alpha\lambda$–parametrization (van den Heuvel, 1976; Webbink, 1984; Livio et al., 1988; Iben et al., 1993; Hurley, Tout, et al., 2002). This formalism relies on two parameters, α and λ, thouroughly described in Section 1.3.

The initial step in this calculation is to determine the total envelope binding energy:

$$E_{\rm bind,i} = -G\left(\frac{M_1 M_{\rm env,1}}{\lambda_1 R_1} + \frac{M_2 M_{\rm env,2}}{\lambda_2 R_2}\right), \tag{2.14}$$

where M and $M_{\rm env}$ denote the total and envelope masses of the stars, respectively, and R is the stellar radius. The subscript 1 (2) always refer to the donor (accretor) star in the binary. If the accretor lacks a formed core, $M_{\rm env,2} = 0$. We can evaluate the change in the orbital energy, $\Delta E_{\rm orb}$, for a binary system entering a CE phase with an initial semimajor axis $a_{\rm i}$ and ending with a post-CE separation $a_{\rm f}$:

$$\Delta E_{\rm orb} = \frac{G M_{\rm c,1} M_{\rm c,2}}{2}\left(a_{\rm f}^{-1} - a_{\rm i}^{-1}\right), \tag{2.15}$$

where $M_{\rm c,1}$ and $M_{\rm c,2}$ are the core masses of the two stars.

For a successful CE ejection, the binding energy in the post-CE configuration, $E_{\rm bind,f}$, must be zero. According to the energy formalism, which assumes orbital energy is the unique reservoir for envelope ejection, the following equation applies:

$$E_{\rm bind,i} = \alpha \Delta E_{\rm orb} \tag{2.16}$$

This condition allows us to derive the post-CE semimajor axis $a_{\rm f}$. If neither star fills its RL after the CE ejection, the phase is considered successful, and the binary evolution continues under these new conditions. Otherwise, SEVN triggers a merger of the two objects.

The two key quantities in this formalism are λ and α. We treat α as a free parameter, typically varying it between 0.5 and 5 in my studies. For λ, SEVN offers several models, many of which are based on fits to stellar evolution models, such as those by Claeys et al. (2014), Klencki, Nelemans, Istrate, and Chruslinska (2021), and Xu and Li (2010). Furthermore, I developed an alternative formalism that includes an optional table property designed

to store information on the envelope binding energies of stellar tracks. This allows the direct integration of the envelope binding energies from the PARSEC stellar tracks, ensuring consistency with the underlying stellar evolution models. I describe the specific changes introduced by this new formalism and their main implications in Chapter 5.

2.2.3 Stellar mergers

When stars merge, the resulting new star's He and CO cores are the sum of the two progenitors' He and CO cores, respectively, and its total mass is the sum of the progenitors' masses. The post-merger star also inherits the percentage of remaining life from the more evolved of its progenitors. SEVN can then classify the new star type consistently by jumping on the correct post-merger stellar evolutionary track.

When compact objects are involved in a stellar merger, SEVN uses a collision table to determine the correct merger product. Specifically, if a star merges with a compact object, the star is completely disrupted, and its mass is lost from the system. Additionally, WDs mergers can trigger a Type Ia SN explosion, leaving no compact remnant. If a WD resulting from a merger exceeds the Chandrasekhar mass limit ($1.44\,M_\odot$), it becomes a NS. Similarly, post-merger NSs with a mass exceeding the maximum NS mass become BHs. In all other scenarios, the post-merger compact object's mass is simply the sum of the progenitor compact objects' masses.

2.2.4 Gravitational waves

GWs emitted by a binary system cause its orbit to shrink over time. Peters (1964) derive the equations predicting the changes in the orbital properties of a binary system due to emission of GWs. The author derives the time average of the energy emission rate as well as the average angular momentum rate, from which he obtains the variations of the semimajor axis and eccentricity as functions of time:

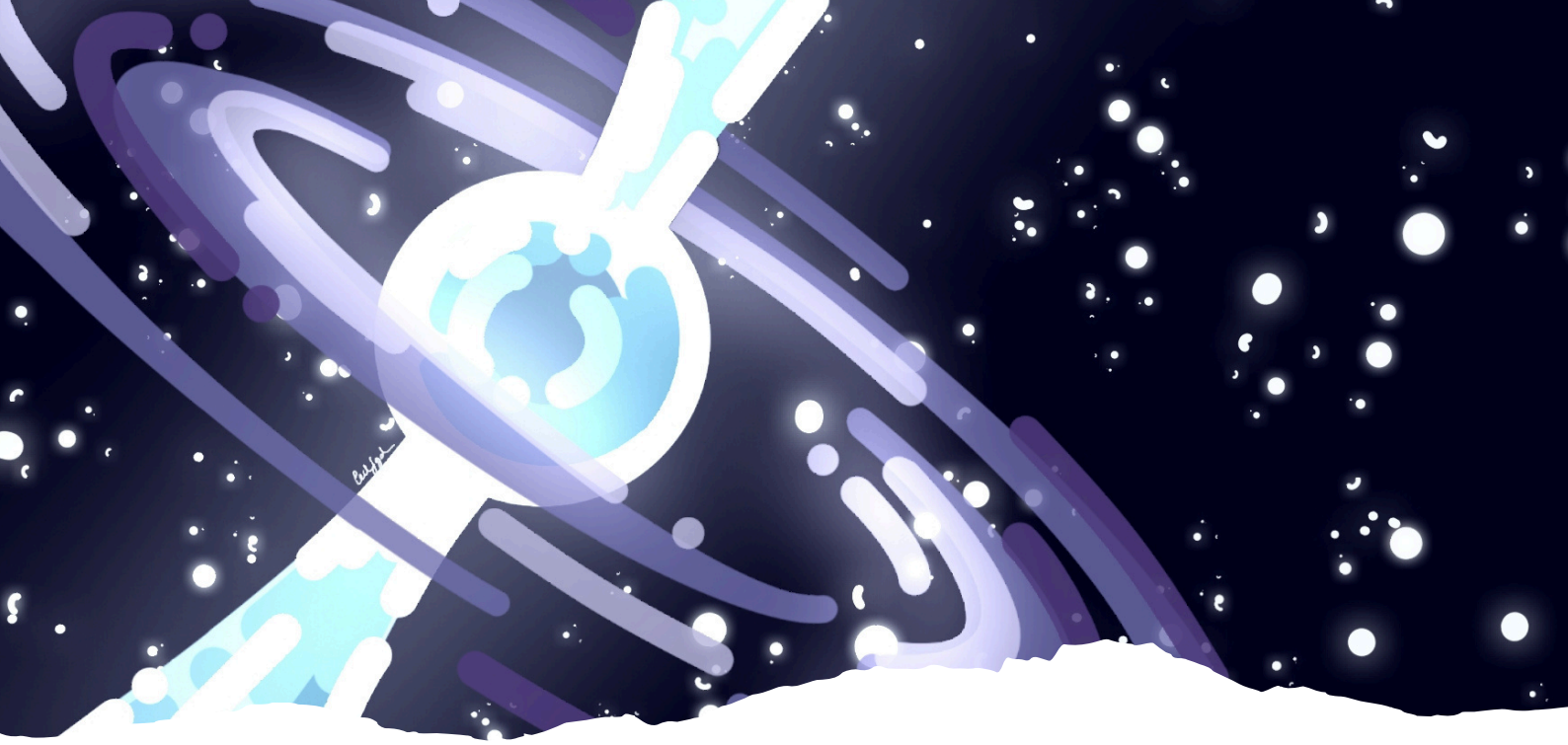
$$\frac{da}{dt} = -\frac{64}{5}\frac{G^3 m_1 m_2 (m_1+m_2)}{c^5 a^3 (1-e^2)^{7/2}}\left(1+\frac{73}{24}e^2+\frac{37}{96}\right), \tag{2.17}$$

$$\frac{de}{dt} = -\frac{304}{15}\frac{G^3 m_1 m_2 (m_1+m_2)}{c^5 a^3 (1-e^2)^{5/2}}\left(1+\frac{121}{304}e^2\right). \tag{2.18}$$

The above equations describe the orbital decay and circularization by GW emission. By solving the system of differential equations 2.17 and 2.18 it is possible to compute the GW-induced merger time. Instead of solving the whole system, SEVN integrates equation 2.17 assuming a constant eccentricity during the evolution. Indeed, this is a good compromise between the required computation time and accuracy of the result (see Appendix D.1 in Iorio et al., 2023). Therefore, a stellar binary with stars of masses M_1 and M_2,initial separation a and eccentricity e, will have an approximate time to the merger of:

$$t_{\rm merg} \simeq \frac{5}{256}\frac{c^5 a^4 (1-e_0^2)^{7/2}}{G^3 (M_1 M_2 (M_1+M_2))}. \tag{2.19}$$

SEVN evaluates the orbital decay due to GW emission whenever $t_{\rm merg}$ is shorter than the Hubble time.



Chapter 3

Binary neutron star populations in the Milky Way

This chapter is based on Sgalletta, Iorio, et al. (2023).

3.1 Introduction

Galactic radio pulsars in BNS systems are a unique laboratory to probe the evolution of BNSs and their progenitors. The understanding of pulsars birth properties might help to shed light on the SN explosion mechanism, since we expect that the newly-born NS properties are tightly correlated with the pre-SN star (Faucher-Giguère et al., 2006; Kapil et al., 2023). Nevertheless, the formation and evolution properties of pulsars are still matter of debate. Earlier efforts attempted to infer the birth distribution of pulsar properties from their observed Galactic population (Ostriker et al., 1969; Faucher-Giguère et al., 2006), the main long-standing issue being that of magnetic field decay (Faucher-Giguère et al., 2006). Binary evolution uncertainties add to the complexity of the picture. Two of the most important unknowns of binary star evolution are the physics of CE (Ivanova, Justham, Chen, et al., 2013; Klencki, Nelemans, Istrate, and Chruslinska, 2021; Röpke et al., 2023) and the natal kick

(Woosley, 1987; Janka and Mueller, 1994; Lai et al., 2001; Hobbs et al., 2005; O'Doherty et al., 2023).

The aim of this work is to characterize the population of Galactic BNSs, by coupling the population synthesis code SEVN (Spera and Mapelli, 2017; Spera, Mapelli, et al., 2019; Mapelli, Spera, et al., 2020) with a Milky-Way (MW) model. We evolve the orbital binary properties, the spin period and magnetic field of pulsars. With this framework, we explore the merger rates, the orbital properties and the population of radio pulsars for a range of parameter combinations. We adopt four MW models, employing semi-empirical prescriptions (Chiappini et al., 1997; Courteau et al., 2014; Pezzulli et al., 2015; Grisoni et al., 2017; Boco, Lapi, Goswami, et al., 2019) and cosmological simulations (Schaye et al., 2014; The EAGLE team, 2017; Nelson, Springel, et al., 2019; Nelson, Pillepich, et al., 2019). Additionally, we explore several parameters, such as the CE efficiency α, the natal kick distribution, the birth distribution of spin periods and surface magnetic fields of pulsars, and the magnetic field decay timescale. Finally, we test our results against the observed Galactic pulsar population.

3.2 Methods

We study the Galactic BNS population by coupling various MW models with BNS catalogues obtained with the SEVN population synthesis code. A general overview of the SEVN code along with a description of the default setup is provided in Chapter 2. In this work, we adopt the default SEVN[1] configuration. In what follows we highlight only the parameters that we varied in our models. We adopt the *rapid-Gauss* model as our fiducial SN explosion model. We decided to introduce this model because both the *rapid* and *delayed* prescriptions by Fryer et al. (2012) fail to reproduce the observed NS mass distribution (Vigna-Gómez et al., 2018). We investigate the impact of different SN models in Appendix A.2. The NS radius is fixed at 11 km (Özel, Psaltis, Narayan, and Santos Villarreal, 2012; Bogdanov, Heinke, et al., 2016; Bauswein et al., 2017; Abbott et al., 2018). In our fiducial model we draw the SN natal kicks according to the model by Giacobbo and Mapelli (2018). In Appendix A.1, we explore different assumptions for the natal kick and their effects on our main results. Finally, we model the CE evolution assuming the fiducial prescription for the λ parameter based on the fitting formulae by Claeys et al. (2014). We vary the efficiency α in our models: $\alpha = 0.5$, 1, 3 and 5. In the following sections we detail the methodology used in our study. Note that all equations in this Chapter adopt the international system of units.

3.2.1 NS properties

To study the evolution of the physical properties of NSs with SEVN, at the time of formation we assign to each NS a spin, a magnetic field and an angle between the rotation and the magnetic axis, α_B. For all of our NSs, we generate $\cos\alpha_B$ from an uniform distribution between 0 and 1. The evolution of each NS depends on its interaction with the companion star.

[1] SEVN is publicly available at https://gitlab.com/sevncodes/sevn.git. The version used in this work is the release *Sgalletta23*: https://gitlab.com/sevncodes/sevn/-/releases/sgalletta23.

If the NS is not accreting matter from the companion, the evolution is the same as if the NS were isolated, i.e. the NS spin and magnetic field decrease with time (*spin down*). In contrast, if the companion star fills its Roche lobe, the infalling matter can transfer angular momentum to the NS, causing the latter to spin up. When the latter process takes place the resulting NS is said to be *recycled*. In fact, observed recycled pulsars are usually characterized by short spin periods and relatively low magnetic fields (Lorimer, 2008; Lorimer, 2011; Özel and Freire, 2016).

Spin down

If the evolution of the pulsar proceeds unperturbed, the pulsar can be seen as a rotating magnet. We model the magnetic field of the pulsar with a dipole and compute the loss of energy accordingly. In fact, as the pulsar rotates it emits electromagnetic radiation, losing rotational energy, that is the pulsar spins down. The angular frequency of the pulsar changes according to Goldreich and Julian, 1969:

$$\dot{\Omega} = -\frac{8\,\pi\,B^2\,R^6\,\sin^2\alpha_{\rm B}\,\Omega^3}{3\,\mu_0\,c^3\,I}, \tag{3.1}$$

where Ω is the angular frequency, B is the surface magnetic field, R is the radius, $\alpha_{\rm B}$ is the angle between the rotational axis and the magnetic axis, I is the moment of inertia of the pulsar, c is the speed of light, and μ_0 is the vacuum magnetic permeability. The time derivative of the angular frequency $\dot{\Omega}$ is linked to Ω through the relation $\dot{\Omega} \propto \Omega^n$, where n is the magnetic braking index. Observational evidence points toward a value of n lying in the range $2.5 - 3.5$ (Manchester, Hobbs, et al., 2005). In addition, we assume that the magnetic field decays with time because of Ohmic dissipation. The finite resistivity in the NS crust, caused by electron scatterings, converts the magnetic energy into heat (Goldreich and Reisenegger, 1992; Konar and Bhattacharya, 1997; Urpin et al., 1997; Konar and Bhattacharya, 1999). Furthermore, observations seem to support the decay of the magnetic field: younger pulsars show in general stronger magnetic fields with respect to older ones (Ostriker et al., 1969). In our models, we evolve the magnetic field following an exponential decay (Kiel et al., 2008; Osłowski et al., 2011; Chattopadhyay et al., 2020; Chattopadhyay et al., 2021):

$$B = (B_0 - B_{\rm min})\,e^{-t/\tau_{\rm d}} + B_{\rm min}, \tag{3.2}$$

where B_0 is the initial surface magnetic field, $B_{\rm min}$ is the minimum surface magnetic field strength and $\tau_{\rm d}$ is the magnetic field decay timescale. We assume that the pulsar magnetic field stops decreasing when it reaches the value $B_{\rm min}$. Throughout this work, we adopt $B_{\rm min} = 10^8$G, as suggested by Zhang and Kojima, 2006. The magnetic field decay timescale $\tau_{\rm d}$ is a free parameter of the model. Its value is controversial: ranging from $2 - 5$ Myr (e.g., Osłowski et al., 2011) to 2000 Myr (e.g., Kiel et al., 2008). Faucher-Giguère et al., 2006 carry out their analysis considering no magnetic field decay at all.

Following Chattopadhyay et al., 2020, we get an analytic expression for the evolution of the angular frequency of the pulsar:

$$\frac{1}{\Omega_{\rm f}^2} = \frac{1}{\Omega_{\rm i}^2} + \frac{16\,\pi\,R^6\,P\sin^2\alpha_{\rm B}}{3\,\mu_0\,c^3\,I} \times \left[B_{\rm min}^2\,\Delta t - \tau_{\rm d}\,B_{\rm min}(B_{\rm f}-B_{\rm i}) - \frac{\tau_{\rm d}}{2}(B_{\rm f}^2 - B_{\rm i}^2)\right], \tag{3.3}$$

where $\Omega_{\rm i}$ and $\Omega_{\rm f}$ are the initial and final angular frequencies, $B_{\rm i}$ and $B_{\rm f}$ are the initial and final magnetic fields, and Δt is the time elapsed between the final and the initial states.

The spin period P and the spin down rate $\dot{P}$ can then be obtained from Ω and $\dot{\Omega}$ through the following relations:

$$P = \frac{2\,\pi}{\Omega} \tag{3.4}$$

$$\dot{P} = -\frac{\dot{\Omega}\,P}{\Omega}. \tag{3.5}$$

We update the values of the NS spin periods and magnetic fields in SEVN after each time-step according to Eqs. 3.2 and 3.3. We can trace the pulsar evolution in the $P-\dot{P}$ diagram. Because of spin down, pulsars evolve towards larger spin periods and lower magnetic fields. In the $P-\dot{P}$ plane, this trend results in a diagonal shift, towards the lower right corner of the plot (see e.g. Figure 2 in Chattopadhyay et al., 2020). The timescale of this evolution depends on the choice of $\tau_{\rm d}$: for shorter values of $\tau_{\rm d}$ the traversal of the $P-\dot{P}$ plane is faster.

Spin up

Matter exchange processes in binary stars, such as those happening during a RLO, can significantly affect the evolution of NS spin and magnetic field. For instance, part of the angular momentum of the exchanged material, can be transferred to the NS, that, consequently, spins up. In SEVN, we have implemented the spin-up process of NSs during RLO mass transfer following the same prescriptions as in Kiel et al., 2008 and Chattopadhyay et al., 2020. The rate of change in the angular momentum of the pulsar $\dot{J}_{\rm acc}$ scales linearly with the amount of accreted mass, that is:

$$\dot{J}_{\rm acc} = \varepsilon\,V_{\rm diff}\,R_{\rm A}^2\,\dot{M}_{\rm NS}, \tag{3.6}$$

where ε is an efficiency factor, set at 1 in our models, $\dot{M}_{\rm NS}$ is the mass accretion rate on the NS, and $R_{\rm A}$ is the magnetic radius. We define $R_{\rm A} = R_{\rm Alfven}/2$. The Alfven radius $R_{\rm Alfven}$ is the radius at which the magnetic pressure equals the ram pressure:

$$R_{\rm Alfven} = \left(\frac{2\,\pi^2}{G\,\mu_0^2}\right)^{1/7} \times \left(\frac{R^6}{\dot{M}_{\rm NS}\,M_{\rm NS}^{1/2}}\right)^{1/7} \times B^{4/7}. \tag{3.7}$$

$V_{\rm diff}$ is the difference between the Keplerian angular velocity at the magnetic radius $\Omega_{\rm K}|_{R_{\rm A}}$ and the co-rotation angular velocity $\Omega_{\rm co}$:

$$V_{\rm diff} = \Omega_{\rm K}|_{R_{\rm A}} - \Omega_{\rm co}. \tag{3.8}$$

We can see from Eq. 3.6, that the condition for the NS to spin up is $V_{\rm diff} > 0$. In this case, the variation in angular momentum of the NS is positive and its spin increases: as matter reaches the magnetic radius, the magnetic pressure dominates and matter follows the magnetic field lines and is accreted on the NS polar caps. In contrast, if $V_{\rm diff} < 0$, then the NS acts as a propeller (Kiel et al., 2008): the velocity of the magnetic field lines at the magnetic radius is higher than the local Keplerian velocity ($\Omega_{\rm co} > \Omega_{\rm K}|_{R_{\rm A}}$) and matter is blown away from the NS (Illarionov et al., 1975). In SEVN, we have implemented the propeller effect as well.

We also assume that the magnetic field decays exponentially with the amount of mass accreted. Observations of the low magnetic fields of binary and millisecond pulsars suggest accretion-induced field decay (Konar and Bhattacharya, 1997). The magnetic field evolves according to the following equation during RLO in our models:

$$B = (B_0 - B_{\rm min}) \times \exp\left(-\frac{\Delta M_{\rm NS}}{\Delta M_{\rm d}}\right) + B_{\rm min}. \tag{3.9}$$

$\Delta M_{\rm NS}$ is the amount of mass accreted by the NS and $\Delta M_{\rm d}$ is the magnetic field decay mass scale, another free-parameter of the model. We fixed $\Delta M_{\rm d}$ to the fiducial value $\Delta M_{\rm d} = 0.025\ {\rm M}_\odot$, which corresponds to the optimal value obtained in Chattopadhyay et al., 2020. We further discuss the values adopted in our simulations in Sec. 3.2.5.

At each time-step, SEVN evaluates if matter accretes onto the NS via RLO. If not, the variations to the spin and magnetic field of the NS are only due to spin down (Eqs. 3.1 and 3.2). Otherwise, the algorithm first evaluates $V_{\rm diff}$. If $V_{\rm diff} > 0$, SEVN calculates also the spin up from Eqs. 3.6 and 3.9:

$$\Omega_{\rm i+1} = \Omega_{\rm i} + \frac{\Delta J_{\rm acc}}{I}, \tag{3.10}$$

where $\Delta J_{\rm acc} = V_{\rm diff} R_{\rm A}^2 \Delta M_{\rm NS}$. At the end of the time-step, SEVN updates both the spin and the magnetic field accordingly. If $V_{\rm diff} < 0$, no matter accretes during that time-step and spin and magnetic fields are updated only accounting for spin down. This accurate treatment of spin up and down benefits from the adaptive time-step formalism of SEVN (Iorio et al., 2023).

According to Chattopadhyay et al., 2020, a CE phase can trigger further spin up of the NS, as suggested by MacLeod and Ramirez-Ruiz, 2015. Here, we decide not to include this possible spin up by CE, because it is quite controversial (Osłowski et al., 2011; Chamandy et al., 2018).

3.2.2 Initial conditions for the SEVN binary catalogues

We sample the masses of the primary stars (M_1) from a Kroupa's initial mass function (Kroupa, 2001), in a range between 5 and 150M$_\odot$:

$$\mathscr{F}(M) \propto M_1^{-2.3} \tag{3.11}$$

We draw the secondary star's mass (M_2), the initial binary orbital period ($P_{\rm orb}$), and the eccentricity following the distributions derived by Sana et al., 2012, which are based on

observations of massive binary stars in young clusters:

$$\mathscr{F}(q) \propto q^{-0.1} \tag{3.12}$$

where $q = M_2/M_1 \in [q_{\rm min}, 1]$, $q_{\rm min} = \max\left(\frac{2.2{\rm M}_\odot}{M_1}, 0.1\right)$, so that the secondary star mass distribution is cut at $2.2{\rm M}_\odot$,

$$\mathscr{F}(P_{\rm orb}) \propto (\log P_{\rm orb})^{-0.55} \tag{3.13}$$

with $0.15 \leq \log(P_{\rm orb}/{\rm d}) \leq 5.5$, and

$$\mathscr{F}(e) \propto e^{-0.42} \tag{3.14}$$

with $0 \leq e \leq 0.9$. For each parameter (described in section 3.2.5), we simulate with SEVN 11 sub-sets varying the metallicity: $Z = 0.0002$, 0.0004, 0.0008, 0.0012, 0.0016, 0.002, 0.004, 0.008, 0.012, 0.016, 0.02. Each SEVN sub-set evolves 10^6 binary systems. Therefore, for each model we ran a total of 1.1×10^7 binaries.

3.2.3 Milky Way models

In our work, we couple the catalogues of binary NS systems from SEVN with a MW-like galaxy. We choose four Galaxy models that have total stellar mass and current SFR as close as possible to the measured values of the MW (Artale, Mapelli, Giacobbo, et al., 2019). Therefore, we require a total stellar mass $(5.43 \pm 0.57) \times 10^{10}$ M$_\odot$ (McMillan, 2017) and a current SFR ~ 1.65 M$_\odot$ yr^{-1} (Licquia et al., 2015). The use of different Galaxy models allows us to test the robustness of our results against the specific features of the chosen MW models. Here below, we describe the four models in detail. We summarize them in Table 3.1.

Constant SFR (Const model)

The first model for the MW assumes a constant SFR, fixed at 1.65 M$_\odot$ yr^{-1}. All binary systems in this model have solar metallicity, $Z = 0.0142$ (Asplund et al., 2009; Vigna-Gómez et al., 2018; Chattopadhyay et al., 2020). The integration of the SFR through cosmic time leads to a total stellar mass $M_\star \sim 1.9 \times 10^{10}$ M$_\odot$, well below the observed value. This MW model has been used by most of the previous works (e.g., Vigna-Gómez et al., 2018; Shao et al., 2018; Chattopadhyay et al., 2020), adopting a fixed SFR at 1 M$_\odot$ yr^{-1}.

The EAGLE model

The EAGLE project [2] (Schaye et al., 2014; The EAGLE team, 2017) comprises a set of cosmological hydrodynamical simulations with comoving box sizes of 25, 50 and 100 Mpc, evolved from redshift $z = 20$ to $z \sim 0$. The simulations are run with the GADGET-3 code (Springel, 2005). A full description of the sub-grid baryonic processes included can be found

[2] https://icc.dur.ac.uk/Eagle/

in Schaye et al. (2014). The cosmological framework adopted is the ΛCDM cosmological model, with cosmological parameters: $\Omega_{\Lambda,0} = 0.693$, $\Omega_{M,0} = 0.307$, $\Omega_{b,0} = 0.048$, $\sigma_8 = 0.8288$, $n_s = 0.9611$, and $h = 0.6777$ (Ade et al., 2016). We selected a MW-like galaxy from the EAGLE run labeled L025N0752, characterized by a periodic box of side 25 Mpc comoving. This is the run with the highest resolution in the EAGLE suite: the baryonic particle and the dark matter mass resolutions are $2.26 \times 10^5 M_\odot$ and $1.21 \times 10^6 M_\odot$, respectively. By imposing the requirements outlined in Section 3.2.3, we selected a best-fitting galaxy identified by the IDs of the halo, Gnr = 23 and the sub-halo, Sgrn = 0. This galaxy is characterized by a total stellar mass $3.65 \times 10^{10} M_\odot$ and a current SFR 1.38 $M_\odot$ yr^{-1}.

The ILLUSTRISTNG model

The ILLUSTRISTNG project [3] consists of three simulation volumes, with comoving box size of 50, 100 and 300 Mpc, from redshift $z = 127$ to $z \sim 0$. The simulations have been run with the moving mesh code AREPO (Springel, 2010). A full description of the baryonic processes included in this simulation can be found in Nelson, Pillepich, et al. (2019) and Pillepich, Nelson, et al. (2019). A ΛCDM cosmological model is assumed, with cosmological parameters from Ade et al. (2016): $\Omega_{\Lambda,0} = 0.6911$, $\Omega_{M,0} = 0.3089$, $\Omega_{b,0} = 0.0486$, $\sigma_8 = 0.8159$, $n_s = 0.9667$ and $h = 0.6774$. We select our MW-like galaxy from the TNG50 run (with 50 Mpc comoving length and baryonic mass resolution of $5.7 \times 10^4\, M_\odot/h$, Nelson, Springel, et al., 2019). The best candidate galaxy for our work is identified by Gnr = 244 and Sgrn = 547844, with a total stellar mass $5.10 \times 10^{10} M_\odot$ and current SFR 1.675 $M_\odot$ yr^{-1}. The galaxy is included in the MW-type catalog released by Pillepich, Sotillo-Ramos, et al. (2023) from the TNG50 simulation.

The empirical (Emp) model

We also include a MW-like model built from empirical relations. We adopt an exponentially decaying SFR function:

$$\mathrm{SFR}(\tau) = A \exp\left(-\tau/\tau_\Psi\right) \tag{3.15}$$

where A is a proportionality constant, τ is the internal Galactic age, defined as the time t_f elapsed since the beginning of significant star formation activity in the Galaxy, and τ_Ψ is the characteristic timescale for the suppression of SFR (Grisoni et al., 2017; Bovy, 2017; Boco, Lapi, Goswami, et al., 2019). This model is commonly adopted to describe low-redshift, disc-dominated galaxies (Chiappini et al., 1997; Courteau et al., 2014; Pezzulli et al., 2015; Grisoni et al., 2017). Integrating the SFR over the cosmic time yields the total stellar mass of the galaxy:

$$M_\star(t_0) = \int_{t_f}^{t_0} \mathrm{SFR}(t)\, \mathrm{d}t, \tag{3.16}$$

where t_0 is the cosmic time today. For our MW-like galaxy, we set $\tau_\Psi = 7$ Gyr, as the SFR decay timescale (Bovy, 2017). To derive the two unknowns in Equations 3.15 and 3.16, A

[3] https://www.tng-project.org/

MW model	$M_\star\,(10^{10}\,\mathrm{M}_\odot)$	SFR $(\mathrm{M}_\odot\,\mathrm{yr}^{-1})$
EAGLE	3.7	1.38
ILLUSTRISTNG	5.1	1.67
Empirical (Emp)	5.0	1.65
Constant (Const)	1.9	1.65

Table 3.1 Properties of the MW models. Columns 1 and 2 refer to the total stellar mass $M_\star$ and current SFR of the considered Galaxy models.

and t_f, we imposed a total stellar mass $M_\star(t_0) = 5\times10^{10}\,\mathrm{M}_\odot$ and a current star formation rate $\mathrm{SFR}(t_0) = 1.65\,\mathrm{M}_\odot\,\mathrm{yr}^{-1}$.

As for the metallicity evolution, we assume the fundamental metallicity relation (FMR, Mannucci, Cresci, et al., 2010; Mannucci, Salvaterra, et al., 2011). The FMR has been obtained empirically through observations of the local galaxies of the Sloan Digital Sky Survey, and its robustness has been confirmed for galaxies up to $z\sim3.5$ (Mannucci, Cresci, et al., 2010; Hunt et al., 2016). The FMR links $M_\star$, SFR and the gas metallicity Z, whereas it is almost independent of redshift (Chruślińska et al., 2021; Boco, Lapi, Chruslinska, et al., 2021; Santoliquido, Mapelli, Artale, et al., 2022). Following this approach, the Galaxy metallicity is evaluated through Eq. 2 of Mannucci, Salvaterra, et al. (2011):

$$12+\log(\mathrm{O/H}) = \begin{cases} 8.90+0.37\,m-0.14\,s-0.19\,m^2 \\ \qquad +0.12\,m\,s-0.054\,s^2 & \text{for } \mu_{0.32}\geq 9.5 \\ 8.93+0.51\,(\mu_{0.32}-10) & \text{for } \mu_{0.32}<9.5 \end{cases} \tag{3.17}$$

with $\mu_{0.32} = \log M_\star - 0.32\log\mathrm{SFR}$, $m = \log M_\star - 10$, and $s = \log\mathrm{SFR}$. We build our empirical model by evaluating the SFR (Eq. 3.15) and the metallicity at a series of time-steps, ranging from ~12 Gyr ago until today. At each time-step, we assume that the metallicity follows a log-normal distribution within the Galaxy, with mean equal to the value predicted by the FMR (Eq. 3.17) and variance $\sigma_{\log Z} = 0.1$ dex.

3.2.4 Populating the MW with BNSs

To populate the MW galaxy models with the catalogues of BNSs evolved with SEVN, we follow the same procedure as outlined in Mapelli, Giacobbo, Ripamonti, et al. (2017) and Mapelli and Giacobbo (2018). For each simulation set, we read the eccentricity e and the semi-major axis a of the binary, the times of the SN explosions t_1 and t_2, the NS masses m_1 and m_2, the spin periods P_1 and P_2 and magnetic fields B_1 and B_2 at the formation of the second compact object. Along with this, we save the total simulated initial stellar mass M_SEVN for each of the 11 metallicity sub-sets.

For the EAGLE and ILLUSTRISTNG models, we read every stellar particle from the snapshot of the Galaxy at redshift $z=0$. In particular, we need the stellar particle mass $m_\star$, its formation redshift $z_\star$, and its metallicity at formation $Z_\star$. For each stellar particle, we select the SEVN catalogue with the metallicity closest to $Z_\star$, and associate it with a number

of BNSs proportional to the ratio $m_\star/M_{\rm SEVN}$:

$$n_{\rm BNS} = N_{\rm SEVN}\frac{m_\star}{M_{\rm SEVN}} f_{\rm corr}\, f_{\rm bin}, \tag{3.18}$$

where $N_{\rm SEVN}$ is the number of BNSs within the selected catalogue, $f_{\rm corr}$, and $f_{\rm bin}$ are correction factors. The factor $f_{\rm corr} = 0.285$ takes into account that we consider only systems with primary star mass $\geq 5M_\odot$. By integrating the Kroupa IMF between 0 and 5 $\mathrm{M}_\odot$, we obtain the relative weight of stars with a mass ≥ 5 $\mathrm{M}_\odot$: this yields $f_{\rm corr} = 0.285$. The factor $f_{\rm bin}$ corrects for the binary fraction, i.e. takes into account that we evolve only binary systems. From Sana et al. (2012), $f_{\rm bin} = 0.4$, which is equivalent to saying that 40% of stellar mass lie in binary systems. We randomly choose, with a Monte Carlo-like approach, $n_{\rm BNS}$ BNSs from the SEVN catalogue.

For the empirical model, we do not have stellar particles, but we can derive the amount of stellar mass formed by the Galaxy $\Delta M_\star$ at each time-step. Knowing the metallicity distribution at the same time-step, we can derive how much mass has been accreted $\Delta m_\star|_Z$, for each of the SEVN metallicities. The sum over all the 11 metallicities is:

$$\Delta m_\star = \sum_{i=1}^{11} \Delta m_\star|_{Z_i} \tag{3.19}$$

So, for each metallicity we evaluate $n_{\rm BNS}$ simply by substituting the value of $\Delta M_\star|_{Z_i}$ in Eq. 3.18. We convert the formation redshift $z_\star$ of each stellar particle in lookback time:

$$t_{\rm lb}(z) = \frac{1}{H_0}\int_0^z \frac{dz'}{(1+z')\sqrt{\Omega_{\rm M,0}\,(z'+1)^3 + \Omega_{\Lambda,0}}} \tag{3.20}$$

choosing the cosmological parameters consistently with the adopted cosmological simulation (Section 3.2.3). Then, the formation time of a BNS within the Galaxy is [4]

$$t_{\rm BNS} = t_\star - \max\,(t_1, t_2), \tag{3.21}$$

where $t_\star$ is the lookback time of the formation of the stellar particle corresponding to the redshift $z_\star$. From now on, all the times will be expressed in lookback times.

We assume that the subsequent evolution is driven only by the emission of GW radiation. Integrating the differential equations for GW radiation, derived in Peters (1964), we evolve the semi-major axis a and the eccentricity e:

$$\begin{aligned}\frac{{\rm d}a}{{\rm d}t} &= -\frac{64}{5}\frac{G^3\, m_1\, m_2 (m_1+m_2)}{c^5\, a^3\,(1-e^2)^{7/2}}\left(1+\frac{73}{24}e^2+\frac{37}{96}e^4\right),\\ \frac{{\rm d}e}{{\rm d}t} &= -\frac{304}{15}\frac{G^3\, m_1\, m_2\,(m_1+m_2)}{c^5\, a^3\,(1-e^2)^{5/2}}\left(1+\frac{121}{304}e^2\right).\end{aligned} \tag{3.22}$$

[4] t_1 and t_2 mark the SN explosion times of the primary and secondary progenitor stars, respectively. An episode of mass transfer during the evolution of the system might revert the initial mass ratio, thus leading to $t_1 > t_2$.

Initial Distribution	$B_{\rm birth}$ range (G)	$B_{\rm birth}$ distribution	$P_{\rm birth}$ range (ms)	$P_{\rm birth}$ distribution
U	$(10^{10}-10^{13})$	Uniform	$(10-100)$	Uniform
FL	$(10^{10}-10^{13})$	Flat in log	$(10-100)$	Uniform
FG	–	Faucher-Giguère et al. (2006)	–	Faucher-Giguère et al. (2006)

Table 3.2 Initial distributions adopted in this work for the spins and magnetic fields.

For the integration, we employ an Euler method with an adaptive time-step: the time-steps are smaller if the system is rapidly evolving (i.e. close to the merger); if the system is instead on a loose-wide orbit, the integration time-steps are larger. This allows us to have a fast algorithm without losing in precision. We evolve each system from $t_{\rm BNS}$ until today, i.e. $t_{\rm lb}=0$. If, during the evolution $a=3\,r_{\rm S}$, where $r_{\rm S}$ is the Schwartzschild radius, we assume that the system has merged and do not evolve it anymore.

In parallel, we evolve the NS spin and magnetic field. In particular, we update the spin and magnetic field according to Eqs. 3.2 and 3.3, with

$$\Delta t = t_{\rm BNS} - t_{\rm BNS,final}, \tag{3.23}$$

where $t_{\rm BNS,final}=t_{\rm merge}$ if the system has merged, or $t_{\rm BNS,final}=0$ (i.e., the present time) otherwise. We repeat the same procedure for each parameter set and for each Galaxy model keeping track of both the set of merged BNSs and the population of BNSs today in the MW.

3.2.5 Simulation set up

We varied several parameters in our model: the SN explosion mechanism prescription (rapid, delayed, rapid-gauss), the CE efficiency parameter α ($\alpha=0.5$, 1, 3, and 5), the initial spin and magnetic-field distributions, and the magnetic field decay timescale $\tau_{\rm d}$. All the models adopt the rapid-gauss prescription to reproduce the masses of the NSs. In the Appendix A.2, we test for comparison also the rapid and the delayed models from Fryer et al. (2012). We investigate different values of the parameter α. In particular we set $\alpha=0.5$, 1, 3, and 5. Both spins and magnetic fields are drawn from initial distributions. We need to make this assumption because the link between the properties of the pre-SN star and those of the NS is highly uncertain. Given the small sample of observed pulsars, the initial distributions are still quite uncertain. There is no agreement in the literature on the favoured initial parameter distributions, see for example Faucher-Giguère et al. (2006) and Osłowski et al. (2011). In our work we consider the initial distributions as free parameters and test some of the most common models in the literature, as summarized in Table 3.2:

1. *uniform* (hereafter, U): the spin period and the magnetic field are drawn uniformly in the range $[10,100]$ ms and $[10^{10},10^{13}]$ G, respectively.

2. *flat-in-log* (hereafter, FL): the spin periods are drawn uniformly between 10 and 100 ms, the magnetic fields are distributed according to a flat-in-log distribution in the range $[10^{10},10^{13}]$ G.

3. *Faucher-Giguère* (hereafter, FG): spin periods and magnetic fields follow the distributions presented in Faucher-Giguère et al. (2006). The spin periods follow a normal distribution with mean $\langle P \rangle = 300$ ms and variance $\sigma_P = 150$ ms, while the magnetic fields are drawn from a log-normal distribution with mean $\langle \log(B/G) \rangle = 12.65$ and variance $\sigma_{\langle \log B \rangle} = 0.55$.

Moreover, we consider different values for the magnetic field decay timescale τ_d (Eq. 3.2): $\tau_d = 0.1$, 0.5, 1 and 2 Gyr. We test our results on the different MW-like galaxies as well (Section 3.2.3). We adopt a uniform terminology for our models. Every model is identified with a string built as follows: '{distr}a{alpha}t{tau}{MW}', where within the brackets we substitute the actual value (or acronym) assumed by that specific parameter in the model. So that, in the place of 'distr' we substitute the acronym for the initial spins and magnetic fields distributions (see Table 3.2); 'alpha' corresponds to the value α for CE efficiency, 'tau' represents the value τ_d of the magnetic field decay timescale, and lastly 'MW' the MW-like galaxy chosen. We use the following abbreviations for the MW models: EAGLE, ILLUSTRISTNG, Emp and Const. For example, model 'Ua3t1Emp' adopts the uniform distribution of initial spin and magnetic field, $\alpha = 3$, $\tau_d = 1$ Gyr, and the empirical MW model. The models are summarized in Table 4.1. We choose 'Ua3t1Emp' as our fiducial model.

3.2.6 Selection effects

To compare our modelled BNSs with observations, we need to account for selection effects. For instance, as a pulsar crosses the death line (see section 3.2.6) it ceases to emit in the radio. Furthermore, pulsars have quite narrow beaming opening angles, thus we can only detect the pulsars whose beam intersects the line of sight. Radio selection effects also depend on the sky location of the source. The flux density scales as the inverse of the distance squared, which means that, for a given intrinsic luminosity, observations are biased towards close pulsars. Moreover, scattering by free electrons in the interstellar medium smears the pulsars' signal, lowering the signal-to-noise ratio (Cordes and Lazio, 2002). Other effects that may affect the observations are pulse nulling and intermittency, i.e. when the pulsed emission ceases for many pulse periods and quasi-periodic on/off cycles, respectively (Lyne, Hobbs, et al., 2010). On top of this, the Doppler shifting of the period caused by orbital motion also smears the pulsar signal (Andersen et al., 2018; Balakrishnan et al., 2022). We use the python implementation of PSRPOP (Lorimer, 2011), PSRPOPPY [5] (Bates et al., 2014), to account for some of the mentioned selection effects. Specifically, we model the death lines and beam geometry, the dependence on sky location, interstellar radio scintillation, pulsar luminosity, and binary selection effects.

Death lines

Pulsars cease to emit in the radio when the magnetic field is not strong enough for the production of electron-positron pairs. The death lines, empirical relations in the $P - \dot{P}$ plane,

[5] https://github.com/samb8s/PsrPopPy

	α	Init. Distr.	τ_d (Gyr)		α	Init. Distr.	τ_d (Gyr)
Ua0.5t0.1Emp	0.5	U	0.1	Ua3t0.1Emp	3	U	0.1
Ua0.5t0.5Emp	0.5	U	0.5	Ua3t0.5Emp	3	U	0.5
Ua0.5t1Emp	0.5	U	1	**Ua3t1Emp**	**3**	**U**	**1**
Ua0.5t2Emp	0.5	U	2	Ua3t2Emp	3	U	2
FLa0.5t0.1Emp	0.5	FL	0.1	FLa3t0.1Emp	3	FL	0.1
FLa0.5t0.5Emp	0.5	FL	0.5	FLa3t0.5Emp	3	FL	0.5
FLa0.5t1Emp	0.5	FL	1	FLa3t1Emp	3	FL	1
FLa0.5t2Emp	0.5	FL	2	FLa3t2Emp	3	FL	2
FGa0.5t0.1Emp	0.5	FG	0.1	FGa3t0.1Emp	3	FG	0.1
FGa0.5t0.5Emp	0.5	FG	0.5	FGa3t0.5Emp	3	FG	0.5
FGa0.5t1Emp	0.5	FG	1	FGa3t1Emp	3	FG	1
FGa0.5t2Emp	0.5	FG	2	FGa3t2Emp	3	FG	2
Ua1t0.1Emp	1	U	0.1	Ua5t0.1Emp	5	U	0.1
Ua1t0.5Emp	1	U	0.5	Ua5t0.5Emp	5	U	0.5
Ua1t1Emp	1	U	1	Ua5t1Emp	5	U	1
Ua1t2Emp	1	U	2	Ua5t2Emp	5	U	2
FLa1t0.1Emp	1	FL	0.1	FLa5t0.1Emp	5	FL	0.1
FLa1t0.5Emp	1	FL	0.5	FLa5t0.5Emp	5	FL	0.5
FLa1t1Emp	1	FL	1	FLa5t1Emp	5	FL	1
FLa1t2Emp	1	FL	2	FLa5t2Emp	5	FL	2
FGa1t0.1Emp	1	FG	0.1	FGa5t0.1Emp	5	FG	0.1
FGa1t0.5Emp	1	FG	0.5	FGa5t0.5Emp	5	FG	0.5
FGa1t1Emp	1	FG	1	FGa5t1Emp	5	FG	1
FGa1t2Emp	1	FG	2	FGa5t2Emp	5	FG	2

Table 3.3 Summary of the simulations. The initial distributions for spins and magnetic fields of NSs (U, FL and FG) are summarized in Table 3.2. All models listed here have been run within the Empirical MW model. We have explored the same grid of parameters with the other MW models (EAGLE, ILLUSTRISTNG, and Const). All models assume the rapid-Gauss prescription for the SN explosion. Our fiducial model is highlighted in boldface in the Table.

mark the locus of points beyond which the pulsars stop emitting: if a pulsar crosses one of these lines in the $P-\dot{P}$ plane, it turns off. We adopt the death lines from Rudak et al. (1994):

$$\begin{aligned} \log \dot{P} &= 3.29 \log P - 16.55 \\ \log \dot{P} &= 0.92 \log P - 18.65. \end{aligned} \tag{3.24}$$

Moreover, to avoid the piling up of pulsars at the death lines, we also add a cut-off on the efficiency of radio emission as in Szary et al. (2014). The radio efficiency ξ_R is defined as:

$$\xi_R = \frac{L}{\dot{E}}, \tag{3.25}$$

where L is the pulsar radio luminosity and $\dot{E} = 4\pi^2 I P^{-3} \dot{P}$ is the pulsar spin down power. Following the model by Szary et al. (2014), if the radio efficiency exceeds a certain threshold ($\xi_R > \xi_{R,max}$), the pulsar ceases to emit. We set the threshold to $\xi_{R,max} = 0.01$, as in Chattopadhyay et al. (2020) and Chattopadhyay et al. (2021). Following these prescriptions, PSRPOPPY classifies a pulsar as dead if either it has crossed the death lines (Eq. 3.24) or if $\xi_R > \xi_{R,max}$.

Beaming fraction

Pulsar radio emission is concentrated on collimated beams with finite width, so that pulsars sweep out only a limited area of the sky. As a consequence, we can detect only a fraction of the whole pulsar population, i.e. those whose beam crosses the observer's line of sight. The beaming fraction f_{beam} represents the fraction of pulsars beaming towards us. Previous studies agree that f_{beam} is period dependent. We adopt the prescription proposed in Tauris and Manchester (1998), an empirical relation obtained by fitting slow-rotating pulsars ($P \gtrsim 100$ ms),

$$f_{beam} = 0.09\,(\log P - 1)^2 + 0.03 \qquad 0 \leq f_{beam} \leq 1, \tag{3.26}$$

where P is the spin period of the pulsar in seconds. Equation 3.26 shows that the beaming fraction is higher for pulsars spinning faster. Therefore such objects are also more likely to be detected. PSRPOPPY takes into account the beaming effects using a rejection sampling method: each pulsar can be detected with a probability f_{beam}, computed according to Eq. 3.26.

Survey sensitivity

We use the radiometer Equation (Dewey et al., 1985; Lorimer and Kramer, 2004) to evaluate the minimum flux that a source must have to be detected

$$S_{min} = \beta \frac{(S/N_{min})\,(T_{rec} + T_{sky})}{G_A \sqrt{n_{pol}\, t_{int}\, \Delta\nu}} \sqrt{\frac{W}{P - W}}, \tag{3.27}$$

where S/N_{min} is the minimum signal-to-noise ratio, β takes into account losses in sensitivity due to sampling antenna and digitalisation noise, n_{pol} is the number of polarizations, T_{rec} and T_{sky} are the receiver and sky temperatures, G_A is the antenna gain, $\Delta\nu$ is the observing bandwidth, t_{int} is the integration time, W is the detected pulse width, and P is the pulse period. Most of the latter quantities are survey dependent (e.g. receiver temperature, observing bandwidth, integration time). PSRPOPPY evaluates the radiometer equation for the Parkes Multibeam Pulsar Survey (Manchester, Lyne, Camilo, et al., 2001, PMSURV), the Swinburne Multibeam Pulsar Survey (Edwards et al., 2001, SWINMB), and the High

Time Resolution Universe Pulsar Survey (Keith, Jameson, et al., 2010, HTRUP). For each survey, $S/N_{\rm min}$ is fixed to the value set by the survey itself. Moreover, the observed pulsars sample considered in our analyses includes only the objects detected by the surveys listed above. The effects caused by the propagation of the pulsed signal through the interstellar medium enters Eq. 3.27 via W. In fact, collisions with free electrons cause a broadening of the received signal. Also, if $W \gtrsim P$ the signal is no longer detectable as the pulse is smeared into the background (Lorimer, 2008; Lorimer, 2011).

PSRPOPPY assesses the observed pulse widths from the following relation (Burgay et al., 2003):

$$W^2 = W_{\rm i}^2 + \tau_{\rm samp}^2 + \left(\tau_{\rm samp}\frac{\rm DM}{\rm DM_0}\right)^2 + \tau_{\rm scatt}^2 \tag{3.28}$$

Here $W_{\rm i}$ is the intrinsic pulse width, $\tau_{\rm samp}$ is the sampling timescale, $\tau_{\rm scatt}$ is the mean scattering timescale. DM and $\rm DM_0$ are the dispersion measures in the direction of the pulsar and the diagonal dispersion of the survey respectively. For simplicity we fix the duty cycle $W_{\rm i}/P = 0.05\%$ for all pulsars (e.g. Lyne and Manchester, 1988).

As the above quantities depend on the sky position of the source, we use the built-in functions of PSRPOPPY to plant our evolved pulsars in the Galaxy. PSRPOPPY employs the distribution obtained in Yusifov et al. (2004) to assign a radial position to each pulsar. Once assessed the position of the pulsar, the sky noise temperature $T_{\rm sky}$ is evaluated accordingly by fitting the Haslam et al. (1981) Table and rescaling for the correct frequency range (Szary et al., 2014). PSRPOPPY evaluates the dispersion measure DM by integrating the electron density $n_{\rm e}$ over the line of sight. For $n_{\rm e}$ we adopt the NE2001 model (Cordes, 2004). Finally, DM is used to evaluate $\tau_{\rm scatt}$ by applying the prescriptions described in Bhat et al. (2004).

The last missing ingredient is the luminosity. We adopt the luminosity function calculated in Faucher-Giguère et al. (2006),

$$\log L = \log L_0 + \alpha_{\rm F06}\log P + \beta_{\rm F06}\log(\dot{P}/10^{-15}) + \delta_L, \tag{3.29}$$

with $L_0 = 0.18\,{\rm mJy\,kpc^2}$, δ_L is drawn from a normal distribution with $\sigma_{\delta_L} = 0.8$, $\alpha_{\rm F06} = -1.5$ and $\beta_{\rm F06} = 0.5$.

For each pulsar in the simulated Galactic population, we evaluate both $S_{\rm min}$ and the flux $F = L/(4\pi\mathscr{D}^2)$, where $\mathscr{D}$ is the pulsar distance. A source is detectable if $F > S_{\rm min}$. We repeat this procedure for each survey, finally combining all the simulated-detected pulsars into a single sample.

Selection effects of binary systems

A comprehensive procedure to account for binary-pulsar selection effects is still unavailable. The Doppler shifting of the period causes a smearing of the signal and thus a reduction in the signal-to-noise ratio (Balakrishnan et al., 2022). This effect is stronger for binary systems with shorter periods and for shorter integration times. The Doppler shifting also depends on the eccentricity of the system. Bagchi et al. (2013) show that the reduction in the signal-to-noise ratio decreases for higher eccentricity. Chattopadhyay et al. (2021) derive a fitting formula from the results of Bagchi et al. (2013). They assume a NS with a mass

of $1.4 M_{\odot}$, 1000 s duration of observation, and 60° inclination angle; then, fitting via linear regression for eccentricities $e = 0.1, 0.5$ and 0.8, they find a detection cut-off

$$P_{\rm orb}/d \geq m \times P/s + c, \tag{3.30}$$

with

$$m = m_{\rm m}\, e + c_{\rm m} \tag{3.31}$$

$$c = m_{\rm c}\, e + c_{\rm c}, \tag{3.32}$$

where $m_{\rm m} = -8.90$, $c_{\rm m} = -27.68$, $m_{\rm c} = -3.40$ and $c_{\rm c} = 5.72$. Thus, pulsars in shorter orbital period binaries are also the most difficult to be detected. We implement the aforementioned fit (Chattopadhyay et al., 2021) in PSRPOPPY.

Final setup

Using the formalism discussed above we apply the radio selection effects on the final population of BNSs in the MW. We consider only the binaries survived in the MW until the present day and run PSRPOPPY on these catalogues. The code returns the sample of pulsars, picked from the initial catalogue, that are detectable by the selected surveys.

We ran PSRPOPPY multiple times on the total population, in order to filter out stochastic fluctuations. In this way, we obtain multiple realisations of the radio-selected pulsars. This procedure has a further advantage: as a bootstrap technique, it augments the statistic of our final sample.

We repeat this process for each of our models. For each simulation, we compare simulated and observed pulsars, according to three surveys (the Parkes Multibeam Pulsar Survey, Swinburne Multibeam Pulsar Survey, and High Time Resolution Universe Pulsar Survey, Section 3.2.6). We list the properties of the pulsars considered in this study in Table 3.4 (Manchester, Hobbs, et al., 2005; Sengar et al., 2022).

3.2.7 Statistical analysis

We briefly summarize here the main points of the statistical framework used to compare the adopted models. In the following, we will denote the properties of the N_D observed pulsars (orbital period $P_{\rm orb}$, eccentricity e, spin period P and rate of change of the spin period $\dot{P}$) with $D = \{P_{\rm orb}, e, P, \dot{P}\}$, whereas θ_i denotes all the hyper-parameters varied through the models (i.e., the SN explosion mechanism, the CE parameter α, the initial spin and magnetic-field distributions, the magnetic-field decay $\tau_{\rm d}$, and the MW model) and, by extension, the $i-$th model itself.

To quantify the relative performance of two competing models in describing the available data, we will compute the Bayes' factor B_{12}[6]:

$$B_{12} = \frac{P(D, N_D|\theta_1)}{P(D, N_D|\theta_2)}. \tag{3.33}$$

In general, the likelihood $P(D|\theta)$ requires to evaluate the probability of the available data conditioned on the model. In this case, however, we do not have a functional relationship between the astrophysical hyper-parameters θ and the pulsar's observed parameters.

On the other hand, we have catalogues of simulated observed pulsars, as described in Section 3.2.6. Each of these catalogues, denoted with $\xi(\theta)$, is composed of N_ξ pulsars, representative of the underlying observed distribution on the four pulsar properties. These realisations can be used to reconstruct this distribution and assign a probability for the data D.

The likelihood therefore becomes

$$\begin{aligned} P(D, N_D|\theta) &= \int P(D, N_D|\xi(\theta), N_\xi)\, P(\xi(\theta), N_\xi|\theta)\, \mathrm{d}\xi\, \mathrm{d}N_\xi = \\ &= \int P(N_D|N_\xi)\, P(D|\xi(\theta))\, P(\xi(\theta), N_\xi|\theta)\, \mathrm{d}\xi\, \mathrm{d}N_\xi\,. \end{aligned} \tag{3.34}$$

The first term, $P(N_D|N_\xi)$, is an inhomogenous Poisson process:

$$P(N_D|N_\xi) = \frac{N_\xi^{N_D} e^{-N_\xi}}{N_D!}. \tag{3.35}$$

The probability $P(D|\xi(\theta))$ is modelled using a Dirichlet process Gaussian mixture model (DPGMM, e.g., Rinaldi and Del Pozzo, 2022a, and references therein). The DPGMM can be used to approximate arbitrary probability densities given a set of samples drawn from the unknown distribution. In particular,

$$P(D|\xi(\theta)) = \int P(D|\lambda)\, P(\lambda|\xi(\theta))\, \mathrm{d}\lambda\,, \tag{3.36}$$

where λ denotes the parameters of the DPGMM.

Both integrals can be calculated via Monte Carlo approximation, since we are able to sample $\xi(\theta)$ and N_ξ using the methods outlined above. Samples for λ, conditioned on a specific realisation of $\xi(\theta)$, are drawn using FIGARO[7].

[6] In general, to do model selection one should compute the odds ratio $O_{12} = B_{12} P(\theta_1)/P(\theta_2)$. However, under the assumption that the two models are a priori equally likely, the odds ratio reduces to the Bayes' factor.

[7] FIGARO is publicly available at https://github.com/sterinaldi/figaro

Radio pulsar	Type	P (ms)	$\dot{P}$ (10^{-18})	B (10^9 G)	$P_{\rm orb}$ (d)	e	$M_{\rm psr}$ ($M_\odot$)	$M_{\rm comp}$ ($M_\odot$)	Dist. (kpc)	$t_{\rm GW}$ (Myr)	Survey
J0737-3039 A[a]	recycled	22.7	1.76	2.0	0.102	0.088	1.338	1.249	1.15	86	PMSURV, HTRU
J0737-3039 B[a]	recycled	277.3	892.0	1590	0.102	0.088	1.249	1.338	1.15	86	PMSURV
J1325-6253 [b]	recycled	28.9	0.048	1.2	1.815	0.064	<1.59	>0.98	4.4	>$t_{\rm H}$	HTRU
J1753-2240[c]	recycled	95.1	0.970	2.7	13.638	0.304	-	-	3.46	$> t_{\rm H}$	PMSURV, HTRU
J1755-2550[d]	young	315.2	2430	270	9.696	0.089	-	> 0.40	10.3	$> t_{\rm H}$	HTRU
J1756-2251[e]	recycled	28.5	1.02	1.7	0.320	0.181	1.341	1.230	0.73	1660	PMSURV, HTRU
J1757-1854[f]	recycled	21.5	2.63	7.6	0.184	0.606	1.338	1.395	7.40	78	HTRU
J1811-1736[g]	recycled	104.2	0.901	3.0	18.779	0.828	< 1.64	> 0.93	5.93	$> t_{\rm H}$	PMSURV, HTRU
B1913+16[h]	recycled	59.0	8.63	7.0	0.323	0.617	1.440	1.389	9.80	301	PMSURV

Table 3.4 Sample of radio pulsars considered in this work. Column 1: pulsar name; column 2: spin P; column 3: spin derivative $\dot{P}$; column 4: magnetic field B; column 5: orbital period $P_{\rm orb}$; column 6: eccentricity e; column 7: pulsar mass $M_{\rm psr}$; column 8: companion mass $M_{\rm comp}$ (here we consider only pulsars which have another NS as companion); column 9: distance from the Sun; column 10: $t_{\rm GW}$ is the merging time of the binary systems, the BNSs with $t_{\rm GW}$ greater than the Huble time ($t_{\rm H}$) are shown with $> t_{\rm H}$. The last column (Column 12) shows in which surveys each pulsar has been discovered, the nomenclature is the same as in Sec. 3.2.6. References: [a] Kramer et al., 2006; Breton et al., 2008 , [b] Sengar et al., 2022, [c] Keith, Eatough, et al., 2009, [d] Ng, Champion, et al., 2015; Ng, Kruckow, et al., 2018 , [e] Faulkner et al., 2004, [f] Cameron et al., 2018, [g] Corongiu et al., 2007, [h] Hulse et al., 1975; Weisberg et al., 2016.

With the Monte Carlo approximation, the full likelihood reads

$$P(D,N_D|\theta) \simeq \frac{1}{M}\sum_{\xi_j(\theta)}^{\xi_M}\left(\frac{\left(N_{\xi_j}^{N_D}e^{-N_{\xi_j}}\right)/N_D!}{K}\sum_{\lambda_k|\xi_j(\theta)}^{\lambda_K}\prod_i P(D_i|\lambda_k)\right), \tag{3.37}$$

where K denotes the number of draws for λ and M the number of realisations for $\xi(\theta)$, and we made also use of the fact that the observations D are independent.

Using Eq. (3.37), we can compute the likelihood for each model and, consequently, discriminate between models. If $B_{12} > 1$, the model θ_1 is favoured over model θ_2. In the following, we will compute the Bayes' factor for each model over our fiducial 'Ua3t1Emp'.

3.3 Results

3.3.1 Merger rates

Figure 3.1 shows the BNS merger rate history for the Galaxy models and for the values of the CE parameter α adopted in this work. Table 3.5 summarizes the BNS merger rates at present time predicted by our models. For comparison, we also show the BNS merger rate of the MW inferred by Pol et al. (2019, $\mathscr{R}_{\rm MW} = 42^{+30}_{-14}{\rm Myr}^{-1}$) and Pol et al. (2020, $\mathscr{R}_{\rm MW} = 37^{+24}_{-11}{\rm Myr}^{-1}$).

The parameter α has a large impact on the BNS merger rate. This result agrees with previous works, showing that almost all BNS mergers form via CE (Tauris, Kramer, et al., 2017; Giacobbo and Mapelli, 2018; Kruckow, Tauris, Langer, Kramer, et al., 2018; Vigna-

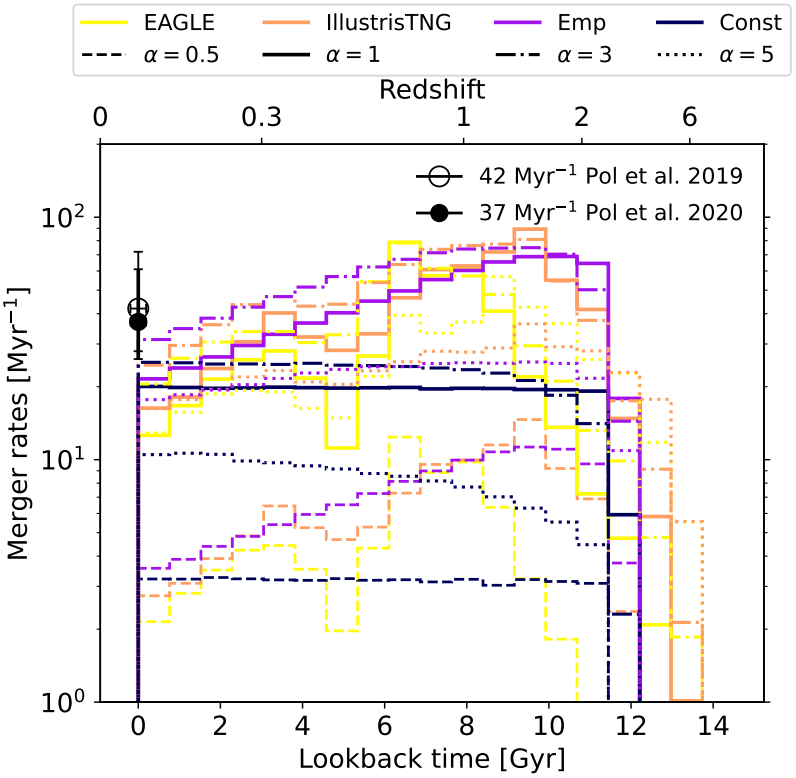


Fig. 3.1 BNS merger rate in the MW as a function of the lookback time for different Galaxy models and values of the CE parameter α. Each colour identifies a Galaxy model. Yellow: EAGLE; pink: ILLUSTRISTNG; purple: Emp; blue: Const. Each line-style is associated with a value of α. Dashed line: $\alpha = 0.5$; solid line: $\alpha = 1$; dash-dotted line: $\alpha = 3$; dotted line: $\alpha = 5$. The circles show the BNS merger rate in the MW inferred from observations: the unfilled circle shows the value by Pol et al. (2019), $\mathscr{R}_{\rm MW} = 42^{+30}_{-14}\,{\rm Myr}^{-1}$; the black filled circle shows the updated value by Pol et al. (2020), $\mathscr{R}_{\rm MW} = 37^{+24}_{-11}\,{\rm Myr}^{-1}$. All simulations shown in this Figure assume $\tau_{\rm d} = 1$ Gyr and the U distribution for initial spins and magnetic fields. We do not expect NS spins and magnetic fields to affect the merger rate. Our fiducial model (Ua3t1Emp, Table 4.1) produces a rate $\mathscr{R}_{\rm MW} = 31.3$ Myr^{-1}, consistent with the rate inferred from the Galactic pulsar binary systems.

Gómez et al., 2018; Mapelli and Giacobbo, 2018; Mapelli, Giacobbo, Santoliquido, et al., 2019; Mandel et al., 2022; Iorio et al., 2023). In general, a larger value of α means that energy is transferred more efficiently to the envelope, facilitating its expulsion. In our models, the highest BNS merger rates are produced for $\alpha = 3$. Different values of α, both higher and lower, yield values of $\mathscr{R}_{\rm MW}$ which are lower than the one inferred from observations by more than one standard deviation.

We find that the merger rate in the local Universe strongly correlates with the SFR of the Galaxy model (Artale, Mapelli, Giacobbo, et al., 2019). As such, the Galaxy models that better reproduce the observed $\mathscr{R}_{\rm MW}$ are also the ones with the current SFR closer to the one of the MW. In particular, the Emp model with $\alpha = 3$ best reproduces the observed BNS merger rates (see Table 3.5). For this reason, we choose the Emp model as our fiducial

MERGER RATES (Myr^{-1})				
	α			
MW model	0.5	1	3	5
EAGLE	2.2	12.6	20.5	12.9
ILLUSTRISTNG	2.7	16.3	24.5	16.2
Emp	3.6	21.5	31.3	17.7
Const	3.2	20.0	25.2	10.5

Table 3.5 BNS merger rate in the MW at present time for different Galaxy models and values of the CE parameter α. All simulations shown in this Figure assume $\tau_d = 1$ Gyr and the U distribution for initial spins and magnetic fields.

model. In contrast, the EAGLE model underestimates the local BNS merger rate of the MW. In general, the merger rate history follows the same evolution with redshift as the SFR of the host galaxy, since most BNSs merge shortly after their formation. Our findings are in agreement with Artale, Mapelli, Giacobbo, et al. (2019), who observe a tight correlation between the BNS merger rate and both the mass and the SFR of the host galaxy (see Artale, Mapelli, Giacobbo, et al., 2019; Artale, Bouffanais, et al., 2020; Artale, Mapelli, Bouffanais, et al., 2020; Chattopadhyay et al., 2021, for more details on this correlation).

3.3.2 Orbital period – eccentricity

Figure 3.2 shows the distributions of our simulated BNSs at lookback time $t_{lb} = 0$ (today) in the orbital period (P_{orb})– eccentricity (e) plane. We show the results varying α and the host Galaxy model. These plots do not include systems that have merged throughout the history of the MW, but only those that survived until today. All the simulations in Figure 3.2 have $\tau_d = 1$ Gyr and an uniform (U) distribution for the initial spins and magnetic fields. Indeed, these parameters do not produce significant variations in the final distribution of the $P_{orb} - e$ plane, as expected. The markers show the observed Galactic pulsars in BNSs systems (Table 3.4).

Different models in Fig. 3.2 share similar trends. It is possible to distinguish a main branch characterized by short orbital periods ($\sim 1 - 10^3$ d) and a second one, much less populated, with orbital periods at $\sim 10^{5-6}$ d. At shorter periods, the distributions are bound by the GW merger timescale ($t_{merge} \lesssim 1$ Myr).

The parameter α has a strong impact on the distribution of BNSs in the $P_{orb} - e$ plane. In particular, the simulations with $\alpha = 5$ predict about twice as many BNSs as the $\alpha = 3$ model, and roughly five times more binaries compared to the $\alpha = 0.5$ model. This is expected as higher α values are associated with a more efficient expulsion of the CE, therefore more systems are able to survive the CE phase. In contrast, as we decrease α, the probability that a system prematurely merges during the CE increases (Iorio et al., 2023). These plots display another interesting feature: low-α simulations ($\alpha = 0.5$, 1) lack BNSs with low eccentricity, which are instead present in the $\alpha = 3$ and 5 models, favouring more eccentric binaries.

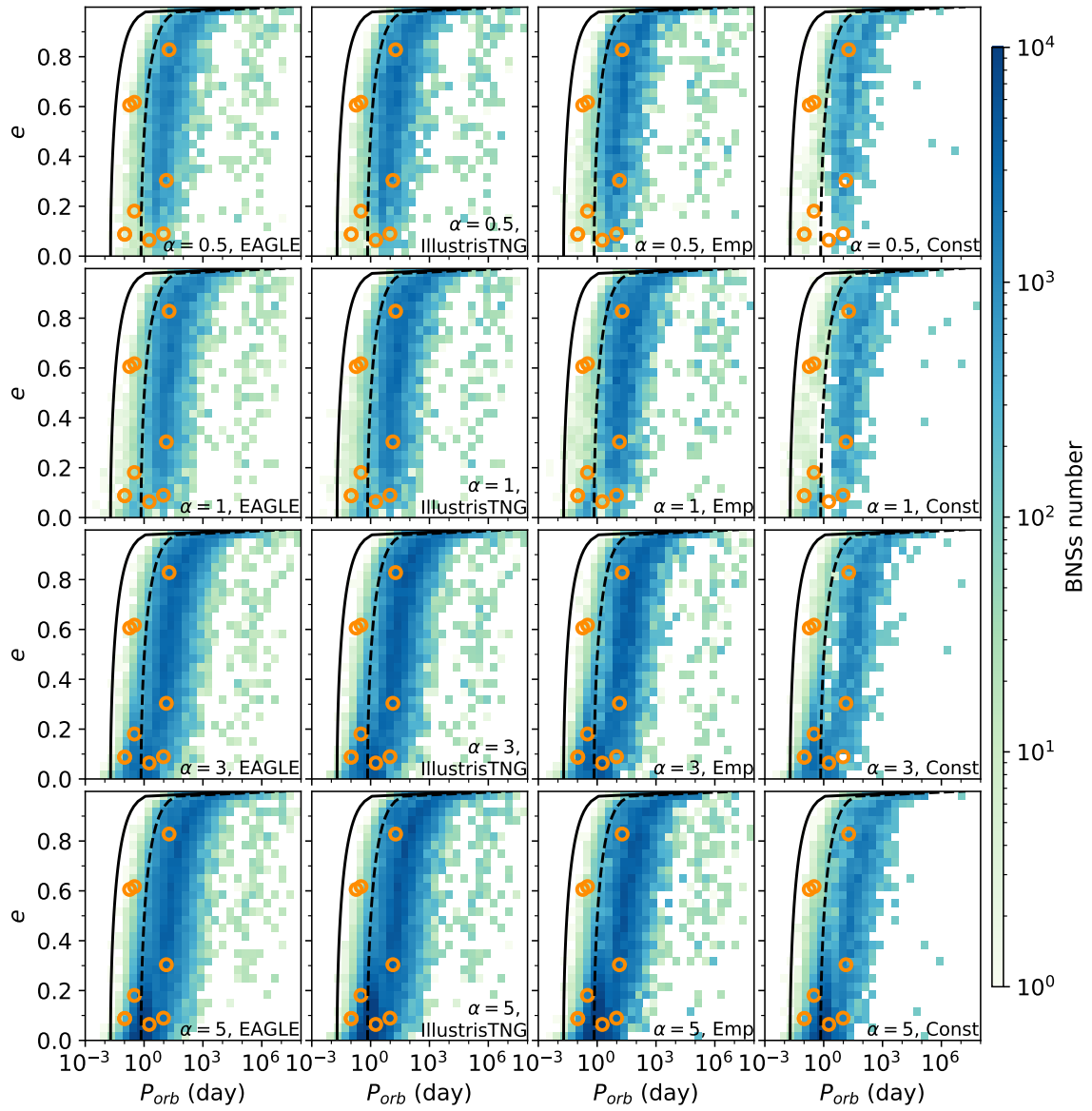


Fig. 3.2 Distribution of the simulated BNSs at the present time in the $P_{\rm orb} - e$ plane. Each column shows the results for a different Galaxy model, from left to right: EAGLE, ILLUSTRISTNG, Emp and Const. The rows show different α values, from top to bottom: $\alpha = 0.5$, 1, 3, and 5. All the models shown here assume $\tau_{\rm d} = 1$ Gyr, and model U for the initial spin and magnetic field. The red circles show the observed population of BNSs selected for this study. The solid black line shows values of constant $t_{\rm GW} = 1$ Myr, while the dashed black line corresponds to $t_{\rm GW}$ equal to the Hubble time. We obtained the lines of constant $t_{\rm GW}$ with equation D6 in Iorio et al. (2023) [9], assuming a mass of $1.35\,{\rm M}_\odot$ for the NSs. Our models qualitatively agree with the observed BNS distribution.

The host Galaxy model also plays a role on the final BNS distribution. In particular, we find that the most important parameter in this case is the total stellar mass $M_\star$ of the mock Galaxy. The procedure we adopt to populate a galaxy implies a direct correlation between

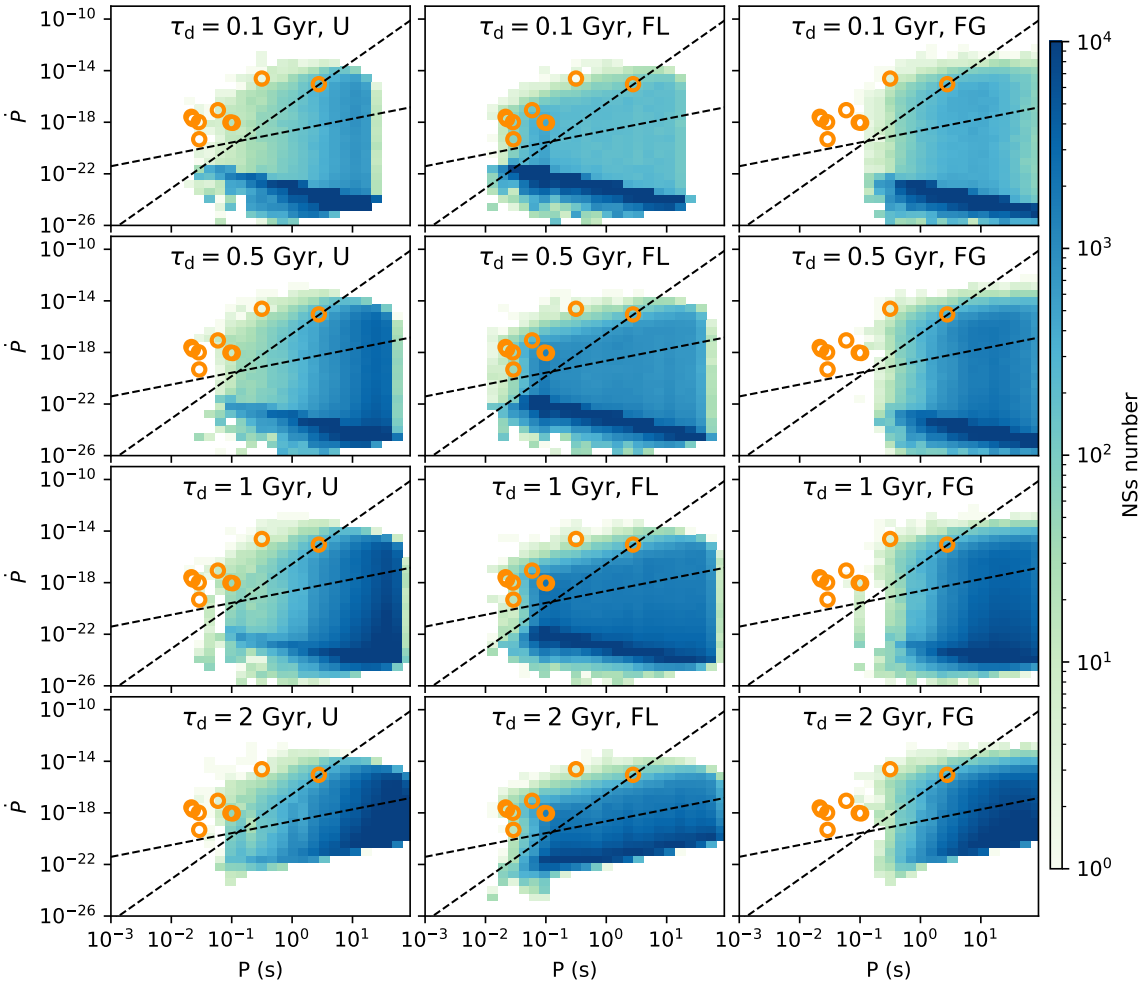


Fig. 3.3 Distribution of the simulated BNSs at the present time in the $P - \dot{P}$ plane. Each column shows the results for a different model of the initial spin and magnetic field, from left to right: uniform (U), flat-in-log (FL), Faucher-Giguère (FG). The rows assume different values of τ_d, from top to bottom: $\tau_d = 0.1, 0.5, 1, 2$ Gyr. All the runs assume $\alpha = 3$ and the Emp MW model. The markers show the observed population of pulsars (Table 3.4). The dashed black lines show the death lines defined in Eq. 3.24.

$M_\star$ and the number of BNSs (see Eq. 3.18). For this reason the Const MW model produces a much lower number of final BNS systems.

Our results qualitatively agree with the observed BNS distribution of orbital periods and eccentricities. A more quantitative comparison is not straightforward owing to observational biases. In fact, eccentric binaries are more difficult to detect (Tauris, Kramer, et al., 2017), having stronger Doppler effects (Chattopadhyay et al., 2021).

3.3.3 $P - \dot{P}$ plane

Figure 3.3 shows the distribution of our simulated BNSs at the present time in the $P - \dot{P}$ plane. We show the results varying τ_d and the model for the initial spins and magnetic fields. Figure 3.3 clearly shows the importance of the initial spin and magnetic field distribution on the final pulsar population. Although the number of pulsars in each model varies with α and with the MW model, the shape of the distribution in the $P - \dot{P}$ plane is not significantly affected. Most of the detected BNSs in the MW data are characterized by a spin period $\lesssim 100$ ms. Most of the pulsars in the data-set are probably recycled (Tauris, Kramer, et al., 2017). The primary-born pulsars in our models do not show striking differences compared to the second-born pulsars.

3.3.4 Selection effects

Figure 3.3 shows the intrinsic astrophysical population, without accounting for radio selection effects. In contrast, Figure 3.4 shows the distribution in the $P - \dot{P}$ plane of the detectable pulsars predicted by our models, obtained as described in Section 3.2.6 and averaging over $N = 100$ realizations of radio-selected pulsar populations. Figure 3.4 shows the iso-density contours for models varying τ_d and the initial distributions of spins and magnetic fields (U, FL, and FG). The shapes of the contours depend on the chosen initial spins and magnetic fields: the pulsar density peak shifts in the parameter space because of these two parameters. The FG distribution generally produces slower spinning pulsars, with larger values of the spin periods P. In contrast, the FL distribution models peak at $P \sim 0.1$s, where the majority of the observed pulsars lies. The U distribution, our fiducial model, shows a broader profile spanning a wider range of spin periods with respect to the other models.

We also calculate the number of pulsars predicted by our models. Our approach is completely self-consistent: we consider the specifics of the chosen surveys to account for radio selection effects, and compare our samples with the pulsars observed by the same surveys. Figure 3.5 shows the mean number of predicted detections averaged over the N realizations of the radio selection effects. The FL model seems to better fit the observed pulsar distribution in the $P - \dot{P}$ plane: the predicted pulsar sample peaks at ~ 0.1 s, where the majority of pulsars lie. However, Figure 3.5 shows that the FL model predicts too many observed BNSs. In fact, it estimates $\sim 10^2$ observable pulsar binary systems, almost 10 times more than the number of detected Galactic BNSs. On the other hand, the FG model strongly underestimates the number of observed pulsars. The U model, instead, not only populates the $P - \dot{P}$ region where the observed pulsars lie, but also predicts the correct number of BNSs. For this reason, we choose the U model as the fiducial one. The reason why the FL model predicts a much higher number of detectable BNSs with respect to both FG and U is that it initializes the bulk of the pulsar population with lower values of both magnetic field and initial spin. Hence, more pulsars are still above the death line at current time in model FL compared to U and FG (Chattopadhyay et al., 2020).

From Figures 3.4 and 3.5, we can see another feature: the samples of detectable BNSs decrease for lower values of τ_d. This happens because younger pulsars constitute the great majority of the detectable pulsars. Since for lower values of τ_d the pulsars move faster in the

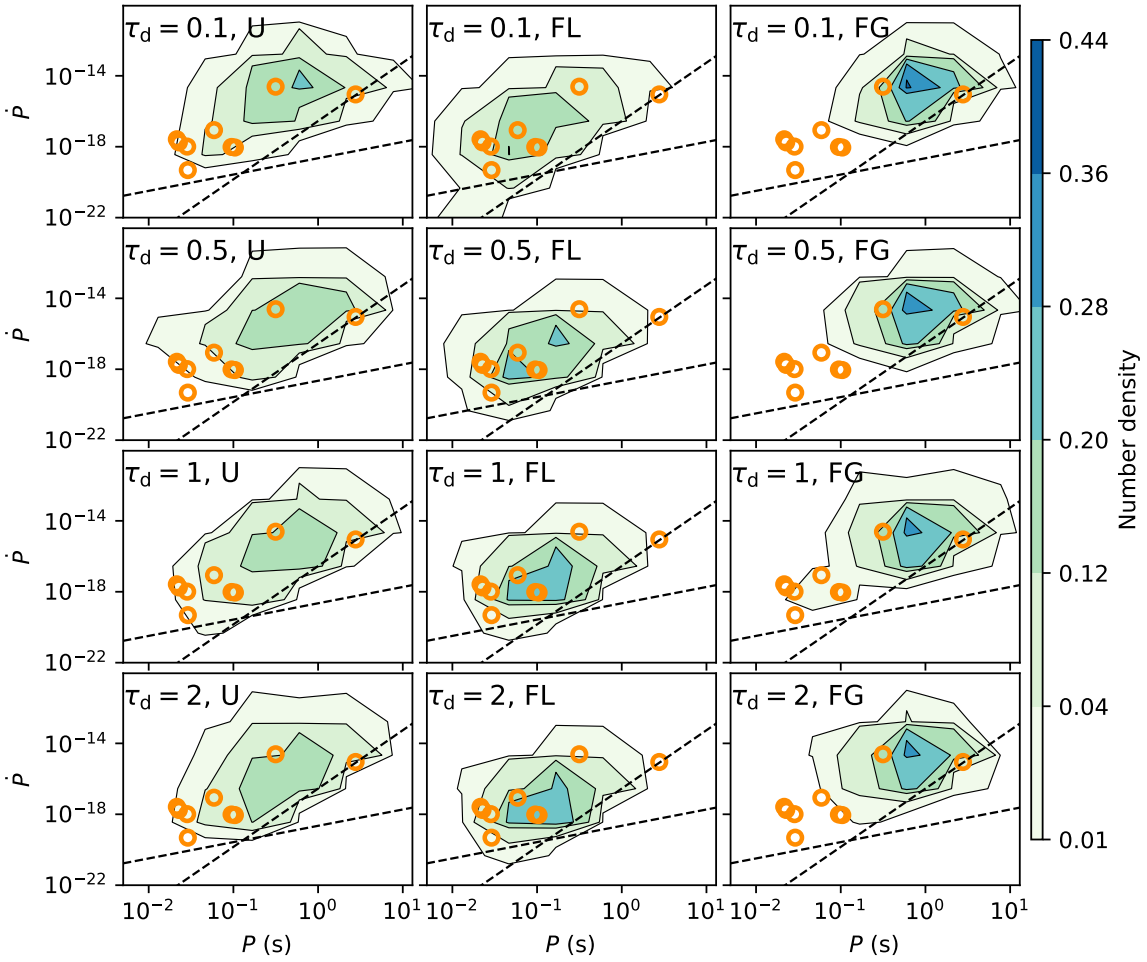


Fig. 3.4 Isocontours showing the number density of detectable pulsars (after applying radio selection effects) in the $P - \dot{P}$ plane. Each column shows the results for a different spin and magnetic field model, from left to right: U, FL, and FG. The rows assume different values of τ_d, from top to bottom: $\tau_d = 0.1$, 0.5, 1, and 2 Gyr. All the runs assume $\alpha = 3$ and the Emp model for the MW. The markers show the observed population of pulsars (Table 3.4). The dashed black lines show the death lines defined in Eq. 3.24. The FG model can hardly account for the pulsars with the shortest periods and lowest values of $\dot{P}$, while models U and FL qualitatively match the location of the observed BNSs in the $P - \dot{P}$ plane.

$P - \dot{P}$ plane, towards larger spin periods and lower magnetic fields, pulsars cross the death line in shorter intervals of time.

Chattopadhyay et al. (2020) produce, in general, more radio selected pulsars with respect to our models, from 5 to 20 times more pulsars than our predictions (excluding their model CE–Z, which assumes no accretion during CE, as in our work, see Section 3.4). Nonetheless, they observe the same trend with τ_d.

Figure 3.6 shows the cumulative distributions of the orbital period, eccentricity, spin period, and spin period derivative, for our fiducial model. We show the distributions we

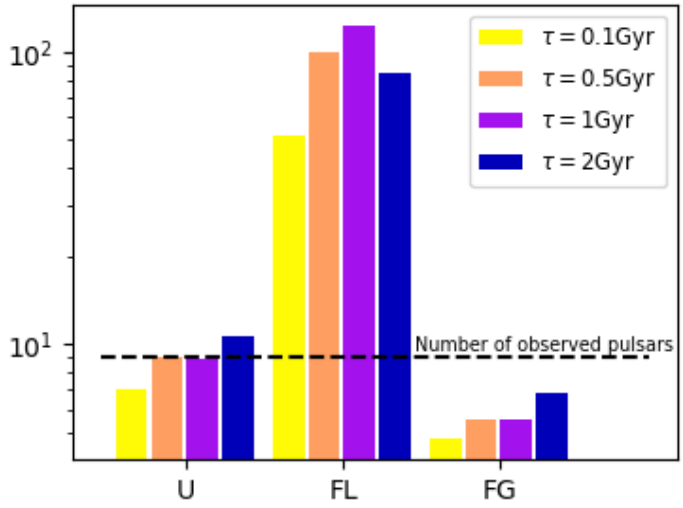


Fig. 3.5 Mean number of radio selected pulsars predicted by our models after averaging over the $N = 100$ realizations of the selection effects, assuming the fiducial $\alpha = 3$ and the Emp MW model. Each bar is a different model: the x-axis shows the spin and magnetic field initial distributions (U, FL, and FG). Each colour is associated to a different τ_d value: yellow, pink, purple, and blue for $\tau_d = 0.1$, 0.5, 1, and 2 Gyr, respectively. The black horizontal dashed line shows the number of observed Galactic BNSs in the considered surveys, N_{obs} =9. The FG (FL) model underestimates (overestimates) the number of observed pulsars, while the U model predicts a number of detectable BNSs which is very close to the observed value.

obtained with and without accounting for the selection effects, for comparison. Radio selection effects select only the non-dead pulsars, characterized in general by smaller spin periods P and larger $\dot{P}$. Furthermore, binary selection effects tend to select circular with respect to eccentric systems. In general, our models match the observed distributions, including the eccentricity distribution, when we account for selection effects.

Figure 3.6 also compares different CE parameters $\alpha = 0.5 - 5$. The choice of α influences the orbital period and especially the eccentricity. The models with $\alpha > 1$ better match the data with respect to those with $\alpha \leq 1$, because the latter produce too many highly eccentric systems. This preference for $\alpha > 1$ when considering the eccentricity distribution points in the same direction as the result of the BNS merger rate: we found the best match with the MW merger rate for $\alpha = 3$.

The distributions of P and $\dot{P}$ do not change much with α, as expected. The Galactic BNSs seem to have a double peaked distribution: the first peak around $P \sim 1$ d, the second one at about 10^2 d (Andrews and Mandel, 2019). However, given the small sample of detected BNSs we do not have enough statistics to claim that such feature is characteristic of the underlying BNS distribution.

[9]The analytical methods to compute the GW merging time are implemented in the function `estimate_gw`, in the publicly available PYTHON module PYBLACK, https://gitlab.com/iogiul/pyblack.

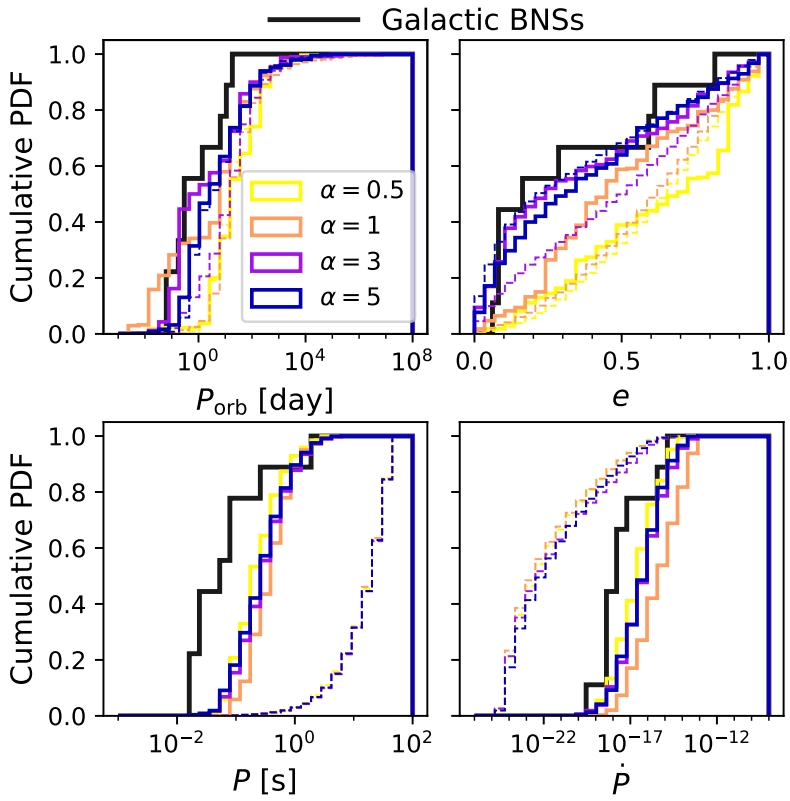


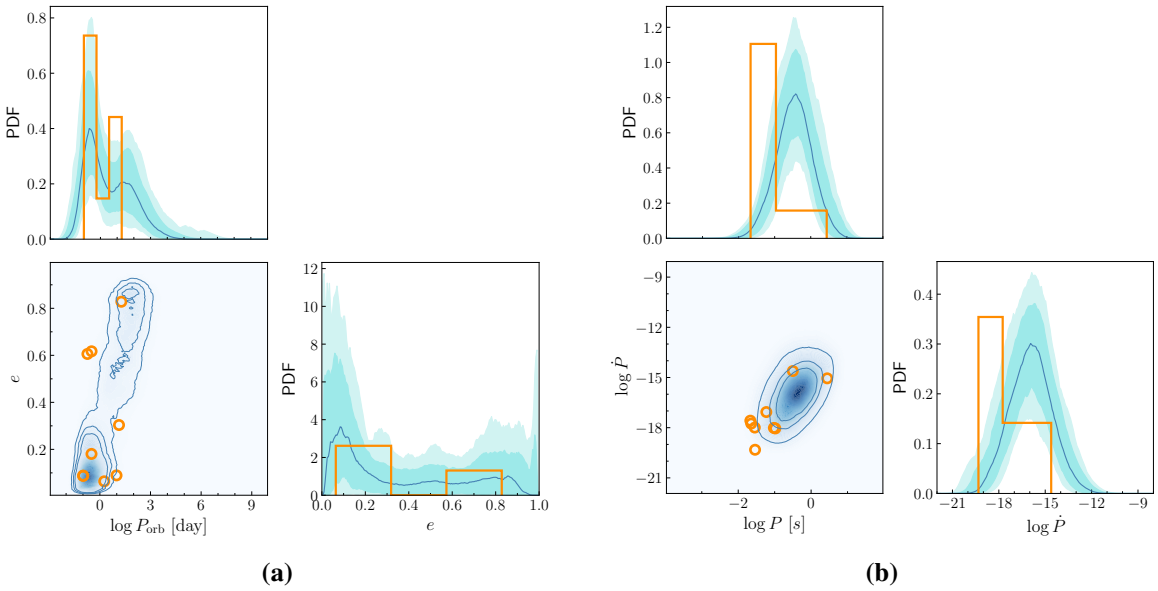
Fig. 3.6 Cumulative distribution of the pulsar parameters $P_{\rm orb}$, e, P and $\dot{P}$ (from top left to bottom right) for the fiducial model parameters. Yellow, pink, purple, and blue solid lines: $\alpha = 0.5$, 1, 3, 5. The dashed thin lines display the underlying astrophysical BNS population, while the solid thick lines show the detectable population, after implementing radio-selection effects. The black solid line marks the cumulative distribution of the observed Galactic BNSs. To account for radio-selection effects is crucial, especially in order to match the observed $P - \dot{P}$ distribution. We also note the good match between observed and simulated orbital eccentricity distribution after accounting for radio-selection effects.

3.3.5 Bayes factors

Table 3.6 shows the Bayes factors of each model, that we obtained as described in Section 3.2.7. For this analysis, we used four BNS parameters: orbital period, eccentricity, spin period and derivative of the spin period. Figures 3.7a and 3.7b show two examples of the DPGMMs we applied to these four parameters in our simulations.

The Bayes factors indicate that the FG distribution is strongly disfavoured in all the models, confirming what we can qualitatively see from Figures 3.4 and 3.5. Also, the U model performs better than the FL model, because the latter produces too many detectable BNSs (Fig. 3.5).

We find that the model with fiducial parameters, but assuming $\tau_{\rm d} = 0.5$ Gyr (Ua3t0.5Emp), produces slightly better results. However, the differences yielded by distinct $\tau_{\rm d}$ values are



(a) **(b)**

Fig. 3.7 Two-dimensional likelihood for $P_{\rm orb}$ and e (panel a) and P and $\dot{P}$ (panel b) averaged over the simulated pulsars catalogues of our fiducial model (Ua3t1Emp), as reconstructed by FIGARO. These likelihoods are obtained by marginalising out P and $\dot{P}$ or $P_{\rm orb}$ and e from the four-dimensional likelihood, respectively. The red circles and histograms show the observed Galactic BNSs (Table 3.4). The blue contour lines in the 2D plot show the 90%, 68%, and 50% credible regions of the median distribution (blue lines in 1D plots). The shaded regions in 1D plots represent the 68% and 90% credible intervals for the marginal probability density for each parameter.

not as appreciable as those produced by different initial spin and magnetic field distributions. Thus, we cannot confidently discard a particular value of $\tau_{\rm d}$ based only on this result.

3.3.6 Predictions for the SKA

Within our framework, we can make predictions for SKA. We applied the radio selection effects setting the parameters of the major SKA surveys (MID and LOW, see Appendix A.3), and studied how the predictions vary for our different models. Table 3.7 shows the resulting number of SKA-detectable BNSs for different models. We see a spread of about two orders of magnitude among the results. Consistently with Figure 3.5, the FL initial distribution predicts ~ 10 times more observable pulsars than the other models. Our fiducial model estimates that SKA will be able to observe 30 ± 6 BNSs, among which 21 ± 4 new detections .

3.4 Discussion

We have explored the BNS population properties within four different Galaxy models: a model with constant (Const) SFR, an empirical (Emp) MW model with exponentially decaying SFR, and two models taken from the EAGLE and ILLUSTRISTNG cosmological

	Uniform (U) τ_d (Gyr)				Flat-in-log (FL) τ_d (Gyr)				Faucher-Giguere (FG) τ_d (Gyr)			
	0.1	0.5	1	2	0.1	0.5	1	2	0.1	0.5	1	2
α												
0.5	-174 (195)	-98 (123)	-167(215)	-67(82)	-4 (37)	-18 (35)	-26 (32)	-35 (33)	-188 (177)	-216 (221)	-241 (261)	-38 (33)
1	-132 (181)	-91 (107)	-90 (124)	-71(112)	-4 (33)	-15 (31)	-29 (31)	-40 (31)	-156 (166)	-125 (157)	-124 (154)	-42 (32)
3	-12 (43)	0.9 (35)	**0 (37)**	0.3 (35)	-11 (28)	-55 (29)	-77 (30)	-45 (30)	-49 (76)	-29 (47)	-30 (58)	-23 (48)
5	1 (34)	-61 (97)	7 (31)	-27 (52)	-18 (28)	-75 (29)	-112 (30)	-163 (30)	-41 (106)	-37 (80)	-24 (53)	-37 (57)

Table 3.6 Logarithmic Bayes factors ($\ln B$) of the simulated models compared to the fiducial model 'Ua3t1Emp', adopting the Emp MW model. The fiducial model is highlighted in bold face in the Table. The FL and FG prescriptions are disfavoured compared to the U model. Due to the low statistics of the observed pulsars sample, we cannot confidently choose a particular model based only on the Bayes Factors.

	Uniform (U) τ_d (Gyr)				Flat-in-log (FL) τ_d (Gyr)				Faucher-Giguere (FG) τ_d (Gyr)			
	0.1	0.5	1	2	0.1	0.5	1	2	0.1	0.5	1	2
α												
0.5	6 (2)	10 (3)	9 (3)	11 (3)	54 (8)	121 (10)	173 (12)	211 (14)	3 (1)	5 (2)	4 (2)	210 (14)
1	9 (3)	13 (3)	10 (3)	14 (3)	84 (8)	145 (13)	196 (12)	241 (13)	6 (2)	6 (2)	7 (3)	240 (14)
3	23 (5)	29 (5)	**30(6)**	36 (5)	155 (12)	316 (19)	411 (18)	288 (17)	17 (4)	21 (4)	20 (4)	22 (5)
5	26 (5)	16 (4)	39 (6)	21 (5)	178 (14)	395 (20)	532 (24)	721 (29)	17 (4)	19 (4)	23 (5)	21 (5)

Table 3.7 Predicted number of pulsars in BNSs detectable by the SKA, after averaging over $N = 100$ realisations of the radio selection effects. We report the standard deviation on the mean within brackets. The fiducial model is highlighted in bold face in the Table.

simulations, respectively (Table 3.1). In all the four models, the Galactic SFR at present day matches the one of the MW. In addition, the Emp, EAGLE, and ILLUSTRISTNG models also match the current total stellar mass of the MW, whereas the Const model results in a factor of ~ 2.5 lower mass Galaxy. Furthermore, the SFR history of the EAGLE and ILLUSTRISTNG galaxies deviate from the simple exponential decay assumed in the Emp model. The adopted models differ from each other in terms of metallicity as well: adopting the FMR, the Emp model is dominated by Solar metallicity stars, whereas the EAGLE and ILLUSTRISTNG models contain a large population of metal-poor stars.

Despite these differences, the $P_{\rm orb} - e$ distribution of BNSs in the Emp, EAGLE, and ILLUSTRISTNG models show similar features. In contrast, the Const model predicts a much lower number of BNSs than the other models. This is a consequence of the lower total stellar mass of the Const model.

The Galactic BNS merger rate is primarily affected by our choice of the common-envelope parameter α. If we assume $\alpha = 3$, the resulting present-day Galactic merger rate is a factor of ~ 10 higher than for $\alpha = 0.5$, and is more consistent with the value inferred from observations (Pol et al., 2019; Pol et al., 2020). The merger rate is also affected by the SFR and metallicity of the adopted Galaxy model (Fig. 3.1).

Our models still represent a rather simplified description of the MW. Matteucci et al. (2019) and Kobayashi et al. (2023) explore detailed models of the MW, accounting also for its chemical enrichment history. They account for BNS mergers, and study if the latter can explain the r-process element abundance. Kobayashi et al. (2023) explain the relative

abundances of elements through BNS mergers only with a dependence of the delay time distribution on metallicity, with lower metallicities yielding shorter delay times. Their comprehensive treatment goes beyond the purpose of this work.

Our models reproduce the orbital period and eccentricity distribution of Galactic BNSs, and match the observed BNS merger rate, in a self-consistent fashion. In particular, our fiducial model reproduces the double peak in the eccentricity distribution (Andrews and Mandel, 2019): observed pulsars cluster around around $e \sim 0.1$ and $e \sim 0.6$, showing instead a gap for $0.3 \lesssim e \lesssim 0.6$. In Figure 3.2 ($\alpha = 3$), we can distinguish two more concentrated regions at eccentricity $e \sim 0.6$ and 0.1. This feature becomes even more evident after the application of radio selection effects (Figure 3.7a). This suggests the importance of observational biases not only for the spins and magnetic fields of pulsars, but also for the orbital properties. Moreover, the distribution of pulsars in the $P_{\rm orb} - e$ plane is almost independent of the chosen MW model, enforcing the robustness of this result.

We can compare our cumulative distributions (solid lines in Fig. 3.6) with the green dashed lines of Figure 6 by Chattopadhyay et al. (2020). Our cumulative distribution of eccentricity is very different from the one reported by Chattopadhyay et al. (2020) because they do not account for binary selection effects. Our Figure 3.2 can be compared with those of Vigna-Gómez et al. (2018) and Kruckow, Tauris, Langer, Kramer, et al. (2018). The distribution of BNSs in Figure 11 of Kruckow, Tauris, Langer, Kramer, et al. (2018) is less populated at high eccentricity with respect to our results. This difference is a consequence of the different kicks and binding energy prescriptions, as discussed in Iorio et al. (2023). Compared to Kruckow, Tauris, Langer, Kramer, et al. (2018) and our results, Vigna-Gómez et al. (2018) produce much tighter binaries (coloured dots of their Figure 2). In fact, most of the BNSs show orbital periods shorter than ~ 10 d. Moreover, the wider systems ($\rm P_{orb} \gtrsim 10^3$ d) are completely missing. This difference is a consequence of the different natal kick models adopted in Vigna-Gómez et al. (2018).

In our models, we did not include any spin-up prescription during the CE phase. In contrast, Chattopadhyay et al. (2020) assume that a NS accretes between 0.04 and 0.1 $\rm M_\odot$ during CE, according to the rates presented in MacLeod and Ramirez-Ruiz (2015). As a result, pulsars spin up much more efficiently during a CE event than during RLO, and their distribution peaks toward smaller spin periods. For this reason, Chattopadhyay et al. (2020) predict many more detectable pulsars compared to our models when they enable accretion during CE. Nevertheless, the role played by the CE phase during spin-up is controversial (Chamandy et al., 2018). Osłowski et al. (2011) assume that the accreted matter during CE contributes only to the magnetic field decay, considering accretion during CE a chaotic process, not able to produce spin-up (Benensohn et al., 1997). Our spin-up treatment does not include the effect of winds as well. Indeed, we might expect the infalling matter produced by winds to be chaotic and thus not efficiently cause the spin-up of the pulsar (Kiel et al., 2008). We can compare Figure 3.5 with Table 4 from Chattopadhyay et al. (2020). The number of detectable pulsars predicted by their models is generally one order of magnitude higher than our predictions. Our predicted numbers of observable pulsars are consistent only with their model CE–*Z*, which does not include spin-up during CE, and predicts 13 observations.

There are large uncertainties about the surface magnetic field: the burial of magnetic field during mass accretion is poorly understood as well as its decay during the isolated pulsar evolution. The τ_d parameter has been varied in the literature from a few Myr (e.g. Osłowski et al., 2011) up to a few Gyr (e.g. Kiel et al., 2008). Another important contribution to the overall uncertainty in the pulsar population is given by the initial distribution of spins and magnetic fields. These are even more important than the magnetic-field decay time τ_d. Several distributions have been proposed for the initial spin and magnetic field (e.g. Igoshev et al., 2022; Faucher-Giguère et al., 2006). However, the lack of statistics does not allow us to draw strong conclusions.

We evaluated a four-dimensional likelihood in the $(P_{\rm orb}, e, P, \dot{P})$ space. Our approach consistently takes into account correlations among parameters, which are instead neglected by other tests (e.g., the Kolmogorov-Smirnov test), frequently used in the pulsar literature. The large errors on the Bayes factor errors reported in Table 3.6 are a consequence of the limited number of observed pulsars, making it difficult to differentiate among the models. However, despite this limitation, the Bayes factor indicate that the FG and FL models are disfavoured with respect to the U prescription.

We can compare our SKA predictions (Table 3.7) to Table 4 of Chattopadhyay et al. (2021). Their fiducial model estimates 78 BNSs containing a radio-detectable pulsar by the SKA telescope. Their result is thus roughly twice our projection. Nevertheless this discrepancy is consistent with the different approach we used. As already stressed, the different CE formalism, accentuates the spin up of their pulsars, resulting in shorter spin periods. In turn, this translates into a higher number of detectable pulsars.

3.5 Summary and conclusions

The BNS population of the MW is the perfect laboratory to test binary-star evolution models. Here, we used the new population synthesis code SEVN (Iorio et al., 2023) to model the population of BNSs in the MW. We implemented a new model for both the spin down and spin up of pulsars in SEVN, while also probing the relevant parameter space (e.g., CE parameter α, initial spin distribution, initial magnetic field distribution, decay time of the magnetic field τ_d). We injected our simulated binaries into four MW models: an empirical model with an exponentially decaying SFR, a model with constant SFR, and two galaxies from the EAGLE and ILLUSTRISTNG cosmological simulations.

We compared our simulated BNS catalogues with the observed Galactic BNSs after applying radio selection effects with PSRPOPPY (Bates et al., 2014). In our analysis, we considered four observable parameters: orbital period, eccentricity, pulsar spin period, and spin period derivative. After modelling our radio-selected pulsars with a Dirichlet process Gaussian mixture model (Rinaldi and Del Pozzo, 2022b), we evaluated the four-dimensional likelihood associated with each model in the aforementioned parameter space. We then compared our models by computing the Bayes factor with respect to the fiducial model.

We also derived the Galactic BNS merger rate from our models and compared it with the one inferred from the observations (Pol et al., 2019; Pol et al., 2020). The CE parameter α has a large impact on both the merger rate and the orbital properties of the BNS population. The

present-day BNS merger rate varies up to one order of magnitude depending on the choice of α. Values of $\alpha < 1$ are disfavoured as they under-predict the merger rates and produce more eccentric systems compared to observations (Fig. 3.6). Assuming the empirical MW prescription, the model with $\alpha = 3$ produces a rate $\mathscr{R}_{\rm MW} = 31.3\,{\rm Myr}^{-1}$ (Fig. 3.1), consistent with the rate inferred from the Galactic pulsar binary systems ($\mathscr{R}_{\rm MW} = 37^{+24}_{-11}\,{\rm Myr}^{-1}$, Pol et al. (2020)).

The distribution of magnetic field and spin period at pulsar formation play a critical role on the final population of detectable pulsars (Fig. 3.4). The Bayes factors favour the uniform (U) distribution of spin periods and magnetic fields, which predicts 5–10 detectable pulsars. In contrast, the flat-in-log (FL) model predicts ~ 100 detectable pulsars (Fig. 3.5) against the **9** observed Galactic pulsars in the considered surveys (the Parkes Multibeam Pulsar Survey, the Swinburne Multibeam Pulsar Survey, and the High Time Resolution Universe Pulsar Survey).

The magnetic field decay timescale $\tau_{\rm d}$ is another free parameter of our model. There are large uncertainties on the physical process leading to the burial of the magnetic field and consequently to the typical timescales associated with it. $\tau_{\rm d}$ dictates the speed at which a pulsar traverses the $P-\dot{P}$ plane and stops emitting radio beams. Given the small sample of Galactic BNSs, we cannot draw strong conclusions on the expected $\tau_{\rm d}$ value.

We have shown that we need to account for radio selection effects in order to reproduce the observed spin period and magnetic field distributions of observed pulsars. Moreover, binary selection effects are critical to correctly match the orbital period and especially the eccentricity distribution of the observed Galactic BNSs.

According to our fiducial model, which matches both the Galactic merger rate and the orbital properties of Galactic BNSs, the SKA will observe ~ 30 BNSs in the Milky Way, among which ~ 20 new detections.

Our results show that we can match the BNS merger rate, as inferred from Galactic radio pulsars, only if we assume an empirical MW model, a value of the CE parameter $\alpha \approx 3$, and the natal kick model by Giacobbo and Mapelli (2020). Such model yields low natal kicks for stripped and ultra-stripped SNe in binary systems. The Galactic BNS merger rate drops by a factor of four for larger natal kicks (Hobbs et al., 2005). This result favours low natal kicks in tight binary systems, as already suggested by previous studies (e.g., Beniamini et al., 2016; Bray et al., 2016; Bray et al., 2018; Vigna-Gómez et al., 2018; Mapelli and Giacobbo, 2018; Willcox et al., 2021; Richards et al., 2023; O'Doherty et al., 2023).

An accurate model for the star formation history of the MW is essential, in order to describe the current BNS merger rate and number of observable pulsars. The treatment of CE is also important but more prone to uncertainties about single star evolution and mass transfer. For example, Santoliquido, Mapelli, Giacobbo, et al. (2021), who adopt a different formalism for single star evolution, predict even larger merger rates for $\alpha > 3$, while the BNS merger rate estimated with SEVN has a peak for $\alpha = 3$ and then decreases for larger values of α (Iorio et al., 2023).

The magnetic field and spin model are essential to match both the number of observed pulsars in BNSs and their position in the $P-\dot{P}$ plane, the FG and FL models being less favoured compared to an uniform distribution for the initial magnetic field and spin period.

However, a link between the initial magnetic field distribution and the underlying physical processes that govern the magnetic field evolution is still highly debated (Konar, 2017; Igoshev et al., 2022; Zhang, Zhang, et al., 2022; Sarin et al., 2023). Here, we have assumed that CE evolution does not contribute to pulsar spin up. This is a crucial assumption and needs further consideration with dedicated hydro-dynamical numerical simulations.



Chapter 4

The more accurately the metal-dependent star formation rate is modeled, the larger the predicted excess of binary black hole mergers

This chapter is based on Sgalletta, Mapelli, et al. (2025)

4.1 Introduction

As the number of gravitational wave detections grows, the merger rate of BBHs can help us to constrain their formation, the properties of their progenitors, and their birth environment (e.g., Belczynski, Kalogera, and Bulik, 2002; Dominik et al., 2013; Neijssel et al., 2019; Baibhav et al., 2019; Mapelli, 2020; Mapelli, 2021; Zevin, Bavera, et al., 2021; Broekgaarden and Berger, 2021; Mandel et al., 2022; Belczynski, Romagnolo, et al., 2022; van Son, de Mink, Callister, et al., 2022; Broekgaarden, Berger, et al., 2022). The merger rate density is the result of the interplay between binary star evolution and the history of cosmic star formation

(Lamberts et al., 2018; Santoliquido, Mapelli, Bouffanais, et al., 2020; Broekgaarden and Berger, 2021; Santoliquido, Mapelli, Artale, et al., 2022; Boesky et al., 2024a; Boesky et al., 2024b; Chruślińska, 2024).

Most previous work relies on averaged SFR density and metallicity distribution relations (e.g., van Son, de Mink, Callister, et al., 2022; Santoliquido, Mapelli, Giacobbo, et al., 2021; Neijssel et al., 2019). This assumption makes it extremely straightforward to calculate the merger rate density evolution, but contains several approximations in the description of the star formation process and metallicity evolution in the Universe. Such assumptions affect both the shape and absolute values of the estimated merger rates, as shown by several authors (Boco, Lapi, Goswami, et al., 2019; Boco, Lapi, Chruslinska, et al., 2021; Santoliquido, Mapelli, Artale, et al., 2022; Briel et al., 2022). Current predictions for BBH merger rates span over three orders of magnitude (see e.g., Mandel et al., 2022). However, emerging trends indicate that state-of-the-art binary population synthesis models tend to predict higher rates than those inferred by LVK, particularly when incorporating the latest observational data to model the Universe (e.g., Neijssel et al., 2019; Broekgaarden and Berger, 2021; Broekgaarden, Berger, et al., 2022; Santoliquido, Mapelli, Artale, et al., 2022; Srinivasan, Lamberts, et al., 2023; Boesky et al., 2024a).

This discrepancy is largely driven by the interplay of merger efficiency and metal-poor star formation (Belczynski, Dominik, et al., 2010; Mapelli, Giacobbo, Santoliquido, et al., 2019; Chruslinska, Nelemans, and Belczynski, 2019; Neijssel et al., 2019; Tang et al., 2020; Santoliquido, Mapelli, Giacobbo, et al., 2021; Broekgaarden and Berger, 2021; Chruślińska, 2024). In fact, the merger efficiency of BBHs is 1–4 orders of magnitude higher in metal-poor than in metal-rich progenitor systems (Klencki, Moe, et al., 2018; Giacobbo and Mapelli, 2018; Spera, Mapelli, et al., 2019; Broekgaarden and Berger, 2021; Iorio et al., 2023; van Son, Roy, et al., 2025). Hence, the merger rate density evolution should be largely boosted by star formation in metal-poor regions, often associated with low-mass galaxies. As discussed by Chruślińska et al. (2021), Boco, Lapi, Chruslinska, et al. (2021), and Chruślińska (2024) the large uncertainties concerning the metallicity evolution in the Universe and the role of metal-poor galaxies might explain a fraction of the overall discrepancy.

Additionally, there is growing evidence that current models provide a poor description of the CE phase and binary evolution via stable mass transfer episodes might be more important than previously assumed for the formation of BBHs (Neijssel et al., 2019; Bavera et al., 2021; Marchant, Pappas, et al., 2021; Gallegos-Garcia, Berry, et al., 2021; Olejak, Belczynski, et al., 2021). Specifically, the stability criteria commonly adopted in population synthesis codes appear to produce unstable mass transfer for a wider range of parameters compared to detailed stellar modeling (Ge, Hjellming, et al., 2010; Ge, Webbink, et al., 2015; Ge, Webbink, et al., 2020; Marchant, Pappas, et al., 2021). This in turn may lead to an overestimate of the BBH merger rates (Gallegos-Garcia, Berry, et al., 2021).

This work is motivated by the considerations above. Firstly, we aim to assess the impact of the metal-dependent SFR on the BBH merger rates. To this end, we adopt and upgrade a detailed Universe model built from observational scaling relations (Boco, Lapi, Goswami, et al., 2019; Boco, Lapi, Chruslinska, et al., 2021) with GALAXY$\mathscr{R}$ATE (Santoliquido, Mapelli, Artale, et al., 2022). We test several SFR – galaxy mass relations, fundamental metallicity

relations, and we explore the impact of low-mass galaxies. Secondly, we investigate the relative contribution of different formation channels to the BBH merger rates. We show that our state-of-the-art data-driven approach produces BBH merger rates consistently above the LVK inferred range. Such a discrepancy is robust against variations in the metal-dependent SFR model. In particular, low-mass galaxies ($M_* < 10^8 M_\odot$) do not contribute more than a factor of ~ 2 to the overall BBH merger rate density and their relative contribution strongly depends on the assumed SFR – galaxy mass relation.

This chapter is organized as follows: Section 4.2 describes the methodology and the main codes used in this work. Section 4.3 provides an overview and a comparison of the adopted Universe models. Sections 4.4.2 and 4.4.3 present the results of the cosmic merger rate density as a function of the cosmic model. Section 4.4.4 details the merger rate density results for the different BBH formation channels. Finally, we discuss the implications of our results in Section 4.5. We summarize our findings in Section 4.6.

4.2 Method

We investigated the BBH merger rate density varying five model parameters, for a total of 360 parameter combinations. We used the code GALAXY$\mathscr{R}$ATE (Santoliquido, Mapelli, Artale, et al., 2022; Santoliquido, Mapelli, Iorio, et al., 2023) to couple binary compact object populations to a synthetic Universe built from observational scaling relations (Mapelli, Giacobbo, Ripamonti, et al., 2017; Artale, Mapelli, Bouffanais, et al., 2020; Santoliquido, Mapelli, Giacobbo, et al., 2021; Santoliquido, Mapelli, Artale, et al., 2022; Santoliquido, Mapelli, Iorio, et al., 2023). The methodology adopted is described below.

4.2.1 Population-synthesis code SEVN

We simulated catalogues of binary compact objects with the SEVN code [1], described in detail in Chapter 2. For the purpose of this work, we adopted the default SEVN settings as described by Iorio et al. (2023). We assumed the *Delayed_gauss* SN prescription, with BH masses determined according to the *delayed* model by Fryer et al. (2012). In our fiducial model, natal kicks are sampled as Giacobbo and Mapelli (2020, hereafter, GM20). We varied the kick prescription testing also a model in which BHs get the same natal kicks as derived for Galactic neutron stars (H05, Hobbs et al., 2005). We adopted the λ parameters specified by Claeys et al. (2014). Our fiducial model assumes a CE efficiency parameter $\alpha = 1$. However, we also explored different α parameters within our models. Section 4.2.6 provides an overview of the parameters explored.

[1] In this work, we used the SEVN version V 2.10.1 (commit 22c9236). SEVN is publicly available at the gitlab repository https://gitlab.com/sevncodes/sevn

4.2.2 Initial conditions

We sampled the masses of the primary star (M_1) from a Kroupa initial mass function (Kroupa, 2001), in a range between 5 and 150 $\mathrm{M}_\odot$:

$$\mathscr{F}(M_1) \propto M_1^{-2.3}. \tag{4.1}$$

We drew the secondary star mass (M_2) within the range $[2.2, 150]\,\mathrm{M}_\odot$ from the observational distribution on $q = M_2/M_1$ (Sana et al., 2012):

$$\mathscr{F}(q) \propto q^{-0.1}, \tag{4.2}$$

with $\max\left(\frac{2.2\,\mathrm{M}_\odot}{M_1}, 0.1\right) \leq q \leq 1$. The orbital periods and eccentricities were also drawn from the distributions derived by Sana et al. (2012):

$$\mathscr{F}(P_{\mathrm{orb}}) \propto (\log P_{\mathrm{orb}})^{-0.55}, \tag{4.3}$$

with $0.15 \leq \log(P_{\mathrm{orb}}/\mathrm{d}) \leq 5.5$, and

$$\mathscr{F}(e) \propto e^{-0.42}, \tag{4.4}$$

with $0 \leq e \leq 1 - (P/2\,\mathrm{days})^{-2/3}$, following the correction by Moe et al. (2017). These distributions are fits to observations of a sample of massive binary stars in open clusters.

We sampled 10^7 binaries and used them as initial conditions for 12 metallicities: $Z =$ 0.0002, 0.0004, 0.0008, 0.0012, 0.0016, 0.002, 0.004, 0.006, 0.008, 0.012, 0.016, and 0.02. The total simulated mass for each metallicity is thus $M_{\mathrm{sim}} = 2.2 \times 10^8 \mathrm{M}_\odot$.

4.2.3 Formation channels

We distinguish four main formation channels of BBHs, following the classification by Broekgaarden, Berger, et al. (2022) and Iorio et al. (2023).

- Channel I: The systems experience a stable mass transfer episode before the first compact object formation and only after they evolve through at least one CE phase.
- Channel II: The systems interact only via stable mass transfer episodes.
- Channel III: At the time of the first compact remnant formation the system has already experienced at least one CE phase and the system is composed of one H-rich star and one without the H envelope.
- Channel IV: Similarly to Channel III, the systems experience at least one CE before the first compact remnant formation, but in this case, at the time of compact remnant formation both stars have lost their H envelopes.

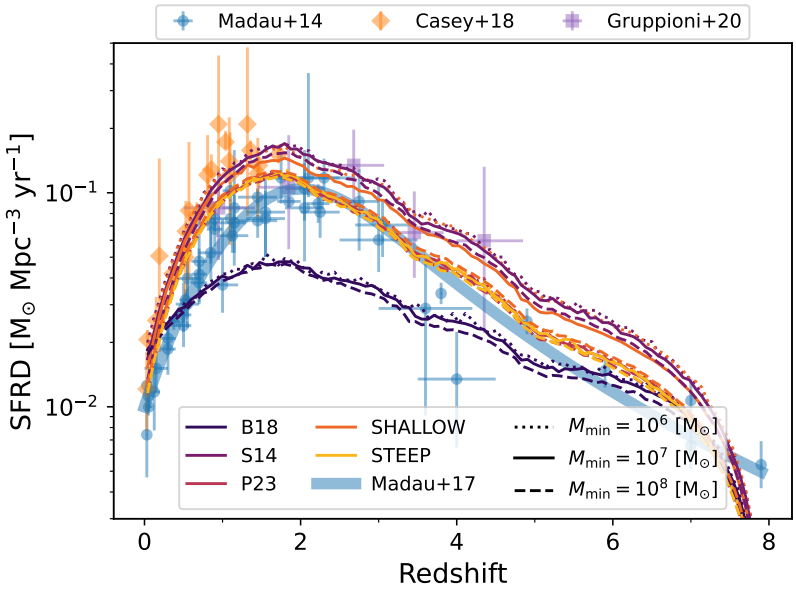


Fig. 4.1 SFR density as a function of redshift for different SFR-M_* relations (different colors). The different linestyles show the results by cutting the galaxy main sequence at different minimum galaxy masses, $M_{\rm min} = 10^6 {\rm M}_\odot$ (dotted), $10^7 {\rm M}_\odot$ (solid) and $10^8 {\rm M}_\odot$ (dashed). The wide blue line shows the fit by Madau and Fragos (2017). The markers show observed data points: the blue dots are are taken from Madau and Dickinson (2014), the orange diamonds are from Casey et al. (2018), and the purple squares are taken from Gruppioni et al. (2020).

4.2.4 Observational scaling relations

In order to model the Universe and populate it with BBHs, we adopted the code GALAXY$\mathscr{R}$ATE [2] (Santoliquido, Mapelli, Artale, et al., 2022). We generated a set of star-forming galaxies from observational scaling relations for an array of formation redshifts, sampling their masses M_*, SFRs, and average metallicities. Here below, we summarize such scaling relations.

We adopted the star-forming galaxy stellar mass function derived by Chruslinska and Nelemans (2019). For each formation redshift, we kept the comoving volume fixed $V \sim (100\,{\rm cMpc})^3$ and sampled a number of star-forming galaxies $\mathscr{N}_{\rm gal}\left(z_{\rm form}\right)$ proportional to the galaxy number density. We sampled galaxy masses in the range $\left[M_{\rm min}, 10^{12} {\rm M}_\odot\right]$. The minimum galaxy mass is a free parameter in our models, we tested different values: $M_{\rm min} = 10^6$, 10^7, and $10^8 {\rm M}_\odot$. We assigned a SFR to every sampled galaxy following a double lognormal distribution, with a first peak centered on the galaxy main sequence, and a second one, on the starbust sequence (Boco, Lapi, Chruslinska, et al., 2021). The parameters adopted are described in Appendix B.1.

The slope of the galaxy main sequence is highly debated, especially moving toward low-mass galaxies ($\lesssim 10^{8.5} {\rm M}_\odot$) and high redshifts. For this reason, we tested several galaxy main sequence definitions. Specifically, we considered the definitions given by Speagle

[2]The code GALAXY$\mathscr{R}$ATE can be found at https://gitlab.com/Filippo.santoliquido/galaxy_rate_open

et al. (2014, hereafter S14), Boogaard et al. (2018, hereafter B18), and Popesso et al. (2023, hereafter P23). In the following equations, the SFR is expressed in $M_\odot yr^{-1}$, and all masses are given in solar units. S14 define the galaxy main sequence as:

$$\log \mathrm{SFR}\,(M_*,t) = (0.84 - 0.026t)\log M_* - 6.51 - 0.11t, \tag{4.5}$$

where t is the age of the Universe in Gyr. The definition by B18 is as follows:

$$\log \mathrm{SFR}\,(M_*,z) = 0.83 \log\left(\frac{M_*}{M_0}\right) - 0.83 + 1.74 \log\left(\frac{1+z}{1+z_0}\right), \tag{4.6}$$

where $M_0 = 10^{8.5} M_\odot$ and $z_0 = 0.55$ are the median values of the data. The fit by P23 is:

$$\log \mathrm{SFR}\,(M_*,t) = a_0 + a_1 t - \log\left[1 + \left(M_*/10^{a_2+a_3 t}\right)^{-a_4}\right], \tag{4.7}$$

with $a_0 = 2.693 \pm 0.012$, $a_1 = -0.186 \pm 0.009$, $a_2 = 10.85 \pm 0.05$, $a_3 = -0.0729 \pm 0.0024$ and $a_4 = 0.99 \pm 0.01$.

Moreover, we built two additional parametric models that explore different slopes of the main sequence relation at low-masses ($M_* < 10^9$ $M_\odot$). In this range, in fact, the data is scarce (see e.g., Popesso et al., 2023) and very uncertain. With this approach, we were able to bracket all possible behaviors of the galaxy main sequence at low-masses. For these models, we cut the fit in P23 at $10^9 M_\odot$, and adopted a constant slope a across cosmic times for lower galaxy masses:

$$\log \mathrm{SFR}\,(M_*,t) = \begin{cases} a \log M_* + b & \text{for } M_* < 10^9\ M_\odot \\ \text{Eq. 4.7} & \text{for } M_* \geq 10^9\ M_\odot. \end{cases} \tag{4.8}$$

We assumed $a = 0.5$, for the SHALLOW model, and $a = 1$ for the STEEP model. We decided such values for the SHALLOW (STEEP) slope to always keep it as the shallowest (steepest) main sequence slope at all redshifts in the low-mass galaxies' tail. The continuity assumption between the two equations sets the value of the second parameter b. See Appendix B.1.2 for more details on the main sequence definitions adopted.

By integrating the galaxies SFR for each redshift bin, we get the SFR density as a function of redshift, shown in Fig. 4.1. We compare the predicted SFR density for all the adopted galaxy models. The model by B18 predicts a lower SFR density with respect to the observational data. This is likely a result of the data sample utilized in B18 reaching up to $z \sim 0.9$, wheareas here we extrapolate their relation to much higher redshifts. All the other galaxy main sequence models predict SFR densities that are consistent with UV and far-IR data (see Madau and Dickinson, 2014, and references therein). The fit by S14 adopts galaxy main sequence data, with galaxy stellar masses within $10^{9.5} < M_* < 10^{11.5} M_\odot$. P23 expand the work by S14, by incorporating the most updated and recent galaxy main sequence data, encompassing the widest range of galaxy stellar mass ($10^{8.5} < M_* < 10^{11.5} M_\odot$) and redshift ($0 < z < 6$) available to date. Thus, we adopted equation 4.7 (Popesso et al., 2023) as our fiducial SFR–M_* relation. Moreover, varying the lower mass limit of the galaxy

main sequence (represented by different line styles) does not significantly impact the SFR density. This is not surprising, as the SFR from low-mass galaxies is suppressed by the galaxy main sequence relation. Therefore, even if these small galaxies are more numerous, the contribution to the total SFR density is negligible compared to the contribution from higher mass galaxies ($M_* \geq 10^8 M_\odot$).

For each galaxy, we sampled an average metallicity based on the fundamental metallicity relation, that links the average metallicity of a galaxy with its stellar mass and SFR (Mannucci, Cresci, et al., 2010; Maiolino et al., 2019). In this work, we compared three different definitions of the fundamental metallicity relation, corresponding to the fits by Mannucci, Salvaterra, et al. (2011), Curti et al. (2020), and Andrews and Martini (2013). The recent work by Nakajima et al. (2023) compares known models of mass–metallicity relations with a comprehensive, up-to-date sample of James Webb Space Telescope (JWST) observations of galaxies at redshift 4 to 10. Their data (see their figure 12) show the fundamental metallicity relation by Andrews and Martini (2013) to best fit these new data up to $z \sim 8$. For this reason, we adopted the fundamental metallicity relation by Andrews and Martini (2013) as our fiducial model. We assumed that the metallicity is distributed following a lognormal function within each galaxy, with a scatter $\sigma_Z = 0.14$. Such an observed scatter (amounting to $\lesssim 0.1$ dex in the local Universe and $\lesssim 0.2$ dex at high redshift) is small since it refers to galaxies at a given redshift with the same stellar mass and SFR. However, the metallicity at a given z is substantially more dispersed over the whole galaxy populations; for instance, averaging the fundamental metallicity relation over stellar mass (via the stellar mass function) yields a mass-metallicity relation characterized by a large and asymmetric dispersion of $\gtrsim 0.35$ dex, in agreement with observational findings (Chruślińska et al., 2021; Boco, Lapi, Chruslinska, et al., 2021). We describe the adopted observational scaling relations in more detail in Appendix B.1 and review all the models' parameters in Section 4.2.6.

We also tested a different approach based on the average evolution of the cosmic SFR and metallicity with COSMO$\mathscr{R}$ATE (Santoliquido, Mapelli, Bouffanais, et al., 2020). In this case, the cosmic SFR density $\psi(z)$ and the average metallicity evolution $\mu(z) = \langle Z/Z_\odot \rangle$ are modeled using the fitting formulae provided by Madau and Fragos (2017):

$$\psi(z) = 0.01 \frac{(1+z)^{2.6}}{1+[(1+z)/3.2]^{6.2}} \mathrm{M_\odot Mpc^{-3} yr^{-1}}, \tag{4.9}$$

$$\log \mu(z) = 0.153 - 0.074 z^{1.34}. \tag{4.10}$$

We spread the metallicities around this average value following a normal distribution with standard deviation $\tilde{\sigma}_Z$:

$$p(Z|z) = \frac{1}{\sqrt{2\pi\tilde{\sigma}_Z^2}} \exp\left[-\frac{[\log(Z/Z_\odot) - \langle \log(Z/Z_\odot) \rangle]^2}{2\tilde{\sigma}_Z^2} \right], \tag{4.11}$$

where $\langle \log Z/Z_\odot \rangle = \mu(z) - \ln 10 \tilde{\sigma}_Z^2/2$. With this simplified approach, we can change the spread of metallicity at a given redshift just by tuning the parameter $\tilde{\sigma}_Z$.

4.2.5 Merger rate density

We evaluate the merger rate density with GALAXY$\mathscr{R}$ATE as Santoliquido, Mapelli, Artale, et al. (2022):

$$\mathscr{R}(z) = \frac{1}{V^3} \int_{z_{\max}}^{z} \left[\sum_{i=1}^{\mathscr{N}_{\rm gal}(z')} \int_{Z_{\min}}^{Z_{\max}} \mathscr{S}_i\left(z', Z\right) \mathscr{F}\left(z', z, Z\right) dZ \right] \frac{dt(z')}{dz'} dz', \tag{4.12}$$

where we sum over all of the formation galaxies, $\mathscr{N}_{\rm gal}(z')$, at redshift z' (i.e., the galaxies where the binary systems form at $z' \geq z$), and then integrate over the redshift between the BBH merger redshift z (i.e., the redshift at which the BBH merges) and the maximum considered formation redshift $z_{\max} = 8$. For the $i-$th galaxy $\mathscr{S}_i(z', Z) = \psi_i(z')\, p_i(Z|z')$, where $\psi_i(z')$ is its SFR and $p_i(Z|z')$ is its metallicity distribution at a given redshift z'. The second term in the integral accounts for the distribution of binaries in our catalogs:

$$\mathscr{F}\left(z', z, Z\right) = \frac{1}{M_{\rm sim}} \frac{\mathscr{N}_{\rm BBH}\left(z', z, Z\right)}{dt} f_{\rm bin} f_{\rm corr}, \tag{4.13}$$

where $\mathscr{N}_{\rm BBH}\left(z', z, Z\right)/dt$ is the rate of BBHs progenitors that form at redshift z' and merge at redshift z, for a given metallicity Z. The factor $f_{\rm bin} = 0.5$ corrects for the fraction of binaries, and $f_{\rm corr} = 0.251$ takes into account the cut at lower masses from our initial sampling conditions (see Section 4.2.2).

4.2.6 Summary of model parameters

We ran our SEVN and GALAXY$\mathscr{R}$ATE simulations over an extensive grid of model parameters, exploring both binary evolution and galaxy modeling uncertainties. We summarize the grid of models in Table 4.1. Specifically, we ran sets of simulations with SEVN varying the CE efficiency parameter $\alpha = 0.5$, 1, 3, and 5. We consider two natal-kick models: GM20, and H05, as defined in Section 5.2.3.

As for the synthetic galaxy models, we vary the minimum galaxy mass assuming $M_{\rm min} = 10^6$, 10^7 and $10^8\,{\rm M}_\odot$. We explore the galaxy main-sequence definitions from S14, B18, P23, as well as our SHALLOW and STEEP models (equation 4.8 with $a = 0.5$ and $a = 1$, respectively). For the fundamental metallicity relations, we compare the fits by Mannucci, Salvaterra, et al. (2011), Andrews and Martini (2013), and Curti et al. (2020). Our fiducial model incorporates the most updated main sequence definition using P23, the fundamental metallicity relation by Andrews and Martini (2013), and a minimum galaxy stellar mass $M_{\rm min} = 10^7 {\rm M}_\odot$.

4.3 A comparative analysis of Universe models

Figure 4.2 provides a schematic overview and comparison of the two approaches to modeling a synthetic Universe. The detailed method offers several improvements over the conventional

	Parameter	Values
Binary evolution	α	0.5, **1**, 3, 5
	SN kick	**GM20** [(a)]
		H05 [(b)]
Galaxy modeling	SFR–M_*	B18 [(c)]
		S14 [(d)]
		P23 [(e)]
		STEEP (eq. 4.8, a=1)
		SHALLOW (eq. 4.8, a=0.5)
	$M_{\rm min}$ [$M_\odot$]	10^6, 10^7, 10^8
	FMR	Mannucci+11 [(f)]
		Andrews+13 [(g)]
		Curti+20 [(h)]

Table 4.1 Summary of the grid of parameters varied in our study. The parameters highlighted in **bold** face are adopted in our fiducial model.
[(a)] Giacobbo and Mapelli (2020) [(b)] Hobbs et al. (2005) [(c)] Boogaard et al. (2018) [(d)] Speagle et al. (2014) [(e)] Popesso et al. (2023) [(f)] Mannucci, Salvaterra, et al. (2011) [(g)] Andrews and Martini (2013) [(h)] Curti et al. (2020)

averaged approach. We note that $\tilde{\sigma}_Z$, used in the averaged model, and σ_Z, used in the detailed model, have two different physical meanings. σ_Z represents the metallicity dispersion around the FMR (i.e., at fixed galaxy stellar mass and SFR), that is then convoluted with the distribution of galaxy masses and SFR to obtain the spread in metallicity at a given redshift. Therefore, even if we assume the distribution around the FMR to be log-normal and with a small scatter ~ 0.14, the overall distribution of metallicities is asymmetric and can have a large scatter, driven by the observed galaxy distribution at that specific redshift.

In contrast, models relying on averaged metallicity evolution require the total scatter ($\tilde{\sigma}_Z$) to artificially encompass the full metallicity distribution at a given redshift. For this reason typical $\tilde{\sigma}_Z$ values of ~ 0.5 are required. In this work, we adopt $\tilde{\sigma}_Z = 0.6$ as fiducial value and $\tilde{\sigma}_Z = 0.1$, even if not realistic, to demonstrate the effect of reducing the low metallicity tail. Moreover, the distribution adopted is symmetric around the average metallicity. Therefore, even if the spread in the averaged model is large enough to mimic the amount of SFR at low-metallicities of the detailed approach, it inevitably produces an unrealistic high-metallicity tail, that is not supported by observations (see e.g., Chruślińska, 2024).

We note that the distribution of metallicities of the averaged models could be improved by adopting a skewed distribution around the mean value (see e.g., van Son, de Mink, Chruślińska, et al., 2023; Fishbach, 2025). Such models allow for a more realistic representation of metallicities, when properly fitted to the data. We do not consider them here as they would ultimately lead to results consistent with our detailed approach.

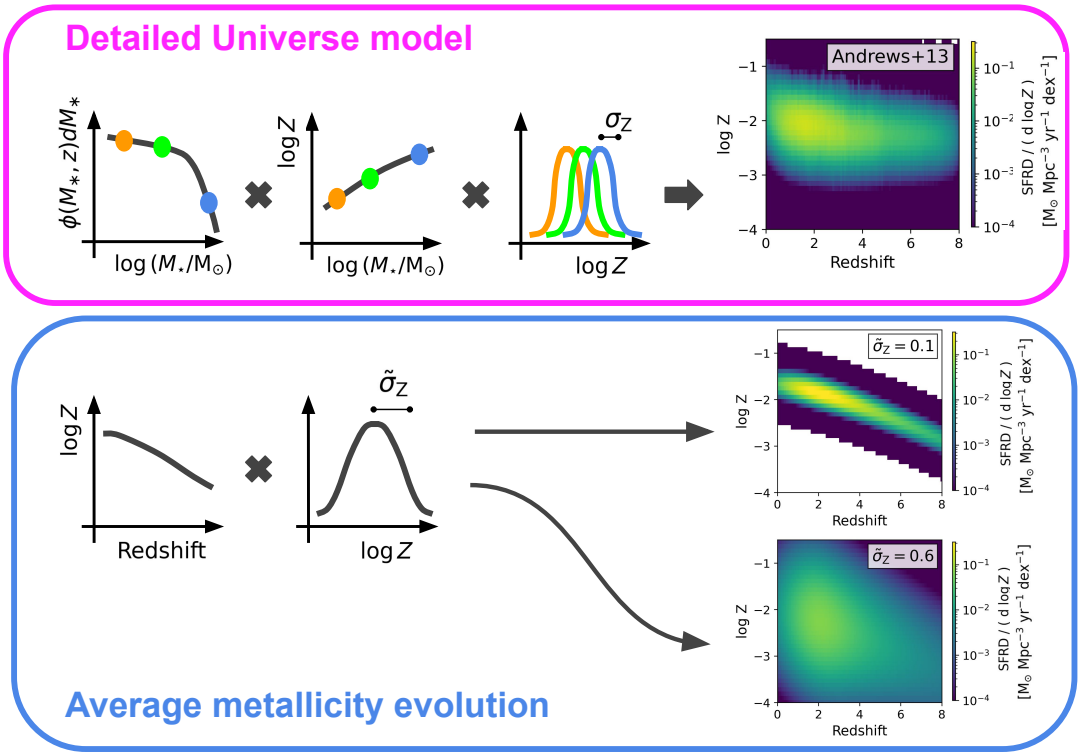


Fig. 4.2 Schematic overview of the different metal-dependent SFR models adopted here. Upper panel: overview of the detailed Universe model, based on observational scaling relations. Lower panel: overview of the model based on the average SFR and metallicity evolution across cosmic time. The plots on the right illustrate the metallicity distributions as a function of redshift for our different prescriptions. For the average metallicity evolution model, we show the distributions assuming both $\tilde{\sigma}_Z = 0.1$ and 0.6.

4.4 Results

4.4.1 Merger efficiency and metallicity

The BBH merger efficiency (i.e., the number of BHs that merge per total initial stellar mass) depends on metallicity, being higher for metal-poor stars (Dominik et al., 2012; Giacobbo, Mapelli, and Spera, 2018; Klencki, Moe, et al., 2018). With SEVN, we find an abrupt drop of three orders of magnitude in the BBH merger efficiency, above $\sim 1/3 Z_\odot$ (Fig. 4.3). The drop mildly depends on the α parameter: it is close to $1/3$ $Z_\odot$ for $\alpha \leq 1$ and shifts to lower metallicities ($\sim 1/10$ $Z_\odot$) for $\alpha = 3$ or 5. For this reason, the fraction of SFR at low metallicity is crucial for determining the BBH merger rate.

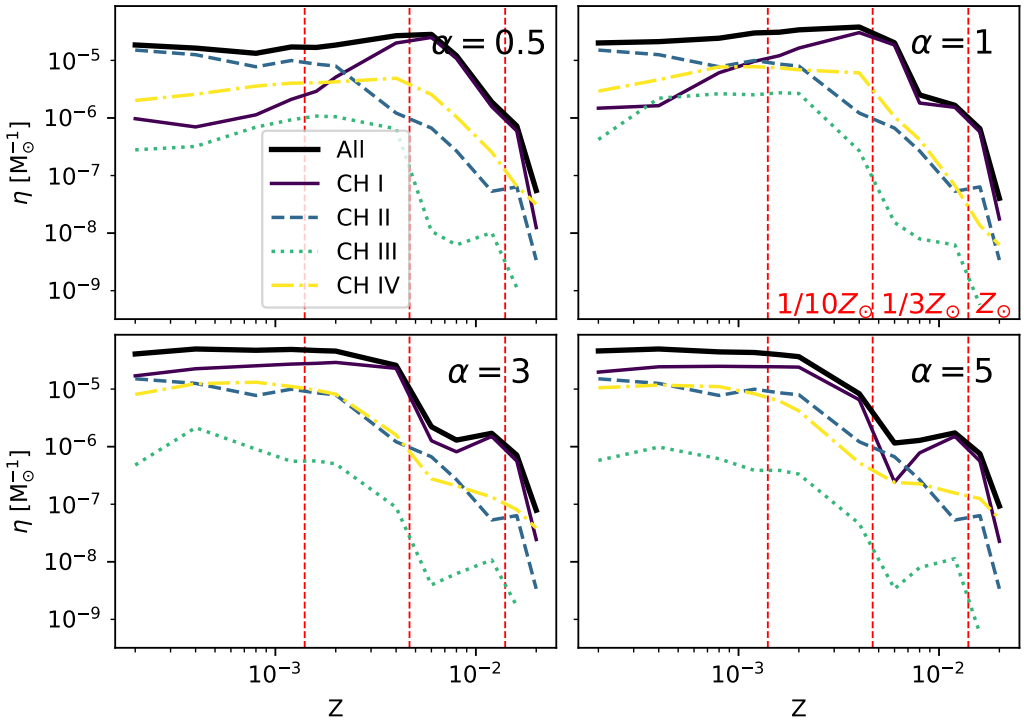


Fig. 4.3 Merger efficiency η for BBHs as a function of metallicity Z. From top to bottom $\alpha = 0.5$, 1, 3, 5. The different colors refer to formation channels I-IV (Section 4.2.3). The vertical red lines highlight metallicity values of $Z = 1/100$, $1/10$, and $1/3$ $Z_\odot$.

4.4.2 The impact of low-mass galaxies

Figure 4.4 shows the relative contribution of different galaxy masses to the total SFR density and to the SFR density below a certain Z threshold. We consider two reference metallicity thresholds: $Z \leq 1/3 Z_\odot$ and $\leq 1/10 Z_\odot$. We compare the results for different main-sequence definitions. In Figure 4.4, we emphasize the SHALLOW and STEEP models (wider lines), because they represent the extreme cases: the former has the shallowest trend, whereas the latter has the steepest decrease in the SFR density at low galaxy masses. This Figure shows the results for galaxies at $z = 0$; however, the following considerations hold for every considered redshift.

We see from Fig. 4.4 that only with the shallowest SFR–M_* relations the contribution from low-mass galaxies is important, for metallicities $Z \leq 1/3$ $Z_\odot$. For the steepest galaxy main-sequence models (e.g., the STEEP model and P23), most of the SFR for metallicities below $1/3$ $Z_\odot$ originates from galaxies with masses in the range of $(10^9 - 10^{10}) M_\odot$ for the fundamental metallicity relations by Andrews and Martini (2013) and Curti et al. (2020), while the contribution from $10^6 M_\odot$ galaxies is about half. The peak in SFR shifts toward galaxy masses of $(10^8 - 10^9) M_\odot$ adopting the models by Mannucci, Salvaterra, et al. (2011). On the other end, shallower main sequence slopes (e.g., the SHALLOW model, S14) show

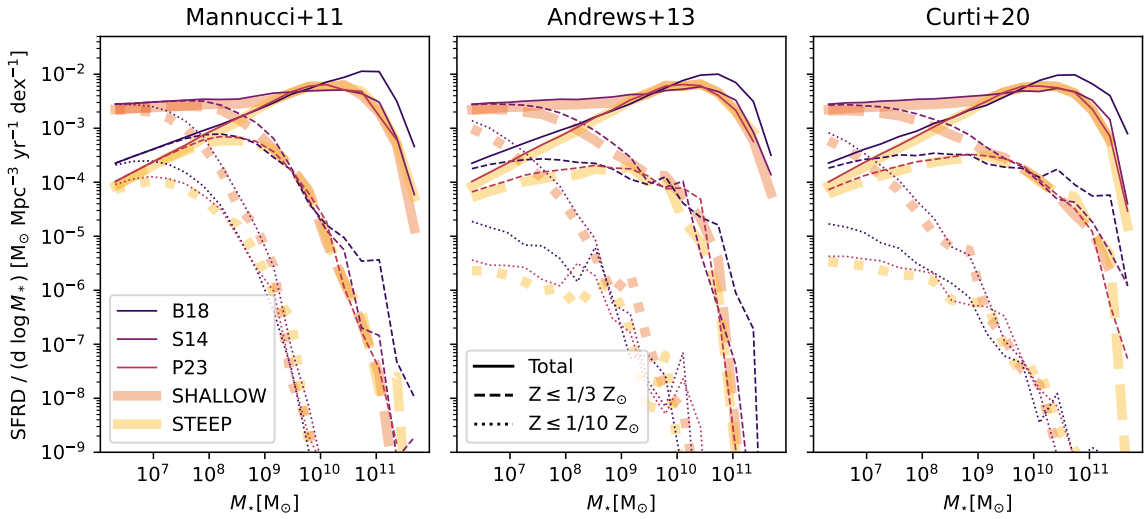


Fig. 4.4 Contribution of galaxies of mass M_* to the SFR density evaluated for different metallicity thresholds at $z = 0$. The x axis represents the galaxy stellar mass M_*, while the lines show the total contribution to the SFR density from all galaxies in a given stellar mass bin, with a metallicity $Z \leq Z_{\rm th}$. The different line styles refer to different metallicity thresholds $Z_{\rm th}$; solid lines:$Z_{\rm th} = 1/3 Z_\odot$, dashed: $Z_{\rm th} = 1/10 Z_\odot$, and dotted:$Z_{\rm th} = 1/100 Z_\odot$. The different colors represent models with different SFR–M_* relations, blue: B18, violet: S14, pink: P23, orange: SHALLOW, yellow: STEEP. Each panel shows the results for a different FMR, from left to right: Mannucci, Salvaterra, et al. (2011), Andrews and Martini (2013), and Curti et al. (2020).

a similar SFR contribution from low mass galaxies up to $\sim 10^8 M_\odot$. Model B18 falls in between these two extreme cases.

If we restrict our attention to even lower metallicities ($Z < 1/10\ Z_\odot$), the contribution from low-mass galaxies becomes important for all the SFR–M_* relations. As a result, for higher α parameters (for which the merging efficiency peaks at smaller metallicities, see Fig. 4.3) the contribution from low-mass galaxies becomes important, regardless of the chosen SFR–M_* relation. While the trend described above is true for all the fundamental metallicity relations, we see from the different panels that the prescriptions by Curti et al. (2020) and Andrews and Martini (2013) predict on average higher metallicities (Fig. B.1).

Several studies have shown how the contribution of starburst galaxies might increase at high redshifts compared to our current treatment. Both Bisigello et al. (2018) and Rinaldi, Caputi, et al. (2022) find that starburst galaxies might contribute to $\gtrsim 50\%$ of the cosmic SFR at redshifts $z \sim 4-5$. Bisigello et al. (2018) finds that starburst galaxies might constitute the $\sim 16\%$ of total galaxies at redshifts $2 < z < 3$. A higher percentage of starburst galaxies at high redshift would have two main effects. First, we would see an increase in the global SFR, as starburst galaxies have an higher SFR at fixed mass. Second, starburst galaxies specifically increase the SFR at low metallicity. In fact, because starburst galaxies have a higher SFR at fixed mass, they typically exhibit lower metallicity due to the FMR. Both factors contribute to an increase in the BBH merger rates, although the impact at $z = 0$ is smaller, as this effect primarily affects redshifts $z \gtrsim 2-3$.

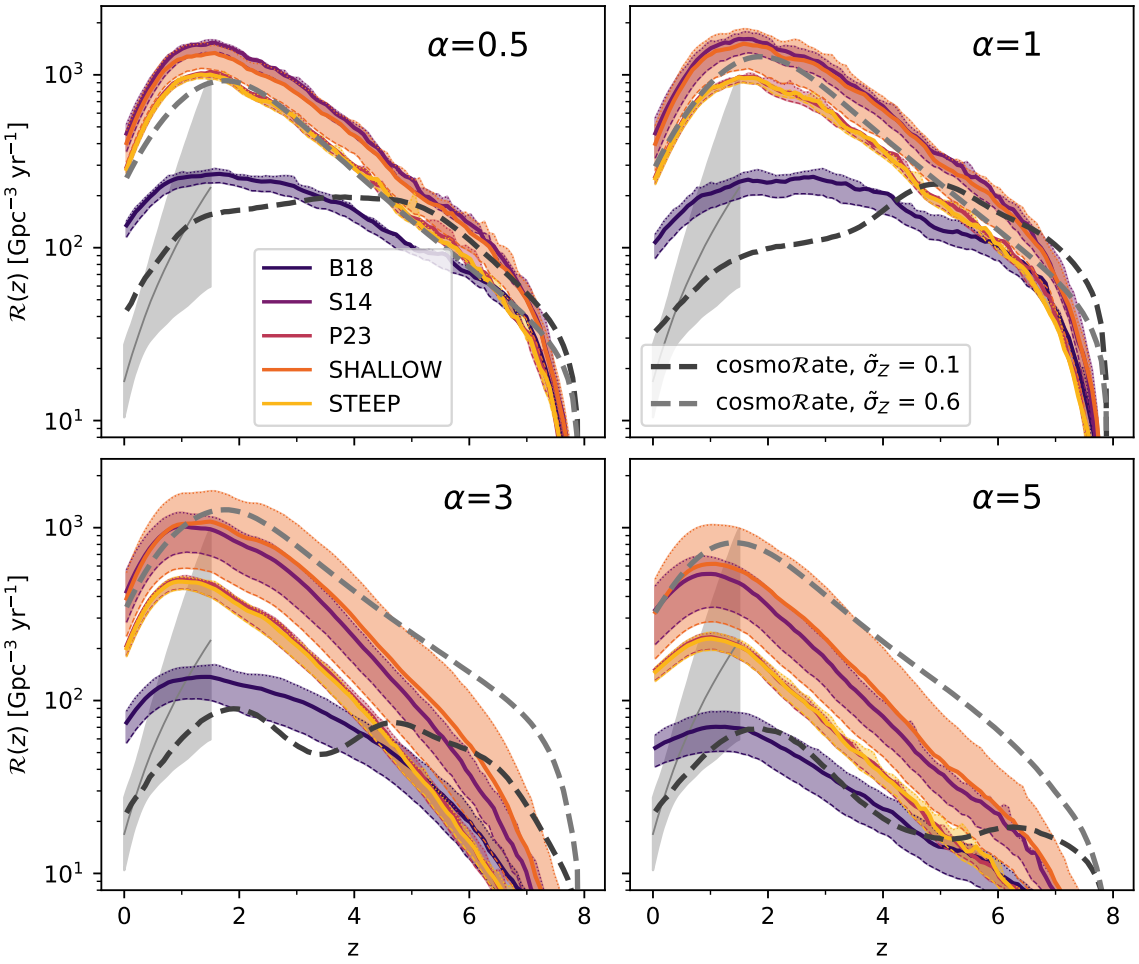


Fig. 4.5 BBH merger rate density as a function of redshift for different observational scaling relations (different colors) and CE α parameters (different panels). Each color is associated with a different SFR–M_* relation, as summarized in the legend in the top left-hand panel. The solid lines show the model with $M_{\rm min} = 10^7$ M$_\odot$. The shaded area encompasses the difference between $M_{\rm min} = 10^6$M$_\odot$ (upper boundary), and $M_{\rm min} = 10^8$M$_\odot$ (lower boundary). All the models assume the fiducial fundamental metallicity relation by Andrews and Martini (2013). The thick dashed lines show the merger rate density obtained with COSMO$\mathscr{R}$ATE (simplified model), assuming the cosmic SFR density by Madau and Dickinson (2014) and a lognormal distribution for the metallicity with a spread $\tilde{\sigma}_{\rm Z} = 0.1$ (dark gray) and 0.6 (light gray). The gray-shaded regions show the MRD inferred by the LVK collaboration: $\mathscr{R}(z) \propto (1+z)^k$(Abbott et al., 2023a).

4.4.3 Cosmic merger rate density

Figure 4.5 shows the BBH cosmic merger rate density we obtain assuming different SFR–M_* relations, adopting the fundamental metallicity plane by Andrews and Martini (2013). The results for the fundamental metallicity relations by Mannucci, Salvaterra, et al. (2011) and Curti et al. (2020) are shown in Appendix B.2. We compare our merger rate densities with the

inferred fit $\mathscr{R}(z) \propto (1+z)^k$ by the LVK collaboration up to the third observing run (Abbott et al., 2023a).

All predicted BBH merger rate densities exceed the LVK estimates across all our galaxy-derived models. The B18 model yields the lowest merger rate density. This is expected as B18 results in the lowest SFR density (see Figure 4.1). As discussed in Section 4.2.4, this is likely due to our extrapolation of the relation in B18 to high redshifts, whereas the data sample considered there is limited to $z \lesssim 0.9$.

The merger rate densities evaluated by setting different minimum galaxy masses differ at most by a factor of ~ 2. Even removing all the galaxies with mass below $10^8 M_\odot$ (lower bound of the shaded areas in Fig. 4.5), the merger rate density is still well above the 90% credible interval from LVK. The magnitude of the difference between assuming $M_{\rm min} = 10^6$, 10^7 and $10^8 M_\odot$ depends on the main sequence definition adopted. As expected, steeper SFR–M_* relations result in smaller differences with the minimum galaxy stellar mass adopted. The differences between $M_{\rm min} = 10^6$, 10^7, and $10^8\,M_\odot$ are bigger for $\alpha = 3$ and $\alpha = 5$, compared to $\alpha = 1$ or $\alpha = 0.5$, as expected from the results described in Section 4.4.2).

Figure 4.5 also compares the merger rate density we obtain through our host-galaxy models (i.e., with GALAXY$\mathscr{R}$ATE) with the merger-rate density calculated adopting an average SFR density and metallicity evolution of the Universe (i.e., with COSMO$\mathscr{R}$ATE). The merger rate density we obtain modeling the host galaxies with observational scaling relations and the one we estimate by assuming an average SFR density agree only when we assume a large metallicity spread ($\tilde{\sigma}_Z = 0.6$, see Sec. 4.2.4) for the latter. Moreover, even assuming a large value of $\tilde{\sigma}_Z$, the predicted shape and steepness of the merger rate density differ in the two models, especially at high redshift and for models with $\alpha > 1$.

4.4.4 Formation channels

Figure 4.6 shows the merger rate density for each BBH formation channel, as defined in 4.2.3, through equation 5.9. Channel I (traditional CE scenario, with at least one CE phase after the formation of the first BH) gives the main contribution to the full BBH merger rate density at all redshifts, if $\alpha \leq 1$. Channel I is subdominant only at high redshift and when $\alpha > 1$. This is the result of longer delay time distributions for channel I, compared to channels II and IV. As a consequence, even if the merger efficiency of channel I is higher at all metallicities (Figure 4.3), channels II and IV dominate the merger rate density at high redshift. Moreover, the longer delay times result in a much steeper shape of the merger rate density for channel I, especially if we adopt a large value of α.

At low redshift, the merger-rate density associated with channel I is always largely above the LVK 90% credible interval. In contrast, the merger rate densities associated with channels II (stable mass transfer), III and IV lie within the observed range reported by LVK for all the considered α parameters. Channel III is by far the least common formation pathway.

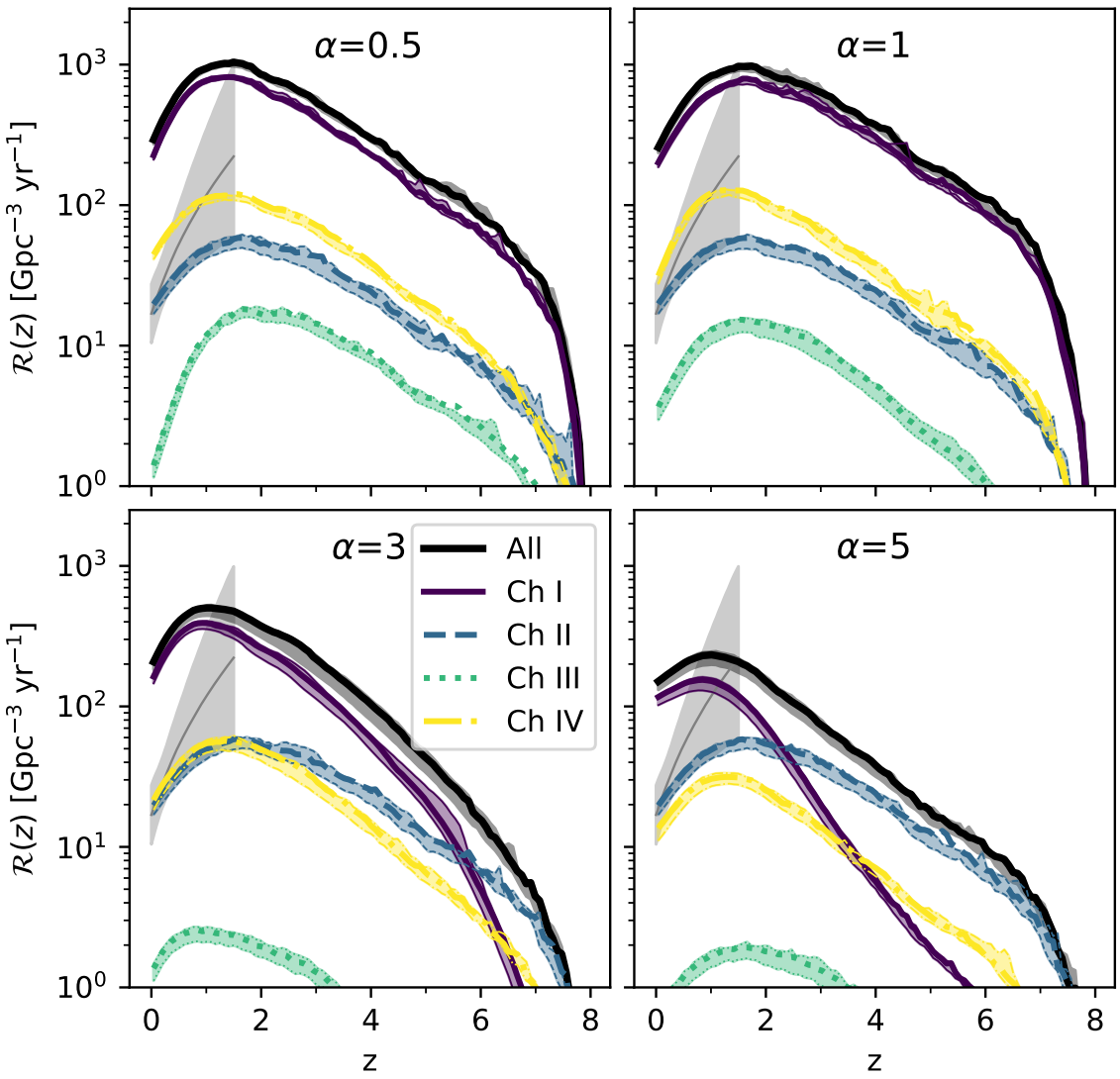


Fig. 4.6 BBH merger rate density as a function of redshift for different BBH formation channels. The solid black lines show the merger rate density of the whole BBH population. The shaded area encompasses the difference between $M_{\rm min} = 10^6 {\rm M}_\odot$ (upper boundary), and $M_{\rm min} = 10^8 {\rm M}_\odot$ (lower boundary). The different panels show the results obtained assuming different CE α parameters. All the models assume the fiducial SFR–M_* relation P23 and the fundamental metallicity relation by Andrews and Martini (2013). The gray-shaded regions show the MRD inferred by the LVK collaboration (Abbott et al., 2023a).

4.5 Discussion

Predictions of BBH merger rate are highly uncertain, as they strongly depend on binary evolution physics and the metal-dependent SFR. Mandel et al. (2022) show that predicted rates can vary by more than three orders of magnitude depending on the adopted assumptions.

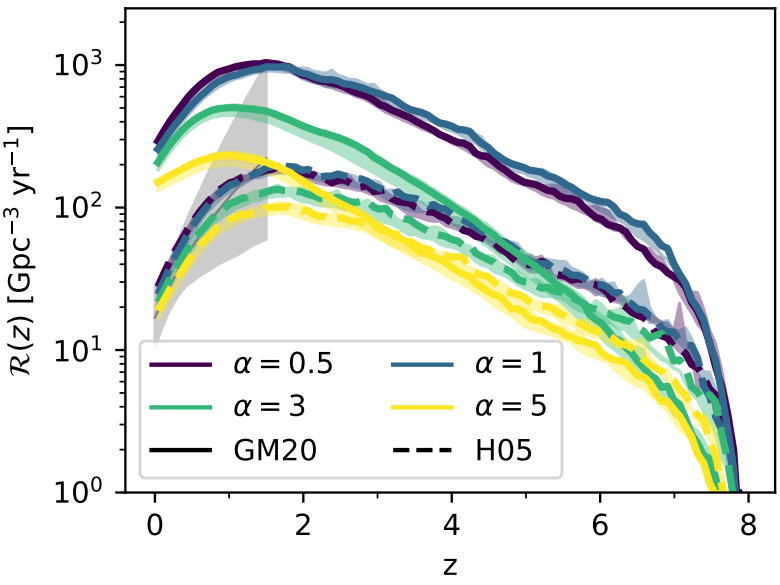


Fig. 4.7 Merger rate density as a function of redshift, for the natal-kick models GM20 (solid lines) and H05 (dashed lines). The line colors show the results obtained assuming different CE efficiency parameters (α). The upper boundaries of the shaded areas show the models obtained with minimum galaxy mass $M_* = 10^6 M_\odot$, whereas for the lower boundary the minimum mass is $10^8 M_\odot$. All the models assume the fiducial observational scaling relations. The gray-shaded region shows the MRD inferred by the LVK collaboration (Abbott et al., 2023a).

Binary population synthesis codes generally tend to overpredict BBH merger rates, suggesting that careful calibration of binary parameters is necessary to bridge the gap with observations. This trend is evident across multiple studies using different population synthesis codes, including STARTRACK (Klencki, Moe, et al., 2018; Chruslinska, Nelemans, and Belczynski, 2019; Olejak, Belczynski, et al., 2021; Olejak, Fryer, et al., 2022; Romagnolo et al., 2023), COMPAS (Neijssel et al., 2019; Broekgaarden and Berger, 2021; Riley, Mandel, et al., 2021; Broekgaarden, Berger, et al., 2022; Stevenson et al., 2022; Rauf et al., 2023; Boesky et al., 2024a), COSMIC (Zevin, Spera, et al., 2020; Srinivasan, Lamberts, et al., 2023), BPASS (Eldridge et al., 2018; Tang et al., 2020), and POSYDON (Bavera et al., 2021; Román-Garza et al., 2021). For similar variations in binary parameters, Boesky et al. (2024a) find rates that are consistent with our results, adopting the COMPAS binary population synthesis code (Riley, Agrawal, et al., 2022). Several studies have explored the contribution of different formation channels to the BBH population. Bavera et al. (2021) and Román-Garza et al. (2021) identify the evolution through at least one CE as the dominant channel in most models. The model reported by Olejak, Belczynski, et al. (2021) predicts a higher contribution to the BBH merger rates from channel I; however, their study highlights that different treatments of mass transfer stability can significantly alter the relative contributions of each channel. Similarly, Dorozsmai et al. (2024) find the stability of mass transfer to be a key factor in enhancing the contribution from the stable mass transfer channel. Notably, in the simulations run with COMPAS (Neijssel et al., 2019; Broekgaarden and Berger, 2021) channel II is dominant

compared to channel I because of the different stability criteria. Finally, the choice of the metal-dependent SFR can have a large impact on the BBH merger rates, as shown by Neijssel et al. (2019), Broekgaarden and Berger (2021), Broekgaarden, Berger, et al. (2022), and Srinivasan, Lamberts, et al. (2023). Specifically, Tang et al. (2020) show that a narrower metallicity distribution leads to lower merger rates, in agreement with our findings.

In this work, we have modeled the host galaxies of BBHs, their SFR and metallicity with the most up-to-date observational scaling relations. Nevertheless, as we improve the description of the metal-dependent SFR, the BBH merger rate density we obtain at low redshift ($10^2 - 10^3\,\mathrm{Gpc^{-3}yr^{-1}}$) is always well above the 90% credible interval inferred by LVK after the third observing run (Fig. 4.5). This is true for all of our models, considering different SFR–M_* relations, different fundamental metallicity relations, and different values of the efficiency parameter for CE ejection.

As discussed above, we can exclude that the overestimate of the BBH merger rate density is a feature of our population-synthesis code SEVN (Iorio et al., 2023). Rather, it is a problem common to current population synthesis codes.

In the following, we discuss several potential solutions to reconcile theoretical predictions and GW data. One possible explanation is that the CE phase occurs less frequently than previously assumed, or that BBH progenitors do not survive the CE phase as often as currently believed. Conversely, the stable mass transfer (channel II) may play a considerably more significant role in BBH formation than previously expected, as already proposed by several authors (Pavlovskii et al., 2017; Neijssel et al., 2019; Misra et al., 2020; Klencki, Nelemans, Istrate, and Pols, 2020; Klencki, Nelemans, Istrate, and Chruslinska, 2021; Olejak, Belczynski, et al., 2021; Shao et al., 2021; Bavera et al., 2021; Marchant, Pappas, et al., 2021; van Son, de Mink, Callister, et al., 2022). In binary population synthesis codes, the CE channel tends to dominate over the others; in contrast, stable mass transfer is prevalent in detailed stellar-structure calculations (e.g., Gallegos-Garcia, Berry, et al., 2021). One of the main factors of uncertainty lies in the criteria for the onset of a CE phase. As proposed by Ge, Webbink, et al. (2020), mass transfer might be stable for a wider range of mass ratios than previously believed, at least under the assumption of adiabatic, conservative mass transfer. Another slightly different interpretation is that the traditional description of semi-major axis evolution during a CE phase (based on the α parameter, Hurley, Tout, et al. (2002)) is too simplified, and does not capture the actual evolution of the system (Hirai et al., 2022; Trani et al., 2022; Di Stefano et al., 2023; Everson et al., 2025). If the orbital separation during a CE phase shrinks less than predicted by the traditional α formalism, then the resulting merger rate density is likely going to be lower (e.g., Hirai et al., 2022; Lau et al., 2022).

Natal kicks also significantly influence the merger rate density (Mapelli and Giacobbo, 2018; Iorio et al., 2023; Boesky et al., 2024a). In Fig. 4.7, we compare our fiducial model with a model in which natal kicks are drawn from a Maxwellian distribution with root-mean square velocity $\sigma = 265$ km s^{-1}, without accounting for the fallback (Hobbs et al., 2005). This model yields substantially higher kicks, leading to lower BBH merger rate densities across all considered α parameters. Thus, another possible way to reconcile observed and predicted merger-rate density is to assume that natal kicks are higher than usually expected for BBHs. However, this also has an impact on the BH mass function, favoring the merger of

more massive binary systems (Iorio et al., 2023). The recent work by Nagarajan et al. (2025) reveal the existence of both strong ($\gtrsim 100$ km s^{-1}) and weak ($\lesssim 50$ km s^{-1}) black hole kicks, potentially indicating a bimodal distribution (see also Verbunt et al., 2017). Although the uncertainties remain too large to conclusively confirm this scenario, these preliminary results suggest that the black hole kick distribution may lie between the two extreme models proposed in our work.

Finally, recent work by Schneider et al. (2021) shows that envelope stripping can affect the final fate and compact remnant mass of massive stars, increasing the minimum zero-age main sequence mass of BH progenitors from ~ 30 M$_\odot$ to ~ 70M$_\odot$. While population calculations still need to be done for this scenario, this might result in a decrease in the BBH merger rate density as well.

A few caveats should be added. Recent work by Rinaldi, Caputi, et al. (2022) suggests that starburst galaxies contribute to $60-90\%$ of the total SFR. Rinaldi, Caputi, et al. (2022) find a clear bimodality between the galaxy main sequence and the starburst sequence for higher massive galaxies, $M_* \geq 10^9$M$_\odot$. Our current approach likely underestimates the impact of starburst galaxies (see also Caputi et al., 2017; Bisigello et al., 2018). Improved modeling of starburst galaxies is beyond the scope of this work. Nevertheless, an higher contribution of starburst galaxies would further increase the predicted BBH merger rates as they tend to be more metal-poor than main sequence galaxies. We would like to remark that models based on the evolution of the average SFR and metallicity over cosmic time (Santoliquido, Mapelli, Giacobbo, et al., 2021, e.g.,) broadly capture our fiducial BBH merger rate densities (Fig. 4.5), when accounting for a wide spread in metallicity for a given redshift bin ($\tilde{\sigma}_Z = 0.6$). This assumption is needed to mimic the complex distribution of metallicities that in our detailed approach naturally results from the spread in galaxy masses and SFRs. We do not vary the $q_{\rm crit}$ prescriptions in this study. However, Figure 22 in Iorio et al. (2023) demonstrates that different $q_{\rm crit}$ prescriptions affect the BBH merger rate density by a factor of ~ 2. Therefore, given the prescriptions available to date, we do not expect this parameter to significantly influence our results. Nevertheless, different conditions for mass-transfer stability may have an impact on the relative contribution from different formation channels (see e.g., Olejak, Belczynski, et al., 2021; Olejak, Fryer, et al., 2022; Dorozsmai et al., 2024). The parameter $f_{\rm bin}$, takes into account the fraction of binary systems in the Universe. This value strongly varies with stellar mass, being close to 1 for massive stars ($M_1 \geq 16$M$_\odot$, see e.g., Sana et al., 2012; Moe et al., 2017) and decreasing for lower primary masses, reaching ~ 0.4 for $M_1 \sim 2$M$_\odot$ (Moe et al., 2017). We adopt a constant $f_{\rm bin} = 0.5$ as a reference value, to account for the whole population of binary systems. It should be noted that $f_{\rm bin}$ only acts as a renormalization factor, rigidly shifting the merger rates upward or downward. Adopting a different $f_{\rm bin}$ value in the range $[0.4, 1]$ would lead to at most a factor of 2 difference in the merger rates.

As a final remark, differences between the BBH mass function obtained from population-synthesis calculations and the one assumed to infer the LVK rates, might bias the comparison between the two merger rate densities. However, the discrepancy between predictions and LVK rates (at least a factor of ~ 10) is too large to be fully accounted for by such BBH mass function differences.

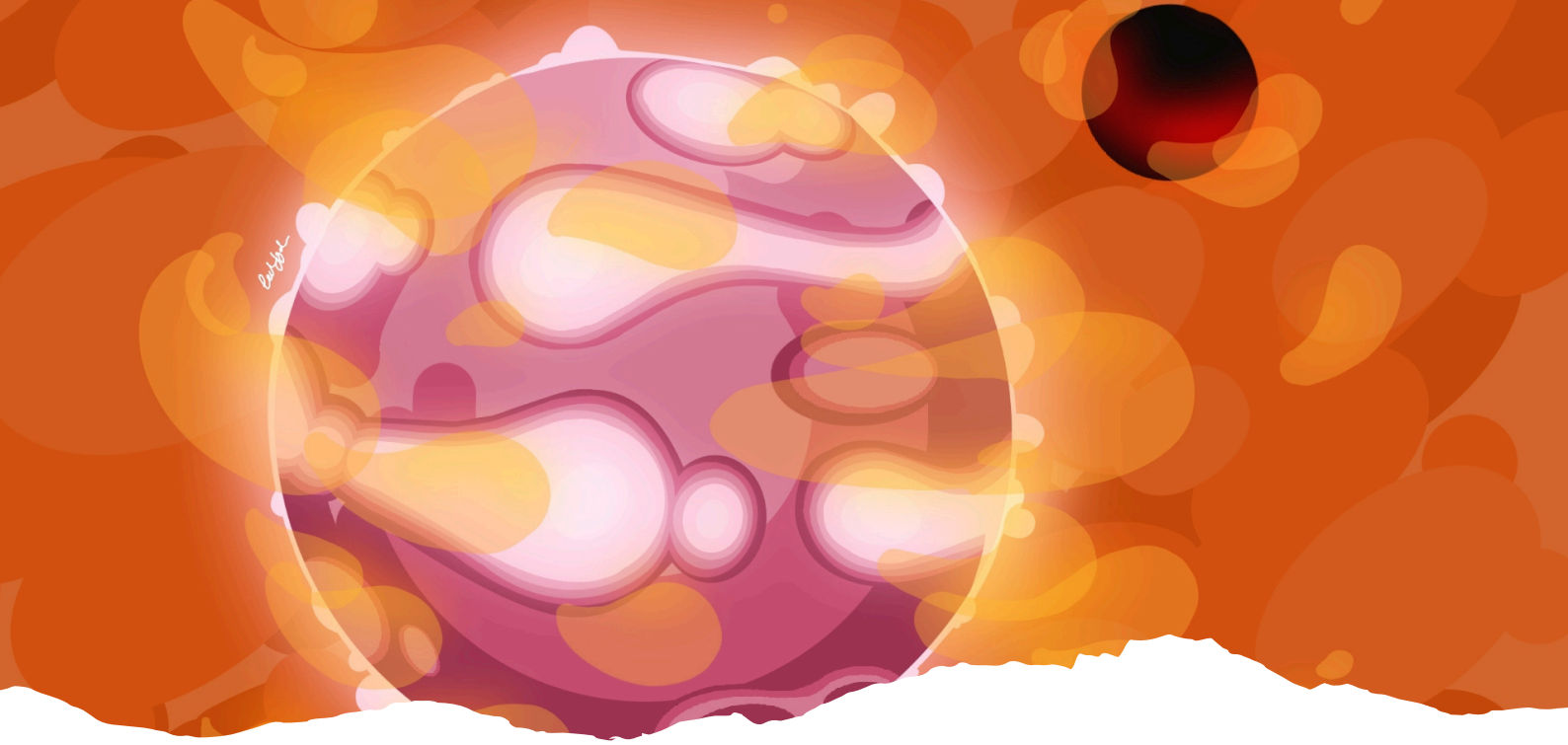
Finally, here we have only considered isolated binary evolution. Including the dynamical formation of BBHs in star clusters and galactic nuclei would only lead to a further increase of the merger rate density because dynamics is known to boost the merger rate density even in a metal-rich environment (Rodriguez and Loeb, 2018; Di Carlo et al., 2020; Mapelli, Bouffanais, et al., 2022; Barber et al., 2025).

4.6 Summary

We have studied the merger rate density of BBHs across cosmic time over 360 combinations of parameters, exploring the effects of different galaxy observational scaling relations and binary evolution models. Furthermore, we have studied the relative impact of different isolated BBH formation channels on the merger rate density. We can summarize our main results as follows.

- Current models of binary population synthesis predict values of the BBH merger rate density at redshift $z \leq 1$ that are well above the 90% credible interval inferred from LVK data (Abbott et al., 2023a).
- The impact of low-mass galaxies ($M_* < 10^8$ M$_\odot$) on the BBH merger rate density is highly dependent on the steepness of the SFR–M_* relation. For steep SFR–M_* relations (Popesso et al., 2023), galaxies with mass $M_* \lesssim 10^7$M$_\odot$ do not contribute significantly to the merger rate density.
- Even removing all the galaxies with mass below 10^8 M$_\odot$ (hence, with lower metallicity), the merger rate density is still well above the 90% credible interval from LVK. Thus, uncertainties in the number of low-mass galaxies do not dramatically affect the merger rate density and do not solve the tension between predicted and observed BBH merger rate density.
- Models based on the average SFR and metallicity evolution need to account for the whole metallicity spread at a given redshift $\tilde{\sigma}_Z \sim 0.6$ in order to mirror detailed Universe prescriptions. In this case, the merger rate densities predicted by the two approaches broadly agree, with differences that become more noticeable toward high redshifts.
- The merger rate density of BBHs is dominated by Channel I, where the systems evolve through at least one CE phase only after the first compact object formation.

Overall, our results clearly indicate that there is a tension between current models of BBH merger rates and values inferred from GW data. We cannot explain this tension through uncertainties on the cosmic SFR density, as we have adopted state-of-the-art models, robustly grounded in observations. Future studies are requested to understand the origin of this tension, addressing -e.g.,- the nature of core collapse, the stability of mass transfer, and the magnitude of natal kicks.



Chapter 5

The impact of envelope binding energies on the merger rate density of binary compact objects

This chapter is based on Sgalletta, Spera, et al. in prep.

5.1 Introduction

The CE is one of the most prominent processes in binary stellar evolution. Nevertheless, the physics of this event is still largely unclear. The $\alpha\lambda-$formalism (van den Heuvel, 1976; Webbink, 1984) is one of the most common approach in population synthesis codes (see also Section 1.3.5). One of the limitations of this model lies in the need of constraining the α parameter to gain predictive power. However, the uncertainties remain prohibitively high (Maxted et al., 2006; Afşar et al., 2008; Zorotovic et al., 2010; De Marco et al., 2011; Iaconi et al., 2019). Furthermore, α may not be constant across different systems, but there may be a distinction between low-mass and high-mass donors (Politano et al., 2007; De Marco et al., 2011; Wilson et al., 2022).

The parameter λ encapsulates the structural properties of a star's envelope, and is intrinsically linked to its stellar mass, metallicity, and evolutionary phase. λ is typically derived from stellar evolution models. However, its determination can vary considerably due to differences among these models. Additionally, there are still open questions regarding the correct evaluation of λ. The primary uncertainties arise from the criterion used to define the core-envelope boundary and from the contributing energy sources that should be considered in the evaluation of the binding energy (Ivanova, Justham, Nandez, et al., 2013; Wang et al., 2016; Kruckow, Tauris, Langer, Szécsi, et al., 2016). The uncertainties on α and λ in turn, reflect on the demographics of binary compact objects, producing variations of orders of magnitude in the resulting merger rates (e.g., Belczynski, Kalogera, and Bulik, 2002; Neijssel et al., 2019; Giacobbo, Mapelli, and Spera, 2018; Mapelli, 2020; Broekgaarden and Berger, 2021; Olejak, Belczynski, et al., 2021; Broekgaarden, Berger, et al., 2022; Iorio et al., 2023; Sgalletta, Iorio, et al., 2023; Boesky et al., 2024a; Sgalletta, Mapelli, et al., 2025).

Kruckow, Tauris, Langer, Szécsi, et al. (2016) and Klencki, Nelemans, Istrate, and Chruslinska (2021) conducted detailed studies of the envelope ejection conditions by massive stars. Their research highlights the risks of adopting precomputed λ prescriptions, showing large discrepancies with stellar envelope binding energies. Furthermore, recent works hint at the importance of convection for the envelope ejection mechanism (Klencki, Nelemans, Istrate, and Chruslinska, 2021; Hirai et al., 2022; Picker et al., 2024).

In this work, we present the envelope binding energies for an extensive set of stars, which goes beyond the current state-of-the-art. The set has been simulated with the PAdova and TRieste Stellar Evolution Code, PARSEC v2.0 (Bressan, Marigo, et al., 2012; Costa, Girardi, et al., 2019; Costa, Bressan, et al., 2021; Nguyen et al., 2022; Costa, Shepherd, et al., 2025; Shepherd et al., 2025). Notably, we extend the analysis to include pure-He stars. We include the new sets of binding energies within SEVN (Spera and Mapelli, 2017; Spera, Mapelli, et al., 2019; Mapelli, 2020; Iorio et al., 2023) and we employ the new formalism to test the cosmic merger rate densities for binary compact objects. In agreement with recent works, our results emphasize the importance of consistent envelope binding energies. Moreover, our results support a functional dependence of the α parameter.

In Section 5.2 we describe the methodology adopted. In section 5.3 we present the envelope binding energies, emphasizing the importance of convection. Furthermore, we describe their implementation in SEVN and show how they compare with existing models. We discuss our findings in Section 5.4 and we conclude in Section 5.5.

5.2 Method

5.2.1 PARSEC

We use the H and pure-He PARSEC v2.0 stellar tracks (Costa, Shepherd, et al., 2025), explained in Section 2.1.2. The tracks include, for each evolutionary timestep, detailed spatial grids of the main stellar properties. To the purposes of our work, we are interested on the radial distance (r), gravitational energy (E_g), internal energy (U), enthalpy (E_h), luminosity (L), H and He concentrations (X_H and X_{He}, respectively).

5.2.2 Envelope binding energy

The envelope binding energy $E_{\rm bind}$ of a star is a key quantity in binary population synthesis codes, primarily because of its pivotal role during the CE phase (see Section 1.3.5). The simplest way to evaluate the binding energy of the envelope is by computing its gravitational binding energy :

$$E_{\rm G} = -\int_{M_{\rm core}}^{M} \frac{Gm}{r(m)} dm \tag{5.1}$$

where M is the total stellar mass, $M_{\rm core}$ is the core mass, m is the local mass coordinate, ranging from 0 in the center of the star to M at its surface. $r(m)$ is the radius from the center at mass coordinate m. The internal energy U (including both thermal and recombination energies) may also contribute lowering the binding energy of the envelope (Dewi et al., 2000), therefore we can define $E_{\rm B}$ as

$$E_{\rm B} = \int_{M_{\rm core}}^{M} \left[-\frac{Gm}{r(m)} + U(m) \right] dm. \tag{5.2}$$

Finally, Ivanova and Chaichenets (2011) first suggested the pressure work term as an additional energy source, contributing to the overall binding energy of the envelope ($E_{\rm H}$):

$$E_{\rm H} = \int_{M_{\rm core}}^{M} \left[-\frac{Gm}{r(m)} + U(m) + \frac{P(m)}{\rho(m)} \right] dm, \tag{5.3}$$

where the term $U + P/\rho$ is known as the specific enthalpy.

The boundary between the core and the envelope is a key quantity for the computation of these integrals. A number of criteria have been proposed (see e.g. Ivanova, Justham, Chen, et al., 2013). We define the He core of a star as the hydrogen-depleted region, where the fraction of hydrogen ($X_{\rm H}$) is lower than a fixed threshold $X_{\rm H,0}$. The commonly adopted value in the literature is $X_{\rm H,0} \sim 0.1$ (Xu and Li, 2010; Ivanova and Chaichenets, 2011; Klencki, Nelemans, Istrate, and Chruslinska, 2021; Marchant, Pappas, et al., 2021). On the other hand, the PARSEC code defines the core as the region where $X_{\rm H,0}$ reaches 10^{-3} by default. We keep $X_{\rm H,0}$ as a free parameter and we vary its value in our models in order to explore its effect. We evaluate $E_{\rm G}$, $E_{\rm B}$ and $E_{\rm H}$ through eq. 5.1, 5.2 and 5.3 at each timestep of the stellar evolution where $M_{\rm core} \neq 0$. We repeat this procedure for every stellar track.

Whether or not a pure-He star can initiate a second unstable mass transfer episode is still unclear. According to the prescription by Hurley, Tout, et al. (2002) mass transfer from pure-He stars can become dynamically unstable, with a high critical mass ratio $q_{\rm crit} = 3$ for He MS stars, but a much smaller one ($q_{\rm crit} < 1$) in more advanced evolutionary stages. Other works assume mass transfer from pure-He stars to always be dynamically stable (Tauris, Langer, et al., 2015; Tauris, Kramer, et al., 2017; Neijssel et al., 2019). In particular, Vigna-Gómez et al. (2018) find that this condition is required in their models in order to explain the population of Galactic binary neutron stars. Nevertheless, Sgalletta, Iorio, et al. (2023) show that this assumption is not necessary adopting SEVN and the PARSEC stellar tracks. Here, we also study the envelope binding energies for pure-He stellar tracks. In this

case, E_G, E_B and E_H are computed with equations 5.1, 5.2 and 5.3, respectively. However, in this case, the lower limit of integration is the CO core mass. The latter is defined in turn, as the He depleted region: $X_{He} < X_{He,0}$, with $X_{He,0}$ a concentration threshold similar to the hydrogen one previously defined.

Here, we study how the binding energies vary for different parameters in our model. We test multiple core separation prescriptions, varying $X_{H,0} = 10^{-1}, 10^{-3}, 10^{-7}$ and $X_{He,0} = 10^{-1}, 10^{-3}, 10^{-7}$. Moreover, we test how the different definitions E_G (eq. 5.1), E_B (eq. 5.2), and E_H (eq. 5.3), impact the results.

5.2.3 SEVN

We include the envelope binding energies computed from the PARSEC stellar tracks as an optional table property in SEVN. We then study the merger rates of binary compact objects produced with the new formalism. To this purpose, we adopt the default SEVN setup, as in Iorio et al. (2023). We study the binary compact objects populations for different α parameters, $\alpha = 0.5$, 1, 3 and 5. We explore the effects of different λ prescriptions by comparing the fit by Claeys et al. (2014), by Klencki, Nelemans, Istrate, and Chruslinska (2021) with our new formalism. Here below, I describe the major changes that our new treatment implies. For a more detailed description of SEVN see also Chapter 2.

Common Envelope: new features

We exploit SEVN flexibility to include the envelope binding energies as optional table properties. Instead of using equation 2.14, we evaluate the envelope binding energy directly from the PARSEC stellar tracks. For a set $X_{H,0}$, we compute the envelope binding energies through the integrals 5.1, 5.2 and 5.3. In this way, we do not need the λ parameter anymore and equation 2.14 becomes:

$$E_{bind,i} = E_{bind,1} + E_{bind,2} \tag{5.4}$$

where $E_{bind,1}$ and $E_{bind,2}$ are the envelope binding energies of the primary and secondary stars. We include the envelope binding energies as optional tables in SEVN. Whenever there is a binary interaction and a mass exchange, SEVN jumps on a new track accordingly to the accreted (or lost) mass. However, this might cause a minor mismatch between the real mass of the star, and the mass that SEVN is reading from the tracks (see Section 2.4 in Iorio et al., 2023, for a detailed description of the evolution algorithm). Therefore, the envelope mass can in turn be different from the real one. For this reason, we rescale the interpolated mass by the factor $f = M_{real}/M_{fake}$. This factor accounts for the fact that if the real mass does not match the mass of the track, then also the energies at play should be rescaled. Moreover, also the He and CO core masses change with different $X_{H,0}$ thresholds, therefore we modify the He and CO tables accordingly, for full consistency. A consequence of this, is that the end of the MS shifts in time, depending on the chosen $X_{H,0}$. As a result, the moment in which a star can enter CE varies (see Section 5.3 for discussion on this point).

5.2.4 Initial conditions for SEVN

In order to study the merger rates of binary compact objects produced with the new formalism, we evolve a population of binaries sampled according to the following initial conditions. We draw the primary star masses $M_{\rm ZAMS,1}$ according to Kroupa (2001), in a range between 5 and 150 $\mathrm{M}_\odot$:

$$\mathscr{F}(M_1) \propto M_1^{-2.3}. \tag{5.5}$$

We sample the mass ratios $q = M_{\rm ZAMS,2}/M_{\rm ZAMS,1}$ according to (Sana et al., 2012):

$$\mathscr{F}(q) \propto q^{-0.1}, \tag{5.6}$$

with $\max\left(\frac{2.2\,\mathrm{M}_\odot}{M_{\rm ZAMS,1}}, 0.1\right) \leq q \leq 1$. We derive in this way the secondary star mass ($M_{\rm ZAMS,2}$), within the range $[2.2, 150]\,\mathrm{M}_\odot$. The orbital periods and eccentricities are distributed according to Sana et al. (2012):

$$\mathscr{F}(P_{\rm orb}) \propto (\log P_{\rm orb})^{-0.55}, \tag{5.7}$$

with $0.15 \leq \log(P_{\rm orb}/\mathrm{d}) \leq 5.5$, and

$$\mathscr{F}(e) \propto e^{-0.42}, \tag{5.8}$$

with $0 \leq e \leq 1 - (P/2\ \mathrm{days})^{-2/3}$ (Moe et al., 2017). We sample 2×10^6 binaries according to these initial conditions. We run this set of binaries for 12 metallicities: $Z = 0.0002$, 0.0004, 0.0008, 0.0012, 0.0016, 0.002, 0.004, 0.006, 0.008, 0.012, 0.016, 0.02. The metallicities that are not included among the single stellar tracks are interpolated within SEVN, as explained in Iorio et al. (2023).

5.2.5 Merger rate density

We evaluate the merger rate density of binary compact objects with GALAXY$\mathscr{R}$ATE (Santoliquido, Mapelli, Artale, et al., 2022). GALAXY$\mathscr{R}$ATE adopts data-driven observational scaling relations to generate a set of star-forming galaxies across cosmic time and populate them with binary compact objects. Here, we use the fiducial setup as described in Sgalletta, Mapelli, et al. (2025). In the following, we give a summary of the adopted relations, a more detailed description of the method adopted can be found in Section 4.2 and Appendix B.1. We sample the galaxy masses $M_\star$ according to the galaxy stellar mass function by Chruslinska and Nelemans (2019), within the range $M_\star \in [10^7, 10^{12}]\,\mathrm{M}_\odot$. We generate in this way $\mathscr{N}_{\rm gal}(z)$ for an array of redshifts, from 0 to $z_{\rm max} = 8$. We assume the galaxy main sequence relation derived in Popesso et al. (2023) to determine the galaxies' star formation rates. Finally, we consider the fundamental metallicity relation by Andrews and Martini (2013) to link the galaxies' mass and star formation rate to their average metallicity. We assume that the metallicities within each galaxy follow a log-normal distribution around this mean value with a scatter $\sigma_{\rm Z} = 0.14$.

Thus, we can estimate the merger rate density as (Santoliquido, Mapelli, Artale, et al., 2022):

$$\mathscr{R}(z) = \frac{1}{V^3} \int_{z_{\max}}^{z} \left[\int_{Z_{\min}}^{Z_{\max}} \mathscr{S}\left(z', Z\right) \mathscr{F}\left(z', z, Z\right) dZ \right] \frac{dt(z')}{dz'} dz', \tag{5.9}$$

where $V \sim (100\,\mathrm{cMpc})^3$ is the total simulated comoving volume. The star formation rate density $\mathscr{S}(z', Z)$ is given by:

$$\mathscr{S}(z', Z) = \sum_{\mathrm{i}=1}^{\mathscr{N}_{\mathrm{gal}}(z')} \psi_{\mathrm{i}}\left(z'\right) p_{\mathrm{i}}\left(Z|z'\right) \tag{5.10}$$

where we sum over all the galaxies $\mathscr{N}_{\mathrm{gal}}(z')$ formed at redshift z'. For the i-th galaxy, $\psi_{\mathrm{i}}(z')$ is its star formation rate and $p_{\mathrm{i}}(Z|z')$ its metallicity distribution. The term $\mathscr{F}(z', z, Z)$ is defined as:

$$\mathscr{F}\left(z', z, Z\right) = \frac{1}{M_{\mathrm{sim}}} \frac{\mathscr{N}\left(z', z, Z\right)}{dt} f_{\mathrm{bin}} f_{\mathrm{corr}}, \tag{5.11}$$

where M_{sim} is the total simulated initial mass, $\frac{\mathscr{N}(z', z, Z)}{dt}$ is the rate of binary compact objects that form at z', with metallicity Z and merge at redshift z. The factor $f_{\mathrm{corr}} = 0.251$ takes into account the incomplete sampling of the initial mass function (see Section 5.2.4), $f_{\mathrm{bin}} = 0.5$ (Moe et al., 2017) represents the fraction of binaries.

5.3 Results

5.3.1 Binding energies

Figure 5.1 shows E_{G}, E_{B} and E_{H} computed for different initial stellar masses and metallicities. For visualization purposes, we only show the evolution of massive stars at $Z = 0.01$ up to the point where they become Wolf-Rayet stars. This is because, during this phase stars begin to shrink (e.g. Costa, Shepherd, et al., 2025), making them less likely to undergo binary interactions. At this metallicity, stars with initial masses $\geq 150\mathrm{M}_{\odot}$ form their cores during the Wolf-Rayet phase already; thus, we omit their evolution from the figure. Low-metallicity stars ($Z \leq 0.0001$) with $M_{\mathrm{ZAMS}} \geq 100\,\mathrm{M}_{\odot}$ typically reach their largest expansion at the end of core He burning, after which they contract. While the final stellar radii depend on both metallicity and initial mass, they never exceed the maximum radius reached during He burning (Costa, Shepherd, et al., 2025). For this reason, we cut the evolution of these stars after they reach their maximum radii from the figure. Finally, in the case of very massive stars ($M_{\mathrm{ZAMS}} \geq 250\,\mathrm{M}_{\odot}$ at $Z = 10^{-11}$ and $M_{\mathrm{ZAMS}} \geq 200\,\mathrm{M}_{\odot}$ at $Z = 0.0001$), radial expansion occurs before core formation. Any binary interaction would occur during the expansion phase. Therefore, from a binary population perspective, the envelope binding energies of these stars will not be relevant. For this reason, we do not show these stars in the plots.

Generally, smaller core masses exert a lower gravitational pull on the envelope. As a consequence, stars with smaller M_{ZAMS} yield lower binding energies at equivalent radii. We find differences in the envelope binding energies within a factor of ~ 2 among the

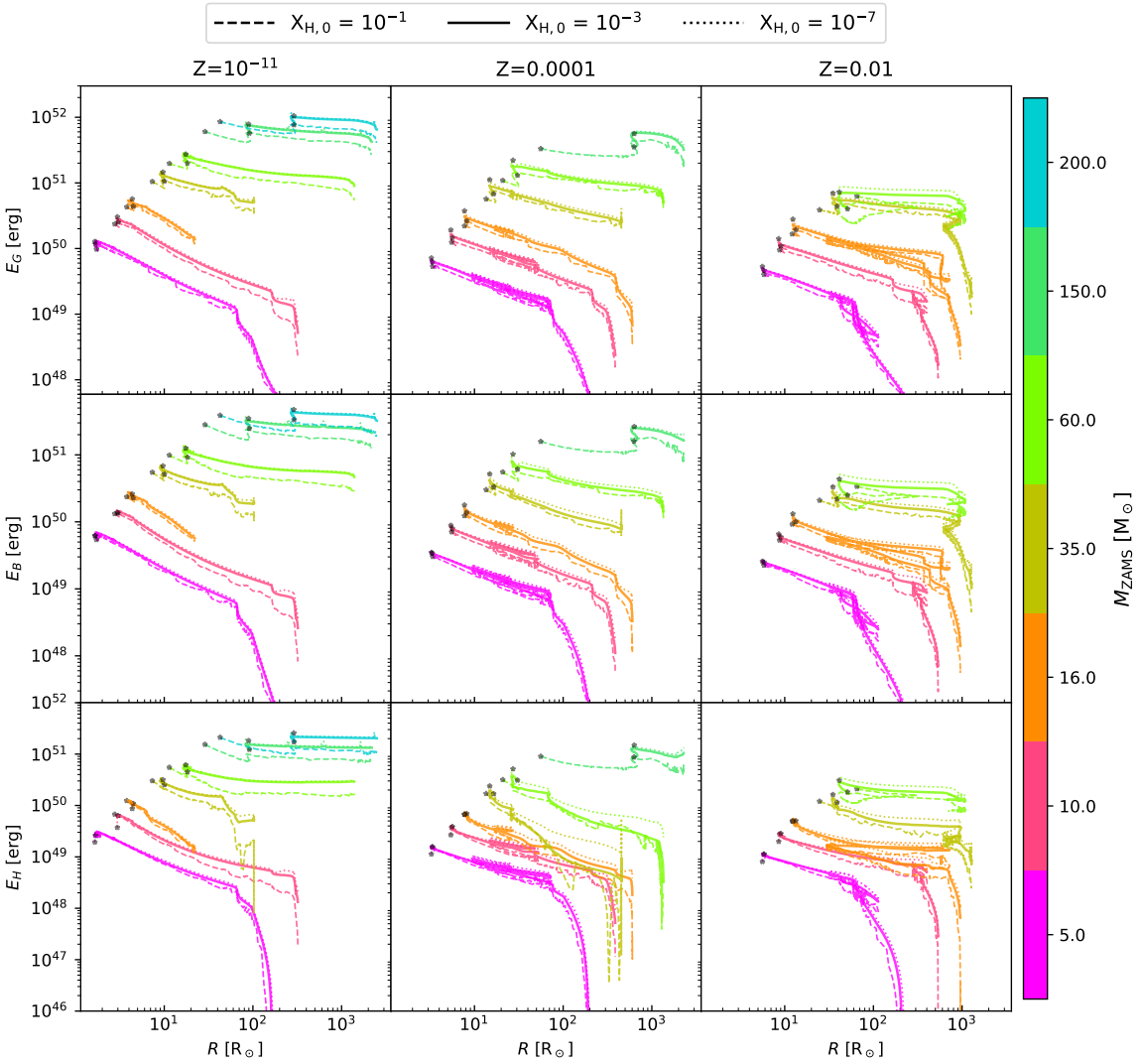


Fig. 5.1 Binding energy $E_{\rm bind}$ evaluated from PARSEC as a function of the radius R for different stellar masses. The rows from top to bottom show $E_{\rm G}$, $E_{\rm B}$ and $E_{\rm H}$, respectively. Different columns represent different metallicities, from left to right: $Z = 10^{-11}$, 0.0001, and 0.01. The black star markers indicate the formation of the He core. Different line styles show the results assuming different $X_{\rm H,0}$ thresholds to define the core-envelope boundaries: $X_{\rm H,0} = 10^{-1}$ dashed lines, $X_{\rm H,0} = 10^{-3}$ solid lines, and $X_{\rm H,0} = 10^{-7}$ dotted lines.

$X_{\rm H,0}$ models, for all the stars and metallicities. Notably, massive stars at low metallicities ($M_{\rm ZAMS} \geq 150{\rm M}_{\odot}$, $Z \leq 0.0001$) undergo significant radial expansion while the core is defined according to $X_{\rm H,0} = 10^{-1}$, but the core has not yet formed under alternative criteria. Such expansion exceeds one order of magnitude in the case of $M_{\rm ZAMS} = 150{\rm M}_{\odot}$, $Z = 0.0001$. This implies that if the star were to interact with a companion during this phase, the outcome could vary drastically depending on the adopted core definition. On the other hand, the

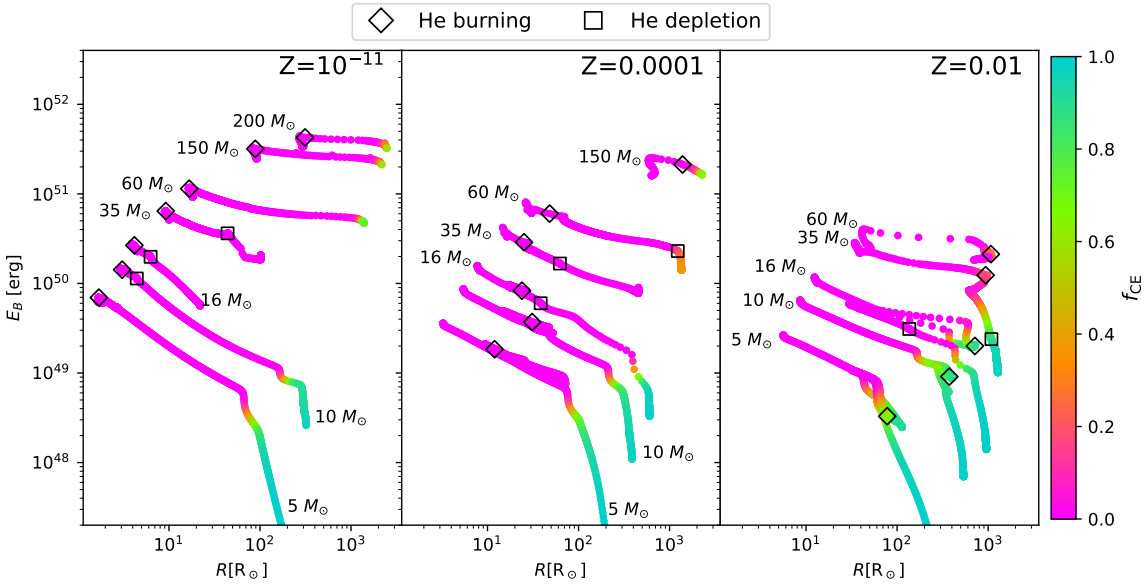


Fig. 5.2 Binding energies $E_{\rm B}$ evolution with radius for different stellar masses. The color code shows the mass fraction of the outer convective envelope $f_{\rm CE}$. Diamonds indicate the beginning of He burning; squares show the end of the core He burning phase. Different columns represent different metallicities, from left to right: $Z = 0.0001$, 0.001 and 0.01. Here, we assume $X_{\rm H,0} = 10^{-3}$.

model employing $X_{\rm H,0} = 10^{-1}$ displays higher fluctuations in the envelope binding energies, suggesting that the core is still growing because hydrogen burning is still ongoing.

The criteria used to define the core have minimal impact on the binding energies compared to the effect played by the various envelope binding energy definitions ($E_{\rm G}$, $E_{\rm B}$ and $E_{\rm H}$). Specifically, $E_{\rm G}$ consistently appears to be almost twice as large as $E_{\rm B}$. The difference between $E_{\rm H}$ and $E_{\rm G}$ is even more pronounced, with $E_{\rm H}$ being about one order of magnitude lower than $E_{\rm G}$. Nevertheless, $E_{\rm H}$ is more prone to instabilities (see e.g. $M_{\rm ZAMS} = 35\,{\rm M}_{\odot}$, $Z = 0.0001$). The reason for this is that the contribution from the enthalpy term progressively approaches the gravitational one as the stars reach the end of their lives. This leads to high fluctuations in $E_{\rm H}$, as the two terms converge. The effect is particularly evident for $X_{\rm H,0} = 10^{-1}$.

Figure 5.2 shows $E_{\rm B}$ as a function of R for several $M_{\rm ZAMS}$ and metallicities. The color scale indicates the fraction of envelope contained within the outer convective zone:

$$f_{\rm CE} = \frac{M_{\rm conv}}{M_{\rm env}} \tag{5.12}$$

where $M_{\rm conv}$ is the mass of the outermost contiguous convective zone of the envelope. We can compare figure 5.2 with Figure 1 in Klencki, Nelemans, Istrate, and Chruslinska (2021). Our models qualitatively agree with Klencki, Nelemans, Istrate, and Chruslinska (2021): we see a drop in the envelope binding energy as the envelopes become mostly convective ($f_{\rm CE} \geq 0.6$). As observed in Klencki, Nelemans, Istrate, and Chruslinska (2021), a deep convective layer does not necessarily mean lower binding energies. Indeed, the massive

stars $M_{\rm ZAMS} \geq 60\,{\rm M}_{\odot}$ at $Z = 10^{-11}$ and $M_{\rm ZAMS} = 150\,{\rm M}_{\odot}$ at $Z = 0.0001$, develop a deep convective envelope ($f_{\rm CE} \sim 0.6$), however, they do not show a drop in $E_{\rm B}$.

For massive stars ($M_{\rm ZAMS} \gtrsim 60\,{\rm M}_{\odot}$), the point of core He depletion occurs after the maximum radial expansion, therefore it does not appear in the plot. At $Z = 0.01$, this stage occurs when the star has already become a Wolf-Rayet, while at $Z \leq 0.0001$, He depletion takes place after the star has reached its maximum expansion radius.

5.3.2 Comparison with the literature

Figures 5.3, 5.4 and 5.5 show the envelope binding energies as a function of time, computed with different prescriptions. Among the models (different colors), we observe differences exceeding an order of magnitude. Such differences dominate over variations arising from distinct core-envelope boundary conditions, independently of the metallicity and stellar mass.

The model proposed by Claeys et al. (2014) consistently underestimates the PARSEC envelope binding energies by more than an order of magnitude as stars approach the giant phase. This is particularly evident at higher metallicities, where the discrepancy can be as high as 3 orders of magnitude (e.g. $M_{\rm ZAMS} = 60\,{\rm M}_{\odot}$). Our binding energies are instead in broad agreement with the model by Klencki, Nelemans, Istrate, and Chruslinska (2021), obtained with MESA. However, extrapolating the model by Klencki, Nelemans, Istrate, and Chruslinska (2021) outside of the original parameter space ($M_{\rm ZAMS} \leq 80\,{\rm M}_{\odot}$, $Z \leq 0.0001$) leads to large discrepancies with our computed values. This is particularly evident for the star with $Z = 10^{-11}$ and $M_{\rm ZAMS} = 100\,{\rm M}_{\odot}$. On the other hand, the prescription by Xu and Li (2010), based on stars with masses between 1 and $100\,{\rm M}_{\odot}$ at $Z = 0.001$ and 0.02, significantly deviates from our model, even considering the same range of stars. These substantial divergences highlight the importance of using envelope binding energies that are consistent with the underlying stellar evolution code.

The adoption of different $X_{\rm H,0}$ affects the core formation times, thus making the duration of the Hertzsprung-gap phase shorter (i.e., $X_{\rm H,0} = 10^{-1}$) or longer (i.e., $X_{\rm H,0} = 10^{-7}$). This effect is likely negligible in binary evolution. In fact, in most cases the stars do not undergo significant radial expansion during the period when the $X_{\rm H,0} = 10^{-1}$ model already has formed an He core, while the $X_{\rm H,0} = 10^{-3}$ one has not. We note that the envelope binding energies computed in Klencki, Nelemans, Istrate, and Chruslinska (2021) assume $X_{\rm H,0} = 10^{-1}$, implying that these stars should form the core simultaneously with our dashed line. However, when this prescription is applied in SEVN with the PARSEC evolutionary tracks, the core forms instead according to the condition $X_{\rm H,0} = 10^{-3}$. As a result, the starting point of the model from Klencki, Nelemans, Istrate, and Chruslinska (2021) coincides with the $X_{\rm H,0} = 10^{-3}$ model, in the plot.

5.3.3 Pure-He stars

Figure 5.6 shows $E_{\rm G}$, $E_{\rm B}$ and $E_{\rm H}$ computed for pure-He tracks with different initial stellar masses and metallicities. For pure-He tracks we show the reference metallicities $Z = 0.0001$, 0.001 and 0.01.

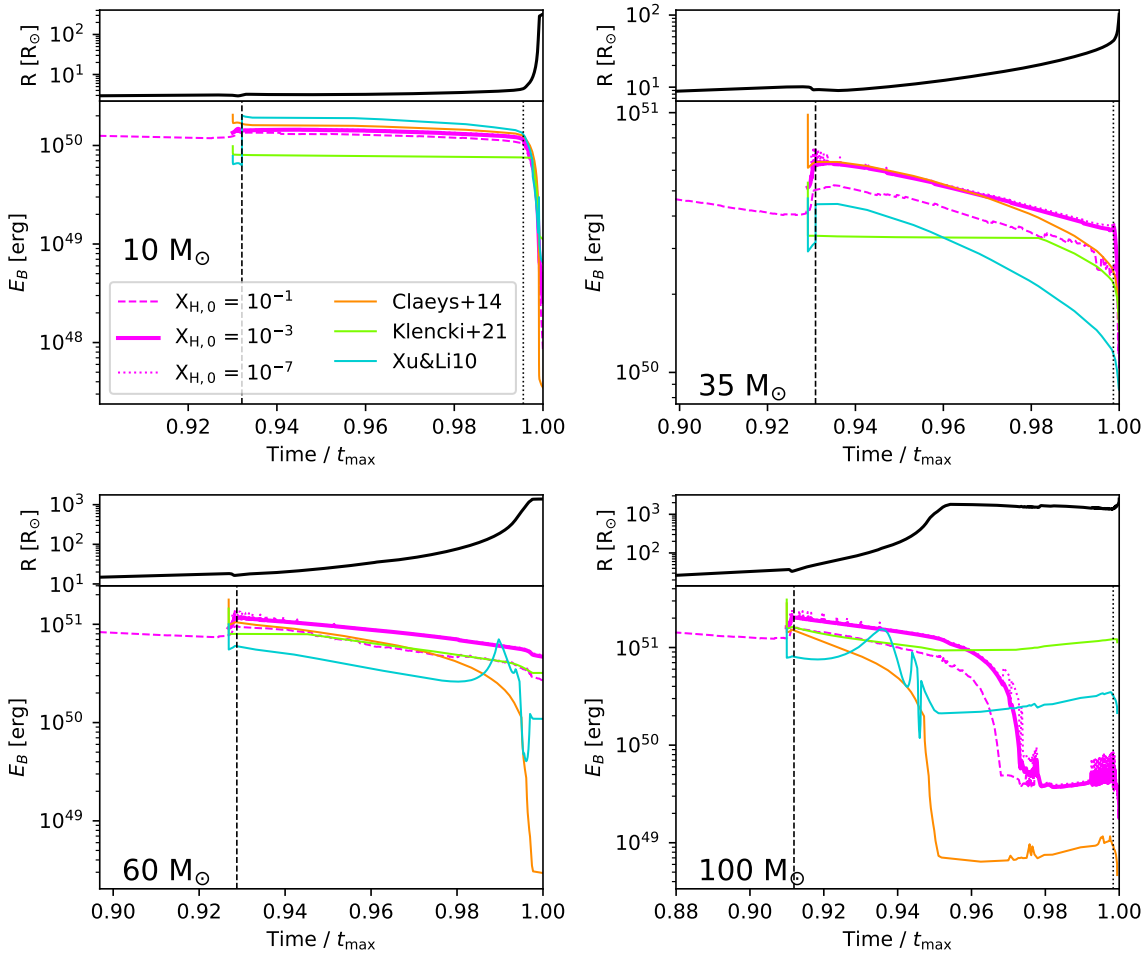


Fig. 5.3 Evolution of the envelope binding energy for a sample of stars with $M_{ZAMS} = 10$ M$_\odot$ (top left), 35 M$_\odot$ (top right), 60 M$_\odot$ (bottom left) and 100 M$_\odot$ (bottom right). All the stars have metallicity $Z = 10^{-11}$. The x-axis indicates the time passed since the stellar formation, normalized by the maximum time. The pink lines show the envelope binding energies E_B computed in this work, for different $X_{H,0}$ thresholds (different linestyles): solid, $X_{H,0} = 10^{-3}$; dashed, $X_{H,0} = 10^{-1}$; dotted, $X_{H,0} = 10^{-7}$. The other colors show different envelope binding energies adapting different λ prescriptions to the PARSEC stellar tracks with SEVN: orange solid line assuming Claeys et al. (2014), green solid line Klencki, Nelemans, Istrate, and Chruslinska (2021), blue solid line Xu and Li (2010). Notice that the lines start in different moments in time for the same stars due to the different core formation conditions, however, for visualization purposes we do not show the full evolution of the $X_{H,0} = 10^{-1}$ model, as it extends well before the other conditions but the star does not evolve much in the meanwhile. The upper panels of each plot show the corresponding evolution of the radii of the stars. The vertical dashed and dotted lines indicate the onset of core-He burning and shell-He burning, respectively.

Pure-He stars remain significantly more compact throughout their lifetimes compared to H-rich stars. As a result, also their envelope binding energies span a much narrower range. Moreover, for a given initial mass, the evolutionary tracks are similar across various

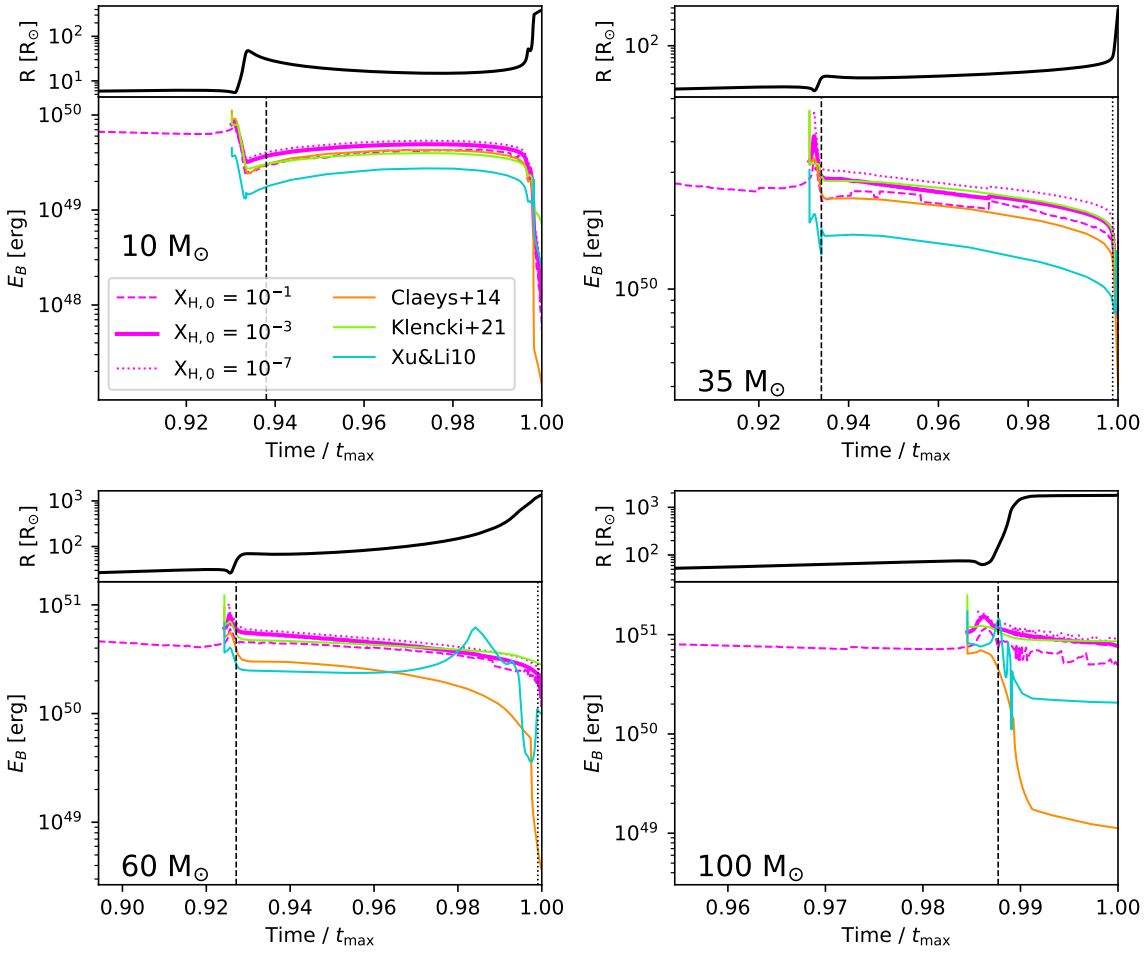


Fig. 5.4 Same as Figure 5.3, but for metallicity $Z = 0.0001$.

metallicities. For a wide mass range ($M_{\rm He} < 1\,{\rm M}_\odot$, $10 < M_{\rm He} < 200\,{\rm M}_\odot$), these stars tend to shrink during most of their lives, thus reducing the likelihood of binary interactions.

Unlike H-rich stars, where the binding energies are significantly affected by the considered energy contributions, pure-He stars show much smaller variations. Typically, $E_{\rm G}$ and $E_{\rm H}$ do not differ by more than a factor of two. However, the core-envelope boundary has a substantial impact, especially for high-mass stars ($M_{\rm He} \geq 30\,{\rm M}_\odot$).

We also compare our new $E_{\rm bind}$ with two additional models. We show the prescription by Claeys et al. (2014), which assumes a constant $\lambda = 0.5$ for pure-He stars (thick solid lines). This is the default value adopted in SEVN when using the models by Claeys et al. (2014) and Klencki, Nelemans, Istrate, and Chruslinska (2021). We also display the fit implemented in COMPAS (thick dotted lines, Riley, Agrawal, et al., 2022):

$$\lambda = 0.3 R_\lambda^{-0.8} \qquad R_\lambda = \min(120, \max(0.25, R)), \tag{5.13}$$

where all quantities are in solar units. SEVN adopts this fit with the Xu and Li (2010) prescription (see Appendix A1.4 in Iorio et al., 2023, for more details).

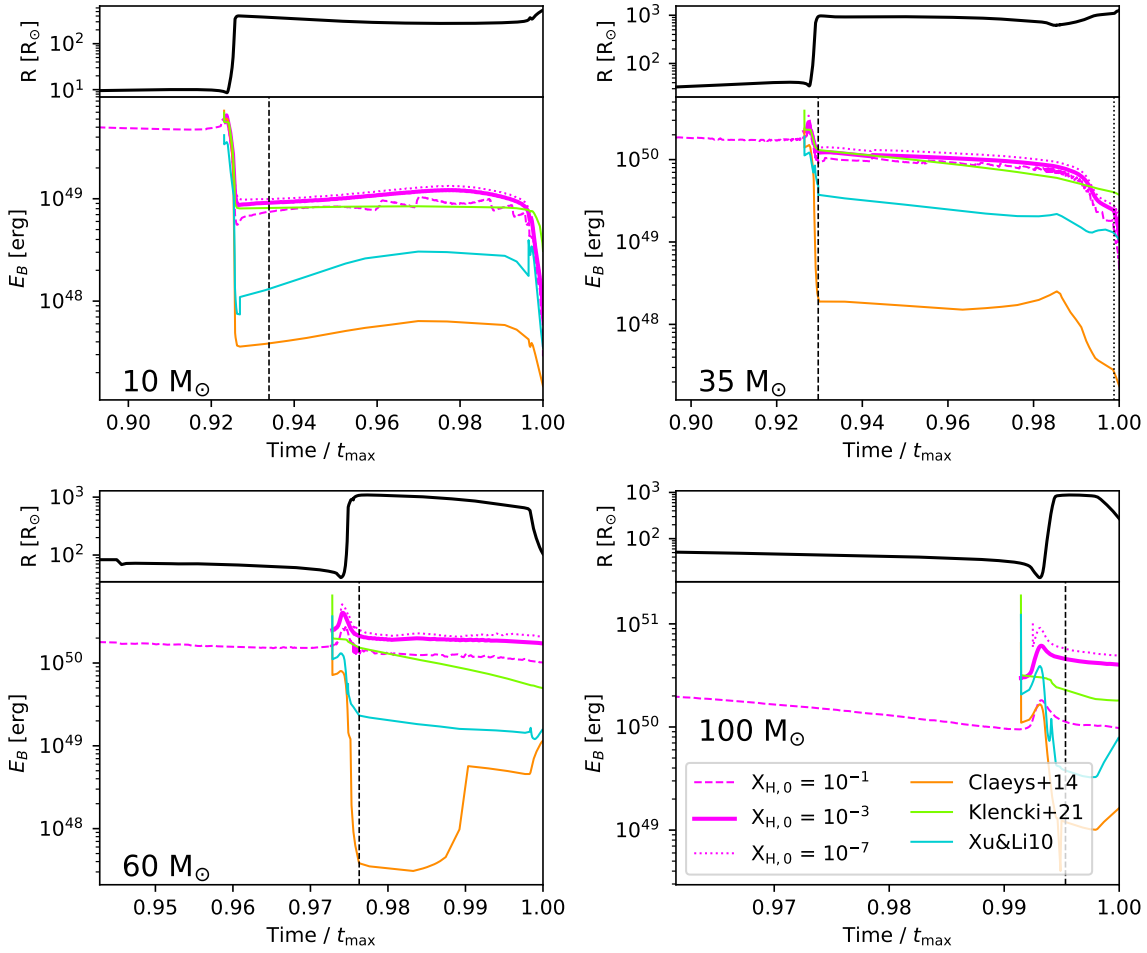


Fig. 5.5 Same as Figure 5.3, but for metallicity $Z = 0.01$.

The $\lambda = 0.5$ model deviates substantially from the PARSEC results. This is evident for low-mass stars ($M_{\rm He} \leq 5, \mathrm{M}_{\odot}$), where discrepancies exceed an order of magnitude toward the end of stellar evolution. On the other hand, the envelope binding energies obtained with Eq. 5.13 are in much better agreement with the $E_{\rm bind}$ by PARSEC. Especially when considering stars with $M_{\rm He} \lesssim 30\,\mathrm{M}_{\odot}$ and the $E_{\rm B}$ model.

5.3.4 Merger rate density

We estimate the merger rate density of binary compact objects following the methodology outlined in Section 5.2.5. Figure 5.8 shows the resulting merger rate densities for BBHs (left), BHNS (middle) and BNSs (right) with our new consistent envelope binding energies (solid lines). We compare the results obtained with PARSEC with the models by Claeys et al. (2014) (dashed lines) and Klencki, Nelemans, Istrate, and Chruslinska (2021) (dotted lines). The merger rates' differences between our new formalism (solid lines) and Claeys et al. (2014) (dashed lines), are as high as a factor of two for many of the models. The effect of the new

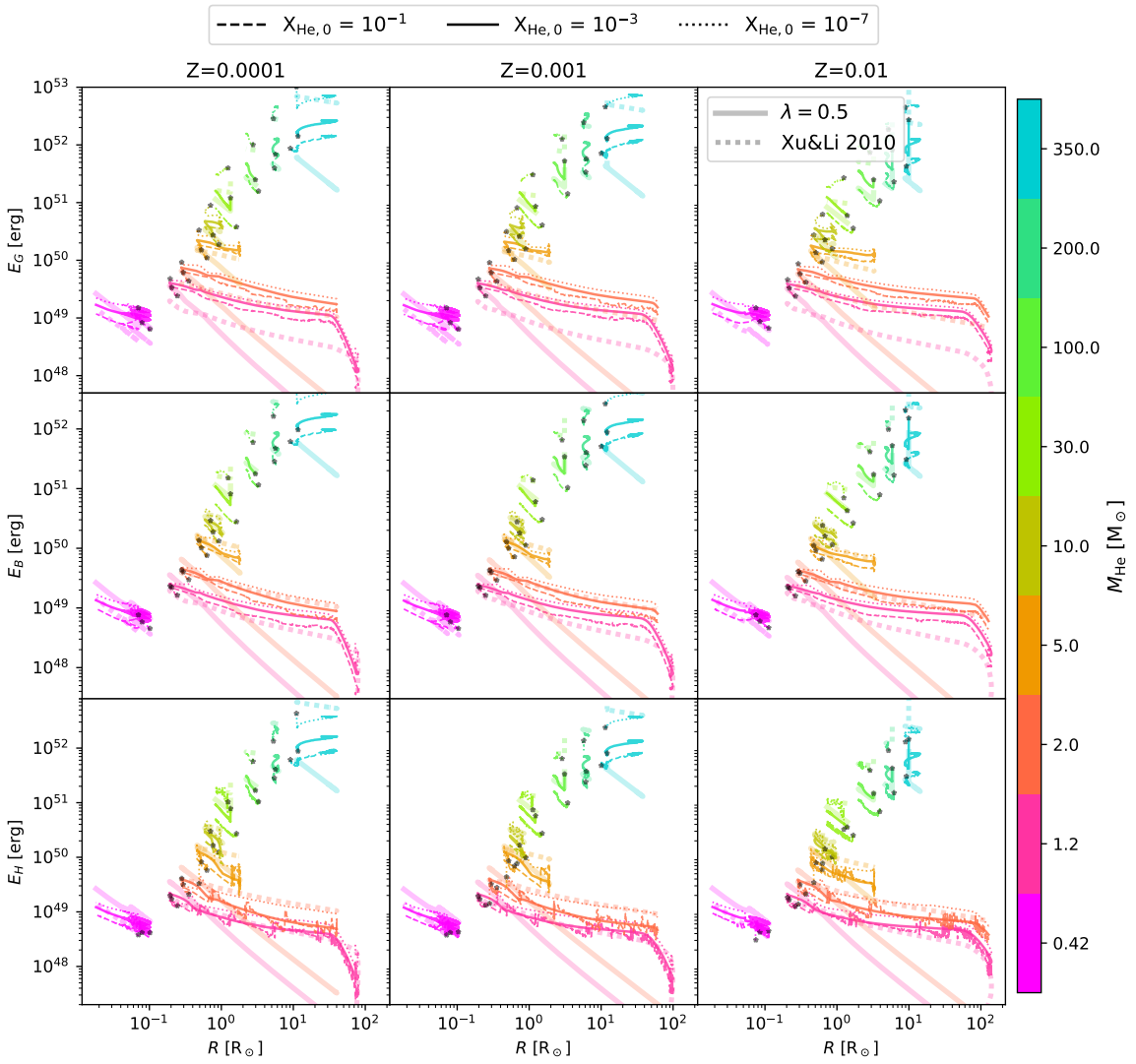


Fig. 5.6 Same as Figure 5.1 but with pure-He tracks. The thick solid lines show the envelope binding energies with constant $\lambda = 0.5$, following Claeys et al. (2014). This is the default value adopted in SEVN for the prescriptions by Claeys et al. (2014) and Klencki, Nelemans, Istrate, and Chruslinska (2021). The thick dotted lines show the envelope binding energies as implemented in COMPAS. This model is used by SEVN with the prescription by Xu and Li (2010).

$E_{\rm bind}$ is to boost the merger rate densities of BBH and BHNS systems for $\alpha \gtrsim 1$. Conversely, the new $E_{\rm bind}$ lead to a suppression in the BNS merger rate densities, with a more apparent effect for $\alpha \leq 1$.

The merger rate densities agree well with the model by Klencki, Nelemans, Istrate, and Chruslinska (2021) (dotted lines). This was expected, given the similarities among the two $E_{\rm bind}$ prescriptions.

Differences in the BBH merger rate densities are primarily driven by variations of the merger efficiency's dependence on metallicity, illustrated in Figure 5.7. For $\alpha = 3, 5$ the

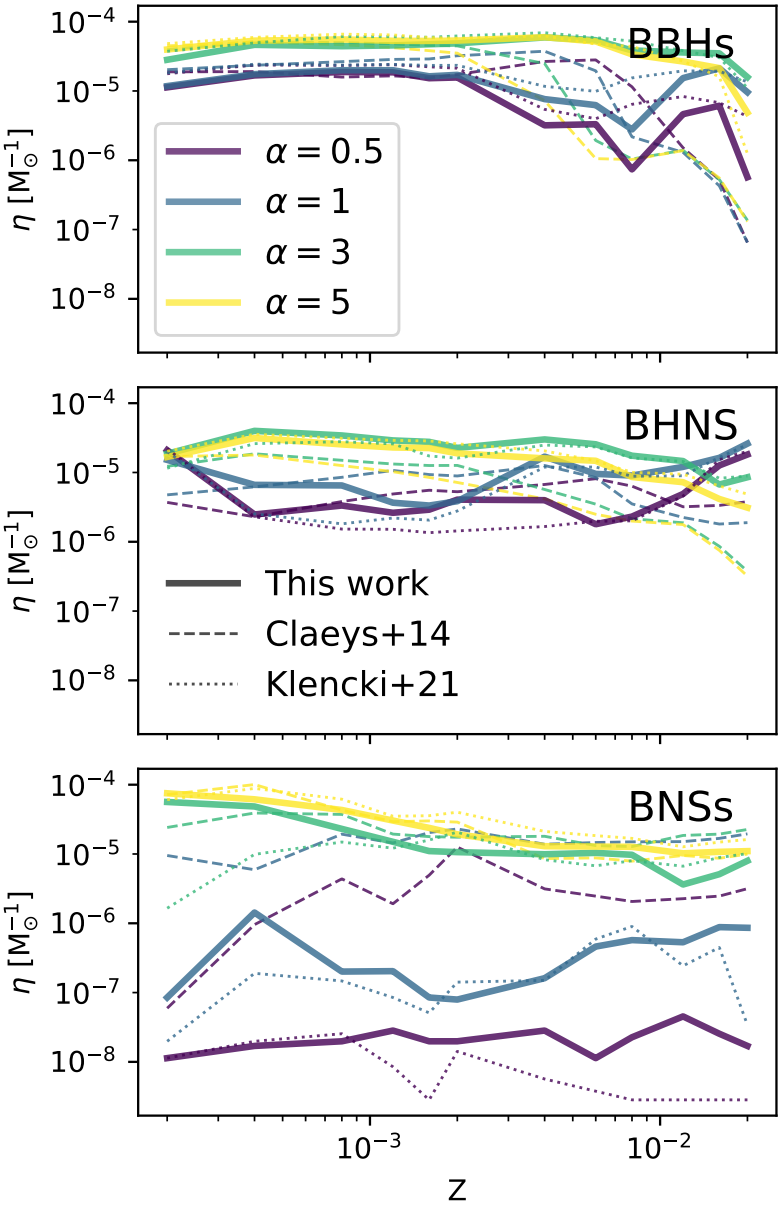


Fig. 5.7 Merger efficiency η for BBHs (top), BHNS(middle) and BNSs (bottom) as a function of metallicity Z. The solid lines represent the results assuming the PARSEC envelope binding energies. The other linestyles assume different λ prescriptions: dashed lines for Claeys et al. (2014), dotted lines for Klencki, Nelemans, Istrate, and Chruslinska (2021). The different colors show results for different α parameters: $\alpha = 0.5$ (purple), 1 (blue), 3 (green) and 5 (yellow).

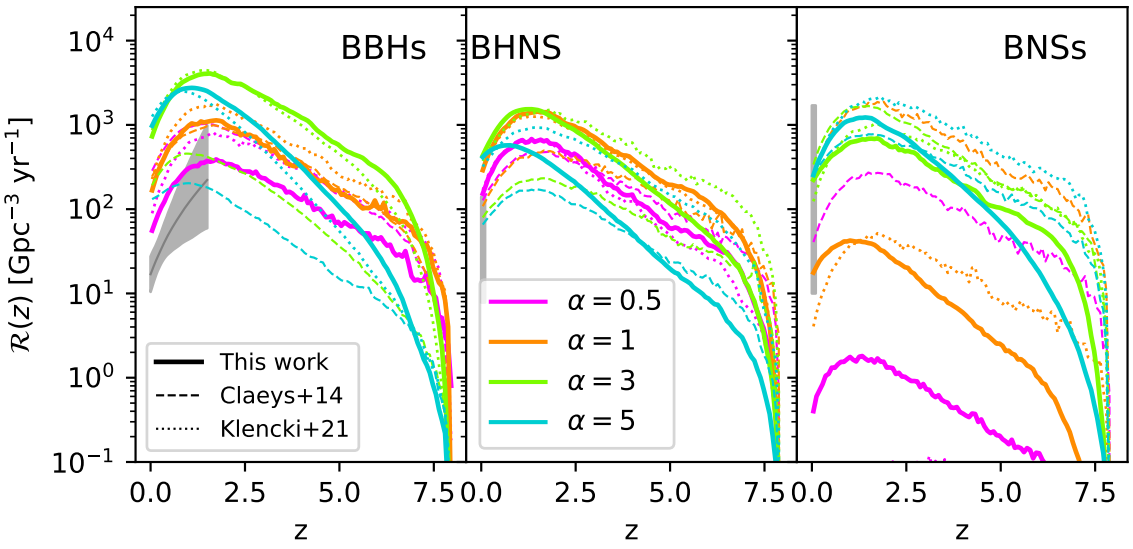


Fig. 5.8 Merger rate density of BBHs (left), BHNS (center) and BNSs (right) for different λ prescriptions and α parameters. The solid lines show the results adopting the λ self-consistent with the PARSEC tracks. The dashed lines assume the λ prescription by Claeys et al. (2014), the dotted lines assume the prescription by Klencki, Nelemans, Istrate, and Chruslinska (2021). The different colors show the different α parameters: pink $\alpha = 0.5$, orange $\alpha = 1$, green $\alpha = 3$ and blue $\alpha = 5$. The grey shaded area shows the merger rate densities inferred by LVK.

envelope binding energies by Claeys et al. (2014) predict a drop in the BBH merger efficiency for $Z \sim 5 \times 10^{-3}$. In contrast, with the PARSEC envelope binding energies, the merger efficiency stays constant up to $Z \sim 10^{-2}$. The latter trend is very similar to the model by Klencki, Nelemans, Istrate, and Chruslinska (2021), where, as showed in Iorio et al. (2023), the drop occurs only for $Z \gtrsim 10^{-2}$. Since higher metallicities play a major role in the cosmic star formation history (Sgalletta, Mapelli, et al., 2025), both the PARSEC and the Klencki, Nelemans, Istrate, and Chruslinska (2021) $E_{\rm bind}$ predict a boost in the BBH merger rate density. On the other hand, for $\alpha < 1$ the BBH merger efficiency is lower than that predicted by the Claeys et al. (2014) model, considering metallicities $2 \times 10^{-3} \lesssim Z \lesssim 10^{-2}$. Similarly, the merger rate density of BNSs for $\alpha = 0.5{,}1$ is significantly suppressed as a consequence of lower merger efficiencies.

The envelope binding energies by Claeys et al. (2014) are consistently lower than those predicted by PARSEC. Higher binding energies have two primary effects: making the shrinkage during CE more efficient, thus leading to lower post-CE separations, and increasing the occurrence of failed CE ejections. For BBH systems at high metallicities (i.e. $Z = 0.02$), the former effect dominates. While most BBHs remain wider in Claeys et al. (2014), the new envelope binding energies facilitate orbital shrinkage. This leads to a substantial population of systems being able to merge within a Hubble time. Conversely, for BNSs systems and low α parameters, failed CE ejections constitute the dominant effect.

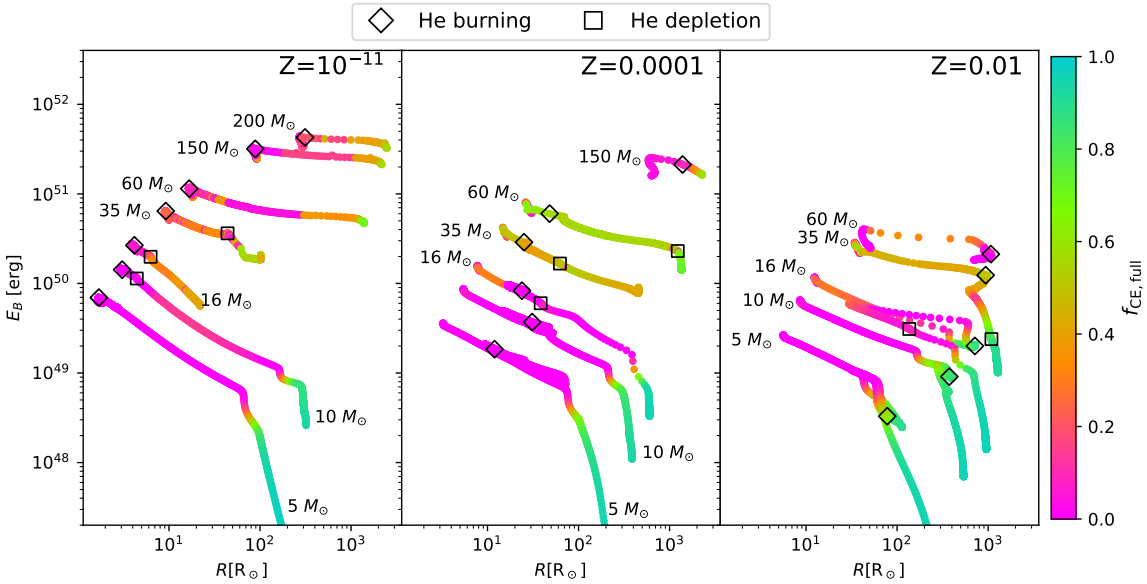


Fig. 5.9 Same as Figure 5.2, but colored by $f_{\mathrm{CE,full}}$, the fraction of the total convective envelope mass over the envelope mass.

5.4 Discussion

Sgalletta, Mapelli, et al. (2025) pointed out that current binary population synthesis codes tend to predict higher BBH merger rate densities compared to inferred rates from the LVK collaboration (Abbott et al., 2023a). The formalism presented here makes this discrepancy even bigger, pushing the BBH and BHNS merger rates even higher. In order to match the observed gravitational wave rates, we might therefore favor models with $\alpha \leq 1$. On the other hand, the models with $\alpha \leq 1$ produce BNS merger rates which are lower than the observed ones for BNSs (Abbott et al., 2023a). A possible solution would be a varying α parameter, depending on the properties of the stars within the CE phase. Studies on double white dwarf systems have already highlighted the possibility of α being a function of the masses of the white dwarfs, as demonstrated by Ivanova, Justham, Nandez, et al. (2013) and Röpke et al. (2023). Similarly, Chruslinska, Belczynski, et al. (2018) proposed different CE ejection mechanisms for BNSs and BBHs to explain their merger rates. Our results support the scenario of a varying α parameter for massive progenitor stars. Furthermore, the recently developed two-stage formalism for CE (Hirai et al., 2022) find evidence for a broad range of α parameters, opposed to a universal value (Picker et al., 2024).

Nevertheless, several caveats remain. Our analysis is based purely on single stellar evolutionary tracks. A detailed response of stars to mass transfer and mass accretion could be crucial in understanding the final fate of these systems. In fact, recent studies suggest that the CE channel might occur less frequently than currently assumed in population synthesis codes (e.g., Ge, Webbink, et al., 2020; Gallegos-Garcia, Berry, et al., 2021; Marchant, Pappas, et al., 2021; van Son, de Mink, Callister, et al., 2022).

A final comment regards the role played by convection in affecting the fate of mass transfer events (Klencki, Nelemans, Istrate, and Chruslinska, 2021; Hirai et al., 2022). Figure 5.9 is the same as 5.2, but the colors show:

$$f_{\rm CE,full} = \frac{M_{\rm conv,full}}{M_{\rm env}}, \tag{5.14}$$

where $M_{\rm conv,full}$ is the total mass of convective envelope, accounting both for the outer convective zone as well as for inner convective zones within the stars envelopes. Compared to Figure 5.2, we observe that stars (especially those with masses ≥ 30 M$_\odot$) develop internal convective regions even before these zones reach the surface of the star. In these cases, the response of the star is unclear. There may be episodes in which the radiative layers are stripped away and the response of the star becomes the same of a convective star. A model that considers only the outer convective layers fails to capture this complexity.

5.5 Summary

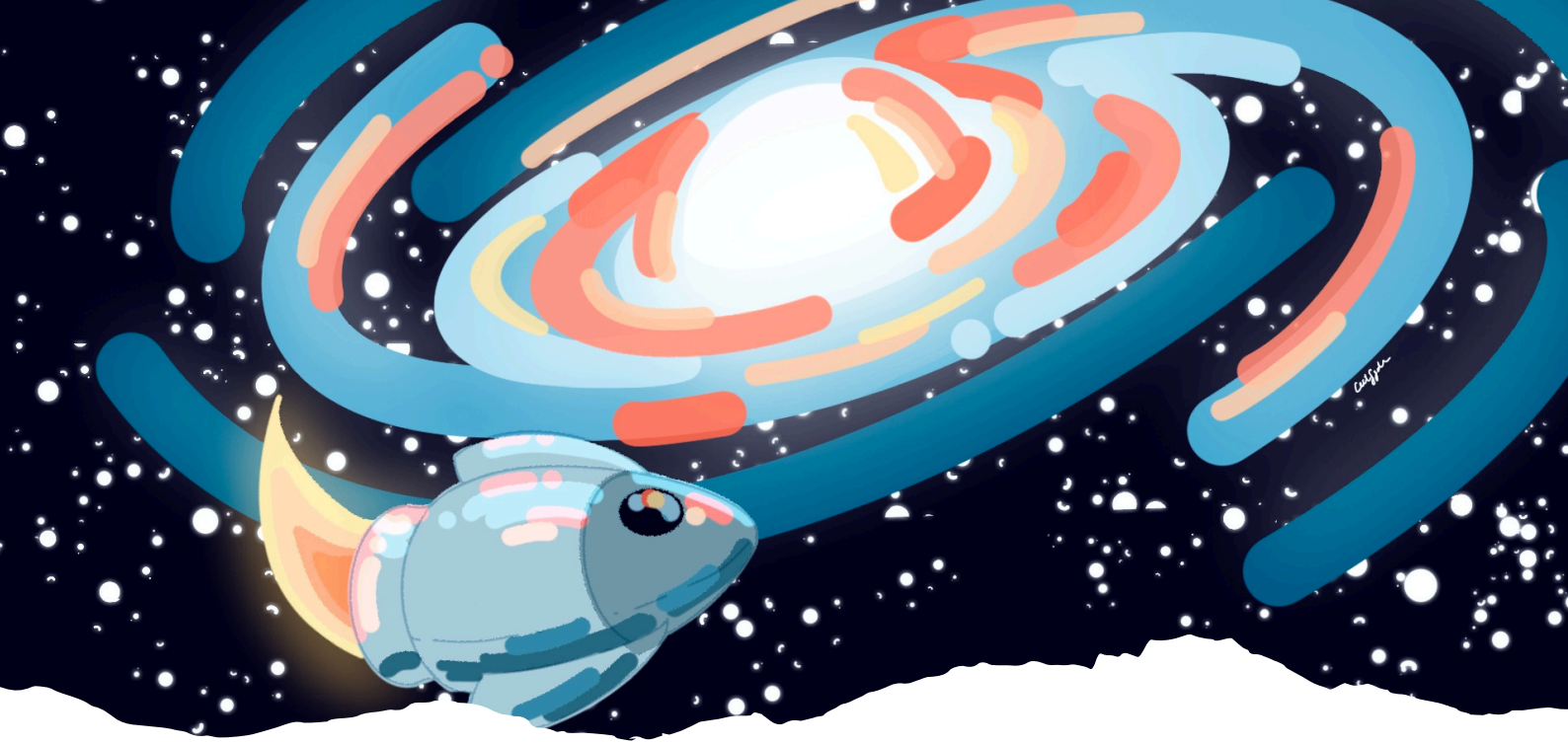
We have derived the envelope binding energies for an extensive set of stars both in terms of masses and metallicities beyond the current state-of-the-art, evolved with the PARSEC code. We have investigated different energy contributions to the envelope binding energy as well as alternative core-boundary criteria. Additionally, we studied how different prescriptions influence the predicted merger rate densities of compact object systems. We summarize the main findings of our work below.

- In the case of H-rich stars, varying the $X_{\rm H,0}$ thresholds affect the envelope binding energies by no more than a factor of ~ 2 in most cases. However, the choice of which energy components to include has a more significant impact, with $E_{\rm H}$ being roughly an order of magnitude smaller than $E_{\rm G}$. Conversely, for pure-He stars, the choice of $X_{\rm He,0}$ has a greater influence on the envelope binding energy than the selected energy contributions.

- The $X_{\rm H,0} = 10^{-1}$ model wildly depends on the relative size of core and envelope, due to ongoing H nuclear burning at the boundaries. In contrast, upon core formation according to the $X_{\rm H,0} = 10^{-3}$ criterion, the resulting H concentration profile is sufficiently steep to show almost no difference from the $X_{\rm H,0} = 10^{-7}$ model.

- The inconsistencies among various envelope binding energy prescriptions, each evaluated with different stellar evolution codes, emphasize the need to adopt binding energies that are consistent with the specific stellar models being used. Additionally, it is crucial to avoid extrapolating these prescriptions beyond the parameter space for which they were originally inferred.

- Differences in envelope binding energy prescriptions directly translate into discrepancies in the predicted merger rate densities, with disparities exceeding an order of magnitude, in agreement with the results in Iorio et al. (2023).



Chapter 6

Conclusions and future directions

In my thesis I focused on some of the main uncertainties in the formation of BCOs through the isolated evolution channel, addressing these from different perspectives. First, I studied the Galactic pulsar population in BNS systems (Chapter 3). Second, I investigated the BBH merger rate density across cosmic time, focusing on the role of the metal-dependent SFR history (Chapter 4). Finally, I addressed one of the most problematic phases in binary stellar evolution: the common envelope. I improved the formalism implemented in SEVN by integrating the envelope binding energies directly from the PARSEC stellar tracks (Chapter 5).

6.1 Galactic binary neutron star populations

Chapter 3 focused on the population of Galactic BNSs. In this work, we investigated key open questions in pulsar evolution, including the birth distributions of spin periods and magnetic fields, as well as the magnetic field evolution. We also explored the effects of the CE phase and SN natal kicks on the BNS population. To this end, we modeled the magnetic field and spin period evolution of pulsars in SEVN, accounting both for spin-down and spin-up during RLO episodes. We coupled the BNSs catalogs generated in this way, with a MW model, testing both empirical prescriptions and cosmological simulations models. Finally,

we tested the results for different parameter combinations against the observed Galactic BNS population.

We found that the birth distributions of spin periods and magnetic fields have the most impact on the present-day distribution of pulsars. Moreover, the CE efficiency α affects the BNSs merger rates of up to one order of magnitude. Additionally, our fiducial model predicts to triplicate the number of observed pulsars in BNS systems, with the advent of SKA.

Overall, this study provides a self-consistent framework that reconciles pulsar observations, orbital properties of known BNSs, and their observed merger rate. Upcoming generations of radio and GW detectors are expected to significantly increase the number of BNS detections, both as electromagnetic and GW sources, enabling tighter constraints on joint analysis such as the one presented in this work.

6.2 Binary black hole merger rate

Due to the strong dependence of BBH merger efficiency on metallicity, the metal-dependent SFR holds a key role in shaping the cosmic BBH merger rate density. In Chapter 4, we employed state-of-the-art, data-driven relations to model the metallicity-dependent SFR and systematically explored the main sources of uncertainty to quantify their impact on the BBH merger rate density.

What emerged, is that incorporating detailed SFR models leads to predicted BBH merger rate densities that exceed the current observed rate by LVK (Abbott et al., 2023a). This tension is solid against uncertainties in the low-mass end of the metal-dependent SFR. In particular, the contribution from low-mass galaxies ($M_\star \leq 10^8, \mathrm{M}_\odot$), characterized by the lowest metallicities, modifies the predicted BBH merger rate density by no more than a factor of ~ 2. These results, suggest that the primary source of the discrepancy lies in uncertainties related to binary stellar evolution physics. For instance, mass transfer may not yet be appropriately modelled in current population synthesis codes.

This work clearly identifies the dominant sources of uncertainty in BBH formation, disentangling the effects of the metal-dependent SFR from those arising from binary evolution physics.

6.3 Envelope binding energies revisited

Finally, Chapter 5 presents the implementation of updated envelope binding energy prescriptions in SEVN, computed directly from the PARSEC stellar tracks. This work emphasizes the importance of adopting a consistent treatment of the envelope binding energies, rather than extrapolating them from pre-computed stellar fits.

We investigated the effects of different core-envelope boundary conditions. The results show that the choice between $X_{\mathrm{H},0} = 10^{-3}$ and $X_{\mathrm{H},0} = 10^{-7}$ leads to minimal differences, due to the steep H profile in the stellar interior. Conversely, adopting a boundary at $X_{\mathrm{H},0} = 10^{-1}$ produces cores that are still growing, suggesting that nuclear burning is still active at the core-envelope boundary.

We also explored the effects of the updated envelope binding energies on the merger rate densities of BCOs. The merger rates densities can vary by more than an order of magnitude assuming different λ prescriptions. In particular, consistent envelope binding energies lead to an enhancement of the BBH and BHNS merger rate densities for $\alpha \gtrsim 1$, as compared to the model by Claeys et al. (2014). On the other hand, the BNS merger rates are consistent with Claeys et al. (2014) model for $\alpha \geq 1$ parameters, while they are significantly suppressed for $\alpha < 1$. In general, the merger rate densities are similar to those obtained assuming the model by Klencki, Nelemans, Istrate, and Chruslinska (2021), as expected given the affinity in the predicted binding energies of the two approaches. In general, the results highlight the sensitivity of merger rate predictions to assumptions made during the CE phase and underline the need for self-consistent envelope binding energies modeling in population synthesis studies.

6.4 Future prospects

This thesis addresses several major challenges in the modeling of binary stellar evolution. However, an exhaustive and satisfactory understanding of the processes at play is still far from reach, and much work remains to be done in this area. In this section, I outline possible future developments and improvements that build on the work presented in this thesis.

6.4.1 Pulsars' formation in dense environments

Thus far, my work has focused exclusively on the isolated binary evolution channel. Nevertheless, already ~ 345 pulsars have been discovered in globular clusters (see the list at https://www3.mpifr-bonn.mpg.de/staff/pfreire/GCpsr.html for a complete catalogue). Notably, a vast majority of them are millisecond pulsars. The properties of isolated pulsars and those in dense environments greatly differ from one another. First off, globular clusters contain a greater fraction of single pulsars. Moreover, the pulsars in binaries are characterized by shorter orbital periods, on average (Camilo and Rasio, 2005). Hence, dynamical interactions are likely decisive for pulsars in dense environments, with formation channels that can be substantially different from those in the Galactic field. Indeed, star clusters host systems where a pulsar can be spun up by accretion from a low-mass companion, and interactions within the cluster can later disrupt the binary, resulting in single millisecond pulsars.

Extending the framework developed in Sgalletta, Iorio, et al. (2023) to the formation of pulsars in dense environments would be instructive towards a comprehensive modeling of the population. To this end, globular clusters like Terzan 5 or 47 Tucanae, each counting $\gtrsim 40$ pulsars (Lyne, Manchester, et al., 1990; Lyne, Mankelow, et al., 2000; Manchester, Lyne, D'Amico, et al., 1990; Manchester, Lyne, Robinson, et al., 1991; Robinson et al., 1995; Camilo, Lorimer, et al., 2000; Freire et al., 2001; Ransom et al., 2005; Hessels et al., 2006; Pan et al., 2016; Cadelano et al., 2018; Andersen et al., 2018; Ridolfi et al., 2021; Bogdanov, Bahramian, et al., 2021; Padmanabh et al., 2024, MeerKAT, TRAPUM project), provide the perfect setting. The rigorous comparison methodology introduced in Sgalletta, Iorio, et al. (2023), can then be used to match the results of the simulations with observations. By doing

so, it would be possible to explore the role of mass transfer and spin-up. The results would supply a complementary view on the pulsar populations as that offered by Galactic BNSs.

Additionally, NSs velocities in the Galactic field ($\sigma = 265\,\mathrm{km\,s^{-1}}$) exceed typical escape velocities of globular clusters. Therefore, many newly born NSs can escape the cluster. A joint analysis of young pulsars in globular clusters and those in the Galactic field can provide useful clues on the magnitude of the natal kicks themselves and the expected number of runaway pulsars, originally residing in stellar clusters.

6.4.2 Neutron star masses

The SN models by Fryer et al. (2012), commonly adopted in population synthesis codes, struggle to reproduce the observed Galactic NS masses (see Appendix A.2). For this reason, in Sgalletta, Iorio, et al. (2023) we modeled the NS masses with a simple gaussian built to fit the Galactic NS properties (Özel, Psaltis, Narayan, and Santos Villarreal, 2012; Kiziltan et al., 2013). However, this approach is suboptimal, as it cancels any relation between the remnant and its pre-SN properties.

Woosley, Sukhbold, et al. (2020) propose a novel set of grids, linking the pre-SN mass to the final remnant mass, for He stars. In particular, using the framework described in Ertl et al. (2020), they compute the remnant mass for stars that have been stripped of their H envelopes. This assumption is made to better resemble the stars evolved in close binary systems at the onset of SN. Notably, according to Woosley, Sukhbold, et al. (2020), the model predicts median NSs masses in the range $1.32 - 1.37\,\mathrm{M_\odot}$. Therefore, the model already suggests a much better agreement with the Galactic NSs masses.

Figure 6.1 shows the compact remnant masses as a function of the ZAMS masses, as predicted by the model by Woosley, Sukhbold, et al. (2020). Interestingly, the model predicts the formation of NSs even for stars with initial masses up to $M_{\mathrm{ZAMS}} \sim 50\,\mathrm{M_\odot}$. Moreover, the model predicts compact objects in the lower-mass gap ($2.5\,\mathrm{M_\odot} \lesssim M_{\mathrm{rem}} \leq 5\,\mathrm{M_\odot}$, gray hatched area). Finally, massive NSs ($M_{\mathrm{rem}} \gtrsim 2\,\mathrm{M_\odot}$) are produced according to this model. Extending this prescription to a population level is crucial. First, to determine its accord with the Galactic NSs masses. Second, to assess its impact on the overall demography, exploring the predictions on the low-mass gap and studying the role and incidence of massive NSs.

6.4.3 Why is the BBH merger rate density so high?

In Sgalletta, Mapelli, et al. (2025) we highlighted the tension in the merger rate density of BBHs between population synthesis predictions and GW observations. We showed that this difference is more likely to be attributed to uncertainties in binary stellar evolution physics, rather than in the metal-dependent SFR. Adding to the complexity, the predicted BBH merger rate densities vary by more than three orders of magnitude for different model assumptions and binary population synthesis codes (Mandel et al., 2022), reflecting major uncertainties in our understanding of massive binary evolution.

For this reason, while in Sgalletta, Mapelli, et al. (2025) we addressed this problem by studying the role of the metal-dependent SFR, it will be important to focus on the underlying

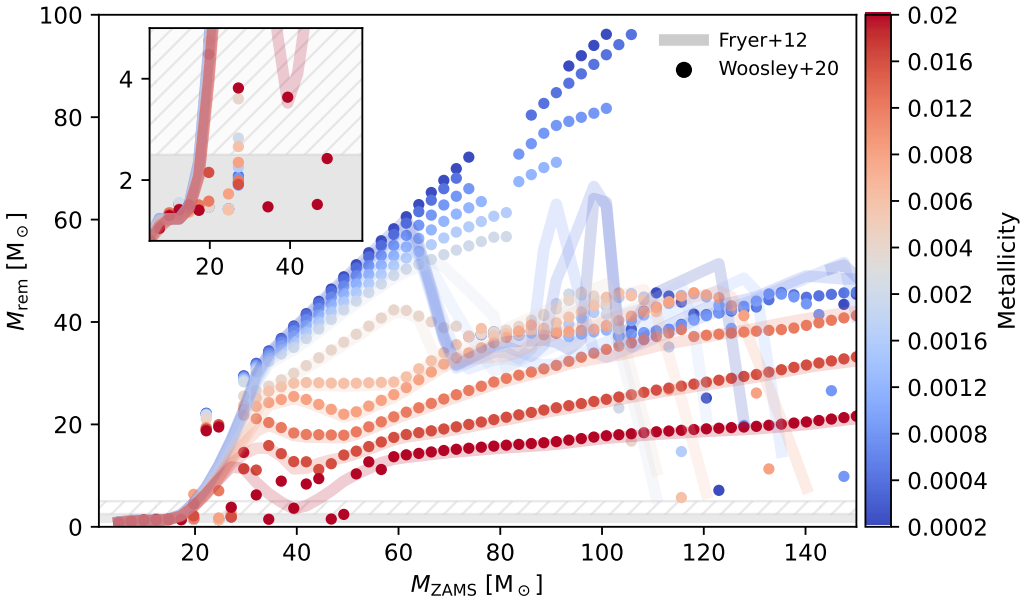


Fig. 6.1 Compact remnant masses ($M_{\rm rem}$) as a function of the ZAMS mass ($M_{\rm ZAMS}$). The scatter points show the model by Woosley, Sukhbold, et al. (2020). The thick continuous lines are evolved with the *delayed* model by Fryer et al. (2012). Different colors show the results for different metallicities, ranging from 0.0002 to 0.02. The gray shaded area highlights the region where NSs are formed ($M_{\rm rem} \leq 3\,{\rm M}_\odot$). The hatched area marks the lower-mass gap. The inset on the top left corner shows a zoom-in of the main plot. Notably, the model by Woosley, Sukhbold, et al. (2020) predicts to form NSs even for stars with $M_{\rm ZAMS} \sim 50$. Plot obtained with the population synthesis code SEVN and the PARSEC stellar tracks.

binary physics in future work. In particular, it is possible to identify three key areas of uncertainty: CE physics, SN explosion mechanism and natal kicks, mass transfer stability criteria. It would be instructive to explore new physically motivated prescriptions with strong potential to impact BBH rate predictions. These include a new two-stage formalism for CE evolution (Hirai et al., 2022), updated SN models that take into account stellar structure altered by prior mass transfer (Schneider et al., 2021), and new critical mass ratio thresholds for mass transfer stability, following (Ge, Webbink, et al., 2020). These prescriptions aim to provide a more realistic treatment of primary processes shaping BBH evolution.

Appendix A

A.1 Kick prescriptions

Figure A.1 shows the BNS merger rate in the MW for different natal kick models. Our Fiducial model, equivalent to the KGM20 model in Iorio et al. (2023), is described in Section 5.2.3. In models Kσ265 and Kσ150, we draw the kick magnitude from a Maxwellian distribution with one-dimensional root-mean square $\sigma = 265$ (Hobbs et al., 2005) and 150 km s^{-1} (Atri et al., 2019), respectively. These last two models are equivalent to Kσ265 and Kσ150 in Iorio et al. (2023). Figure A.1 shows that the natal kick model has a dramatic impact on the merger rate. In particular, our fiducial model is the only one that matches the observed rate, because it accounts for low natal kicks for stripped and ultra-stripped SNe (Giacobbo and Mapelli, 2020). We will focus on the impact of natal kicks on the main properties of Galactic BNSs and black hole–NS systems in a follow-up study (Sgalletta et al., in prep.).

A.2 Masses

Figure A.2 shows the BNS masses we obtained for the *delayed*, *rapid* and *Delayed_gauss* SN models, as described in Section 2.1.3. The distributions computed with the rapid and delayed models by Fryer et al. (2012) produce a strong peak of the secondary mass at about 1.2M$_\odot$, failing to reproduce the observed masses of the Galactic BNSs. In contrast, the rapid-gauss model matches the observed population by construction. We decided to exclude the masses from the statistical analysis in Section 3.3.5 because the only models that matches the observation does it by construction.

A.3 SKA survey parameters

Table A.1 shows the SKA survey parameters in the MID- and LOW- frequency ranges (Stappers et al., 2018) we used to obtain Table 3.7.

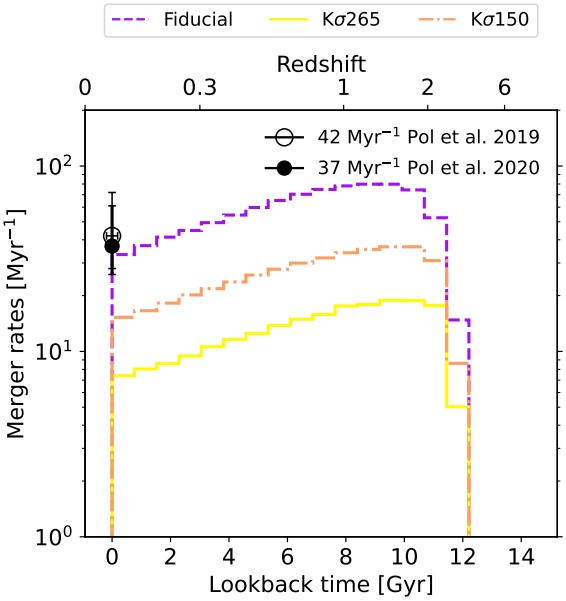


Fig. A.1 BNS merger rate in the MW as a function of the look-back time for different natal kick models. Purple dashed line: fiducial model (Ua3t1Emp); pink dot-dashed line: Kσ265 model, yellow solid line: Kσ150 model. The circles show the BNS merger rate in the MW inferred from observations, as in Figure 3.1. All simulations shown in this Figure assume our fiducial model parameters: $\tau_{\rm d} = 1$Gyr, the U distribution for initial spins and magnetic fields, the Emp MW model and $\alpha = 3$. The natal kick model has a dramatic impact on the MW merger rate. Our fiducial model is the only one that matches the observed rate.

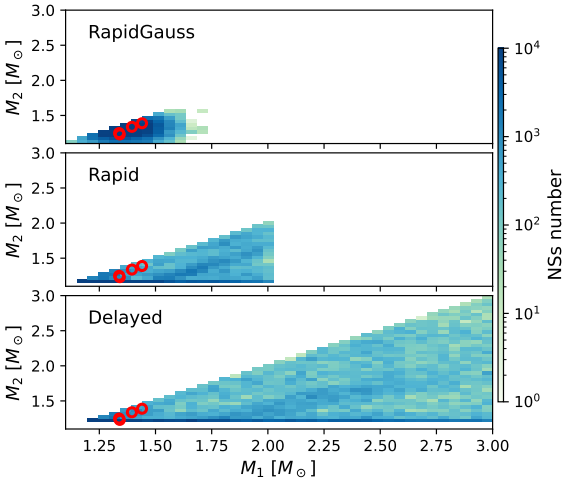


Fig. A.2 Secondary versus primary mass of the simulated BNSs, for the three different SN prescriptions adopted in this work. From top to bottom: rapid-gauss, rapid, and delayed. Here, the primary (secondary) is the most (least) massive NS of each BNS. The colour shows the number of binaries in each cell. The red circles are the observed Galactic BNS masses (some of the circles overlap in this Figure).

Survey	$\Delta\nu$ (MHz)	G_A (K/Jy)	T_{rec} (K)	τ_{sampl} (ms)	t_{int} (s)	Sky coverage
LOW	100	26.85	56	0.1	600	$-90^\circ < \delta < 30^\circ$
MID	300	3.92	20	0.1	600	$-90^\circ < \delta < 30^\circ$

Table A.1 Adopted parameters for the LOW and MID SKA surveys (Stappers et al., 2018). The columns show the bandwidth $\Delta\nu$, the antenna gain G_A, the system temperature T_{rec}, the sampling time τ_{sampl}, the integration time t_{int} and the sky coverages, respectively.

Appendix B

B.1 Observational scaling relations

Below, we provide the details of the observational scaling relations adopted in this work. We follow the approach presented by Santoliquido, Mapelli, Artale, et al. (2022).

B.1.1 Galaxy stellar mass function

Our adopted galaxy stellar mass function takes the form of a Schechter function:

$$\phi(M_*, z)\, dM_* = \phi_{\rm N}(z)\, e^{-M_*/M_{\rm cut}(z)} \left(\frac{M_*}{M_{\rm cut}(z)}\right)^{-\alpha_{\rm GSMF}} dM_*, \tag{B.1}$$

where $\phi_{\rm N}(z)$ is a normalization factor and $M_{\rm cut}(z)$ is the galaxy stellar mass at which the function transitions from a power law at low masses to an exponential decay at high masses. In our models, we use the fit derived by Chruslinska, Nelemans, and Belczynski (2019) and based on a wide catalog of galaxy stellar mass function relations over separate redshift bins.

B.1.2 Star formation rate

We draw the SFR of galaxies from the following double lognormal distribution (Sargent et al., 2012; Rodighiero et al., 2015; Schreiber, C. et al., 2015):

$$\begin{aligned}\mathscr{P}(\log {\rm SFR}|M_*, z) = A_{\rm MS} \exp\left[-\frac{(\log {\rm SFR} - \langle \log {\rm SFR}\rangle_{\rm MS})^2}{2\sigma^2_{\rm MS}}\right] + \\ + A_{\rm SB} \exp\left[-\frac{(\log {\rm SFR} - \langle \log {\rm SFR}\rangle_{\rm SB})^2}{2\sigma^2_{\rm SB}}\right],\end{aligned} \tag{B.2}$$

where $A_{\rm MS} = 0.97$ and $A_{\rm SB} = 0.243$ constants (Sargent et al., 2012). $\langle \log {\rm SFR}\rangle_{\rm MS}$ and $\sigma_{\rm MS}$ are the average SFR of the main sequence and its dispersion. We adopt several definitions of the galaxy main sequence, as described in section 4.2.4. For all of our models we use the

fiducial value $\sigma_{\rm MS} = 0.188$ dex (Santoliquido, Mapelli, Artale, et al., 2022). In a similar way, $\langle \log {\rm SFR} \rangle_{\rm SB}$ and $\sigma_{\rm SB}$ are the average and the standard deviation of the galaxy starburst sequence. The latter is defined as in Sargent et al. (2012),

$$\langle \log {\rm SFR} \rangle_{\rm SB} = \langle \log {\rm SFR} \rangle_{\rm MS} + 0.59 \tag{B.3}$$

Moreover, we assume $\sigma_{SB} = 0.243$ dex. We couple the galaxy stellar mass function with the distribution of SFR as described above.

B.1.3 Fundamental metallicity relations

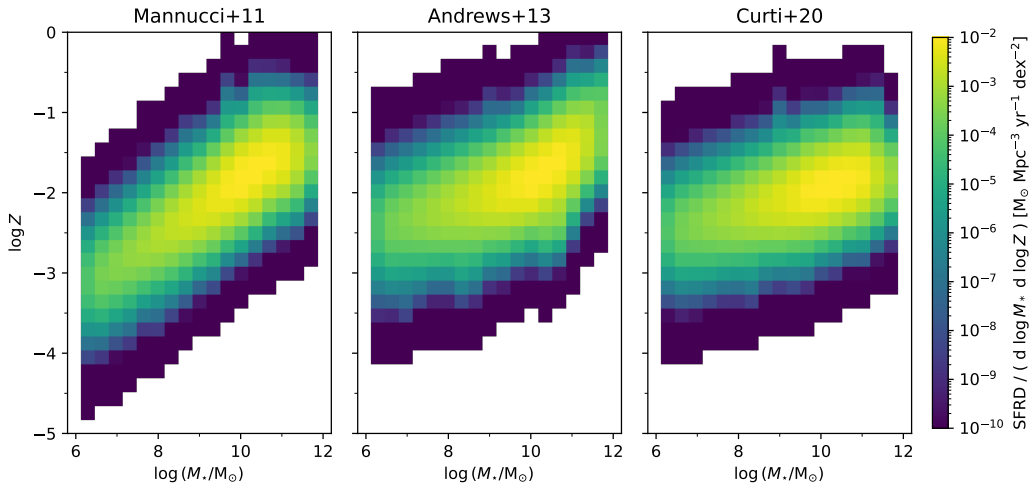


Fig. B.1 SFR density per galaxy mass (x axes) and metallicity bins (y axes) at $z = 0$. Each panel shows the result for a different FMR relation, from left to right: Mannucci, Salvaterra, et al. (2011), Andrews and Martini (2013) and Curti et al. (2020).

We consider three different fundamental metallicity relations. We adopt the fit from Mannucci, Salvaterra, et al. (2011):

$$\begin{aligned} 12 + \log({\rm O/H}) &= 8.90 + 0.37m - 0.14s - 0.19m^2 + 0.12ms - 0.054s^2 \quad \text{for } \mu_{0.32} \geq 9.5 \\ &= 8.93 + 0.51(\mu_{0.32} - 10) \quad \text{for } \mu_{0.32} < 9.5 \end{aligned} \tag{B.4}$$

where $m = \log M_* - 10$ and $s = \log {\rm SFR}$ and $\mu_{0.32} = \log M_* - 0.32 \log {\rm SFR}$, all the quantities are in solar units.

We derive an additional fit for the fundamental metallicity relation based on figure 12 by Andrews and Martini (2013)

$$12 + \log({\rm O/H}) = 0.43(\log M_* - 0.66 \log {\rm SFR}) + 4.59 \tag{B.5}$$

Lastly, we consider the metallicity relation calculated in Curti et al. (2020):

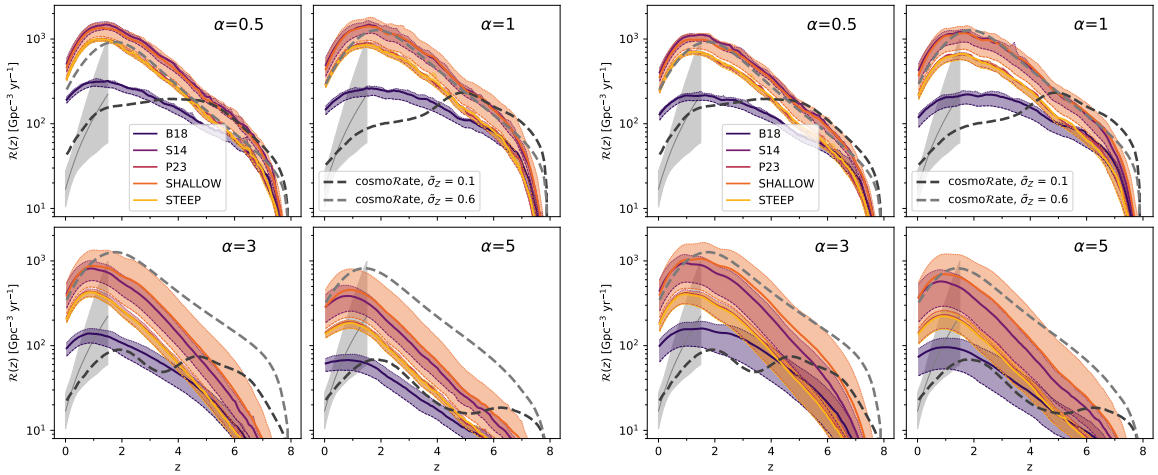
$$12 + \log(\mathrm{O/H}) = Z_0 - \gamma/\beta \log\left(1 + (M_*/M_0(\mathrm{SFR}))^{-\beta}\right) \tag{B.6}$$

where $M_0(\mathrm{SFR}) = m_0 + m_1 \log \mathrm{SFR}$ and $Z_0 = 8.779 \pm 0.005$, $m_0 = 10.11 \pm 0.03$, $m_1 = 0.56 \pm 0.01$, $\gamma = 0.31 \pm 0.01$ and $\beta = 2.1 \pm 0.4$. For the purposes of our simulations, we convert these relations into absolute metallicities. We adopt the solar metallicity values from Caffau et al. (2011): $Z_\odot = 0.0153$ and $12 + \log(\mathrm{O/H})_\odot = 8.76$.

Figure B.1 compares the distributions of SFR density as a function of galaxy stellar mass and metallicity, for different fundamental metallicity relations at $z = 0$. The differences are particularly noticeable for low–mass galaxies, where the model by Mannucci, Salvaterra, et al. (2011) clearly predicts lower metallicities compared to the other two prescriptions. Curti et al. (2020) predicts the flattest relation, with less than an order of magnitude difference in metallicty between the low and high–mass galaxies.

B.2 Merger rate densities

Figures B.2a and B.2b show the BBH cosmic merger rate densities obtained for different SFR–M_* relations, adopting the fundamental metallicity relations by Curti et al. (2020) and Mannucci, Salvaterra, et al. (2011), respectively.



(a) Same as Fig. 4.5 but for the FMR by Curti et al. (2020).

(b) Same as Fig. 4.5 but for the FMR by Mannucci, Salvaterra, et al. (2011).

Fig. B.2 BBH cosmic merger rate densities for different SFR–M_* relations, using two different fundamental metallicity relations.

References

[1] A. G. Abac et al. "Observation of Gravitational Waves from the Coalescence of a 2.5–4.5 M $_\odot$ Compact Object and a Neutron Star". In: 970.2, L34 (Aug. 2024), p. L34. DOI: 10.3847/2041-8213/ad5beb. arXiv: 2404.04248 [astro-ph.HE].

[2] J. Abadie et al. "First Search for Gravitational Waves from the Youngest Known Neutron Star". In: 722.2 (Oct. 2010), pp. 1504–1513. DOI: 10.1088/0004-637X/722/2/1504. arXiv: 1006.2535 [gr-qc].

[3] B. P. Abbott et al. "Observation of Gravitational Waves from a Binary Black Hole Merger". In: *Phys. Rev. Lett.* 116 (6 Feb. 2016), p. 061102. DOI: 10.1103/PhysRevLett.116.061102. URL: https://link.aps.org/doi/10.1103/PhysRevLett.116.061102.

[4] B. P. Abbott et al. "Gravitational Waves and Gamma-Rays from a Binary Neutron Star Merger: GW170817 and GRB 170817A". In: 848.2, L13 (Oct. 2017), p. L13. DOI: 10.3847/2041-8213/aa920c. arXiv: 1710.05834 [astro-ph.HE].

[5] B. P. Abbott et al. "GW170104: Observation of a 50-Solar-Mass Binary Black Hole Coalescence at Redshift 0.2". In: *Phys. Rev. Lett.* 118 (22 June 2017), p. 221101. DOI: 10.1103/PhysRevLett.118.221101. URL: https://link.aps.org/doi/10.1103/PhysRevLett.118.221101.

[6] B. P. Abbott et al. "GW170817: Observation of Gravitational Waves from a Binary Neutron Star Inspiral". In: 119.16, 161101 (Oct. 2017), p. 161101. DOI: 10.1103/PhysRevLett.119.161101. arXiv: 1710.05832 [gr-qc].

[7] B. P. Abbott et al. "Multi-messenger Observations of a Binary Neutron Star Merger". In: 848.2, L12 (Oct. 2017), p. L12. DOI: 10.3847/2041-8213/aa91c9. arXiv: 1710.05833 [astro-ph.HE].

[8] B. P. Abbott et al. "GW170817: Measurements of Neutron Star Radii and Equation of State". In: 121.16, 161101 (Oct. 2018), p. 161101. DOI: 10.1103/PhysRevLett.121.161101. arXiv: 1805.11581 [gr-qc].

[9] B. P. Abbott et al. "Binary Black Hole Population Properties Inferred from the First and Second Observing Runs of Advanced LIGO and Advanced Virgo". In: 882.2, L24 (Sept. 2019), p. L24. DOI: 10.3847/2041-8213/ab3800. arXiv: 1811.12940 [astro-ph.HE].

[10] B. P. Abbott et al. "GWTC-1: A Gravitational-Wave Transient Catalog of Compact Binary Mergers Observed by LIGO and Virgo during the First and Second Observing Runs". In: *Physical Review X* 9.3, 031040 (July 2019), p. 031040. DOI: 10.1103/PhysRevX.9.031040. arXiv: 1811.12907 [astro-ph.HE].

[11] B. P. Abbott et al. "GW190425: Observation of a Compact Binary Coalescence with Total Mass $\sim 3.4\,M_\odot$". In: 892.1, L3 (Mar. 2020), p. L3. DOI: 10.3847/2041-8213/ab75f5. arXiv: 2001.01761 [astro-ph.HE].

[12] R. Abbott et al. "GW190521: A Binary Black Hole Merger with a Total Mass of 150 $M_\odot$". In: 125.10, 101102 (Sept. 2020), p. 101102. DOI: 10.1103/PhysRevLett.125.101102. arXiv: 2009.01075 [gr-qc].

[13] R. Abbott et al. "GW190814: Gravitational Waves from the Coalescence of a 23 Solar Mass Black Hole with a 2.6 Solar Mass Compact Object". In: *The Astrophysical Journal Letters* 896.2 (June 2020), p. L44. DOI: 10.3847/2041-8213/ab960f. URL: https://dx.doi.org/10.3847/2041-8213/ab960f.

[14] R. Abbott et al. "Properties and Astrophysical Implications of the 150 $M_\odot$ Binary Black Hole Merger GW190521". In: 900.1, L13 (Sept. 2020), p. L13. DOI: 10.3847/2041-8213/aba493. arXiv: 2009.01190 [astro-ph.HE].

[15] R. Abbott et al. "GWTC-2: Compact Binary Coalescences Observed by LIGO and Virgo during the First Half of the Third Observing Run". In: *Phys. Rev. X* 11 (2 June 2021), p. 021053. DOI: 10.1103/PhysRevX.11.021053. URL: https://link.aps.org/doi/10.1103/PhysRevX.11.021053.

[16] R. Abbott et al. "Observation of Gravitational Waves from Two Neutron Star-Black Hole Coalescences". In: 915.1, L5 (July 2021), p. L5. DOI: 10.3847/2041-8213/ac082e. arXiv: 2106.15163 [astro-ph.HE].

[17] R. Abbott et al. "Population Properties of Compact Objects from the Second LIGO–Virgo Gravitational-Wave Transient Catalog". In: *The Astrophysical Journal Letters* 913.1 (May 2021), p. L7. DOI: 10.3847/2041-8213/abe949. URL: https://dx.doi.org/10.3847/2041-8213/abe949.

[18] R. Abbott et al. "Population of Merging Compact Binaries Inferred Using Gravitational Waves through GWTC-3". In: *Phys. Rev. X* 13 (1 Mar. 2023), p. 011048. DOI: 10.1103/PhysRevX.13.011048. URL: https://link.aps.org/doi/10.1103/PhysRevX.13.011048.

[19] R. Abbott et al. "GWTC-3: Compact Binary Coalescences Observed by LIGO and Virgo during the Second Part of the Third Observing Run". In: *Phys. Rev. X* 13 (4 Dec. 2023), p. 041039. DOI: 10.1103/PhysRevX.13.041039. URL: https://link.aps.org/doi/10.1103/PhysRevX.13.041039.

[20] Helmut A. Abt et al. "The Frequency and Formation Mechanism of B2–B5 Main-Sequence Binaries". In: 74 (Oct. 1990), p. 551. DOI: 10.1086/191508.

[21] P. A. R. Ade et al. "Planck 2015 results. XIII. Cosmological parameters". In: 594, A13 (Sept. 2016), A13. DOI: 10.1051/0004-6361/201525830. arXiv: 1502.01589 [astro-ph.CO].

[22] M. Afşar et al. "Two-colour photometry of the binary planetary nebula nuclei UU Sagitte and V477 Lyrae: oversized secondaries in post-common-envelope binaries". In: 391.2 (Dec. 2008), pp. 802–814. DOI: 10.1111/j.1365-2966.2008.13927.x. arXiv: 0810.0949 [astro-ph].

[23] Gabriella Agazie et al. "The NANOGrav 15 yr Data Set: Evidence for a Gravitational-wave Background". In: 951.1, L8 (July 2023), p. L8. DOI: 10.3847/2041-8213/acdac6. arXiv: 2306.16213 [astro-ph.HE].

[24] Poojan Agrawal et al. "The fates of massive stars: exploring uncertainties in stellar evolution with METISSE". In: 497.4 (Oct. 2020), pp. 4549–4564. DOI: 10.1093/mnras/staa2264. arXiv: 2005.13177 [astro-ph.SR].

[25] Bridget C. Andersen et al. "A Fourier Domain "Jerk" Search for Binary Pulsars". In: 863.1, L13 (Aug. 2018), p. L13. DOI: 10.3847/2041-8213/aad59f. arXiv: 1807.07900 [astro-ph.HE].

[26] Brett H. Andrews and Paul Martini. "The Mass-Metallicity Relation with the Direct Method on Stacked Spectra of SDSS Galaxies". In: 765.2, 140 (Mar. 2013), p. 140. DOI: 10.1088/0004-637X/765/2/140. arXiv: 1211.3418 [astro-ph.CO].

[27] Jeff J. Andrews and Ilya Mandel. "Double Neutron Star Populations and Formation Channels". In: 880.1, L8 (July 2019), p. L8. DOI: 10.3847/2041-8213/ab2ed1. arXiv: 1904.12745 [astro-ph.HE].

[28] M Celeste Artale, Michela Mapelli, Nicola Giacobbo, et al. "Host galaxies of merging compact objects: mass, star formation rate, metallicity, and colours". In: *MNRAS* 487.2 (May 2019), pp. 1675–1688. DOI: 10.1093/mnras/stz1382. eprint: https://academic.oup.com/mnras/article-pdf/487/2/1675/28766230/stz1382.pdf. URL: https://doi.org/10.1093/mnras/stz1382.

[29] M. Celeste Artale, Yann Bouffanais, et al. "An astrophysically motivated ranking criterion for low-latency electromagnetic follow-up of gravitational wave events". In: 495.2 (June 2020), pp. 1841–1852. DOI: 10.1093/mnras/staa1252. arXiv: 2002.11214 [astro-ph.GA].

[30] M. Celeste Artale, Michela Mapelli, Yann Bouffanais, et al. "Mass and star formation rate of the host galaxies of compact binary mergers across cosmic time". In: 491.3 (Jan. 2020), pp. 3419–3434. DOI: 10.1093/mnras/stz3190. arXiv: 1910.04890 [astro-ph.GA].

[31] Pawel Artymowicz et al. "Dynamics of Binary-Disk Interaction. I. Resonances and Disk Gap Sizes". In: 421 (Feb. 1994), p. 651. DOI: 10.1086/173679.

[32] Z. Arzoumanian et al. "The Velocity Distribution of Isolated Radio Pulsars". In: 568.1 (Mar. 2002), pp. 289–301. DOI: 10.1086/338805. arXiv: astro-ph/0106159 [astro-ph].

[33] Martin Asplund et al. "The Chemical Composition of the Sun". In: 47.1 (Sept. 2009), pp. 481–522. DOI: 10.1146/annurev.astro.46.060407.145222. arXiv: 0909.0948 [astro-ph.SR].

[34] P Atri et al. "Potential kick velocity distribution of black hole X-ray binaries and implications for natal kicks". In: *Monthly Notices of the Royal Astronomical Society* 489.3 (Aug. 2019), pp. 3116–3134. DOI: 10.1093/mnras/stz2335. eprint: https://academic.oup.com/mnras/article-pdf/489/3/3116/30155202/stz2335.pdf. URL: https://doi.org/10.1093/mnras/stz2335.

[35] Kareem El-Badry, Hans-Walter Rix, Yvette Cendes, et al. "A red giant orbiting a black hole". In: 521.3 (May 2023), pp. 4323–4348. DOI: 10.1093/mnras/stad799. arXiv: 2302.07880 [astro-ph.SR].

[36] Kareem El-Badry, Hans-Walter Rix, Eliot Quataert, et al. "A Sun-like star orbiting a black hole". In: 518.1 (Jan. 2023), pp. 1057–1085. DOI: 10.1093/mnras/stac3140. arXiv: 2209.06833 [astro-ph.SR].

[37] Manjari Bagchi et al. "On the detectability of eccentric binary pulsars". In: *Monthly Notices of the Royal Astronomical Society* 432 (Feb. 2013). DOI: 10.1093/mnras/stt559.

[38] Vishal Baibhav et al. "Gravitational-wave detection rates for compact binaries formed in isolation: LIGO/Virgo O3 and beyond". In: *Phys. Rev. D* 100 (6 Sept. 2019), p. 064060. DOI: 10.1103/PhysRevD.100.064060. URL: https://link.aps.org/doi/10.1103/PhysRevD.100.064060.

[39] Vishnu Balakrishnan et al. "Coherent search for binary pulsars across all Five Keplerian parameters in radio observations using the template-bank algorithm". In: 511.1 (Mar. 2022), pp. 1265–1284. DOI: 10.1093/mnras/stab3746. arXiv: 2112.11991 [astro-ph.IM].

[40] Sambaran Banerjee et al. "Stellar-mass black holes in star clusters: implications for gravitational wave radiation". In: 402.1 (Feb. 2010), pp. 371–380. DOI: 10.1111/j.1365-2966.2009.15880.x. arXiv: 0910.3954 [astro-ph.SR].

[41] Jordan Barber et al. “Formation and evolution of binary black holes in N-body simulations of star clusters with up to two million stars”. In: 538.2 (Apr. 2025), pp. 639–658. DOI: 10.1093/mnras/staf279. arXiv: 2410.03832 [astro-ph.GA].

[42] Z. Barkat et al. “Dynamics of Supernova Explosion Resulting from Pair Formation”. In: 18.10 (Mar. 1967), pp. 379–381. DOI: 10.1103/PhysRevLett.18.379.

[43] S. D. Bates et al. “PSRPOPPy: an open-source package for pulsar population simulations”. In: 439.3 (Apr. 2014), pp. 2893–2902. DOI: 10.1093/mnras/stu157. arXiv: 1311.3427 [astro-ph.IM].

[44] Aldo Batta et al. “The Formation of Rapidly Rotating Black Holes in High-mass X-Ray Binaries”. In: 846.2, L15 (Sept. 2017), p. L15. DOI: 10.3847/2041-8213/aa8506. arXiv: 1708.00570 [astro-ph.HE].

[45] Andreas Bauswein et al. “Neutron-star Radius Constraints from GW170817 and Future Detections”. In: 850.2, L34 (Dec. 2017), p. L34. DOI: 10.3847/2041-8213/aa9994. arXiv: 1710.06843 [astro-ph.HE].

[46] Simone S. Bavera et al. “The impact of mass-transfer physics on the observable properties of field binary black hole populations”. In: 647, A153 (Mar. 2021), A153. DOI: 10.1051/0004-6361/202039804. arXiv: 2010.16333 [astro-ph.HE].

[47] M. Bejger et al. “Constraints on the dense matter equation of state from the measurements of PSR J0737-3039A moment of inertia and PSR J0751+1807 mass”. In: 364.2 (Dec. 2005), pp. 635–639. DOI: 10.1111/j.1365-2966.2005.09575.x. arXiv: astro-ph/0508105 [astro-ph].

[48] K. Belczynski, J. Klencki, et al. “Evolutionary roads leading to low effective spins, high black hole masses, and O1/O2 rates for LIGO/Virgo binary black holes”. In: 636, A104 (Apr. 2020), A104. DOI: 10.1051/0004-6361/201936528. arXiv: 1706.07053 [astro-ph.HE].

[49] K. Belczynski, A. Romagnolo, et al. “The Uncertain Future of Massive Binaries Obscures the Origin of LIGO/Virgo Sources”. In: *The Astrophysical Journal* 925.1 (Jan. 2022), p. 69. DOI: 10.3847/1538-4357/ac375a. URL: https://dx.doi.org/10.3847/1538-4357/ac375a.

[50] Krzysztof Belczynski, Michal Dominik, et al. “The Effect of Metallicity on the Detection Prospects for Gravitational Waves”. In: 715.2 (June 2010), pp. L138–L141. DOI: 10.1088/2041-8205/715/2/L138. arXiv: 1004.0386 [astro-ph.HE].

[51] Krzysztof Belczynski, Daniel E. Holz, et al. “The first gravitational-wave source from the isolated evolution of two stars in the 40-100 solar mass range”. In: 534.7608 (June 2016), pp. 512–515. DOI: 10.1038/nature18322. arXiv: 1602.04531 [astro-ph.HE].

[52] Krzysztof Belczynski, Vassiliki Kalogera, and Tomasz Bulik. “A Comprehensive Study of Binary Compact Objects as Gravitational Wave Sources: Evolutionary Channels, Rates, and Physical Properties”. In: 572.1 (June 2002), pp. 407–431. DOI: 10.1086/340304. arXiv: astro-ph/0111452 [astro-ph].

[53] Krzysztof Belczynski, Vassiliki Kalogera, Frederic A. Rasio, et al. “Compact Object Modeling with the StarTrack Population Synthesis Code”. In: 174.1 (Jan. 2008), pp. 223–260. DOI: 10.1086/521026. arXiv: astro-ph/0511811 [astro-ph].

[54] Matthew J. Benacquista et al. “Relativistic Binaries in Globular Clusters”. In: *Living Reviews in Relativity* 16.1, 4 (Dec. 2013), p. 4. DOI: 10.12942/lrr-2013-4. arXiv: 1110.4423 [astro-ph.SR].

[55] J. S. Benensohn et al. “Hydrodynamical Studies of Wind Accretion onto Compact Objects: Two-dimensional Calculations”. In: 478.2 (Mar. 1997), pp. 723–733. DOI: 10.1086/303835. arXiv: astro-ph/9610245 [astro-ph].

[56] Paz Beniamini et al. “Formation of double neutron star systems as implied by observations”. In: 456.4 (Mar. 2016), pp. 4089–4099. DOI: 10.1093/mnras/stv2903. arXiv: 1510.03111 [astro-ph.HE].

[57] H. A. Bethe et al. “Revival of a stalled supernova shock by neutrino heating”. In: 295 (Aug. 1985), pp. 14–23. DOI: 10.1086/163343.

[58] N. D. Ramesh Bhat et al. “Multifrequency Observations of Radio Pulse Broadening and Constraints on Interstellar Electron Density Microstructure”. In: 605.2 (Apr. 2004), pp. 759–783. DOI: 10.1086/382680. arXiv: astro-ph/0401067 [astro-ph].

[59] D. Bhattacharya et al. “Formation and evolution of binary and millisecond radio pulsars”. In: 203.1-2 (Jan. 1991), pp. 1–124. DOI: 10.1016/0370-1573(91)90064-S.

[60] L. Bisigello et al. “Analysis of the SFR-M* plane at z < 3: single fitting versus multi-Gaussian decomposition”. In: 609, A82 (Jan. 2018), A82. DOI: 10.1051/0004-6361/201731399. arXiv: 1706.06154 [astro-ph.GA].

[61] A. Blaauw. “On the origin of the O- and B-type stars with high velocities (the “run-away” stars), and some related problems”. In: 15 (May 1961), p. 265.

[62] L. Boco, A. Lapi, M. Chruslinska, et al. “Evolution of Galaxy Star Formation and Metallicity: Impact on Double Compact Object Mergers”. In: 907.2, 110 (Feb. 2021), p. 110. DOI: 10.3847/1538-4357/abd3a0. arXiv: 2012.02800 [astro-ph.GA].

[63] L. Boco, A. Lapi, S. Goswami, et al. “Merging Rates of Compact Binaries in Galaxies: Perspectives for Gravitational Wave Detections”. In: 881.2, 157 (Aug. 2019), p. 157. DOI: 10.3847/1538-4357/ab328e. arXiv: 1907.06841 [astro-ph.GA].

[64] Adam P. Boesky et al. “Investigating the Cosmological Rate of Compact Object Mergers from Isolated Massive Binary Stars”. In: 976.1, 24 (Nov. 2024), p. 24. DOI: 10.3847/1538-4357/ad7fe3. arXiv: 2405.01630 [astro-ph.HE].

[65] Adam P. Boesky et al. “The Binary Black Hole Merger Rate Deviates from the Cosmic Star Formation Rate: A Tug of War between Metallicity and Delay Times”. In: 976.1, 23 (Nov. 2024), p. 23. DOI: 10.3847/1538-4357/ad7fe4. arXiv: 2405.01623 [astro-ph.HE].

[66] Slavko Bogdanov, Arash Bahramian, et al. “A Deep Chandra X-Ray Observatory Study of the Millisecond Pulsar Population in the Globular Cluster Terzan 5”. In: 912.2, 124 (May 2021), p. 124. DOI: 10.3847/1538-4357/abee78. arXiv: 2012.12944 [astro-ph.HE].

[67] Slavko Bogdanov, Craig O. Heinke, et al. “Neutron Star Mass-Radius Constraints of the Quiescent Low-mass X-Ray Binaries X7 and X5 in the Globular Cluster 47 Tuc”. In: 831.2, 184 (Nov. 2016), p. 184. DOI: 10.3847/0004-637X/831/2/184. arXiv: 1603.01630 [astro-ph.HE].

[68] E. Böhm-Vitense. “Über die Wasserstoffkonvektionszone in Sternen verschiedener Effektivtemperaturen und Leuchtkräfte. Mit 5 Textabbildungen”. In: 46 (Jan. 1958), p. 108.

[69] C. T. Bolton. “Identification of Cygnus X-1 with HDE 226868”. In: 235.5336 (Feb. 1972), pp. 271–273. DOI: 10.1038/235271b0.

[70] Leindert A. Boogaard et al. “The MUSE Hubble Ultra Deep Field Survey. XI. Constraining the low-mass end of the stellar mass - star formation rate relation at z < 1”. In: 619, A27 (Nov. 2018), A27. DOI: 10.1051/0004-6361/201833136. arXiv: 1808.04900 [astro-ph.GA].

[71] Jo Bovy. “Stellar inventory of the solar neighbourhood using Gaia DR1”. In: 470.2 (Sept. 2017), pp. 1360–1387. DOI: 10.1093/mnras/stx1277. arXiv: 1704.05063 [astro-ph.GA].

[72] Marica Branchesi et al. “Science with the Einstein Telescope: a comparison of different designs”. In: 2023.7, 068 (July 2023), p. 068. DOI: 10.1088/1475-7516/2023/07/068. arXiv: 2303.15923 [gr-qc].

[73] J. C. Bray et al. “Neutron star kicks and their relationship to supernovae ejecta mass”. In: 461.4 (Oct. 2016), pp. 3747–3759. DOI: 10.1093/mnras/stw1275. arXiv: 1605.09529 [astro-ph.HE].

[74] J. C. Bray et al. “Neutron star kicks - II. Revision and further testing of the conservation of momentum ‘kick’ model”. In: 480.4 (Nov. 2018), pp. 5657–5672. DOI: 10.1093/mnras/sty2230. arXiv: 1804.04414 [astro-ph.SR].

[75] Katelyn Breivik, Sourav Chatterjee, et al. “Revealing Black Holes with Gaia”. In: 850.1, L13 (Nov. 2017), p. L13. DOI: 10.3847/2041-8213/aa97d5. arXiv: 1710.04657 [astro-ph.SR].

[76] Katelyn Breivik, Scott Coughlin, et al. “COSMIC Variance in Binary Population Synthesis”. In: 898.1, 71 (July 2020), p. 71. DOI: 10.3847/1538-4357/ab9d85. arXiv: 1911.00903 [astro-ph.HE].

[77] A. G. Bressan, C. Chiosi, et al. “Mass loss and overshooting in massive stars”. In: 102.1 (Sept. 1981), pp. 25–30.

[78] Alessandro Bressan, Paola Marigo, et al. “PARSEC: stellar tracks and isochrones with the PAdova and TRieste Stellar Evolution Code”. In: 427.1 (Nov. 2012), pp. 127–145. DOI: 10.1111/j.1365-2966.2012.21948.x. arXiv: 1208.4498 [astro-ph.SR].

[79] Rene P. Breton et al. “Relativistic Spin Precession in the Double Pulsar”. In: *Science* 321.5885 (July 2008), p. 104. DOI: 10.1126/science.1159295. arXiv: 0807.2644 [astro-ph].

[80] Max M Briel et al. “Estimating transient rates from cosmological simulations and BPASS”. In: *Monthly Notices of the Royal Astronomical Society* 514.1 (Apr. 2022), pp. 1315–1334. DOI: 10.1093/mnras/stac1100. URL: https://doi.org/10.1093/mnras/stac1100.

[81] Floor S. Broekgaarden and Edo Berger. “Formation of the First Two Black Hole-Neutron Star Mergers (GW200115 and GW200105) from Isolated Binary Evolution”. In: 920.1, L13 (Oct. 2021), p. L13. DOI: 10.3847/2041-8213/ac2832. arXiv: 2108.05763 [astro-ph.HE].

[82] Floor S. Broekgaarden, Edo Berger, et al. “Impact of massive binary star and cosmic evolution on gravitational wave observations - II. Double compact object rates and properties”. In: 516.4 (Nov. 2022), pp. 5737–5761. DOI: 10.1093/mnras/stac1677. arXiv: 2112.05763 [astro-ph.HE].

[83] M. Burgay et al. “An increased estimate of the merger rate of double neutron stars from observations of a highly relativistic system”. In: 426.6966 (Dec. 2003), pp. 531–533. DOI: 10.1038/nature02124. arXiv: astro-ph/0312071 [astro-ph].

[84] M. Cadelano et al. “Discovery of Three New Millisecond Pulsars in Terzan 5”. In: 855.2, 125 (Mar. 2018), p. 125. DOI: 10.3847/1538-4357/aaac2a. arXiv: 1801.09929 [astro-ph.HE].

[85] E. Caffau et al. “Solar Chemical Abundances Determined with a CO5BOLD 3D Model Atmosphere”. In: 268.2 (Feb. 2011), pp. 255–269. DOI: 10.1007/s11207-010-9541-4. arXiv: 1003.1190 [astro-ph.SR].

[86] A. D. Cameron et al. “The High Time Resolution Universe Pulsar Survey - XIII. PSR J1757-1854, the most accelerated binary pulsar”. In: 475.1 (Mar. 2018), pp. L57–L61. DOI: 10.1093/mnrasl/sly003. arXiv: 1711.07697 [astro-ph.HE].

[87] F. Camilo, D. R. Lorimer, et al. "Observations of 20 Millisecond Pulsars in 47 Tucanae at 20 Centimeters". In: 535.2 (June 2000), pp. 975–990. DOI: 10.1086/308859. arXiv: astro-ph/9911234 [astro-ph].

[88] F. Camilo and F. A. Rasio. "Pulsars in Globular Clusters". In: *Binary Radio Pulsars*. Ed. by Fred A. Rasio et al. Vol. 328. Astronomical Society of the Pacific Conference Series. July 2005, p. 147. DOI: 10.48550/arXiv.astro-ph/0501226. arXiv: astro-ph/0501226 [astro-ph].

[89] K. I. Caputi et al. "Star Formation in Galaxies at z $\sim$ 4-5 from the SMUVS Survey: A Clear Starburst/Main-sequence Bimodality for Hα Emitters on the SFR-M* Plane". In: 849.1, 45 (Nov. 2017), p. 45. DOI: 10.3847/1538-4357/aa901e. arXiv: 1705.06179 [astro-ph.GA].

[90] Caitlin M. Casey et al. "The Brightest Galaxies in the Dark Ages: Galaxies' Dust Continuum Emission during the Reionization Era". In: 862.1, 77 (July 2018), p. 77. DOI: 10.3847/1538-4357/aac82d. arXiv: 1805.10301 [astro-ph.GA].

[91] Luke Chamandy et al. "Accretion in common envelope evolution". In: *Monthly Notices of the Royal Astronomical Society* 480.2 (July 2018), pp. 1898–1911. DOI: 10.1093/mnras/sty1950. eprint: https://academic.oup.com/mnras/article-pdf/480/2/1898/25438634/sty1950.pdf. URL: https://doi.org/10.1093/mnras/sty1950.

[92] S. Chandrasekhar. "The highly collapsed configurations of a stellar mass (Second paper)". In: 95 (Jan. 1935), pp. 207–225. DOI: 10.1093/mnras/95.3.207.

[93] Debatri Chattopadhyay et al. "Modelling double neutron stars: radio and gravitational waves". In: 494.2 (May 2020), pp. 1587–1610. DOI: 10.1093/mnras/staa756. arXiv: 1912.02415 [astro-ph.HE].

[94] Debatri Chattopadhyay et al. "Modelling neutron star-black hole binaries: future pulsar surveys and gravitational wave detectors". In: 504.3 (July 2021), pp. 3682–3710. DOI: 10.1093/mnras/stab973. arXiv: 2011.13503 [astro-ph.HE].

[95] Hai-Liang Chen, Xuefei Chen, et al. "Formation of Black Widows and Redbacks—Two Distinct Populations of Eclipsing Binary Millisecond Pulsars". In: 775.1, 27 (Sept. 2013), p. 27. DOI: 10.1088/0004-637X/775/1/27. arXiv: 1308.4107 [astro-ph.SR].

[96] Kaiyou Chen and Malvin Ruderman. "Pulsar Death Lines and Death Valley". In: 402 (Jan. 1993), p. 264. DOI: 10.1086/172129.

[97] C. Chiappini et al. "The Chemical Evolution of the Galaxy: The Two-Infall Model". In: 477.2 (Mar. 1997), pp. 765–780. DOI: 10.1086/303726. arXiv: astro-ph/9609199 [astro-ph].

[98] Martyna Chruslinska, Krzysztof Belczynski, et al. "Double neutron stars: merger rates revisited". In: 474.3 (Mar. 2018), pp. 2937–2958. DOI: 10.1093/mnras/stx2923. arXiv: 1708.07885 [astro-ph.HE].

[99] Martyna Chruslinska and Gijs Nelemans. "Metallicity of stars formed throughout the cosmic history based on the observational properties of star-forming galaxies". In: 488.4 (Oct. 2019), pp. 5300–5326. DOI: 10.1093/mnras/stz2057. arXiv: 1907.11243 [astro-ph.GA].

[100] Martyna Chruslinska, Gijs Nelemans, and Krzysztof Belczynski. "The influence of the distribution of cosmic star formation at different metallicities on the properties of merging double compact objects". In: 482.4 (Feb. 2019), pp. 5012–5017. DOI: 10.1093/mnras/sty3087. arXiv: 1811.03565 [astro-ph.HE].

[101] Martyna Chruślińska. "Chemical Evolution of the Universe and its Consequences for Gravitational-Wave Astrophysics". In: *Annalen der Physik* 536.2, 2200170 (Feb. 2024), p. 2200170. DOI: 10.1002/andp.202200170. arXiv: 2206.10622 [astro-ph.GA].

[102] Martyna Chruślińska et al. "The impact of the FMR and starburst galaxies on the (low metallicity) cosmic star formation history". In: 508.4 (Dec. 2021), pp. 4994–5027. DOI: 10.1093/mnras/stab2690. arXiv: 2109.06187 [astro-ph.GA].

[103] J. S. W. Claeys et al. "Theoretical uncertainties of the Type Ia supernova rate". In: 563, A83 (Mar. 2014), A83. DOI: 10.1051/0004-6361/201322714. arXiv: 1401.2895 [astro-ph.SR].

[104] Stirling A. Colgate et al. "The Hydrodynamic Behavior of Supernovae Explosions". In: 143 (Mar. 1966), p. 626. DOI: 10.1086/148549.

[105] J. M. Cordes. "NE2001: A New Model for the Galactic Electron Density and its Fluctuations". In: *Milky Way Surveys: The Structure and Evolution of our Galaxy*. Ed. by Dan Clemens et al. Vol. 317. Astronomical Society of the Pacific Conference Series. Dec. 2004, p. 211.

[106] J. M. Cordes and T. J. W. Lazio. "NE2001.I. A New Model for the Galactic Distribution of Free Electrons and its Fluctuations". In: *arXiv e-prints*, astro-ph/0207156 (July 2002), astro–ph/0207156. arXiv: astro-ph/0207156 [astro-ph].

[107] A. Corongiu et al. "The binary pulsar PSR J1811-1736: evidence of a low amplitude supernova kick". In: 462.2 (Feb. 2007), pp. 703–709. DOI: 10.1051/0004-6361:20054385. arXiv: astro-ph/0611436 [astro-ph].

[108] G. Costa, K. G. Shepherd, et al. "Evolutionary tracks, ejecta, and ionizing photons from intermediate-mass to very massive stars with PARSEC". In: 694, A193 (Feb. 2025), A193. DOI: 10.1051/0004-6361/202452573. arXiv: 2501.12917 [astro-ph.SR].

[109] Guglielmo Costa, Alessandro Bressan, et al. "Formation of GW190521 from stellar evolution: the impact of the hydrogen-rich envelope, dredge-up, and $^{12}C(\alpha, \gamma)^{16}O$ rate on the pair-instability black hole mass gap". In: 501.3 (Mar. 2021), pp. 4514–4533. DOI: 10.1093/mnras/staa3916. arXiv: 2010.02242 [astro-ph.SR].

[110] Guglielmo Costa, Léo Girardi, et al. "Mixing by overshooting and rotation in intermediate-mass stars". In: *Monthly Notices of the Royal Astronomical Society* 485.4 (Mar. 2019), pp. 4641–4657. DOI: 10.1093/mnras/stz728. arXiv: https://academic.oup.com/mnras/article-pdf/485/4/4641/28227835/stz728.pdf [astro-ph.SR]. URL: https://doi.org/10.1093/mnras/stz728.

[111] Stéphane Courteau et al. "Galaxy masses". In: *Reviews of Modern Physics* 86.1 (Jan. 2014), pp. 47–119. DOI: 10.1103/RevModPhys.86.47. arXiv: 1309.3276 [astro-ph.CO].

[112] J. A. Crawford. "On the Subgiant Components of Eclipsing Binary Systems." In: 121 (Jan. 1955), p. 71. DOI: 10.1086/145965.

[113] G. Cresci et al. "Fundamental metallicity relation in CALIFA, SDSS-IV MaNGA, and high-z galaxies". In: 627, A42 (July 2019), A42. DOI: 10.1051/0004-6361/201834637. arXiv: 1811.06015 [astro-ph.GA].

[114] Mirko Curti et al. "The mass-metallicity and the fundamental metallicity relation revisited on a fully T_e-based abundance scale for galaxies". In: 491.1 (Jan. 2020), pp. 944–964. DOI: 10.1093/mnras/stz2910. arXiv: 1910.00597 [astro-ph.GA].

[115] Marco Dall'Amico, Michela Mapelli, Giuliano Iorio, et al. "Impact of accretion-induced chemically homogeneous evolution on stellar and compact binary populations". In: *arXiv e-prints*, arXiv:2501.04778 (Jan. 2025), arXiv:2501.04778. DOI: 10.48550/arXiv.2501.04778. arXiv: 2501.04778 [astro-ph.HE].

[116] Marco Dall'Amico, Michela Mapelli, Stefano Torniamenti, et al. "Eccentric black hole mergers via three-body interactions in young, globular, and nuclear star clusters". In: 683, A186 (Mar. 2024), A186. DOI: 10.1051/0004-6361/202348745. arXiv: 2303.07421 [astro-ph.HE].

[117] Thibault Damour. "Coalescence of two spinning black holes: An effective one-body approach". In: 64.12 (Dec. 2001), p. 124013. DOI: 10.1103/PhysRevD.64.124013. arXiv: gr-qc/0103018 [gr-qc].

[118] Thibault Damour and J. H. Taylor. "Strong-field tests of relativistic gravity and binary pulsars". In: 45.6 (Mar. 1992), pp. 1840–1868. DOI: 10.1103/PhysRevD.45.1840.

[119] G. H. Darwin. "A tidal theory of the evolution of satellites". In: *The Observatory* 3 (July 1879), pp. 79–84.

[120] K. De et al. "A hot and fast ultra-stripped supernova that likely formed a compact neutron star binary". In: *Science* 362.6411 (Oct. 2018), pp. 201–206. DOI: 10.1126/science.aas8693. arXiv: 1810.05181 [astro-ph.HE].

[121] E. De Donder et al. "The relative frequency of type II and I_(b,c) supernovae and the birth rate of double compact star binaries". In: 333 (May 1998), pp. 557–564.

[122] Erwin De Donder et al. "The influence of binaries on galactic chemical evolution". In: 48.10 (Sept. 2004), pp. 861–975. DOI: 10.1016/j.newar.2004.07.001. arXiv: astro-ph/0410024 [astro-ph].

[123] M. de Kool. "Common Envelope Evolution and Double Cores of Planetary Nebulae". In: 358 (July 1990), p. 189. DOI: 10.1086/168974.

[124] C. De Loore et al. "Evolution of Massive Close Binaries. II: The Post X-Ray Binary Stage: Origin of Run-away and Binary Pulsars". In: 36.1 (Aug. 1975), pp. 219–225. DOI: 10.1007/BF00681952.

[125] Orsola De Marco et al. "On the α formalism for the common envelope interaction". In: 411.4 (Mar. 2011), pp. 2277–2292. DOI: 10.1111/j.1365-2966.2010.17891.x. arXiv: 1010.4374 [astro-ph.SR].

[126] S. E. de Mink, M. Cantiello, et al. "Rotational mixing in massive binaries. Detached short-period systems". In: 497.1 (Apr. 2009), pp. 243–253. DOI: 10.1051/0004-6361/200811439. arXiv: 0902.1751 [astro-ph.SR].

[127] S. E. de Mink and I. Mandel. "The chemically homogeneous evolutionary channel for binary black hole mergers: rates and properties of gravitational-wave events detectable by advanced LIGO". In: 460.4 (Aug. 2016), pp. 3545–3553. DOI: 10.1093/mnras/stw1219. arXiv: 1603.02291 [astro-ph.HE].

[128] S. Degl'Innocenti et al. "The FRANEC stellar evolutionary code". In: 316.1-4 (Aug. 2008), pp. 25–30. DOI: 10.1007/s10509-007-9560-2.

[129] R. J. Dewey et al. "A search for low-luminosity pulsars." In: 294 (July 1985), pp. L25–L29. DOI: 10.1086/184502.

[130] J. D. M. Dewi et al. "On the energy equation and efficiency parameter of the common envelope evolution". In: 360 (Aug. 2000), pp. 1043–1051. DOI: 10.48550/arXiv.astro-ph/0007034. arXiv: astro-ph/0007034 [astro-ph].

[131] Ugo N. Di Carlo et al. "Binary black holes in young star clusters: the impact of metallicity". In: 498.1 (Oct. 2020), pp. 495–506. DOI: 10.1093/mnras/staa2286. arXiv: 2004.09525 [astro-ph.HE].

[132] Rosanne Di Stefano et al. "SCATTER: A New Common Envelope Formalism". In: 944.1, 87 (Feb. 2023), p. 87. DOI: 10.3847/1538-4357/acae9b. arXiv: 2212.06770 [astro-ph.HE].

[133] Michal Dominik et al. "Double Compact Objects. I. The Significance of the Common Envelope on Merger Rates". In: 759.1, 52 (Nov. 2012), p. 52. DOI: 10.1088/0004-637X/759/1/52. arXiv: 1202.4901 [astro-ph.HE].

[134] Michal Dominik et al. "Double Compact Objects. II. Cosmological Merger Rates". In: 779.1, 72 (Dec. 2013), p. 72. DOI: 10.1088/0004-637X/779/1/72. arXiv: 1308.1546 [astro-ph.HE].

[135] Andris Dorozsmai et al. "Importance of stable mass transfer and stellar winds for the formation of gravitational wave sources". In: 530.4 (June 2024), pp. 3706–3739. DOI: 10.1093/mnras/stae152. arXiv: 2207.08837 [astro-ph.SR].

[136] Robert C. Duncan et al. "Formation of Very Strongly Magnetized Neutron Stars: Implications for Gamma-Ray Bursts". In: 392 (June 1992), p. L9. DOI: 10.1086/186413.

[137] R. T. Edwards et al. "The Swinburne intermediate-latitude pulsar survey". In: 326.1 (Sept. 2001), pp. 358–374. DOI: 10.1046/j.1365-8711.2001.04637.x. arXiv: astro-ph/0105126 [astro-ph].

[138] P. P. Eggleton. "Aproximations to the radii of Roche lobes." In: 268 (May 1983), pp. 368–369. DOI: 10.1086/160960.

[139] Peter Eggleton. *Evolutionary Processes in Binary and Multiple Stars*. 2006.

[140] Peter P. Eggleton. "The evolution of low mass stars". In: 151 (Jan. 1971), p. 351. DOI: 10.1093/mnras/151.3.351.

[141] Peter P. Eggleton. "Composition changes during stellar evolution". In: 156 (Jan. 1972), p. 361. DOI: 10.1093/mnras/156.3.361.

[142] S. Ekström et al. "Grids of stellar models with rotation. I. Models from 0.8 to 120 $M_{\odot}$ at solar metallicity (Z = 0.014)". In: 537, A146 (Jan. 2012), A146. DOI: 10.1051/0004-6361/201117751. arXiv: 1110.5049 [astro-ph.SR].

[143] J J Eldridge et al. "A consistent estimate for gravitational wave and electromagnetic transient rates". In: *Monthly Notices of the Royal Astronomical Society* 482.1 (Oct. 2018), pp. 870–880. DOI: 10.1093/mnras/sty2714. eprint: https://academic.oup.com/mnras/article-pdf/482/1/870/26182720/sty2714.pdf. URL: https://doi.org/10.1093/mnras/sty2714.

[144] EPTA Collaboration et al. "The second data release from the European Pulsar Timing Array. III. Search for gravitational wave signals". In: 678, A50 (Oct. 2023), A50. DOI: 10.1051/0004-6361/202346844. arXiv: 2306.16214 [astro-ph.HE].

[145] T. Ertl et al. "The Explosion of Helium Stars Evolved with Mass Loss". In: 890.1, 51 (Feb. 2020), p. 51. DOI: 10.3847/1538-4357/ab6458. arXiv: 1910.01641 [astro-ph.HE].

[146] Rosa Wallace Everson et al. "The Energy Sharing Timescale in an Analytic Framework for Common Envelope Hydrodynamics". In: 979.1, L11 (Jan. 2025), p. L11. DOI: 10.3847/2041-8213/ada0ae. arXiv: 2410.07036 [astro-ph.HE].

[147] R. Farmer et al. "Mind the Gap: The Location of the Lower Edge of the Pair-instability Supernova Black Hole Mass Gap". In: 887.1, 53 (Dec. 2019), p. 53. DOI: 10.3847/1538-4357/ab518b. arXiv: 1910.12874 [astro-ph.SR].

[148] Will M. Farr et al. "The Mass Distribution of Stellar-mass Black Holes". In: 741.2, 103 (Nov. 2011), p. 103. DOI: 10.1088/0004-637X/741/2/103. arXiv: 1011.1459 [astro-ph.GA].

[149] Claude-André Faucher-Giguère et al. "Birth and Evolution of Isolated Radio Pulsars". In: 643.1 (May 2006), pp. 332–355. DOI: 10.1086/501516. arXiv: astro-ph/0512585 [astro-ph].

[150] A. J. Faulkner et al. “The Parkes Multibeam Pulsar Survey - V. Finding binary and millisecond pulsars”. In: 355.1 (Nov. 2004), pp. 147–158. DOI: 10.1111/j.1365-2966.2004.08310.x. arXiv: astro-ph/0408228 [astro-ph].

[151] Maya Fishbach. “Probing cosmic chemical enrichment with next-generation gravitational-wave observatories”. In: *Classical and Quantum Gravity* 42.5, 055009 (Mar. 2025), p. 055009. DOI: 10.1088/1361-6382/adaf70. arXiv: 2411.08658 [astro-ph.HE].

[152] B. P. Flannery et al. “On the origin of the binary pulsar PSR 1913+16.” In: 39 (Feb. 1975), pp. 61–67.

[153] William A. Fowler et al. “Neutrino Processes and Pair Formation in Massive Stars and Supernovae.” In: 9 (Dec. 1964), p. 201. DOI: 10.1086/190103.

[154] Tassos Fragos et al. “POSYDON: A General-purpose Population Synthesis Code with Detailed Binary-evolution Simulations”. In: 264.2, 45 (Feb. 2023), p. 45. DOI: 10.3847/1538-4365/ac90c1. arXiv: 2202.05892 [astro-ph.SR].

[155] P. C. Freire et al. “Timing the millisecond pulsars in 47 Tucanae”. In: 326.3 (Sept. 2001), pp. 901–915. DOI: 10.1046/j.1365-8711.2001.04493.x. arXiv: astro-ph/0103372 [astro-ph].

[156] Chris L. Fryer et al. “Compact Remnant Mass Function: Dependence on the Explosion Mechanism and Metallicity”. In: 749.1, 91 (Apr. 2012), p. 91. DOI: 10.1088/0004-637X/749/1/91. arXiv: 1110.1726 [astro-ph.SR].

[157] Gaia Collaboration et al. “Discovery of a dormant 33 solar-mass black hole in pre-release Gaia astrometry”. In: 686, L2 (June 2024), p. L2. DOI: 10.1051/0004-6361/202449763. arXiv: 2404.10486 [astro-ph.GA].

[158] Monica Gallegos-Garcia, Christopher P. L. Berry, et al. “Binary Black Hole Formation with Detailed Modeling: Stable Mass Transfer Leads to Lower Merger Rates”. In: 922.2, 110 (Dec. 2021), p. 110. DOI: 10.3847/1538-4357/ac2610. arXiv: 2107.05702 [astro-ph.HE].

[159] Monica Gallegos-Garcia, Maya Fishbach, et al. “Do High-spin High-mass X-Ray Binaries Contribute to the Population of Merging Binary Black Holes?” In: 938.2, L19 (Oct. 2022), p. L19. DOI: 10.3847/2041-8213/ac96ef. arXiv: 2207.14290 [astro-ph.HE].

[160] Hongwei Ge, Michael S. Hjellming, et al. “Adiabatic Mass Loss in Binary Stars. I. Computational Method”. In: 717.2 (July 2010), pp. 724–738. DOI: 10.1088/0004-637X/717/2/724. arXiv: 1005.3099 [astro-ph.SR].

[161] Hongwei Ge, Ronald F. Webbink, et al. “Adiabatic Mass Loss in Binary Stars. II. From Zero-age Main Sequence to the Base of the Giant Branch”. In: 812.1, 40 (Oct. 2015), p. 40. DOI: 10.1088/0004-637X/812/1/40. arXiv: 1507.04843 [astro-ph.SR].

[162] Hongwei Ge, Ronald F. Webbink, et al. “Adiabatic Mass Loss in Binary Stars. III. From the Base of the Red Giant Branch to the Tip of the Asymptotic Giant Branch”. In: 899.2, 132 (Aug. 2020), p. 132. DOI: 10.3847/1538-4357/aba7b7. arXiv: 2007.09848 [astro-ph.SR].

[163] C. Georgy et al. “Grids of stellar models with rotation. II. WR populations and supernovae/GRB progenitors at Z = 0.014”. In: 542, A29 (June 2012), A29. DOI: 10.1051/0004-6361/201118340. arXiv: 1203.5243 [astro-ph.SR].

[164] Nicola Giacobbo and Michela Mapelli. “The progenitors of compact-object binaries: impact of metallicity, common envelope and natal kicks”. In: 480.2 (Oct. 2018), pp. 2011–2030. DOI: 10.1093/mnras/sty1999. arXiv: 1806.00001 [astro-ph.HE].

[165] Nicola Giacobbo and Michela Mapelli. "Revising Natal Kick Prescriptions in Population Synthesis Simulations". In: 891.2, 141 (Mar. 2020), p. 141. DOI: 10.3847/1538-4357/ab7335. arXiv: 1909.06385 [astro-ph.HE].

[166] Nicola Giacobbo, Michela Mapelli, and Mario Spera. "Merging black hole binaries: the effects of progenitor's metallicity, mass-loss rate and Eddington factor". In: 474.3 (Mar. 2018), pp. 2959–2974. DOI: 10.1093/mnras/stx2933. arXiv: 1711.03556 [astro-ph.SR].

[167] Peter Goldreich and William H. Julian. "Pulsar Electrodynamics". In: 157 (Aug. 1969), p. 869. DOI: 10.1086/150119.

[168] Peter Goldreich and Andreas Reisenegger. "Magnetic Field Decay in Isolated Neutron Stars". In: 395 (Aug. 1992), p. 250. DOI: 10.1086/171646.

[169] Peter L. Gonthier et al. "Role of Beam Geometry in Population Statistics and Pulse Profiles of Radio and Gamma-Ray Pulsars". In: 604.2 (Apr. 2004), pp. 775–790. DOI: 10.1086/382070. arXiv: astro-ph/0312565 [astro-ph].

[170] John Goodricke. "A Series of Observations on, and a Discovery of, the Period of the Variation of the Light of the Bright Star in the Head of Medusa, Called Algol. In a Letter from John Goodricke, Esq. to the Rev. Anthony Shepherd, D. D. F. R. S. and Plumian Professor at Cambridge". In: *Philosophical Transactions of the Royal Society of London Series I* 73 (Jan. 1783), pp. 474–482.

[171] V. Grisoni et al. "The AMBRE project: chemical evolution models for the Milky Way thick and thin discs". In: 472.3 (Dec. 2017), pp. 3637–3647. DOI: 10.1093/mnras/stx2201. arXiv: 1706.02614 [astro-ph.GA].

[172] C. Gruppioni et al. "The ALPINE-ALMA [CII] survey. The nature, luminosity function, and star formation history of dusty galaxies up to z 6". In: 643, A8 (Nov. 2020), A8. DOI: 10.1051/0004-6361/202038487. arXiv: 2006.04974 [astro-ph.GA].

[173] J. E. Gunn et al. "On the Nature of Pulsars. III. Analysis of Observations". In: 160 (June 1970), p. 979. DOI: 10.1086/150487.

[174] Evan D. Hall et al. "Metrics for next-generation gravitational-wave detectors". In: *Classical and Quantum Gravity* 36.22, 225002 (Nov. 2019), p. 225002. DOI: 10.1088/1361-6382/ab41d6. arXiv: 1902.09485 [astro-ph.IM].

[175] C. G. T. Haslam et al. "A 408 MHz all-sky continuum survey. I - Observations at southern declinations and for the North Polar region." In: 100 (July 1981), pp. 209–219.

[176] A. Heger et al. "The Nucleosynthetic Signature of Population III". In: 567.1 (Mar. 2002), pp. 532–543. DOI: 10.1086/338487. arXiv: astro-ph/0107037 [astro-ph].

[177] Jason W. T. Hessels et al. "A Radio Pulsar Spinning at 716 Hz". In: *Science* 311.5769 (Mar. 2006), pp. 1901–1904. DOI: 10.1126/science.1123430. arXiv: astro-ph/0601337 [astro-ph].

[178] A. Hewish et al. "Observation of a Rapidly Pulsating Radio Source". In: 217.5130 (Feb. 1968), pp. 709–713. DOI: 10.1038/217709a0.

[179] Ryosuke Hirai et al. "A Two-stage Formalism for Common-envelope Phases of Massive Stars". In: 937.2, L42 (Oct. 2022), p. L42. DOI: 10.3847/2041-8213/ac9519. arXiv: 2209.05328 [astro-ph.SR].

[180] Michael S. Hjellming et al. "Thresholds for Rapid Mass Transfer in Binary System. I. Polytropic Models". In: 318 (July 1987), p. 794. DOI: 10.1086/165412.

[181] G. Hobbs et al. “A statistical study of 233 pulsar proper motions”. In: *Monthly Notices of the Royal Astronomical Society* 360.3 (July 2005), pp. 974–992. DOI: 10.1111/j.1365-2966.2005.09087.x. arXiv: https://academic.oup.com/mnras/article-pdf/360/3/974/3209564/360-3-974.pdf [astro-ph]. URL: https://doi.org/10.1111/j.1365-2966.2005.09087.x.

[182] Su-Shu Huang. “Modes of Mass Ejection by Binary Stars and the Effect on Their Orbital Periods.” In: 138 (Aug. 1963), p. 471. DOI: 10.1086/147659.

[183] R. A. Hulse et al. “Discovery of a pulsar in a binary system.” In: 195 (Jan. 1975), pp. L51–L53. DOI: 10.1086/181708.

[184] Leslie Hunt et al. “Coevolution of metallicity and star formation in galaxies to z 3.7 - II. A theoretical model”. In: 463.2 (Dec. 2016), pp. 2020–2031. DOI: 10.1093/mnras/stw2091. arXiv: 1608.05418 [astro-ph.GA].

[185] Jarrod R. Hurley, Onno R. Pols, et al. “Comprehensive analytic formulae for stellar evolution as a function of mass and metallicity”. In: 315.3 (July 2000), pp. 543–569. DOI: 10.1046/j.1365-8711.2000.03426.x. arXiv: astro-ph/0001295 [astro-ph].

[186] Jarrod R. Hurley, Christopher A. Tout, et al. “Evolution of binary stars and the effect of tides on binary populations”. In: 329.4 (Feb. 2002), pp. 897–928. DOI: 10.1046/j.1365-8711.2002.05038.x. arXiv: astro-ph/0201220 [astro-ph].

[187] P. Hut. “Tidal evolution in close binary systems.” In: 99 (June 1981), pp. 126–140.

[188] Roberto Iaconi et al. “Speaking with one voice: simulations and observations discuss the common envelope α parameter”. In: 490.2 (Dec. 2019), pp. 2550–2566. DOI: 10.1093/mnras/stz2756. arXiv: 1902.02039 [astro-ph.SR].

[189] Icko Iben Jr. et al. “Common Envelopes in Binary Star Evolution”. In: 105 (Dec. 1993), p. 1373. DOI: 10.1086/133321.

[190] Andrei P. Igoshev et al. “Initial periods and magnetic fields of neutron stars”. In: 514.3 (Aug. 2022), pp. 4606–4619. DOI: 10.1093/mnras/stac1648. arXiv: 2205.06823 [astro-ph.HE].

[191] A. F. Illarionov et al. “Why the Number of Galactic X-ray Stars Is so Small?” In: 39 (Feb. 1975), p. 185.

[192] Giuliano Iorio et al. “Compact object mergers: exploring uncertainties from stellar and binary evolution with SEVN”. In: 524.1 (Sept. 2023), pp. 426–470. DOI: 10.1093/mnras/stad1630. arXiv: 2211.11774 [astro-ph.HE]. URL: https://doi.org/10.1093/mnras/stad1630.

[193] N. Ivanova and S. Chaichenets. “Common Envelope: Enthalpy Consideration”. In: 731.2, L36 (Apr. 2011), p. L36. DOI: 10.1088/2041-8205/731/2/L36. arXiv: 1103.2790 [astro-ph.SR].

[194] N. Ivanova, S. Justham, X. Chen, et al. “Common envelope evolution: where we stand and how we can move forward”. In: 21, 59 (Feb. 2013), p. 59. DOI: 10.1007/s00159-013-0059-2. arXiv: 1209.4302 [astro-ph.HE].

[195] N. Ivanova, S. Justham, J. L. Avendano Nandez, et al. “Identification of the Long-Sought Common-Envelope Events”. In: *Science* 339.6118 (2013), pp. 433–435. DOI: 10.1126/science.1225540. eprint: https://www.science.org/doi/pdf/10.1126/science.1225540. URL: https://www.science.org/doi/abs/10.1126/science.1225540.

[196] N. Ivanova, Ph. Podsiadlowski, et al. “Hydrodynamical simulations of the stream-core interaction in the slow merger of massive stars”. In: 334.4 (Aug. 2002), pp. 819–832. DOI: 10.1046/j.1365-8711.2002.05543.x. arXiv: astro-ph/0109524 [astro-ph].

[197] R. G. Izzard, L. M. Dray, et al. “Population nucleosynthesis in single and binary stars. I. Model”. In: 460.2 (Dec. 2006), pp. 565–572. DOI: 10.1051/0004-6361:20066129.

[198] R. G. Izzard, E. Glebbeek, et al. "Population synthesis of binary carbon-enhanced metal-poor stars". In: 508.3 (Dec. 2009), pp. 1359–1374. DOI: 10.1051/0004-6361/200912827. arXiv: 0910.2158 [astro-ph.SR].

[199] Robert G. Izzard, Christopher A. Tout, et al. "A new synthetic model for asymptotic giant branch stars". In: 350.2 (May 2004), pp. 407–426. DOI: 10.1111/j.1365-2966.2004.07446.x. arXiv: astro-ph/0402403 [astro-ph].

[200] H. -T. Janka and E. Mueller. "Neutron star recoils from anisotropic supernovae." In: 290 (Oct. 1994), pp. 496–502.

[201] Hans-Thomas Janka. "Explosion Mechanisms of Core-Collapse Supernovae". In: *Annual Review of Nuclear and Particle Science* 62.1 (Nov. 2012), pp. 407–451. DOI: 10.1146/annurev-nucl-102711-094901. arXiv: 1206.2503 [astro-ph.SR].

[202] S. Janssens et al. "Uncovering astrometric black hole binaries with massive main-sequence companions with Gaia". In: 658, A129 (Feb. 2022), A129. DOI: 10.1051/0004-6361/202141866. arXiv: 2111.06427 [astro-ph.SR].

[203] Jiachen Jiang. "Fifty Years After the Discovery of the First Stellar-Mass Black Hole: A Review of Cyg X-1". In: *Galaxies* 12.6, 80 (Nov. 2024), p. 80. DOI: 10.3390/galaxies12060080. arXiv: 2411.12507 [astro-ph.HE].

[204] Vicky Kalogera and Gordon Baym. "The Maximum Mass of a Neutron Star". In: 470 (Oct. 1996), p. L61. DOI: 10.1086/310296. arXiv: astro-ph/9608059 [astro-ph].

[205] Vicky Kalogera, B. S. Sathyaprakash, et al. "The Next Generation Global Gravitational Wave Observatory: The Science Book". In: *arXiv e-prints*, arXiv:2111.06990 (Nov. 2021), arXiv:2111.06990. DOI: 10.48550/arXiv.2111.06990. arXiv: 2111.06990 [gr-qc].

[206] Veome Kapil et al. "Calibration of neutron star natal kick velocities to isolated pulsar observations". In: 519.4 (Mar. 2023), pp. 5893–5901. DOI: 10.1093/mnras/stad019. arXiv: 2209.09252 [astro-ph.HE].

[207] Victoria M. Kaspi. "Grand unification of neutron stars". In: *Proceedings of the National Academy of Science* 107.16 (Apr. 2010), pp. 7147–7152. DOI: 10.1073/pnas.1000812107. arXiv: 1005.0876 [astro-ph.HE].

[208] Victoria M. Kaspi and Andrei M. Beloborodov. "Magnetars". In: 55.1 (Aug. 2017), pp. 261–301. DOI: 10.1146/annurev-astro-081915-023329. arXiv: 1703.00068 [astro-ph.HE].

[209] A. Kawka et al. "New binaries among UV-selected, hot subdwarf stars and population properties". In: 450.4 (July 2015), pp. 3514–3548. DOI: 10.1093/mnras/stv821. arXiv: 1504.03241 [astro-ph.SR].

[210] E. Keane, B. Bhattacharyya, et al. "A Cosmic Census of Radio Pulsars with the SKA". In: *Advancing Astrophysics with the Square Kilometre Array (AASKA14)*. Apr. 2015, 40, p. 40. DOI: 10.22323/1.215.0040. arXiv: 1501.00056 [astro-ph.IM].

[211] E. F. Keane, M. Kramer, et al. "Rotating Radio Transients: new discoveries, timing solutions and musings". In: 415.4 (Aug. 2011), pp. 3065–3080. DOI: 10.1111/j.1365-2966.2011.18917.x. arXiv: 1104.2727 [astro-ph.SR].

[212] M. J. Keith, R. P. Eatough, et al. "Discovery of 28 pulsars using new techniques for sorting pulsar candidates". In: 395.2 (May 2009), pp. 837–846. DOI: 10.1111/j.1365-2966.2009.14543.x. arXiv: 0901.3570 [astro-ph.SR].

[213] M. J. Keith, A. Jameson, et al. "The High Time Resolution Universe Pulsar Survey - I. System configuration and initial discoveries". In: 409.2 (Dec. 2010), pp. 619–627. DOI: 10.1111/j.1365-2966.2010.17325.x. arXiv: 1006.5744 [astro-ph.HE].

[214] Paul D. Kiel et al. "Populating the Galaxy with pulsars – I. Stellar and binary evolution". In: *Monthly Notices of the Royal Astronomical Society* 388.1 (July 2008), pp. 393–415. DOI: 10.1111/j.1365-2966.2008.13402.x. eprint: https://academic.oup.com/mnras/article-pdf/388/1/393/18722056/mnras0388-0393.pdf. URL: https://doi.org/10.1111/j.1365-2966.2008.13402.x.

[215] R. Kippenhahn et al. "Entwicklung in engen Doppelsternsystemen I. Massenaustausch vor und nach Beendigung des zentralen Wasserstoff-Brennens". In: 65 (Jan. 1967), p. 251.

[216] Bülent Kiziltan et al. "The Neutron Star Mass Distribution". In: 778.1, 66 (Nov. 2013), p. 66. DOI: 10.1088/0004-637X/778/1/66. arXiv: 1011.4291 [astro-ph.GA].

[217] J. Klencki, M. Moe, et al. "Impact of inter-correlated initial binary parameters on double black hole and neutron star mergers". In: 619, A77 (Nov. 2018), A77. DOI: 10.1051/0004-6361/201833025. arXiv: 1808.07889 [astro-ph.HE].

[218] Jakub Klencki, Gijs Nelemans, Alina G. Istrate, and Martyna Chruslinska. "It has to be cool: Supergiant progenitors of binary black hole mergers from common-envelope evolution". In: 645, A54 (Jan. 2021), A54. DOI: 10.1051/0004-6361/202038707. arXiv: 2006.11286 [astro-ph.SR].

[219] Jakub Klencki, Gijs Nelemans, Alina G. Istrate, and Onno Pols. "Massive donors in interacting binaries: effect of metallicity". In: 638, A55 (June 2020), A55. DOI: 10.1051/0004-6361/202037694. arXiv: 2004.00628 [astro-ph.SR].

[220] Chiaki Kobayashi et al. "Can Neutron Star Mergers Alone Explain the r-process Enrichment of the Milky Way?" In: 943.2, L12 (Feb. 2023), p. L12. DOI: 10.3847/2041-8213/acad82. arXiv: 2211.04964 [astro-ph.HE].

[221] Henry A. Kobulnicky et al. "A New Look at the Binary Characteristics of Massive Stars". In: 670.1 (Nov. 2007), pp. 747–765. DOI: 10.1086/522073.

[222] Sushan Konar. "Magnetic Fields of Neutron Stars". In: *Journal of Astrophysics and Astronomy* 38.3, 47 (Sept. 2017), p. 47. DOI: 10.1007/s12036-017-9467-4. arXiv: 1709.07106 [astro-ph.HE].

[223] Sushan Konar and Dipankar Bhattacharya. "Magnetic field evolution of accreting neutron stars". In: *Monthly Notices of the Royal Astronomical Society* 284.2 (Jan. 1997), pp. 311–317. DOI: 10.1093/mnras/284.2.311. eprint: https://academic.oup.com/mnras/article-pdf/284/2/311/18199846/284-2-311.pdf. URL: https://doi.org/10.1093/mnras/284.2.311.

[224] Sushan Konar and Dipankar Bhattacharya. "Magnetic field evolution of accreting neutron stars — II". In: *Monthly Notices of the Royal Astronomical Society* 303.3 (Mar. 1999), pp. 588–594. DOI: 10.1046/j.1365-8711.1999.02287.x. eprint: https://academic.oup.com/mnras/article-pdf/303/3/588/3219432/303-3-588.pdf. URL: https://doi.org/10.1046/j.1365-8711.1999.02287.x.

[225] V. I. Kondratiev et al. "New Limits on Radio Emission from X-ray Dim Isolated Neutron Stars". In: 702.1 (Sept. 2009), pp. 692–706. DOI: 10.1088/0004-637X/702/1/692. arXiv: 0907.0054 [astro-ph.GA].

[226] M Kramer and N Wex. "TOPICAL REVIEW: The double pulsar system: a unique laboratory for gravity". In: *Classical and Quantum Gravity* 26.7, 073001 (Apr. 2009), p. 073001. DOI: 10.1088/0264-9381/26/7/073001.

[227] M. Kramer et al. "Tests of General Relativity from Timing the Double Pulsar". In: *Science* 314.5796 (Oct. 2006), pp. 97–102. DOI: 10.1126/science.1132305. arXiv: astro-ph/0609417 [astro-ph].

[228] M. Kramer et al. "Strong-Field Gravity Tests with the Double Pulsar". In: *Physical Review X* 11.4, 041050 (Oct. 2021), p. 041050. DOI: 10.1103/PhysRevX.11.041050. arXiv: 2112.06795 [astro-ph.HE].

[229] Pavel Kroupa. "On the variation of the initial mass function". In: 322.2 (Apr. 2001), pp. 231–246. DOI: 10.1046/j.1365-8711.2001.04022.x. arXiv: astro-ph/0009005 [astro-ph].

[230] M. U. Kruckow, Patrick G. Neunteufel, et al. "A Catalog of Potential Post-Common Envelope Binaries". In: 920.2, 86 (Oct. 2021), p. 86. DOI: 10.3847/1538-4357/ac13ac. arXiv: 2107.05221 [astro-ph.SR].

[231] M. U. Kruckow, T. M. Tauris, N. Langer, D. Szécsi, et al. "Common-envelope ejection in massive binary stars. Implications for the progenitors of GW150914 and GW151226". In: 596, A58 (Nov. 2016), A58. DOI: 10.1051/0004-6361/201629420. arXiv: 1610.04417 [astro-ph.SR].

[232] M. U. Kruckow, Thomas M. Tauris, Norbert Langer, Michael Kramer, et al. "Progenitors of gravitational wave mergers: binary evolution with the stellar grid-based code COMBINE". In: 481.2 (Dec. 2018), pp. 1908–1949. DOI: 10.1093/mnras/sty2190. arXiv: 1801.05433 [astro-ph.SR].

[233] Matthias U. Kruckow, Jeff J. Andrews, et al. "The formation of black holes in non-interacting isolated binaries: Gaia black holes as calibrators of stellar winds from massive stars". In: 692, A141 (Dec. 2024), A141. DOI: 10.1051/0004-6361/202452356. arXiv: 2410.18501 [astro-ph.SR].

[234] A. Kruszewski. "Exchange of Matter in Close Binary Systems III. Changes in Period Caused by Exchange of Matter". In: 14 (Jan. 1964), p. 241.

[235] Rolf-Peter Kudritzki et al. "Winds from Hot Stars". In: 38 (Jan. 2000), pp. 613–666. DOI: 10.1146/annurev.astro.38.1.613.

[236] S. R. Kulkarni. "Optical Identification of Binary Pulsars: Implications for Magnetic Field Decay in Neutron Stars". In: 306 (July 1986), p. L85. DOI: 10.1086/184711.

[237] Dong Lai et al. "Pulsar Jets: Implications for Neutron Star Kicks and Initial Spins". In: 549.2 (Mar. 2001), pp. 1111–1118. DOI: 10.1086/319455. arXiv: astro-ph/0007272 [astro-ph].

[238] A. Lamberts et al. "Predicting the binary black hole population of the Milky Way with cosmological simulations". In: 480.2 (Oct. 2018), pp. 2704–2718. DOI: 10.1093/mnras/sty2035. arXiv: 1801.03099 [astro-ph.GA].

[239] Andrea Lapi et al. "Semi-empirical Models of Galaxy Formation and Evolution". In: *arXiv e-prints*, arXiv:2502.12764 (Feb. 2025), arXiv:2502.12764. DOI: 10.48550/arXiv.2502.12764. arXiv: 2502.12764 [astro-ph.GA].

[240] Mike Y M Lau et al. "Common envelopes in massive stars: towards the role of radiation pressure and recombination energy in ejecting red supergiant envelopes". In: *Monthly Notices of the Royal Astronomical Society* 512.4 (Jan. 2022), pp. 5462–5480. DOI: 10.1093/mnras/stac049. eprint: https://academic.oup.com/mnras/article-pdf/512/4/5462/43411018/stac049.pdf. URL: https://doi.org/10.1093/mnras/stac049.

[241] Jamie A. P. Law-Smith et al. "Successful Common Envelope Ejection and Binary Neutron Star Formation in 3D Hydrodynamics". In: *arXiv e-prints*, arXiv:2011.06630 (Nov. 2020), arXiv:2011.06630. DOI: 10.48550/arXiv.2011.06630. arXiv: 2011.06630 [astro-ph.HE].

[242] Hugo Levato et al. "Stellar Multiplicity in the Scorpius-Centaurus Association". In: 64 (June 1987), p. 487. DOI: 10.1086/191204.

[243] Timothy C. Licquia et al. “Improved Estimates of the Milky Way’s Stellar Mass and Star Formation Rate from Hierarchical Bayesian Meta-Analysis”. In: 806.1, 96 (June 2015), p. 96. DOI: 10.1088/0004-637X/806/1/96. arXiv: 1407.1078 [astro-ph.GA].

[244] Mario Livio et al. “The Common Envelope Phase in the Evolution of Binary Stars”. In: 329 (June 1988), p. 764. DOI: 10.1086/166419.

[245] D. R. Lorimer and M. Kramer. *Handbook of Pulsar Astronomy*. Vol. 4. 2004.

[246] Duncan Lorimer. “PSRPOP: Pulsar Population Modelling Programs”. In: *Astrophysics Source Code Library* (July 2011), pp. 07019–.

[247] Duncan R. Lorimer. “Binary and Millisecond Pulsars”. In: *Living Reviews in Relativity* 11.1, 8 (Nov. 2008), p. 8. DOI: 10.12942/lrr-2008-8. arXiv: 0811.0762 [astro-ph].

[248] Ryan S. Lynch et al. “The Timing of Nine Globular Cluster Pulsars”. In: 745.2, 109 (Feb. 2012), p. 109. DOI: 10.1088/0004-637X/745/2/109. arXiv: 1112.2612 [astro-ph.HE].

[249] A. G. Lyne, M. Burgay, et al. “A Double-Pulsar System: A Rare Laboratory for Relativistic Gravity and Plasma Physics”. In: *Science* 303.5661 (Feb. 2004), pp. 1153–1157. DOI: 10.1126/science.1094645. arXiv: astro-ph/0401086 [astro-ph].

[250] A. G. Lyne and R. N. Manchester. “The shape of pulsar radio beams.” In: 234 (Oct. 1988), pp. 477–508. DOI: 10.1093/mnras/234.3.477.

[251] A. G. Lyne, R. N. Manchester, et al. “An eclipsing millisecond pulsar in the globular cluster Terzan 5”. In: 347.6294 (Oct. 1990), pp. 650–652. DOI: 10.1038/347650a0.

[252] A. G. Lyne, S. H. Mankelow, et al. “Radio pulsars in Terzan 5”. In: 316.3 (Aug. 2000), pp. 491–493. DOI: 10.1046/j.1365-8711.2000.03517.x. arXiv: astro-ph/0003070 [astro-ph].

[253] Andrew Lyne, George Hobbs, et al. “Switched Magnetospheric Regulation of Pulsar Spin-Down”. In: *Science* 329.5990 (July 2010), p. 408. DOI: 10.1126/science.1186683. arXiv: 1006.5184 [astro-ph.GA].

[254] Morgan MacLeod, Andrea Antoni, et al. “Common Envelope Wind Tunnel: Coefficients of Drag and Accretion in a Simplified Context for Studying Flows around Objects Embedded within Stellar Envelopes”. In: *The Astrophysical Journal* 838.1, 56 (Mar. 2017), p. 56. DOI: 10.3847/1538-4357/aa6117. arXiv: 1704.02372 [astro-ph.SR]. URL: https://dx.doi.org/10.3847/1538-4357/aa6117.

[255] Morgan MacLeod and Enrico Ramirez-Ruiz. “Asymmetric Accretion Flows within a Common Envelope”. In: 803.1, 41 (Apr. 2015), p. 41. DOI: 10.1088/0004-637X/803/1/41. arXiv: 1410.3823 [astro-ph.SR].

[256] Piero Madau and Mark Dickinson. “Cosmic Star-Formation History”. In: 52 (Aug. 2014), pp. 415–486. DOI: 10.1146/annurev-astro-081811-125615. arXiv: 1403.0007 [astro-ph.CO].

[257] Piero Madau and Tassos Fragos. “Radiation Backgrounds at Cosmic Dawn: X-Rays from Compact Binaries”. In: 840.1, 39 (May 2017), p. 39. DOI: 10.3847/1538-4357/aa6af9. arXiv: 1606.07887 [astro-ph.GA].

[258] R. Maiolino et al. “De re metallica: the cosmic chemical evolution of galaxies”. In: 27.1, 3 (Feb. 2019), p. 3. DOI: 10.1007/s00159-018-0112-2. arXiv: 1811.09642 [astro-ph.GA].

[259] R. N. Manchester, G. B. Hobbs, et al. “The Australia Telescope National Facility Pulsar Catalogue”. In: 129.4 (Apr. 2005), pp. 1993–2006. DOI: 10.1086/428488. arXiv: astro-ph/0412641 [astro-ph].

[260] R. N. Manchester, A. G. Lyne, F. Camilo, et al. "The Parkes multi-beam pulsar survey - I. Observing and data analysis systems, discovery and timing of 100 pulsars". In: 328.1 (Nov. 2001), pp. 17–35. DOI: 10.1046/j.1365-8711.2001.04751.x. arXiv: astro-ph/0106522 [astro-ph].

[261] R. N. Manchester, A. G. Lyne, N. D'Amico, et al. "A 5.75-millisecond pulsar in the globular cluster 47 Tucanae". In: 345.6276 (June 1990), pp. 598–600. DOI: 10.1038/345598a0.

[262] R. N. Manchester, A. G. Lyne, C. Robinson, et al. "Discovery of ten millisecond pulsars in the globular cluster 47 Tucanae". In: 352.6332 (July 1991), pp. 219–221. DOI: 10.1038/352219a0.

[263] Richard N. Manchester and Joseph H. Taylor. *Pulsars*. 1977.

[264] Ilya Mandel et al. "Rates of compact object coalescences". In: *Living Reviews in Relativity* 25.1, 1 (Dec. 2022), p. 1. DOI: 10.1007/s41114-021-00034-3. arXiv: 2107.14239 [astro-ph.HE].

[265] F. Mannucci, G. Cresci, et al. "A fundamental relation between mass, star formation rate and metallicity in local and high-redshift galaxies". In: 408.4 (Nov. 2010), pp. 2115–2127. DOI: 10.1111/j.1365-2966.2010.17291.x. arXiv: 1005.0006 [astro-ph.CO].

[266] F. Mannucci, R. Salvaterra, et al. "The metallicity of the long GRB hosts and the fundamental metallicity relation of low-mass galaxies". In: 414.2 (June 2011), pp. 1263–1268. DOI: 10.1111/j.1365-2966.2011.18459.x. arXiv: 1011.4506 [astro-ph.CO].

[267] M. Mapelli, E. Ripamonti, et al. "Ultra-luminous X-ray sources and remnants of massive metal-poor stars". In: 408.1 (Oct. 2010), pp. 234–253. DOI: 10.1111/j.1365-2966.2010.17048.x. arXiv: 1005.3548 [astro-ph.CO].

[268] Michela Mapelli. "Massive black hole binaries from runaway collisions: the impact of metallicity". In: 459.4 (July 2016), pp. 3432–3446. DOI: 10.1093/mnras/stw869. arXiv: 1604.03559 [astro-ph.GA].

[269] Michela Mapelli. "Binary black hole mergers: formation and populations". In: *Frontiers in Astronomy and Space Sciences* 7, 38 (July 2020), p. 38. DOI: 10.3389/fspas.2020.00038. arXiv: 2105.12455 [astro-ph.HE].

[270] Michela Mapelli. "Formation Channels of Single and Binary Stellar-Mass Black Holes". In: *Handbook of Gravitational Wave Astronomy*. Ed. by Cosimo Bambi et al. 2021, 16, p. 16. DOI: 10.1007/978-981-15-4702-7_16-1.

[271] Michela Mapelli, Yann Bouffanais, et al. "The cosmic evolution of binary black holes in young, globular, and nuclear star clusters: rates, masses, spins, and mixing fractions". In: 511.4 (Apr. 2022), pp. 5797–5816. DOI: 10.1093/mnras/stac422. arXiv: 2109.06222 [astro-ph.HE].

[272] Michela Mapelli and Nicola Giacobbo. "The cosmic merger rate of neutron stars and black holes". In: 479.4 (Oct. 2018), pp. 4391–4398. DOI: 10.1093/mnras/sty1613. arXiv: 1806.04866 [astro-ph.HE].

[273] Michela Mapelli, Nicola Giacobbo, Emanuele Ripamonti, et al. "The cosmic merger rate of stellar black hole binaries from the Illustris simulation". In: 472.2 (Dec. 2017), pp. 2422–2435. DOI: 10.1093/mnras/stx2123. arXiv: 1708.05722 [astro-ph.GA].

[274] Michela Mapelli, Nicola Giacobbo, Filippo Santoliquido, et al. "The properties of merging black holes and neutron stars across cosmic time". In: 487.1 (July 2019), pp. 2–13. DOI: 10.1093/mnras/stz1150. arXiv: 1902.01419 [astro-ph.HE].

[275] Michela Mapelli, Mario Spera, et al. "Impact of the Rotation and Compactness of Progenitors on the Mass of Black Holes". In: 888.2, 76 (Jan. 2020), p. 76. DOI: 10.3847/1538-4357/ab584d. arXiv: 1909.01371 [astro-ph.HE].

[276] Pablo Marchant and Julia Bodensteiner. "The Evolution of Massive Binary Stars". In: 62.1 (Sept. 2024), pp. 21–61. DOI: 10.1146/annurev-astro-052722-105936. arXiv: 2311.01865 [astro-ph.SR].

[277] Pablo Marchant, Norbert Langer, et al. "A new route towards merging massive black holes". In: 588, A50 (Apr. 2016), A50. DOI: 10.1051/0004-6361/201628133. arXiv: 1601.03718 [astro-ph.SR].

[278] Pablo Marchant and Takashi J. Moriya. "The impact of stellar rotation on the black hole mass-gap from pair-instability supernovae". In: 640, L18 (Aug. 2020), p. L18. DOI: 10.1051/0004-6361/202038902. arXiv: 2007.06220 [astro-ph.HE].

[279] Pablo Marchant, Kaliroë M. W. Pappas, et al. "The role of mass transfer and common envelope evolution in the formation of merging binary black holes". In: 650, A107 (June 2021), A107. DOI: 10.1051/0004-6361/202039992. arXiv: 2103.09243 [astro-ph.SR].

[280] Pablo Marchant, Mathieu Renzo, et al. "Pulsational Pair-instability Supernovae in Very Close Binaries". In: 882.1, 36 (Sept. 2019), p. 36. DOI: 10.3847/1538-4357/ab3426. arXiv: 1810.13412 [astro-ph.HE].

[281] Ben Margalit et al. "Constraining the Maximum Mass of Neutron Stars from Multi-messenger Observations of GW170817". In: 850.2, L19 (Dec. 2017), p. L19. DOI: 10.3847/2041-8213/aa991c. arXiv: 1710.05938 [astro-ph.HE].

[282] Natalie Mashian et al. "Hunting black holes with Gaia". In: 470.3 (Sept. 2017), pp. 2611–2616. DOI: 10.1093/mnras/stx1410. arXiv: 1704.03455 [astro-ph.HE].

[283] Francesca Matteucci et al. "Binary neutron stars and production of heavy elements". In: *Rendiconti Lincei. Scienze Fisiche e Naturali* 30 (Dec. 2019), pp. 85–88. DOI: 10.1007/s12210-018-0754-z.

[284] P. F. L. Maxted et al. "Survival of a brown dwarf after engulfment by a red giant star". In: 442.7102 (Aug. 2006), pp. 543–545. DOI: 10.1038/nature04987. arXiv: astro-ph/0608054 [astro-ph].

[285] Paul J. McMillan. "The mass distribution and gravitational potential of the Milky Way". In: 465.1 (Feb. 2017), pp. 76–94. DOI: 10.1093/mnras/stw2759. arXiv: 1608.00971 [astro-ph.GA].

[286] Matthew T. Miles et al. "The MeerKAT Pulsar Timing Array: the first search for gravitational waves with the MeerKAT radio telescope". In: 536.2 (Jan. 2025), pp. 1489–1500. DOI: 10.1093/mnras/stae2571. arXiv: 2412.01153 [astro-ph.HE].

[287] M. Coleman Miller et al. "The masses and spins of neutron stars and stellar-mass black holes". In: 548 (Jan. 2015), pp. 1–34. DOI: 10.1016/j.physrep.2014.09.003. arXiv: 1408.4145 [astro-ph.HE].

[288] James C. A. Miller-Jones et al. "Cygnus X-1 contains a 21-solar mass black hole—Implications for massive star winds". In: *Science* 371.6533 (Mar. 2021), pp. 1046–1049. DOI: 10.1126/science.abb3363. arXiv: 2102.09091 [astro-ph.HE].

[289] D. Misra et al. "The origin of pulsating ultra-luminous X-ray sources: Low- and intermediate-mass X-ray binaries containing neutron star accretors". In: 642, A174 (Oct. 2020), A174. DOI: 10.1051/0004-6361/202038070. arXiv: 2004.01205 [astro-ph.HE].

[290] Maxwell Moe et al. "Mind Your Ps and Qs: The Interrelation between Period (P) and Mass-ratio (Q) Distributions of Binary Stars". In: 230.2, 15 (June 2017), p. 15. DOI: 10.3847/1538-4365/aa6fb6. arXiv: 1606.05347 [astro-ph.SR].

[291] I. A. Morrison et al. "The Moment of Inertia of the Binary Pulsar J0737-3039A: Constraining the Nuclear Equation of State". In: 617.2 (Dec. 2004), pp. L135–L138. DOI: 10.1086/427235. arXiv: astro-ph/0411353 [astro-ph].

[292] Bernhard Müller, Daniel W. Gay, et al. “Multidimensional simulations of ultra-stripped supernovae to shock breakout”. In: 479.3 (Sept. 2018), pp. 3675–3689. DOI: 10.1093/mnras/sty1683. arXiv: 1803.03388 [astro-ph.SR].

[293] Bernhard Müller, Hans-Thomas Janka, and Alexander Heger. “New Two-dimensional Models of Supernova Explosions by the Neutrino-heating Mechanism: Evidence for Different Instability Regimes in Collapsing Stellar Cores”. In: 761.1, 72 (Dec. 2012), p. 72. DOI: 10.1088/0004-637X/761/1/72. arXiv: 1205.7078 [astro-ph.SR].

[294] Bernhard Müller, Hans-Thomas Janka, and Andreas Marek. “A New Multi-dimensional General Relativistic Neutrino Hydrodynamics Code for Core-collapse Supernovae. II. Relativistic Explosion Models of Core-collapse Supernovae”. In: 756.1, 84 (Sept. 2012), p. 84. DOI: 10.1088/0004-637X/756/1/84. arXiv: 1202.0815 [astro-ph.SR].

[295] Pranav Nagarajan et al. “Mixed Origins: Strong Natal Kicks for Some Black Holes and None for Others”. In: 137.3, 034203 (Mar. 2025), p. 034203. DOI: 10.1088/1538-3873/adb6d6. arXiv: 2411.16847 [astro-ph.GA].

[296] Kimihiko Nakajima et al. “JWST Census for the Mass-Metallicity Star Formation Relations at z = 4-10 with Self-consistent Flux Calibration and Proper Metallicity Calibrators”. In: 269.2, 33 (Dec. 2023), p. 33. DOI: 10.3847/1538-4365/acd556. arXiv: 2301.12825 [astro-ph.GA].

[297] Coenraad J. Neijssel et al. “The effect of the metallicity-specific star formation history on double compact object mergers”. In: 490.3 (Dec. 2019), pp. 3740–3759. DOI: 10.1093/mnras/stz2840. arXiv: 1906.08136 [astro-ph.SR].

[298] G. Nelemans and C. A. Tout. “Reconstructing the evolution of white dwarf binaries: further evidence for an alternative algorithm for the outcome of the common-envelope phase in close binaries”. In: 356.2 (Jan. 2005), pp. 753–764. DOI: 10.1111/j.1365-2966.2004.08496.x. arXiv: astro-ph/0410301 [astro-ph].

[299] G. Nelemans, F. Verbunt, et al. “Reconstructing the evolution of double helium white dwarfs: envelope loss without spiral-in”. In: 360 (Aug. 2000), pp. 1011–1018. DOI: 10.48550/arXiv.astro-ph/0006216. arXiv: astro-ph/0006216 [astro-ph].

[300] Dylan Nelson, Annalisa Pillepich, et al. “First results from the TNG50 simulation: galactic outflows driven by supernovae and black hole feedback”. In: 490.3 (Dec. 2019), pp. 3234–3261. DOI: 10.1093/mnras/stz2306. arXiv: 1902.05554 [astro-ph.GA].

[301] Dylan Nelson, Volker Springel, et al. “The IllustrisTNG simulations: public data release”. In: *Computational Astrophysics and Cosmology* 6.1, 2 (May 2019), p. 2. DOI: 10.1186/s40668-019-0028-x. arXiv: 1812.05609 [astro-ph.GA].

[302] C. Ng, D. J. Champion, et al. “The High Time Resolution Universe Pulsar Survey - XII. Galactic plane acceleration search and the discovery of 60 pulsars”. In: 450.3 (July 2015), pp. 2922–2947. DOI: 10.1093/mnras/stv753. arXiv: 1504.08000 [astro-ph.HE].

[303] C. Ng, M. U. Kruckow, et al. “PSR J1755-2550: a young radio pulsar with a massive, compact companion”. In: 476.4 (June 2018), pp. 4315–4326. DOI: 10.1093/mnras/sty482. arXiv: 1802.08248 [astro-ph.HE].

[304] C. T. Nguyen et al. “PARSEC V2.0: Stellar tracks and isochrones of low- and intermediate-mass stars with rotation”. In: 665, A126 (Sept. 2022), A126. DOI: 10.1051/0004-6361/202244166. arXiv: 2207.08642 [astro-ph.SR].

[305] Evan O’Connor et al. “Black Hole Formation in Failing Core-Collapse Supernovae”. In: 730.2, 70 (Apr. 2011), p. 70. DOI: 10.1088/0004-637X/730/2/70. arXiv: 1010.5550 [astro-ph.HE].

[306] Tyrone N. O'Doherty et al. "An observationally derived kick distribution for neutron stars in binary systems". In: 521.2 (May 2023), pp. 2504–2524. DOI: 10.1093/mnras/stad680. arXiv: 2303.01059 [astro-ph.HE].

[307] A. Olejak, K. Belczynski, et al. "Impact of common envelope development criteria on the formation of LIGO/Virgo sources". In: 651, A100 (July 2021), A100. DOI: 10.1051/0004-6361/202140520. arXiv: 2102.05649 [astro-ph.HE].

[308] Aleksandra Olejak, Chris L. Fryer, et al. "The role of supernova convection for the lower mass gap in the isolated binary formation of gravitational wave sources". In: 516.2 (Oct. 2022), pp. 2252–2271. DOI: 10.1093/mnras/stac2359. arXiv: 2204.09061 [astro-ph.HE].

[309] J. R. Oppenheimer et al. "On Massive Neutron Cores". In: *Physical Review* 55.4 (Feb. 1939), pp. 374–381. DOI: 10.1103/PhysRev.55.374.

[310] Jerome A. Orosz. "Inventory of black hole binaries". In: *A Massive Star Odyssey: From Main Sequence to Supernova*. Ed. by Karel van der Hucht et al. Vol. 212. IAU Symposium. Jan. 2003, p. 365. DOI: 10.48550/arXiv.astro-ph/0209041. arXiv: astro-ph/0209041 [astro-ph].

[311] S. Osłowski et al. "Population synthesis of double neutron stars". In: 413.1 (May 2011), pp. 461–479. DOI: 10.1111/j.1365-2966.2010.18147.x. arXiv: 0903.3538 [astro-ph.GA].

[312] J. P. Ostriker et al. "On the Nature of Pulsars. I. Theory". In: 157 (Sept. 1969), p. 1395. DOI: 10.1086/150160.

[313] Jeremiah P. Ostriker et al. "Do Pulsars Make Supernovae?" In: 164 (Mar. 1971), p. L95. DOI: 10.1086/180699.

[314] Feryal Özel and Paulo Freire. "Masses, Radii, and the Equation of State of Neutron Stars". In: 54 (Sept. 2016), pp. 401–440. DOI: 10.1146/annurev-astro-081915-023322. arXiv: 1603.02698 [astro-ph.HE].

[315] Feryal Özel, Dimitrios Psaltis, Tolga Güver, et al. "The Dense Matter Equation of State from Neutron Star Radius and Mass Measurements". In: 820.1, 28 (Mar. 2016), p. 28. DOI: 10.3847/0004-637X/820/1/28. arXiv: 1505.05155 [astro-ph.HE].

[316] Feryal Özel, Dimitrios Psaltis, Ramesh Narayan, and Jeffrey E. McClintock. "The Black Hole Mass Distribution in the Galaxy". In: 725.2 (Dec. 2010), pp. 1918–1927. DOI: 10.1088/0004-637X/725/2/1918. arXiv: 1006.2834 [astro-ph.GA].

[317] Feryal Özel, Dimitrios Psaltis, Ramesh Narayan, and Antonio Santos Villarreal. "On the Mass Distribution and Birth Masses of Neutron Stars". In: 757.1, 55 (Sept. 2012), p. 55. DOI: 10.1088/0004-637X/757/1/55. arXiv: 1201.1006 [astro-ph.HE].

[318] B. Paczynski. "Common Envelope Binaries". In: *Structure and Evolution of Close Binary Systems*. Ed. by Peter Eggleton et al. Vol. 73. Jan. 1976, p. 75.

[319] B. Paczyński. "Evolutionary Processes in Close Binary Systems". In: 9 (Jan. 1971), p. 183. DOI: 10.1146/annurev.aa.09.090171.001151.

[320] B. Paczyński and R. Sienkiewicz. "Evolution of Close Binaries VIII. Mass Exchange on the Dynamical Time Scale". In: 22 (Jan. 1972), pp. 73–91.

[321] P. V. Padmanabh et al. "Discovery and timing of ten new millisecond pulsars in the globular cluster Terzan 5". In: 686, A166 (June 2024), A166. DOI: 10.1051/0004-6361/202449303. arXiv: 2403.17799 [astro-ph.HE].

[322] Z. Pan et al. "Discovery of two new pulsars in 47 Tucanae (NGC 104)". In: 459.1 (June 2016), pp. L26–L30. DOI: 10.1093/mnrasl/slw037. arXiv: 1603.01348 [astro-ph.HE].

[323] G. G. Pavlov et al. “Central Compact Objects in Supernova Remnants”. In: *Young Neutron Stars and Their Environments*. Ed. by Fernando Camilo et al. Vol. 218. IAU Symposium. Jan. 2004, p. 239. DOI: 10.48550/arXiv.astro-ph/0311526. arXiv: astro-ph/0311526 [astro-ph].

[324] K. Pavlovskii et al. “Stability of mass transfer from massive giants: double black hole binary formation and ultraluminous X-ray sources”. In: 465.2 (Feb. 2017), pp. 2092–2100. DOI: 10.1093/mnras/stw2786. arXiv: 1606.04921 [astro-ph.HE].

[325] Bill Paxton, Lars Bildsten, et al. “Modules for Experiments in Stellar Astrophysics (MESA)”. In: 192.1, 3 (Jan. 2011), p. 3. DOI: 10.1088/0067-0049/192/1/3. arXiv: 1009.1622 [astro-ph.SR].

[326] Bill Paxton, Pablo Marchant, et al. “Modules for Experiments in Stellar Astrophysics (MESA): Binaries, Pulsations, and Explosions”. In: 220.1, 15 (Sept. 2015), p. 15. DOI: 10.1088/0067-0049/220/1/15. arXiv: 1506.03146 [astro-ph.SR].

[327] P. C. Peters. “Gravitational Radiation and the Motion of Two Point Masses”. In: *Phys. Rev.* 136 (4B Nov. 1964), B1224–B1232. DOI: 10.1103/PhysRev.136.B1224. URL: https://link.aps.org/doi/10.1103/PhysRev.136.B1224.

[328] Gabriele Pezzulli et al. “Accretion, radial flows and abundance gradients in spiral galaxies”. In: *Monthly Notices of the Royal Astronomical Society* 455.3 (Nov. 2015), pp. 2308–2322. DOI: 10.1093/mnras/stv2397. eprint: https://academic.oup.com/mnras/article-pdf/455/3/2308/9378962/stv2397.pdf. URL: https://doi.org/10.1093/mnras/stv2397.

[329] Lewis Picker et al. “Fits for the Convective Envelope Mass in Massive Stars”. In: 969.1, 1 (July 2024), p. 1. DOI: 10.3847/1538-4357/ad4a5d. arXiv: 2402.13180 [astro-ph.SR].

[330] Annalisa Pillepich, Dylan Nelson, et al. “First results from the TNG50 simulation: the evolution of stellar and gaseous discs across cosmic time”. In: 490.3 (Dec. 2019), pp. 3196–3233. DOI: 10.1093/mnras/stz2338. arXiv: 1902.05553 [astro-ph.GA].

[331] Annalisa Pillepich, Diego Sotillo-Ramos, et al. “Milky Way and Andromeda analogs from the TNG50 simulation”. In: *arXiv e-prints*, arXiv:2303.16217 (Mar. 2023), arXiv:2303.16217. DOI: 10.48550/arXiv.2303.16217. arXiv: 2303.16217 [astro-ph.GA].

[332] Ph. Podsiadlowski et al. “The double pulsar J0737-3039: testing the neutron star equation of state”. In: 361.4 (Aug. 2005), pp. 1243–1249. DOI: 10.1111/j.1365-2966.2005.09253.x. arXiv: astro-ph/0506566 [astro-ph].

[333] Nihan Pol et al. “Future Prospects for Ground-based Gravitational-wave Detectors: The Galactic Double Neutron Star Merger Rate Revisited”. In: 870.2, 71 (Jan. 2019), p. 71. DOI: 10.3847/1538-4357/aaf006. arXiv: 1811.04086 [astro-ph.HE].

[334] Nihan Pol et al. “An Updated Galactic Double Neutron Star Merger Rate Based on Radio Pulsar Populations”. In: *Research Notes of the American Astronomical Society* 4.2, 22 (Feb. 2020), p. 22. DOI: 10.3847/2515-5172/ab7307. arXiv: 2002.10225 [astro-ph.HE].

[335] Michael Politano et al. “Population Synthesis Studies of Close Binary Systems Using a Variable Common Envelope Efficiency Parameter. I. Dependence on Secondary Mass”. In: 665.1 (Aug. 2007), pp. 663–679. DOI: 10.1086/518997. arXiv: astro-ph/0702662 [astro-ph].

[336] P. Popesso et al. “The main sequence of star-forming galaxies across cosmic times”. In: 519.1 (Feb. 2023), pp. 1526–1544. DOI: 10.1093/mnras/stac3214. arXiv: 2203.10487 [astro-ph.GA].

[337] S. B. Popov et al. “A tale of two populations: rotating radio transients and X-ray dim isolated neutron stars”. In: 369.1 (June 2006), pp. L23–L26. DOI: 10.1111/j.1745-3933.2006.00166.x. arXiv: astro-ph/0603258 [astro-ph].

[338] S. F. Portegies Zwart and F. Verbunt. “Population synthesis of high-mass binaries.” In: 309 (May 1996), pp. 179–196.

[339] Simon F. Portegies Zwart and Stephen L. W. McMillan. “Black Hole Mergers in the Universe”. In: 528.1 (Jan. 2000), pp. L17–L20. DOI: 10.1086/312422. arXiv: astro-ph/9910061 [astro-ph].

[340] Andrea Possenti et al. “Population Synthesis of Millisecond and Submillisecond Pulsars”. In: 497.2 (Apr. 1998), pp. L97–L100. DOI: 10.1086/311286. arXiv: astro-ph/9802257 [astro-ph].

[341] M. Punturo et al. “The Einstein Telescope: a third-generation gravitational wave observatory”. In: *Classical and Quantum Gravity* 27.19, 194002 (Oct. 2010), p. 194002. DOI: 10.1088/0264-9381/27/19/194002.

[342] Ying Qin et al. “On the Origin of Black Hole Spin in High-mass X-Ray Binaries”. In: 870.2, L18 (Jan. 2019), p. L18. DOI: 10.3847/2041-8213/aaf97b. arXiv: 1810.13016 [astro-ph.SR].

[343] G. Rakavy et al. “Instabilities in Highly Evolved Stellar Models”. In: 148 (June 1967), p. 803. DOI: 10.1086/149204.

[344] Scott M. Ransom et al. “Twenty-One Millisecond Pulsars in Terzan 5 Using the Green Bank Telescope”. In: *Science* 307.5711 (Feb. 2005), pp. 892–896. DOI: 10.1126/science.1108632. arXiv: astro-ph/0501230 [astro-ph].

[345] Liana Rauf et al. “Exploring binary black hole mergers and host galaxies with SHARK and COMPAS”. In: 523.4 (Aug. 2023), pp. 5719–5737. DOI: 10.1093/mnras/stad1757. arXiv: 2302.08172 [astro-ph.GA].

[346] Daniel J. Reardon et al. “Search for an Isotropic Gravitational-wave Background with the Parkes Pulsar Timing Array”. In: 951.1, L6 (July 2023), p. L6. DOI: 10.3847/2041-8213/acdd02. arXiv: 2306.16215 [astro-ph.HE].

[347] Serena Repetto et al. “Investigating stellar-mass black hole kicks”. In: 425.4 (Oct. 2012), pp. 2799–2809. DOI: 10.1111/j.1365-2966.2012.21549.x. arXiv: 1203.3077 [astro-ph.GA].

[348] Clifford E. Rhoades et al. “Maximum Mass of a Neutron Star”. In: 32.6 (Feb. 1974), pp. 324–327. DOI: 10.1103/PhysRevLett.32.324.

[349] S. M. Richards et al. “New constraints on the Bray conservation-of-momentum natal kick model from multiple distinct observations”. In: 522.3 (July 2023), pp. 3972–3985. DOI: 10.1093/mnras/stad977. arXiv: 2208.02407 [astro-ph.HE].

[350] A. Ridolfi et al. “Eight new millisecond pulsars from the first MeerKAT globular cluster census”. In: 504.1 (June 2021), pp. 1407–1426. DOI: 10.1093/mnras/stab790. arXiv: 2103.04800 [astro-ph.HE].

[351] Jeff Riley, Poojan Agrawal, et al. “Rapid Stellar and Binary Population Synthesis with COMPAS”. In: 258.2, 34 (Feb. 2022), p. 34. DOI: 10.3847/1538-4365/ac416c. arXiv: 2109.10352 [astro-ph.IM].

[352] Jeff Riley, Ilya Mandel, et al. “Chemically homogeneous evolution: a rapid population synthesis approach”. In: 505.1 (July 2021), pp. 663–676. DOI: 10.1093/mnras/stab1291. arXiv: 2010.00002 [astro-ph.SR].

[353] Pierluigi Rinaldi, Karina I. Caputi, et al. “The Galaxy Starburst/Main-sequence Bimodality over Five Decades in Stellar Mass at z $\approx$ 3-6.5”. In: 930.2, 128 (May 2022), p. 128. DOI: 10.3847/1538-4357/ac5d39. arXiv: 2112.03935 [astro-ph.GA].

[354] Stefano Rinaldi and Walter Del Pozzo. "(H)DPGMM: a hierarchy of Dirichlet process Gaussian mixture models for the inference of the black hole mass function". In: 509.4 (Feb. 2022), pp. 5454–5466. DOI: 10.1093/mnras/stab3224. arXiv: 2109.05960 [astro-ph.IM].

[355] Stefano Rinaldi and Walter Del Pozzo. "Rapid localization of gravitational wave hosts with FIGARO". In: 517.1 (Nov. 2022), pp. L5–L10. DOI: 10.1093/mnrasl/slac101. arXiv: 2205.07252 [astro-ph.IM].

[356] Mallory S. E. Roberts. "Surrounded by spiders! New black widows and redbacks in the Galactic field". In: *Neutron Stars and Pulsars: Challenges and Opportunities after 80 years*. Ed. by Joeri van Leeuwen. Vol. 291. IAU Symposium. Mar. 2013, pp. 127–132. DOI: 10.1017/S174392131202337X. arXiv: 1210.6903 [astro-ph.HE].

[357] Clive Robinson et al. "Millisecond pulsars in the globular cluster 47 Tucanae". In: 274.2 (May 1995), pp. 547–554. DOI: 10.1093/mnras/274.2.547.

[358] G. Rodighiero et al. "RELATIONSHIP BETWEEN STAR FORMATION RATE AND BLACK HOLE ACCRETION AT z = 2: THE DIFFERENT CONTRIBUTIONS IN QUIESCENT, NORMAL, AND STARBURST GALAXIES". In: *The Astrophysical Journal Letters* 800.1 (Feb. 2015), p. L10. DOI: 10.1088/2041-8205/800/1/L10. URL: https://dx.doi.org/10.1088/2041-8205/800/1/L10.

[359] Carl L. Rodriguez, Sourav Chatterjee, et al. "Binary black hole mergers from globular clusters: Masses, merger rates, and the impact of stellar evolution". In: 93.8, 084029 (Apr. 2016), p. 084029. DOI: 10.1103/PhysRevD.93.084029. arXiv: 1602.02444 [astro-ph.HE].

[360] Carl L. Rodriguez and Abraham Loeb. "Redshift Evolution of the Black Hole Merger Rate from Globular Clusters". In: 866.1, L5 (Oct. 2018), p. L5. DOI: 10.3847/2041-8213/aae377. arXiv: 1809.01152 [astro-ph.HE].

[361] A. Romagnolo et al. "The role of stellar expansion on the formation of gravitational wave sources". In: 525.1 (Oct. 2023), pp. 706–720. DOI: 10.1093/mnras/stad2366. arXiv: 2211.15800 [astro-ph.HE].

[362] Jaime Román-Garza et al. "The Role of Core-collapse Physics in the Observability of Black Hole Neutron Star Mergers as Multimessenger Sources". In: 912.2, L23 (May 2021), p. L23. DOI: 10.3847/2041-8213/abf42c. arXiv: 2012.02274 [astro-ph.HE].

[363] Friedrich K. Röpke et al. "Simulations of common-envelope evolution in binary stellar systems: physical models and numerical techniques". In: *Living Reviews in Computational Astrophysics* 9.1, 2 (Dec. 2023), p. 2. DOI: 10.1007/s41115-023-00017-x. arXiv: 2212.07308 [astro-ph.SR].

[364] B. Rudak et al. "The line of death, the line of birth". In: *Monthly Notices of the Royal Astronomical Society* 267.3 (Apr. 1994), pp. 513–517. DOI: 10.1093/mnras/267.3.513. eprint: https://academic.oup.com/mnras/article-pdf/267/3/513/2974470/mnras267-0513.pdf. URL: https://doi.org/10.1093/mnras/267.3.513.

[365] Krystal Ruiz-Rocha et al. "Properties of "Lite" Intermediate-mass Black Hole Candidates in LIGO-Virgo's Third Observing Run". In: 985.2, L37 (June 2025), p. L37. DOI: 10.3847/2041-8213/adc5f8. arXiv: 2502.17681 [astro-ph.HE].

[366] Gautham N. Sabhahit et al. "Mass-loss implementation and temperature evolution of very massive stars". In: 514.3 (Aug. 2022), pp. 3736–3753. DOI: 10.1093/mnras/stac1410. arXiv: 2205.09125 [astro-ph.SR].

[367] Johan Samsing et al. "The Formation of Eccentric Compact Binary Inspirals and the Role of Gravitational Wave Emission in Binary-Single Stellar Encounters". In: 784.1, 71 (Mar. 2014), p. 71. DOI: 10.1088/0004-637X/784/1/71. arXiv: 1308.2964 [astro-ph.HE].

[368] H. Sana et al. “Binary Interaction Dominates the Evolution of Massive Stars”. In: *Science* 337.6093 (July 2012), p. 444. DOI: 10.1126/science.1223344. arXiv: 1207.6397 [astro-ph.SR].

[369] Filippo Santoliquido, Michela Mapelli, M Celeste Artale, et al. “Modelling the host galaxies of binary compact object mergers with observational scaling relations”. In: *Monthly Notices of the Royal Astronomical Society* 516.3 (Aug. 2022), pp. 3297–3317. DOI: 10.1093/mnras/stac2384. arXiv: https://academic.oup.com/mnras/article-pdf/516/3/3297/45877676/stac2384.pdf [astro-ph.HE]. URL: https://doi.org/10.1093/mnras/stac2384.

[370] Filippo Santoliquido, Michela Mapelli, Yann Bouffanais, et al. “The Cosmic Merger Rate Density Evolution of Compact Binaries Formed in Young Star Clusters and in Isolated Binaries”. In: 898.2, 152 (Aug. 2020), p. 152. DOI: 10.3847/1538-4357/ab9b78. arXiv: 2004.09533 [astro-ph.HE].

[371] Filippo Santoliquido, Michela Mapelli, Nicola Giacobbo, et al. “The cosmic merger rate density of compact objects: impact of star formation, metallicity, initial mass function, and binary evolution”. In: 502.4 (Apr. 2021), pp. 4877–4889. DOI: 10.1093/mnras/stab280. arXiv: 2009.03911 [astro-ph.HE].

[372] Filippo Santoliquido, Michela Mapelli, Giuliano Iorio, et al. “Binary black hole mergers from population III stars: uncertainties from star formation and binary star properties”. In: 524.1 (Sept. 2023), pp. 307–324. DOI: 10.1093/mnras/stad1860. arXiv: 2303.15515 [astro-ph.GA].

[373] M. T. Sargent et al. “The Contribution of Starbursts and Normal Galaxies to Infrared Luminosity Functions at z < 2”. In: 747.2, L31 (Mar. 2012), p. L31. DOI: 10.1088/2041-8205/747/2/L31. arXiv: 1202.0290 [astro-ph.CO].

[374] Nikhil Sarin et al. “Confronting the Neutron Star Population with Inverse Cascades”. In: 952.1, L21 (July 2023), p. L21. DOI: 10.3847/2041-8213/ace363. arXiv: 2305.14347 [astro-ph.HE].

[375] Joop Schaye et al. “The EAGLE project: simulating the evolution and assembly of galaxies and their environments”. In: *Monthly Notices of the Royal Astronomical Society* 446.1 (Nov. 2014), pp. 521–554. DOI: 10.1093/mnras/stu2058. eprint: https://academic.oup.com/mnras/article-pdf/446/1/521/4139718/stu2058.pdf. URL: https://doi.org/10.1093/mnras/stu2058.

[376] F. R. N. Schneider et al. “Pre-supernova evolution, compact-object masses, and explosion properties of stripped binary stars”. In: 645, A5 (Jan. 2021), A5. DOI: 10.1051/0004-6361/202039219. arXiv: 2008.08599 [astro-ph.SR].

[377] Schreiber, C. et al. “The Herschel view of the dominant mode of galaxy growth from z = 4 to the present day”. In: 575 (2015), A74. DOI: 10.1051/0004-6361/201425017. URL: https://doi.org/10.1051/0004-6361/201425017.

[378] E. Schreier et al. “Evidence for the Binary Nature of Centaurus X-3 from UHURU X-Ray Observations.” In: 172 (Mar. 1972), p. L79. DOI: 10.1086/180896.

[379] Martin Schwarzschild. *Structure and evolution of the stars.* 1958.

[380] R Sengar et al. “The High Time Resolution Universe Pulsar Survey – XVII. PSR J13256253, a low eccentricity double neutron star system from an ultra-stripped supernova”. In: *Monthly Notices of the Royal Astronomical Society* 512.4 (Mar. 2022), pp. 5782–5792. DOI: 10.1093/mnras/stac821. eprint: https://academic.oup.com/mnras/article-pdf/512/4/5782/44083704/stac821.pdf. URL: https://doi.org/10.1093/mnras/stac821.

[381] Cecilia Sgalletta, Giuliano Iorio, et al. “Binary neutron star populations in the Milky Way”. In: 526.2 (Dec. 2023), pp. 2210–2229. DOI: 10.1093/mnras/stad2768. arXiv: 2305.04955 [astro-ph.HE].

[382] Cecilia Sgalletta, Michela Mapelli, et al. "The more accurately the metal-dependent star formation rate is modeled, the larger the predicted excess of binary black hole mergers". In: 698, A144 (June 2025), A144. DOI: 10.1051/0004-6361/202452757. arXiv: 2410.21401 [astro-ph.HE].

[383] Cecilia Sgalletta, Mario Spera, et al. "Revisiting envelope binding energies: a comprehensive study from population III to metal-rich stars". 2025. in preparation.

[384] Yong Shao et al. "On the Role of Supernova Kicks in the Formation of Galactic Double Neutron Star Systems". In: 867.2, 124 (Nov. 2018), p. 124. DOI: 10.3847/1538-4357/aae648. arXiv: 1810.03324 [astro-ph.HE].

[385] Yong Shao et al. "Population Synthesis of Black Hole Binaries with Compact Star Companions". In: 920.2, 81 (Oct. 2021), p. 81. DOI: 10.3847/1538-4357/ac173e. arXiv: 2107.03565 [astro-ph.HE].

[386] Kendall G. Shepherd et al. "Enhanced Mass Loss of Very Massive Stars: Impact on the Evolution, Binary Processes, and Remnant Mass Spectrum". In: *arXiv e-prints*, arXiv:2505.10206 (May 2025), arXiv:2505.10206. DOI: 10.48550/arXiv.2505.10206. arXiv: 2505.10206 [astro-ph.SR].

[387] N. Shibazaki et al. "Does mass accretion lead to field decay in neutron stars?" In: 342.6250 (Dec. 1989), pp. 656–658. DOI: 10.1038/342656a0.

[388] Steinn Sigurdsson et al. "Primordial black holes in globular clusters". In: 364.6436 (July 1993), pp. 423–425. DOI: 10.1038/364423a0.

[389] Filippo Simonato et al. "Impact of stellar winds on the pair-instability supernova rate". In: *arXiv e-prints*, arXiv:2505.07959 (May 2025), arXiv:2505.07959. DOI: 10.48550/arXiv.2505.07959. arXiv: 2505.07959 [astro-ph.HE].

[390] G. E. Soberman et al. "Stability criteria for mass transfer in binary stellar evolution." In: 327 (Nov. 1997), pp. 620–635. DOI: 10.48550/arXiv.astro-ph/9703016. arXiv: astro-ph/9703016 [astro-ph].

[391] Noam Soker. "Energy and angular momentum deposition during common envelope evolution". In: 9.5 (June 2004), pp. 399–408. DOI: 10.1016/j.newast.2004.01.004. arXiv: astro-ph/0311168 [astro-ph].

[392] Noam Soker. "The jet feedback mechanism (JFM) in stars, galaxies and clusters". In: 75 (Dec. 2016), pp. 1–23. DOI: 10.1016/j.newar.2016.08.002. arXiv: 1605.02672 [astro-ph.HE].

[393] J. S. Speagle et al. "A Highly Consistent Framework for the Evolution of the Star-Forming "Main Sequence" from z ~0-6". In: 214.2, 15 (Oct. 2014), p. 15. DOI: 10.1088/0067-0049/214/2/15. arXiv: 1405.2041 [astro-ph.GA].

[394] Mario Spera and Michela Mapelli. "Very massive stars, pair-instability supernovae and intermediate-mass black holes with the sevn code". In: 470.4 (Oct. 2017), pp. 4739–4749. DOI: 10.1093/mnras/stx1576. arXiv: 1706.06109 [astro-ph.SR].

[395] Mario Spera, Michela Mapelli, et al. "Merging black hole binaries with the SEVN code". In: 485.1 (May 2019), pp. 889–907. DOI: 10.1093/mnras/stz359. arXiv: 1809.04605 [astro-ph.HE].

[396] Mario Spera, Alessandro Alberto Trani, et al. "Compact Binary Coalescences: Astrophysical Processes and Lessons Learned". In: *Galaxies* 10.4, 76 (June 2022), p. 76. DOI: 10.3390/galaxies10040076. arXiv: 2206.15392 [astro-ph.HE].

[397] Volker Springel. "The cosmological simulation code GADGET-2". In: 364.4 (Dec. 2005), pp. 1105–1134. DOI: 10.1111/j.1365-2966.2005.09655.x. arXiv: astro-ph/0505010 [astro-ph].

[398] Volker Springel. "E pur si muove: Galilean-invariant cosmological hydrodynamical simulations on a moving mesh". In: 401.2 (Jan. 2010), pp. 791–851. DOI: 10.1111/j.1365-2966.2009.15715.x. arXiv: 0901.4107 [astro-ph.CO].

[399] H. C. Spruit et al. "Circumbinary Disks and Cataclysmic Variable Evolution". In: 548.2 (Feb. 2001), pp. 900–907. DOI: 10.1086/319030. arXiv: astro-ph/0010194 [astro-ph].

[400] G. Srinivasan and E. P. J. van den Heuvel. "Some constraints on the evolutionary history of the binary pulsar PSR1913+16." In: 108 (Apr. 1982), pp. 143–147.

[401] Rahul Srinivasan, Astrid Lamberts, et al. "Understanding the progenitor formation galaxies of merging binary black holes". In: 524.1 (Sept. 2023), pp. 60–75. DOI: 10.1093/mnras/stad1825. arXiv: 2303.04017 [astro-ph.HE].

[402] David H. Staelin et al. "Pulsating Radio Sources near the Crab Nebula". In: *Science* 162.3861 (Dec. 1968), pp. 1481–1483. DOI: 10.1126/science.162.3861.1481.

[403] B. W. Stappers et al. "The prospects of pulsar timing with new-generation radio telescopes and the Square Kilometre Array". In: *Philosophical Transactions of the Royal Society of London Series A* 376.2120, 20170293 (May 2018), p. 20170293. DOI: 10.1098/rsta.2017.0293.

[404] Simon Stevenson et al. "Constraints on the contributions to the observed binary black hole population from individual evolutionary pathways in isolated binary evolution". In: 517.3 (Dec. 2022), pp. 4034–4053. DOI: 10.1093/mnras/stac2936. arXiv: 2210.05040 [astro-ph.HE].

[405] Yudai Suwa et al. "Neutrino-driven explosions of ultra-stripped Type Ic supernovae generating binary neutron stars". In: 454.3 (Dec. 2015), pp. 3073–3081. DOI: 10.1093/mnras/stv2195. arXiv: 1506.08827 [astro-ph.HE].

[406] Andrzej Szary et al. "Radio Efficiency of Pulsars". In: 784.1, 59 (Mar. 2014), p. 59. DOI: 10.1088/0004-637X/784/1/59. arXiv: 1402.0228 [astro-ph.HE].

[407] R. E. Taam et al. "Magnetic Field Decay and the Origin of Neutron Star Binaries". In: 305 (June 1986), p. 235. DOI: 10.1086/164243.

[408] Petra N. Tang et al. "Dependence of gravitational wave transient rates on cosmic star formation and metallicity evolution history". In: 493.1 (Mar. 2020), pp. L6–L10. DOI: 10.1093/mnrasl/slz183. arXiv: 1912.04474 [astro-ph.GA].

[409] T. M. Tauris, M. Kramer, et al. "Formation of Double Neutron Star Systems". In: 846.2, 170 (Sept. 2017), p. 170. DOI: 10.3847/1538-4357/aa7e89. arXiv: 1706.09438 [astro-ph.HE].

[410] T. M. Tauris and R. N. Manchester. "On the Evolution of Pulsar Beams". In: *Monthly Notices of the Royal Astronomical Society* 298.3 (Aug. 1998), pp. 625–636. DOI: 10.1046/j.1365-8711.1998.01369.x. eprint: https://academic.oup.com/mnras/article-pdf/298/3/625/4068352/298-3-625.pdf. URL: https://doi.org/10.1046/j.1365-8711.1998.01369.x.

[411] Thomas M. Tauris, Norbert Langer, et al. "Ultra-stripped supernovae: progenitors and fate". In: 451.2 (Aug. 2015), pp. 2123–2144. DOI: 10.1093/mnras/stv990. arXiv: 1505.00270 [astro-ph.SR].

[412] Thomas M. Tauris, Edward P. J. van den Heuvel, and Gerrit J. Savonije. "Formation of Millisecond Pulsars with Heavy White Dwarf Companions:Extreme Mass Transfer on Subthermal Timescales". In: 530.2 (Feb. 2000), pp. L93–L96. DOI: 10.1086/312496. arXiv: astro-ph/0001013 [astro-ph].

[413] Tauris and van den Heuvel. *Physics of Binary Star Evolution. From Stars to X-ray Binaries and Gravitational Wave Sources*. 2023. DOI: 10.48550/arXiv.2305.09388.

[414] The EAGLE team. "The EAGLE simulations of galaxy formation: Public release of particle data". In: *arXiv e-prints*, arXiv:1706.09899 (June 2017), arXiv:1706.09899. DOI: 10.48550/arXiv.1706.09899. arXiv: 1706.09899 [astro-ph.GA].

[415] Richard C. Tolman. "Static Solutions of Einstein's Field Equations for Spheres of Fluid". In: *Physical Review* 55.4 (Feb. 1939), pp. 364–373. DOI: 10.1103/PhysRev.55.364.

[416] Christopher A. Tout et al. "Rapid binary star evolution for N-body simulations and population synthesis". In: 291.4 (Nov. 1997), pp. 732–748. DOI: 10.1093/mnras/291.4.732.

[417] Alessandro Alberto Trani et al. "Revisiting the common envelope evolution in binary stars: A new semianalytic model for N -body and population synthesis codes". In: 106.4, 043014 (Aug. 2022), p. 043014. DOI: 10.1103/PhysRevD.106.043014. arXiv: 2205.13537 [astro-ph.SR].

[418] Marcella Ugliano et al. "Progenitor-explosion Connection and Remnant Birth Masses for Neutrino-driven Supernovae of Iron-core Progenitors". In: 757.1, 69 (Sept. 2012), p. 69. DOI: 10.1088/0004-637X/757/1/69. arXiv: 1205.3657 [astro-ph.SR].

[419] V. Urpin et al. "Magnetic and spin evolution of isolated neutron stars with the crustal magnetic field". In: *Monthly Notices of the Royal Astronomical Society* 292.1 (Nov. 1997), pp. 167–176. DOI: 10.1093/mnras/292.1.167. eprint: https://academic.oup.com/mnras/article-pdf/292/1/167/4004331/292-1-167.pdf. URL: https://doi.org/10.1093/mnras/292.1.167.

[420] E. P. J. van den Heuvel. "Late Stages of Close Binary Systems". In: *Structure and Evolution of Close Binary Systems*. Ed. by Peter Eggleton et al. Vol. 73. IAU Symposium. Jan. 1976, p. 35.

[421] E. P. J. van den Heuvel. "Models for the formation of binary and millisecond radio pulsars". In: *Journal of Astrophysics and Astronomy* 5.3 (Sept. 1984), pp. 209–233. DOI: 10.1007/BF02714540.

[422] E. P. J. van den Heuvel. "Interacting binaries: topics in close binary evolution." In: *Saas-Fee Advanced Course 22: Interacting Binaries*. Ed. by S. N. Shore et al. Jan. 1994, pp. 263–474.

[423] E. P. J. van den Heuvel. "The binary pulsar PSRJ2145-0750: a system originating from a low or intermediate mass X-ray binary with a donor star on the asymptotic giant branch?" In: 291 (Nov. 1994), pp. L39–L42.

[424] E. P. J. van den Heuvel and C. De Loore. "The nature of X-ray binaries III. Evolution of massive close binaries with one collapsed component - with a possible application to Cygnus X-3." In: 25 (June 1973), p. 387.

[425] L. A. C. van Son, S. E. de Mink, T. Callister, et al. "The Redshift Evolution of the Binary Black Hole Merger Rate: A Weighty Matter". In: 931.1, 17 (May 2022), p. 17. DOI: 10.3847/1538-4357/ac64a3. arXiv: 2110.01634 [astro-ph.HE].

[426] L. A. C. van Son, S. E. de Mink, M. Chruślińska, et al. "The Locations of Features in the Mass Distribution of Merging Binary Black Holes Are Robust against Uncertainties in the Metallicity-dependent Cosmic Star Formation History". In: 948.2, 105 (May 2023), p. 105. DOI: 10.3847/1538-4357/acbf51. arXiv: 2209.03385 [astro-ph.GA].

[427] L. A. C. van Son, S. K. Roy, et al. "Not Just Winds: Why Models Find That Binary Black Hole Formation Is Metallicity-dependent, while Binary Neutron Star Formation Is Not". In: 979.2, 209 (Feb. 2025), p. 209. DOI: 10.3847/1538-4357/ada14a. arXiv: 2411.02484 [astro-ph.HE].

[428] Frank Verbunt et al. “The observed velocity distribution of young pulsars”. In: 608, A57 (Dec. 2017), A57. DOI: 10.1051/0004-6361/201731518. arXiv: 1708.08281 [astro-ph.HE].

[429] Alejandro Vigna-Gómez et al. “On the formation history of Galactic double neutron stars”. In: 481.3 (Dec. 2018), pp. 4009–4029. DOI: 10.1093/mnras/sty2463. arXiv: 1805.07974 [astro-ph.SR].

[430] Jorick S. Vink. “Theory and Diagnostics of Hot Star Mass Loss”. In: 60 (Aug. 2022), pp. 203–246. DOI: 10.1146/annurev-astro-052920-094949. arXiv: 2109.08164 [astro-ph.SR].

[431] Jorick S. Vink et al. “Mass-loss predictions for O and B stars as a function of metallicity”. In: 369 (Apr. 2001), pp. 574–588. DOI: 10.1051/0004-6361:20010127. arXiv: astro-ph/0101509 [astro-ph].

[432] Chen Wang et al. “The binding energy parameter for common envelope evolution”. In: *Research in Astronomy and Astrophysics* 16.8 (Aug. 2016), p. 009. DOI: 10.1088/1674-4527/16/8/126. URL: https://dx.doi.org/10.1088/1674-4527/16/8/126.

[433] R. F. Webbink. “Double white dwarfs as progenitors of R Coronae Borealis stars and type I supernovae.” In: 277 (Feb. 1984), pp. 355–360. DOI: 10.1086/161701.

[434] R. F. Webbink. “Stellar evolution and binaries”. In: *Interacting Binary Stars*. Ed. by J. E. Pringle et al. 1985, p. 39.

[435] B. Louise Webster et al. “Cygnus X-1-a Spectroscopic Binary with a Heavy Companion ?” In: 235.5332 (Jan. 1972), pp. 37–38. DOI: 10.1038/235037a0.

[436] J. M. Weisberg et al. “Relativistic Measurements from Timing the Binary Pulsar PSR B1913+16”. In: 829.1, 55 (Sept. 2016), p. 55. DOI: 10.3847/0004-637X/829/1/55. arXiv: 1606.02744 [astro-ph.HE].

[437] Linqing Wen. “On the Eccentricity Distribution of Coalescing Black Hole Binaries Driven by the Kozai Mechanism in Globular Clusters”. In: 598.1 (Nov. 2003), pp. 419–430. DOI: 10.1086/378794. arXiv: astro-ph/0211492 [astro-ph].

[438] Norbert Wex. “Testing Relativistic Gravity with Radio Pulsars”. In: *arXiv e-prints*, arXiv:1402.5594 (Feb. 2014), arXiv:1402.5594. DOI: 10.48550/arXiv.1402.5594. arXiv: 1402.5594 [gr-qc].

[439] Reinhold Willcox et al. “Constraints on Weak Supernova Kicks from Observed Pulsar Velocities”. In: 920.2, L37 (Oct. 2021), p. L37. DOI: 10.3847/2041-8213/ac2cc8. arXiv: 2107.04251 [astro-ph.HE].

[440] E. C. Wilson et al. “Convection reconciles the difference in efficiencies between low-mass and high-mass common envelopes”. In: 516.2 (Oct. 2022), pp. 2189–2195. DOI: 10.1093/mnras/stac2300. arXiv: 2203.06091 [astro-ph.SR].

[441] S. E. Woosley. “The Birth of Neutron Stars”. In: *The Origin and Evolution of Neutron Stars*. Ed. by D. J. Helfand et al. Vol. 125. Jan. 1987, p. 255.

[442] S. E. Woosley. “Pulsational Pair-instability Supernovae”. In: 836.2, 244 (Feb. 2017), p. 244. DOI: 10.3847/1538-4357/836/2/244. arXiv: 1608.08939 [astro-ph.HE].

[443] S. E. Woosley, A. Heger, et al. “The evolution and explosion of massive stars”. In: *Reviews of Modern Physics* 74.4 (Nov. 2002), pp. 1015–1071. DOI: 10.1103/RevModPhys.74.1015.

[444] S. E. Woosley, Tuguldur Sukhbold, et al. “The Birth Function for Black Holes and Neutron Stars in Close Binaries”. In: 896.1, 56 (June 2020), p. 56. DOI: 10.3847/1538-4357/ab8cc1. arXiv: 2001.10492 [astro-ph.HE].

[445] Heng Xu, Siyuan Chen, et al. "Searching for the Nano-Hertz Stochastic Gravitational Wave Background with the Chinese Pulsar Timing Array Data Release I". In: *Research in Astronomy and Astrophysics* 23.7, 075024 (July 2023), p. 075024. DOI: 10.1088/1674-4527/acdfa5. arXiv: 2306.16216 [astro-ph.HE].

[446] Xiao-Jie Xu and Xiang-Dong Li. "On the Binding Energy Parameter λ of Common Envelope Evolution". In: 716.1 (June 2010), pp. 114–121. DOI: 10.1088/0004-637X/716/1/114. arXiv: 1004.4957 [astro-ph.SR].

[447] Masaki S. Yamaguchi et al. "Detecting Black Hole Binaries by Gaia". In: 861.1, 21 (July 2018), p. 21. DOI: 10.3847/1538-4357/aac5ec. arXiv: 1710.09839 [astro-ph.SR].

[448] S. -C. Yoon, N. Langer, et al. "Single star progenitors of long gamma-ray bursts. I. Model grids and redshift dependent GRB rate". In: 460.1 (Dec. 2006), pp. 199–208. DOI: 10.1051/0004-6361:20065912. arXiv: astro-ph/0606637 [astro-ph].

[449] S. -C. Yoon, S. E. Woosley, et al. "Type Ib/c Supernovae in Binary Systems. I. Evolution and Properties of the Progenitor Stars". In: 725.1 (Dec. 2010), pp. 940–954. DOI: 10.1088/0004-637X/725/1/940. arXiv: 1004.0843 [astro-ph.SR].

[450] I. Yusifov et al. "Revisiting the radial distribution of pulsars in the Galaxy". In: 422 (Aug. 2004), pp. 545–553. DOI: 10.1051/0004-6361:20040152. arXiv: astro-ph/0405559 [astro-ph].

[451] Michael Zevin, Simone S. Bavera, et al. "One Channel to Rule Them All? Constraining the Origins of Binary Black Holes Using Multiple Formation Pathways". In: 910.2, 152 (Apr. 2021), p. 152. DOI: 10.3847/1538-4357/abe40e. arXiv: 2011.10057 [astro-ph.HE].

[452] Michael Zevin, Mario Spera, et al. "Exploring the Lower Mass Gap and Unequal Mass Regime in Compact Binary Evolution". In: 899.1, L1 (Aug. 2020), p. L1. DOI: 10.3847/2041-8213/aba74e. arXiv: 2006.14573 [astro-ph.HE].

[453] B. -B. Zhang, Z. J. Zhang, et al. "A hyper flare of a weeks-old magnetar born from a binary-neutron-star merger". In: *arXiv e-prints*, arXiv:2205.07670 (May 2022), arXiv:2205.07670. DOI: 10.48550/arXiv.2205.07670. arXiv: 2205.07670 [astro-ph.HE].

[454] C. M. Zhang and Y. Kojima. "The bottom magnetic field and magnetosphere evolution of neutron star in low-mass X-ray binary". In: 366.1 (Feb. 2006), pp. 137–143. DOI: 10.1111/j.1365-2966.2005.09802.x. arXiv: astro-ph/0410248 [astro-ph].

[455] M. Zorotovic et al. "Post-common-envelope binaries from SDSS. IX: Constraining the common-envelope efficiency". In: 520, A86 (Sept. 2010), A86. DOI: 10.1051/0004-6361/200913658. arXiv: 1006.1621 [astro-ph.SR].